Experimental Study of Thermal and Mechanical Properties of Hydrated Lime Asphalt Concrete and Numerical Modelling of Constructed Pavement Performance

Azedin A Ibrik Hashem Al Ashaibi

School of Science, Engineering, and Environment

The University of Salford

Greater Manchester

United Kingdom

Submitted in Partial Fulfilment of the Requirements for the

Degree of Doctor of Philosophy in Civil Engineering

April 2023

ABSTRACT

The flexible pavement suffers primarily from three types of distress: fatigue cracking, thermal cracking, and permanent deformation. Thermal effects from climate are a significant in distress and early aging of pavements, and particularly in extreme weather contexts. To facilitate durable pavement design and construction, a deep understanding of the temperature profile within pavement structures becomes essential in order to assess internal stress and strain conditions together with mechanical loading from traffic. Two major fields of research are important in evaluating thermal effects on pavement structures. One relates to asphalt concrete material properties, thermal and mechanical, and their interactions. The other concerns service conditions like weather and climatic variation, which affect energy exchange at the surface. Obtaining complete and accurate material property values and characteristics for variation under coupled thermo-mechanical loading is a primary task in asphalt materials research.

Using mineral additions to improve asphalt concrete properties has been widely adopted as an effective approach. Among the mineral fillers used, hydrated lime [$Ca(OH)_2$] has been shown to offer outstanding benefits in terms of both effectiveness and cost. Earlier research at the University of Salford has revealed that replacing limestone dust, a conventional mineral filler, with hydrated lime at 2.5% of total aggregate weight optimised mechanical properties at three different temperatures. In addition to this, it is also widely reported that using hydrated lime as a partial mineral filler helps in improvement of asphalt concrete's capacity to resist the three typical distresses of constructed pavements.

To date, most research on hydrated lime modified asphalt concrete has primarily focused on improvement in mechanical properties, aiming to optimize the quantity of additive used.. There is little research involving experimental tests for thermal properties and measurements of mechanical properties under more complex conditions and under both thermal and mechanical loadings. In addition, little research has been found in literature to analyse the stress and strain condition of pavement structures constructed using hydrated lime modified concrete, and particularly, using a numerical modelling approach to understand the practical meaning and evaluate the benefits of using hydrated lime concrete under service conditions, taking account of climatic influences and weather.

In light of this background and existing deficiencies in research so far, this research project aims to conduct further experimental tests to fill gaps still to be addressed for a complete material database for hydrated lime modified concretes. Three experiment tests have been conducted and compared for two asphalt concrete mixes: one has no use of hydrated lime, the other one uses hydrated lime to replace the conventional limestone dust mineral filler at 2.5% of the total aggregate weight. The three tests are: 1) thermal property measurement; 2) fatigue testing at three temperatures; and 3) triaxial testing at three temperatures. Mathematical models have been proposed for each of the test results to characterise the measurements. These models are later implemented in finite element modelling to analyse the performance of the pavement structures constructed. Following the experimental study, to contribute a deep understanding the stress-stain conditions of the pavement which uses hydrated lime modified concrete, and the corresponding impacts on the distress resistance of the pavement's structure, mathematical modelling and numerical simulation are performed for real world service conditions using climatic weather survey data. Three modelling case studies are performed. They are: 1) use of the measured thermal properties to evaluate the temperature profile within the pavement structure under simple temperature boundary conditions; 2) use of the fatigue test results to evaluate and compare the fatigue life of the constructed pavement with and without hydrated lime modified concrete, in which a complex climatic boundary condition is introduced to simulate real-world service conditions; and 3) use of triaxial test results to predict and compare rutting deformation for the constructed pavement with and without use of hydrated lime modified concretes. The boundary conditions adopted are the same as those of the preceding case.

The research findings indicate that incorporating hydrated lime in the mineral filler of asphalt concrete improves its thermal properties. Thermal conductivity was increased by 27%, 7% and 17% for wearing, levelling and base courses respectively, while the specific heat was increased by 25%, 6% and 16% for the same courses. This led to enhanced heat transfer to the sublayer, although it had minimal impact on localized temperature profiles within the pavement structure. The hydrated lime pavement experiences approximately 1.5% less deformation and 39% lower stress levels under traffic loads alone. However, during winter, the thermal effect increases the maximum total internal tensile stress in the hydrated lime pavement by 26%. Modelling analysis reveals that the surface region of the hydrated lime pavement is primarily affected by local maximum tensile stress. Both experimental and modelling results confirm that the use of 2.5% hydrated lime in hot mix asphalt concrete significantly enhances pavement deformation resistance and fatigue life, thereby reinforcing the overall benefits of hydrated lime -modified asphalt concrete in practical applications.

DECLARATION

This thesis was completed following the Regulations and Code of Practice for Research Programs set by the University, and no part of it has been used in submission for a previous academic degree or award. I declare that the work in this thesis is my sole work, apart from where the work of others is specifically and appropriately referenced and explicitly acknowledged. Where others have assisted me or work has been collaborative, this is also clearly stated. Quotations and other content produced by others are acknowledged in the text and sources provided in the reference section. All ideas put forward in this thesis are my own, except for those cited from other sources.

Signature:

AZEDIN ALASHAIBI (5/4/2023)

ACKNOWLEDGEMENTS

Before all else, I give thanks to Allah, for the many gifts He has given.

I will forever be thankful to my father's soul, as he was my constant kind and benevolent example, and provided a firm foundation beneath my feet so that I could tread confidently the path to academic achievement, based on merit.

Words are inadequate to convey how deeply and sincerely I am thankful to Dr. Yu Wang, my supervisor throughout this journey. Dr. Wang's mentorship has been tireless and his guidance invaluable, and he has been a constant source of motivation. Dr. Wang not only opened up research opportunities and inspired me to approach the work of a researcher with confidence, but above all, provided freedom of research. In addition to his academic supervision as I developed and conducted this research project, Dr. Wang has provided a role model more broadly for me in my professional life.

My special gratitude is due to my external supervisor, Dr. Amjad Albayati, at the University of Baghdad in Iraq, who guided and facilitated my work in the laboratory, offering both moral and practical support, which I appreciate deeply and will not forget. I am also deeply grateful to Dr. Juliana Byzyka and Prof. Miklas Scholz, my co-supervisors, who gave generously of their time, knowledge and advice throughout my Ph.D. journey. I would like to extend my grateful thanks to my home nation of Libya, for financially supporting me in this course of study. I am also very grateful to my colleagues Mohammed, Ahmad and Masoud, whose friendship and support has been much appreciated in completing this journey.

Publications

- Al Ashaibi, A. *et al.* (2022) 'Thermal properties of hydrated lime-modified asphalt concrete and modelling evaluation for their effect on the constructed pavements in service', *Sustainability*. MDPI, 14(13), p. 7827.

- Wang, Y., Al Ashaibi, A., Albayati, A. and Haynes, J. (2022) 'Experimental study of temperature effect on the mechanical tensile fatigue of hydrated lime modified asphalt concrete and case application for the analysis of climatic effect on constructed pavement', *Case Studies in Construction Materials*. Elsevier, p. e01622.

- Wang, Y., Al Ashaibi, A., Albayati, A. and Haynes, B. J. (2022) 'Thermal fatigue analysis of pavement design using hydrated lime modified asphalt concrete', *The International Journal of Pavement Engineering and Asphalt Technology*. Liverpool John Moores University, 23.

- Al Ashaibi, A., Wang, Y., Albayati, A. and Haynes, I. (2022) Triaxial Test for the Asphalt Concrete Modified by Hydrated Lime and Rutting Resistance Assessment of the Constructed Pavement, "International Forum on Infrastructure and Civil Engineering" 06-08-2023 February in Porto, Portugal.

TABLE OF CONTENTS

LIST OF TABLES

LIST OF FIGURES

ABBREVIATIONS

1D	One-dimensional
2D	Two-dimensional
$\boldsymbol{a}$	Thermal Diffusivity
AADT	Annual Average Daily Traffic
AASHTO	American Association of State Highway and Transportation Officials
AC	Asphalt Concrete
ASHRAE	American Society of Heating, Refrigerating, and Air-conditioning Engineers
ASTM	American Society for Testing and Materials
AV	Air Void
B	Base Course
$\mathbf{C_p}$	Specific Heat Capacity
CB	Control Base
CBR	California Bearing Ratio
CL	Control Leveling
CTC	Coefficient of Thermal Contraction
CTE	Coefficient of Thermal Expansion
CW	Control Wearing
DSR	Dynamic Shear Rheometer
EICM	Enhanced Integrated Climatic Model
ESAL	Equivalent Single Axle Load
$\boldsymbol{\varepsilon_t}$	Initial Tensile Strain
FDM	Finite Difference Model

FEA	Finite Element Analysis
FEM	Finite Element Method
FN	Flow Number
FVM	Finite Volume Method
GHI	Global Horizontal Irradiance
GMM	Theoretical Maximum Specific Gravity
h_c	Heat Transfer Coefficient
HL	Hydrated Lime
HL2.5B	Base with 2.5% Hydrated Lime
HL2.5L	Leveling with 2.5% Hydrated Lime
HL2.5W	Wearing with 2.5% Hydrated Lime
HMA	Hot Mix Asphalt
K	Thermal Conductivity
L	Leveling Course
LTPP	Long-term Pavement Performance
LVDT	Linear Variable Differential Transducer
LVDTs	Linear Variable Differential Transformers
M-EPD	Mechanical-Empirical Pavement Design
MR	Resilient Modulus
NCHRP	National Cooperative Highway Research Program
OAC	Optimum Asphalt Content
ODEs	Ordinary Differential Equations
PCC	Portland Cement Concrete
PDE	Partial Differential Equation
PG	Performance Grading

PGS	Performance Grading System
QTM500	Quick Thermal Conductivity Meter
SHRP	Strategic Highway Research Program
TSRST	Thermal Stress Restrained Test
UGM	Unbound Granular Material
UHI	Urban Heat Island
VFA	Void in Aggregate Filled with Asphalt
VHC	Volumetric Heat Capacity
VMA	Void in Mineral Aggregate
W	Wearing Course
$\boldsymbol{\varepsilon_p}$	Permanent Deformation

CHAPTER 1 – INTRODUCTION

1.1 General background

Increased travel and communication requirements have been met by developing huge networks of roads and other infrastructure across each major continent. However, providing cost-effective and efficient road systems for safely transporting goods and people presents a range of difficult challenges, which have been addressed differently from country to country in line with conditions and requirements.

For developed nations, including the UK, paved roadways are classed as a significant national asset, contributing both socially and economically. Pavements may be classed as: flexible, with an asphalt-based structure; rigid, with a concrete-based structure; or composite. The UK's Road surfaces consist mostly of flexible asphalt pavements, with 95% of the network using this construction type. Flexible pavements are designed for the effective support of vehicle loads, which are distributed into the subgrade while not significantly deforming underlying soils. Asphalt pavements also offer reduced permeability to water, as well as providing skid resistance and reduced tyre polishing effects, and providing a smooth travel experience for the user (Nikolaides, 2014).

Existing roads networks which are between four- and five-decades old show significant deterioration, and attention has focused on how to effectively maintain or replace aging infrastructure. However, the novel approaches being applied must be capable of adapting to climate change-induced weather events of increasing severity, ranging from severe drought and high temperatures to extreme floods. Conditions in the surrounding environment and irregularly occurring heavy loads are significant factors affecting the pace at which pavements deteriorate.

Country conditions differ by regional climate, the local natural resource base, and the state of the economy. Thus, research continues into road construction approaches and materials, in order to address those conditions and meet transport requirements. A large number of studies seek to enhance current materials or investigate novel materials, in addition to further developing design approaches and technological tools to help in constructing road systems with high efficiency and cost-effectiveness. Moreover, highways authorities seek to develop road infrastructure with a long service life through minimally disruptive projects.

Modification of asphalt concrete using mineral additives as a micro-filler has been widely adopted and has proved to be effective in improving flexible pavement durability. Among the varied functional mineral additives, hydrated lime (HL) has been, for some time, of particular interest, due to its outstanding effectiveness, wide availability, and economical cost (Lesueur, Petit and Ritter, 2013; Bouron et al., 2021). A previous study at the University of Salford has found that adding 2.5% hydrated lime by overall aggregate weight to partially replace the same weight of conventional limestone dust filler can effectively enhance the fatigue resistance of hot mix asphalt (HMA) concrete to lengthen the operational lifespan of constructed pavements (Al-Tameemi et al., 2019). As a continuing work, the current research aims to further study the thermal-mechanical properties of 2.5% hydrated lime modified asphalt concrete. Both experimental work and modelling have been performed, which have not only produced some important initial first-hand data but also contribute to the modelling methodology and analytical findings for coupled thermal-mechanical effects on the pavement structure, and the benefits of the use of hydrated lime in asphalt concrete and pavement engineering.

1.2 Problem Statement

Asphalt pavements are constructed in order to provide for the safe, smooth and cost-effective transit of vehicles from one location to another. However, such pavements may perform this function at a less than acceptable level due to negative impacts from various factors, including poor quality controls when they are constructed, traffic loads, climate, and the materials' mechanical and thermal characteristics. This can lead to less serviceable pavements, or to roughening of the pavement surface, resulting in serious damage or even failure. The effects of loading on flexible pavements can lead to two main failure types: a build-up of permanent deformations (ruts); and fatigue cracking.

Flexible asphalt pavements demonstrate sensitivity to their surrounding environment, and when conditions in that environment become less suitable, this can accelerate the process of degradation in the pavement's condition. For areas in which the climate is deteriorating, the actions taken by highway authorities to respond to this issue may involve greater cost than previously. Where action is not taken, the road user incurs further cost based on increased risk, slower travel times and greater fuel use. At the country level, this can contribute significantly to the overall costs brought by climate change and could require extensions to the budget allocated to adapting to changing conditions and mitigating climate change for a sustainable future.

Failure can occur in asphalt pavements because of an altered climatic context and changing use, including significant variations in temperature from the changing climate, as well as repetitive loads from heavy traffic. While these are primary variables affecting failure in hot mix asphalt concrete pavements with hydrated lime additions, knowledge on the effects of combined thermomechanical loading remains inadequate to the task of offering reliable guidelines for the design of pavements using this type of material (Taherkhani and Tajdini 2019; Lagos-Varas, Movilla-Quesada, et al. 2022). Knowledge gaps exist within rutting and thermal fatigue analyses with HL-modified HMA concretes in conditions of varying traffic loading and temperature conditions. Moreover, there is a general lack of research concerning this type of concrete. Increased knowledge of the effects of coupled thermomechanical load on asphalt mixes' performance would be beneficial in improving that performance. Existing studies demonstrate the effectiveness of asphalt concrete mixes with 2.5% hydrated lime filler in increasing rut and fatigue crack resistance, as well as enhanced resilient modulus and lower moisture damage vulnerability (Al-Tameemi *et al.*, 2019). Nevertheless, further data and guidance is required for the application of these mixes in designing and constructing flexible pavements if they are to prove reliable in withstanding real-life service conditions. The current study addresses these knowledge gaps through experimental work which measures the thermal characteristics of 2.5% hydrated lime modified HMA concrete, comparing these with mixtures containing no hydrated lime. It investigates fatigue life when subject to various temperature conditions: namely, at 15°C, 20°C, and 25°C, compared with earlier work which was restricted to 20°C. Moreover, triaxial testing is performed to measure pavement deformation.

1.3 Aims and Objectives

The aim of this research is to extend understanding of the effect of coupled thermal and mechanical loading on the thermal and mechanical properties of hydrated lime modified HMA concrete, and use numerical modelling to predict the stress condition, fatigue life and permanent deformation of the constructed pavement structure under real world service conditions, considering both climatic and traffic factors. To fulfil this aim, the objectives below were planned for the research project.

1. Literature review of previous research on the pavement design for thermal-mechanical coupled influence. The review focuses on the effect of heat transfer theory, failure mechanisms, and on developing a thermal model for pavements and theory explaining thermal mechanical problems.

2. Experimental study to measure the thermal properties of HMA concretes using and without use of hydrated lime for mineral filler. In total, three HMA concrete mixes were investigated, which were used for the wearing course, levelling course and base course in pavement construction.

3. Experimental study to compare the fatigue life of HMA concrete using and without using hydrated lime for mineral filler. Third point loading tests were conducted for the HMA mix used for the wearing course in pavement construction. The tests were performed under three different temperature conditions.

4. Triaxial tests for HMA concretes using and without using hydrated lime for mineral filler. The triaxial tests were performed under three different temperature conditions.

5. Material property characterization for the results obtained from the above experimental tests. The proposed characterization models were implemented in numerical modelling to compare the behaviour of pavements constructed using HMA concretes with and without hydrated lime modification.

6. Numerical modelling analyses for pavement structures under coupled climatic and traffic loads conditions to compare the improvement of hydrated lime modification on the fatigue life span and rutting resistance of the constructed pavement structure in real world conditions.

1.4 Research Methodology

The experimental work presented in this thesis consisted of three phases. Firstly, two asphalt mixtures for flexible pavements were produced: one was modified with 2.5% hydrated lime (HL); and the other mixture was with no hydrated lime content, as a control. All mixes were prepared following the Marshall design protocol (Al-Tameemi *et al.*, 2019) . Each raw material used was confirmed to be in line with the American Society for Testing and Materials (ASTM). The mineral filler in the experiments consisted of hydrated lime and limestone dust, at percentages by overall aggregate weight in the mixture of 5% for the base layer mix, 6% for the levelling mix and 7% for the wearing layer mix. Hydrated lime was added to mixtures to replace 2.5% of the limestone dust by weight. It was added in dry state into the mix, using the standard process for mineral filler additives. A single asphalt cement was adopted, which has a penetration grade of 40-50. In phase two of the research, thermal properties were measured for the mixtures with 2.5% hydrated lime and with 0 % hydrated lime.

Three experimental studies were performed to compare the hydrated lime modified HMA mixes with the control mixes for their thermal-mechanical properties, including thermal conductivity, thermal capacity, fatigue life and confined deformation at three different temperatures. Using the experimental data, two-dimensional (2D) finite element modelling was further conducted to analyse a pavement structure and evaluate the effect of the use of hydrated lime modified HMA concrete in a real-world scenario on structural stress and strain condition, fatigue life, and rutting deformation, considering coupled traffic and climatic impacts.

1.5 Thesis Outline

The thesis is composed of seven chapters, as follows:

1. **Chapter One** sets out the background to the study and formulates the problem statement. It also presents the study's aims and objectives, briefly describes its methodological approach, provides a chapter outline of the thesis, and discusses research implications.

2. **Chapter Two** reviews literature related to flexible pavements, and specifically on: the effects of hydrated lime as an additive to asphalt concrete mixes, variables which lead asphalt concretes to fail, permanent deformation/rutting, and thermal fatigue and fatigue cracking.

Thermal characteristics and methods used to analyse heat transfer in flexible pavements are also reviewed here. Various approaches to temperature prediction in pavements are discussed, including finite element analysis, numerical analysis, analytical and theory-based methods, as well as probability-based and statistical approaches. Also, this chapter provides a sound scientific basis for modelling to predict flexible pavement performance, for which several concepts from advanced mathematics are needed. In this section, these concepts are introduced, along with the required notational methods for their application.

3. **Chapter Three** sets out the calculation and testing methods applied to fulfil the study's objectives. The chapter discusses the preparation of the asphalt concrete samples with hydrated lime, as well as describing how thermal conductivity is tested, and how other thermal characteristics are measured, including diffusivity and specific heat capacity. The results and discussion are also presented. The test methods for flexural fatigue cracking at three temperature levels, 15°C, 20°C and 25°C, are provided.

4. **Chapter Four** The thermal properties of hydrated lime modified asphalt concrete and modelling of thermomechanical response of pavement using hydrated lime modified concrete are presented and discussed in detail.

5. **Chapter Five** A case study is given for climatic thermal effects on the fatigue life of hydrated lime modified asphalt concrete pavement. and the chapter presents modelling for coupled thermomechanical effects on pavement structures,

6. **Chapter Six** Triaxial testing is presented, measuring resilient and permanent deformations for the mixes with and without the addition of hydrated lime. This testing was applied at three temperature levels: 20°C, 40°Cand 60°C, at different values of confined pressure. A modelling case study of pavement rutting prediction was then conducted.

7. **Chapter Seven** provides the conclusions and recommendations.

1.6 Research Implications

This study focuses on the thermal properties, fatigue life and rutting resistance of hydrated lime modified HMA concrete mixes for all types of pavement layer application. The experimental study is an extension of a previous PhD research completed at the university of Salford to perform elaborated tests for the above-mentioned material properties which are yet to be investigated but are essential for pavement design and numerical modelling analysis for the behaviours of constructed pavements. The fatigue tests were conducted under three different temperatures. The temperature effect has been characterized by a mathematical expression for the parameters of the S-N curve formulation. Rutting resistance tests were performed under tri-axially stressed conditions and different temperatures. The results reflect the material deformation behaviour under coupled thermomechanical loading, a complex situation simulating real-world service conditions. Mathematical characterization for the deformation behaviour under triaxial conditions has been proposed.

Numerical modelling was developed based on the above experimental results and characterization models, and this allows for a case investigation to be conducted to compare pavement structures constructed using hydrated lime modified HMA concrete and concrete with no hydrated lime. Through this modelling, the constructed pavement structures were analysed and compared when exposed to combined climatic weather conditions and traffic loads. The numerical results provide insights in order to understand and make assessments of how hydrated lime modified HMA concretes can be used in pavement design practice to optimise its benefits in terms of cost and service life, from construction to maintenance of pavements. Finally, this study provides a practical guide through which to understand climatic stress factors and how sensitive HMA concretes with added hydrated lime are to these stresses, as well as the effects of the changing climate for flexible pavements, and how to understand and study climate resilience in this type of pavement. In addition, the research has synthesised current understandings of known and unknown factors in sustainability and climate resilience in HMA concrete in the presence or absence of hydrated lime as a partial mineral filler. Furthermore, this study will benefit anyone studying or seeking to understand climate resilience in the flexible pavement.

CHAPTER 2 - LITERATURE REVIEW

2.1 Flexible Pavement

One of the primary functions of pavements is distributing wheel loadings to a far greater subgrade area in comparison with the wheel-pavement contact area, lowering maximal stress on the subgrade to a level where soil deformations stay inside acceptable limits within the pavement's expected service life, as shown in Figure 2.1.

The vast majority of road surfaces in most countries use flexible pavement: a structural system constructed with asphalt concrete using bituminous material for binder. An asphalt pavement can offer the same firmness as a pavement constructed from Portland cement-based concrete if comparatively large thicknesses of asphalt layers are applied using a specified temperature.

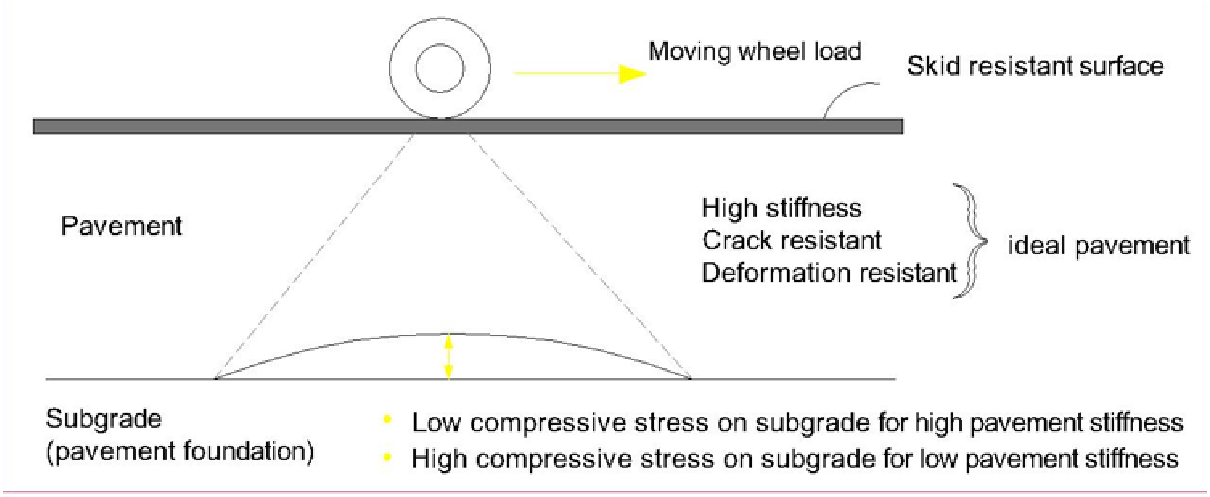

Figure 2.1 Load Spreading within a Pavement Structure (Siripun, 2010)

The modern flexible pavement structure as depicted in Figure 2.2 consists of specifically designed layers to support loading from traffic and distribute the loading to the soil bed or to specifically chosen materials in embankments. These layers' purposes are:

- **Friction Course**

The topmost pavement layer is called the friction course, and acts to prevent skidding on the surface.

- **Structural Course**

The structural course acts to distribute traffic loads to the base course.

- **Base Course**

The base course can be made up of a single or multiple layers which support the structural course while also distributing loading downward to the sub-base/sub-grade.

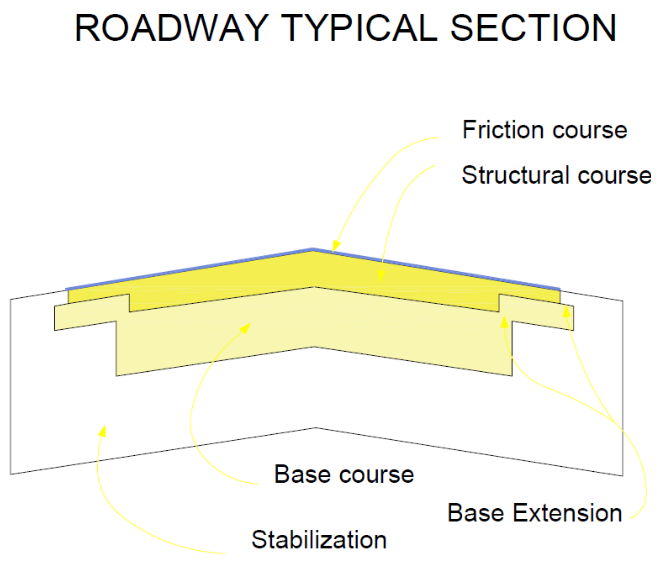

Figure 2.2 The Detail of Manual: The Flexible Pavement Layer (FDOT, 2018)

2.2 Hydrated Lime

Hydrated lime was first added to conventional HMA concrete about fifty years ago (Chachas, 1971; Little, Epps and Sebaaly, 2006). The earliest research into use of this additive investigated how it affected adhesive qualities between binders and mineral mixtures. Hydrated lime was found to be able to enhance the frost and water-resistance of HMA (Hanson, Graves and Brown, 1994; Luxemburk, 1996), due to better bitumen-aggregate binding (Iwański, *et al.*, 2015). Hydrated lime is in particular recommended for use with aggregates of an acid pH (containing more than 65% SiO2). In this case, the calcium cations of hydrated lime react with the silica compounds at the aggregate particle surfaces to generate a strong ionic bond.

Extensive laboratory studies and field tests have accumulated a large amount of data and indisputable evidence for the benefits of hydrated lime on the mechanical properties of asphalt concrete mixes, and the performance and service life of their constructed pavements under a wide range of traffic loads and environmental conditions. These include significant reduction in aging of the bitumen and increased resistance to permanent deformation (rutting), moisture damage, thermal and fatigue cracking (Petersen, Plancher and Harnsberger, 1987; Huang *et al.*, 2002; Petersen, 2009).

There are several methods for incorporating hydrated lime within asphalt mixes. Most frequently, hydrated lime is blended in a pug mill alongside the aggregate materials for treatment before placing aggregates in a drum dryer for a drum/batch plant. The addition of water then allows the hydrated lime and aggregates to react (Sebaaly, Hitti and Weitzel, 2003; Little, Epps and Sebaaly, 2006). It is also possible to add the lime immediately after adding heated asphalt after aggregates have been drum dried. Alternatively, hydrated lime can be made into slurry and added to stored aggregates, which are then left for a period to maximise the completeness of the lime-aggregate reaction.

2.3 Hydrated Lime Impacts on the Properties of Asphalt Mixtures

For the last four decades (Hicks, 1991; Lesueur, Petit and H.-J. Ritter, 2013), hydrated lime has been added to asphalt mixes to make them less susceptible to water attack, being applied in around 1 in 10 US asphalt mixes (Hicks & Scholz, 2003). It has been argued that lime offers multiple impacts as a filling material, being classed as an active component (Sebaaly, Hitti and Weitzel, 2003; Huang *et al.*, 2005; Little, Epps and Sebaaly, 2006; Lesueur, 2010). Practical applications in North America (Lesueur, Petit and Ritter, 2013) have suggested an effective hydrated lime addition rate to be between 1 and 1.5% by aggregate dry weight. According to Hicks and Scholz’s (2003) estimations, the addition of hydrated lime extends service life for pavements by between 20 and 50%.

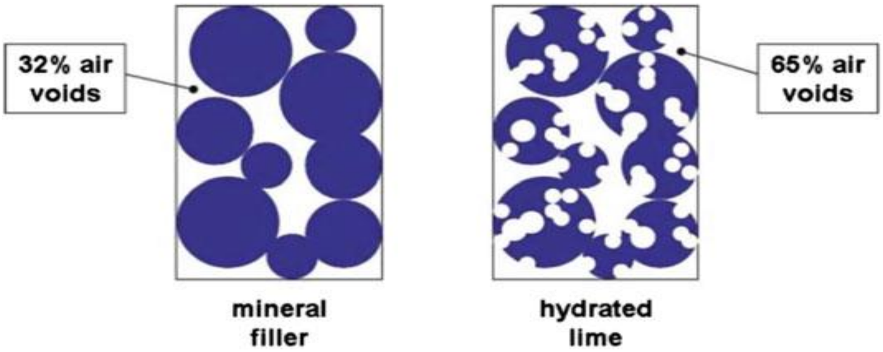

Figure 2.3 The Microscopic Structure of Hydrated Lime (right) Particles Compared with the Structure of a Conventional Mineral Filler (left) (Little et al., 2018).

Hydrated lime has a larger volume of Rigden air voids, at approximately 65% when in a compacted and dry state in comparison with 30~34% of other mineral fillers (Lesueur, Petit and Ritter, 2013). This is because of the porous nature of hydrated lime particles as illustrated in Figure 2.3.

Hydrated lime is chemically reactive with bitumen particles. It firstly interacts through neutralisation of the polar molecules of the bitumen adsorption (Petersen, Plancher and Harnsberger, 1987; Zou et al., 2013). Following neutralisation by hydrated lime, bitumen particles will be easily diffused within the mix to increase contact with the aggregate surfaces rather than being clogged together. The bitumen film on aggregate surfaces adheres more strongly to the aggregate particles due to the neutral/alkaline pH of the binder phase interfaces (Stroup-Gardiner and Newcomb, 1990; Bagampadde, Isacsson and Kiggundu, 2004).

There is ample evidence to support the effect of hydrated lime as a mineral filler across the normal spectrum of pavement temperatures. At high temperatures, its stiffening properties are enhanced, partly based on its physical filler function, with less stiffening seen at temperatures under 25 °C (Wortelboer et al., 1996; Johansson and Isacsson, 1998; Hopman et al., 1999; Lesueur and Little, 1999; Pilat, Radziszewski and Kalabiska, 2000; Lackner et al., 2005; Khattak and Kyatham, 2008), as shown in Figure 2.4.

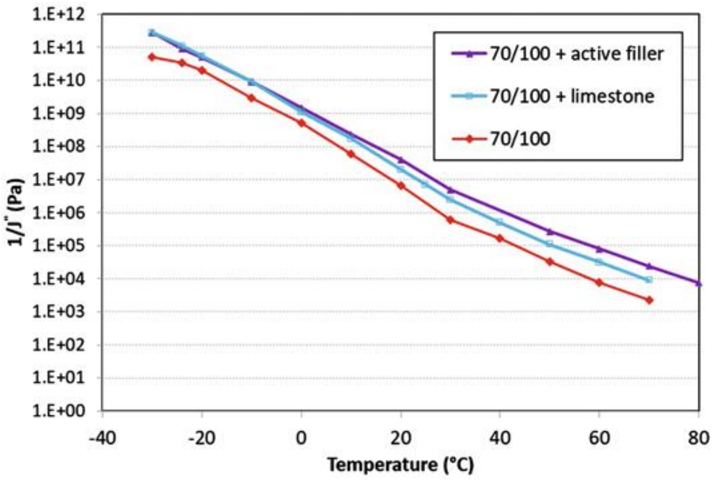

Figure 2.4 Hydrated Lime and Limestone Fillers Compared via Hypothesised Compliance at 10 Radians per Second against Temperature. Filler was added at 50% by weight, base asphalt was 70/100 penetration. In active filler, limestone was replaced 40% with hydrated lime (Wortelboer et al., 1996; Little et al., 2018).

A study of used bitumen from the field showed that aged asphalt mixes with hydrated lime were soft in comparison to reference specimens (Chachas, 1971). It has also been identified that aging bitumen modified with hydrated lime is less sensitive, with viscosity increasing at a slower rate compared to unmodified mixtures (Petersen, Plancher and Harnsberger, 1987). This is due to the fact that adding hydrated lime reduces carbonyl production while increasing the content of asphaltenes. This makes the mixture less prone to hardening (Verhasselt and Puiatti, 2004).

Hydrated lime's solvent properties allow calcium ions to be precipitated of the surface of aggregates (Lesueur, Petit and Ritter, 2013). Thus, silica sands and gravels combined with hydrated lime become more resistant to moisture damage, and wet surfaces of aggregates can therefore be treated with this substance (Blažek et al., 2000). Based on the reaction of atmospheric carbon dioxide and hydrated lime, and the calcium carbonate precipitated as a result, roughness and thus surface area is increased, and bitumen bonding is strengthened (Ramond and Lesueur, 2004). When used together with limestone aggregates, hydrated lime will not have the same impact as on silica-based aggregates, but will nevertheless enhance aggregate-bitumen bonding (Huang et al., 2005; Khattak and Kyatham, 2008). Moreover, hydrated lime has been shown to alter and stabilise the behaviour of clays.

Hydrated lime has been found to have a significant stiffening effect on mastic, as measured through rises in softening threshold (Verhasselt and Puiatti, 2004; Grabowski, Wilanowicz and Sobol, 2009). This is a highly significant factor to ensure that a bitumen mixture can resist permanent deformation: i.e., stiffer mastic makes such mixtures more resistant to rut formation. On the other hand, stiffening the mastic too much can cause the bituminous mixture to be less resistant to both thermal cracking and fatigue (Grabowski and Wilanowicz, 1997). Based on these considerations, the quantity of hydrated lime must remain within limits, and empirical determination of the appropriate amount is necessary as a controlling factor for mastic stiffening.

Adding hydrated lime enhances bituminous mixes in terms of mechanical properties (Wortelboer et al., 1996; Witczak and Bari, 2004). The additive caused increases of between 8% and 65% in a bituminous mixture's dynamic modulus when investigated over a temperature spectrum between −10°C and 54.4°C and across frequencies between 0.1 Hz and 25 Hz, as correlated with the quantity of hydrated lime added.

Wide-ranging studies demonstrate that higher concentrations of hydrated lime produce mixtures which are more resistant to rutting, for percentages between 2 % weight and 5 % weight, or in quantities of as much as 30% to replace mineral fillers within mixtures (Baig and Wahhab, 1998; Bari and Witczak, 2005; Souza, Allen and Kim, 2008) .

Hydrated lime has also been tested as an additive to HMA mix production. In general, the findings show an impact of hydrated lime in making the mixtures more frost and water resistant (Kennedy, 1983; Hesami et al., 2013), although knowledge for this type of production is more limited. Similar findings have been reported in exploratory research on the use of hydrated lime for HMA concrete mixtures. More study of this is required (Khodaii, Tehrani and Haghshenas, 2012).

In spite of a large volume of reported research on hydrated lime modified asphalt concrete, this earlier work focused on mechanical properties under different temperature and environmental exposure conditions to identify the optimum rate of addition (Al-Tameemi, Wang and Albayati, 2016; Iwański, 2020; Al-Marafi, 2021). A recent durability investigation on a pavement with five years in service showed that hydrated lime addition increased resistance to moisture damage, but that the differences between 0.5 and 1.5 % hydrated lime addition were very limited (Bouron et al., 2021). Other experimental work in laboratory showed that utilization of hydrated lime as a filler at 2.5% content demonstrated a significant improvement in the resistance of the mixture to water, freezing and thawing cracking (Al-Bayati, Oyeyi and Tighe, 2020). Another previous laboratorial study has also reported that partial replacement of a base limestone filler using 2.5% hydrated lime by total aggregate weight produced an optimum improvement in wider mechanical properties covering permanent deformation, fatigue life and moisture susceptibility Al-Tameemi *et al.*, 2016; Al-Tameemi *et al.*, 2019; Al-Bayati *et al.*, 2022) . However, so far, little research has been reported on the thermal properties of HL modified asphalt concrete, although a better understanding of the thermal response of such concrete is important and needs to be evaluated at the stage of pavement design. To fill this gap, this study first reports an experimental work conducted to determine the thermal properties of two types of asphalt concrete mixes: with and without HL modification. Thereafter, the experimental results are implemented in numerical modelling to analyse the thermal and mechanical behaviour of a pavement structure using asphalt concrete under a scenario of coupled traffic loading and environmental temperature variation.

2.4 Distress in Asphalt Pavement

Pavements frequently suffer from distress, mostly seen at the surface of roads. Distress can come from vehicle loads, climate factors, construction issues, poor maintenance and inadequate materials. Distress falls into different categories and may be functional or structural. The latter relates to issues with the pavement's load-carrying capacity compared to its intended capacity, and the former refers to issues with safety and smoothness of the travel experience. Both classes of distress should be taken into consideration, setting related failure criteria for pavement design. Pavement performance measures are needed to diagnose the type and severity of distress present in a pavement. The Federal Highway Administration published its Distress Identification Manual for the Long-term Pavement Performance Program in 2003 (Miller and Bellinger, 2003) and this addresses distress types, their identification, and data collection.

2.5 Parameters Causing Failure to Asphalt Pavement

Asphalt pavements can degrade based on a single or multiple factors, including due to traffic loads, aging of bituminous materials, and climate (Walker, 1984; Mfinanga, Ochiai and

Yasufuku, 1996; Chatti, Salama and El Mohtar, 2004; Adlinge and Gupta, 2013), deficiencies in construction, and weakness in the subgrade (Adlinge and Gupta, 2013). Frequent failure modes include alligator/fatigue cracking, transverse/thermal cracking, longitudinal, block, slippage and reflective cracking, as well as shoving, rutting, depressions, corrugation, overlay bumps, potholes and stripping/ravelling.

Deterioration of pavements can occur when subject to wheel loading, which leads the surface layer to deflect or bend (Figure 2.5). When bending occurs, this causes compression to the top of the pavement's surface layer, while the lower section of the layer stretches. When the pavement is bent repeatedly, fatigue cracks appear and the pavement fails (Walker, 1984; Lesueur and Youtcheff, 2014). Deflection increases in line with loading repetitions and axle loads, shortening the life of the pavement correspondingly. Thus, the base and surface layers are each important in offering protection from vehicle loads. Surface layers need to have sufficient strength and thickness to withstand stress from wheel loads, while base layers must both facilitate distribution of loads into the subgrade in a way that does not damage it, and prevent moisture damage occurring to the pavement (Walker, 1984). Traffic load-induced effects can include fatigue cracking, rutting, reduced skid resistance, block cracking, bleeding and reflective cracking (Lesueur and Youtcheff, 2014).

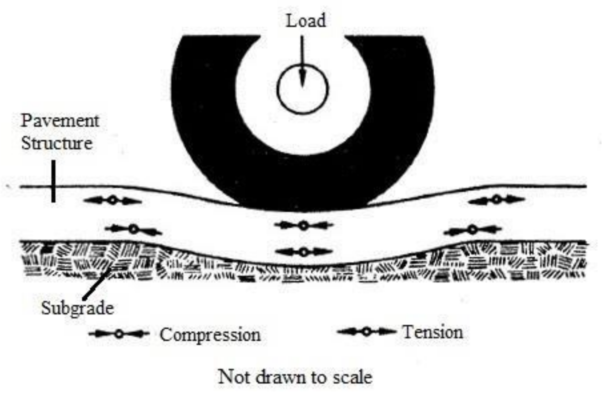

Figure 2.5 Impact of Repeated Traffic Loading in Asphalt Pavement Effect of Climate (Walker, 1984; Byzyka, 2018).

While, according to Terrel and Shute, (1989), water, temperature and air are significant for Asphalt Concrete (AC) mixtures' longevity, the first two of these climate factors have received the most attention in relation to flexible pavements. Moisture and temperatures have been found to significantly affect deformation characteristics in unbound granular material. The primary sources of thermal energy in pavements are the sun's radiation and air temperatures. Temperature in pavements also relates to the material used, and its capacity to absorb and store energy, through characteristics including albedo, thermal conductivity and heat capacity. Pavement moisture levels often depend on the height of groundwater, and precipitation. In regions with a moderate climate and access to high quality aggregate and asphalt cement mixes, vehicle loads are the primary factor in pavement degradation and the types of distress which emerge as a result. However, pavements may fail before their expected lifespan where low-quality material and high vehicle loadings combine with extreme climates/weather events.

Terrel and Al-Swailmi (1994) report various sources of damage in the environment, including water, based on groundwater and precipitation, and variation in temperatures, such as in freezing-thawing cycles, along with asphalt aging, traffic loads and approaches to pavement construction. Moreover, wind affects convection at the pavement surface, affecting temperatures. Temperature impacts on asphaltic materials' creep properties, thermal stress, rutting, low-temperature and fatigue cracking, and how the subgrade performs. Air temperatures significantly influence soils in freezing-thawing conditions (Mfinanga, Ochiai and Yasufuku, 1996). Precipitation significantly affects both asphalt and soil layers where top-down and/or bottom-up cracking allows moisture to infiltrate the pavement (Dawson, 2008). This harms asphalt bonding, weakens soils and reduces pavement supports, leading to alligator cracks, rutting, stripping (Mfinanga, Ochiai and Yasufuku, 1996; Adlinge and Gupta, 2013), potholes and flushing (Lesueur and Youtcheff, 2014). Al-Qadi et al. (2005) report environmental temperatures as a significant factor in low-temperature cracking of asphalt pavements. Low temperatures can cause shrinkage with severe aging of binders, altering pavement volumes and making materials stiffer, and raising the risk of the pavement cracking. With more rapid changes in pavement temperature, binder aging is also increased, with a higher likelihood of low-temperature cracking occurring (Kliewer, Zeng and Vinson, 1996).

As part of the Strategic Highway Research Program (SHRP), a system to grade binders by performance in low-temperature conditions was established via laboratory testing. The Performance Grading (PG) 64-32 classification for instance relates to a binder with a tolerance of 64°C from 7-day design temperatures, with crack-free performance expected at temperatures down to -32°C. Standard conversion procedures are used to measure pavement surface temperatures, and this temperature is taken as between 10 and 15°C warmer than surrounding air temperature. The SHRP design standards define in-field air temperatures.

The ideal temperature spectrum to establish thermal fatigue in pavements is considered to be -7°C - 21°C. At temperatures under -7°C, the main type of cracking which occurs is low temperature cracking, and at over 21°C, thermal cracking is not seen (Carpenter, 1983). A number of studies have investigated low-temperature cracking based on variations in temperature, and reports show that cracking becomes more frequent where pavement temperatures dip below the temperature of glass transition (Jackson and Vinson, 1996). Moreover, Shah (2004) found that the best-performing grading system (PGS) for low-temperature cracking was the PGS. In addition, Nam and Bahia (2004) state that, to establish the way asphalt concretes will perform in low temperatures, the glass temperature must be determined. Research from the Minnesota Department of Highways (2007) showed that broadly speaking, glass temperature was similar to fracture temperature in the mixes examined.

A study of pavement temperatures on long-term pavement performance (LTPP) reveals cooling rates for asphalt concrete pavement of between 1.4 and 2.7°C/hour (Alavi, Pouranian and Hajj, 2014). In an early study, Fabb (1974) investigated cooling rates of 5°C, 10°C and 27°C per hour and did not find an association between cooling rates and fracture temperatures. A later study using cooling rates of 3°C, 6°C, 12°C, 18°C, 24°C and 30°C identified that cracking temperatures are not much different when the cooling rate is above 5°C (Alavi, Pouranian and Hajj, 2014). The SHRP studied the impact of a number of variables on low-temperature behaviours in asphalt mixes using the thermal stress restrained test (TSRST). The variables used were type of binder, aggregate, air void content of mixes, aging, rate of cooling, and sample sizes. In addition, varied impacts were observed upon tensile strength. While earlier research finds that cooling rates over 5°C do not impact cracking temperatures, Bahia et al. (2012) find that cracking temperatures increase with more rapid cooling, while fracture stress is reduced.

2.6 Failure Mechanisms

Several factors can be responsible for roads failing to achieve the performance expected of them, as set out in the Distress Guide (2015). The most frequently seen failure modes are permanent deformation (rutting) and fatigue cracking (alligator cracking). Such distress can have various causes, such as poor material and ratio selection, as well as overloading from traffic in comparison to design parameters, impacts from the surrounding environment, including moisture levels and temperatures, deterioration of asphalt due to aging processes, etc. It is essential at the design stage that these factors are considered for the sake of pavement reliability and sustainability in service.

2.7 Fatigue Cracking

Cracking refers to the development of partial breakages or minor openings either at the upper surface (top-down cracks) or bottom (bottom-up cracks) of the asphaltic grades of a pavement. Through allowing water ingress in the pavement's lower layers, cracking causes pavements to deteriorate comparatively more quickly. Fatigue cracking refers to interconnected cracking which develops on the asphalt pavement's surface or stable base layer when subject to repetitive traffic loads (Huang, 2004; Zou et al., 2005). Horizontal stresses at the lower surface of the asphalt courses tend to be weaker than the material's tensile strength, but on continued repetitive loading, fatigue damage frequently develops, with upward, bottom-up propagation of cracking. Developing from the early, interconnected cracking stage, cracks increase to produce multi-faceted, sharply angled segments, with sides shorter than 30cm long. In the advanced stages, alligator patterns form: alligator and fatigue cracking are synonymous. This form of cracking is frequently seen within the wheel-paths of roads which frequently carry high-weight vehicles, but only emerges after repeated loads. Once fatigue cracking occurs, it can develop quickly with weakening in the pavement, significantly degrading the quality of the road. Fatigue cracking is classed as a significant structural problem indicating serious damage, and this cracking is assessed by measuring its area spread (in metres squared or feet squared) as a percentage of surface area of the unit. Fatigue cracking is generally rated by severity level as high, medium or low.

Tangella *et al*. (1990) summarises approaches to measuring fatigue, including a number of test types: centre-point flexural, third-point flexural, cantilever flexural, diametral, uniaxial and rotating cantilever. Third-point fatigue testing may offer greater accuracy in simulation of defects likely to emerge in practice within asphalt concrete pavements during service, as stress is placed on a greater proportion of the sample than for other tests such as cantilever testing (Tayebali *et al.*, 1992).

Laboratory testing to characterise fatigue applies either constant strain or constant stress as the controlled load. In tests which use constant stress loading, stress is maintained at the same level for the duration of the test. As repeat loading damages the test sample, the mix becomes less stiff as microcracks appear, leading to incremental tensile strain as the load is repeated. In a constant strain test, strain remains the same over multiple repeated loadings. Based on damage to the sample under repeated loads, to maintain constant strain, stress must be reduced, with stiffness being reduced based on the number of times the load is repeated (NCHRP, 2004).

2.8 Thermal Fatigue Cracking

While researchers began exploring thermal cracking in the 1960s, it was not until the following decade that thermal fatigue was shown clearly to have a role in transvers cracking *(*Al-Qadi *et al.,* 2005). In the 1970s, serious transverse crack phenomena were observed in West Texas USA, despite the lack of exposure to severe cold, and it was found that this cracking correlated with temperature-based fatigue (Carpenter *et al.,* 1974). Subsequent work pointed to a link between serious thermal cracking and different variables (Carpenter and Lytton, 1977; Anderson and Epps, 1983). There has been argument about the ability of temperature variation above the temperature-based fracture point to lead to instantaneous cracking, based on the extremely gradual load development of thermal fatigue in comparison to that associated with traffic loads. Nevertheless, a study by Sugawara and A (1984) demonstrated that the lifespan of a AC was significantly reduced through suffering thermal fatigue in comparison with traffic load, due to comparatively higher levels of thermal stress. A later work (Gerritsen and Jongeneel, 1988) in the laboratory demonstrated the potential for traffic load fatigue to occur within AC materials from low-frequency loads, as analogous to the induction of cycling loads based on temperature variation. An experimental study of thermal-fatigue-linked strain magnitude (Al-Qadi *et al.*, 2005) found that it was not load-cycle frequency but high levels of stress or strain per cycle which was significant in inducing thermal fatigue.

Jackson and Vinson (1996) evaluated potential for cracking based on thermal fatigue. They concluded that thermal fatigue distress represents a particular kind of cracking at low temperatures rather than being a mode of distress in itself. However, this conflicts with other reported work (Shahin and McCullough, 1972; Vinson, Janoo and Haas, 1989; Epps, 1999; Al-Qadi, Elseifi and Yoo, 2005), which concludes that where cracking occurs as thermal fatigue from fluctuating temperatures in a comparatively low range of temperatures, this can be classified as a separate mode. Another study involved fatigue testing through a slow frequency beam to assess how resistant mixtures were. Controlled strain modes were applied in simulating rates of thermal stress, and it was found that thermal fatigue can be responsible for pavement transverse cracking events (Epps, 1999).

In summary, fatigue cracking from traffic loading leads to failure from repetition of loading, with bottom-up progression of fatigue. In contrast, thermal fatigue cracking is a top-down process from the surface to the lowest layer (Gerritsen and Jongeneel, 1988).

Pavement design for an extended lifespan forms a key area of study in sustainable road design. As asphalt pavements age, they are prone to fatigue cracks, which are a significant factor influencing pavements' active lifespan. Based on this, designing asphalt pavements which are more resistant to fatigue is a significant concern in order to develop pavements with longer lifespans. In this study, additions of hydrated lime were made to asphalt mixtures to evaluate their effects on fatigue resistance over time.

As the number of vehicles using roads has increased, fatigue cracking frequently arises as an issue which inhibits the usual flows of passengers and goods, as well as reducing the lifespan of pavements, contributing to the growing cost of maintaining and repairing roads and bringing negative impacts for infrastructure quality and the economy (Pouranian and Shishehbor, 2019; Mantalovas and Di Mino, 2020; Wang *et al.*, 2021). Increasing vehicle loads and their impact on aging in asphalt pavements is accompanied also by thermal oxygen aging, and the two combined negatively affect pavement lifespan (Alae *et al.*, 2020; Saleh *et al.*, 2020; Zhang *et al.*, 2022). Methods of identifying damage to pavements which allow for faults to be observed rapidly and maintenance carried out have been put forward by Garbowski and Gajewski (2017) and Garbowski and Pożarycki (2017): an area which has increasingly been significant in developing a worldwide plan for sustainable development, enhancing asphalt pavements' thermal resistance in terms of aging while reducing fatigue cracking. This would extend the active lifespan of such pavements, with importance for the transport construction industry.

Previous studies demonstrate that asphalt-mix pavements incur fatigue damage mostly with asphalt mortar and asphalt constituents (Shen, Chiu and Huang, 2010; Wang, Wang and Chen, 2014). Moreover, as asphalt mixes are mixed, pavements laid and their service life proceeds, these constituents are aged by thermal oxygen processes, making them more vulnerable to fatigue damage. When pavements are designed, additives and fibrous materials are included in the mixes, making them more resistant to high temperatures (Brovelli *et al.*, 2014; Meng *et al.*, 2020). Hydrated lime is frequently added as it offers enhanced physical adsorption, is strongly chemically active, and is capable of retarding asphalt aging, as well as altering the mix's characteristics at higher and lower temperatures (Little and Petersen, 2005; Das and Singh, 2021; Mondal and Ransinchung, 2022; Wang *et al.*, 2022). Das and Singh (2017) demonstrated experimentally that when hydrated lime replaced 20% of the mineral dust within asphalt, the mixture was notably more resistant to aging from high temperatures. Moreover, Mwanza et al. (2012) report a gradual rise in asphalt's softening point as HL is added, as well as reduced ductile and penetrative properties. In another study, it was revealed through rheological performance analyses that adding HL improved asphalt mastic's fatigue and permanent deformation resistance (Mohammad *et al.*, 2000).

A number of recent studies have examined fatigue performance in asphalt mixes based on one theory only, and this limits the comparability of findings due to limited control of these. However, this concern has been addressed through widespread research globally by different authors. Izadi *et al.* (2018) provide precise characterisation of asphalt mix properties across various stages of aging via the dissipated energy approach, in which dissipation of energy under repetitive loads and fatigue response are precisely characterised. Liu *et al.* (2020) assessed fatigue properties for asphalt concretes under different load frequencies and in various age conditions by applying an S-N fatigue equation. Work reported by Lv *et al.* (2020) identified aging as the most significant factor in initial elastic modulus for an asphalt mixture, and energy dissipation stabilisation rate and fatigue life were clearly correlated. Sun *et al.* (2015) also demonstrated that fatigue resistance was strongly linked with self-healing performance in asphalt mixes. Diao *et al.* (2023) state that fatigue resistance can be assessed using 3rd point bending fatigue testing. Their findings show that adding HL can enhance asphalt binders' adhesive qualities, and strongly enhance fatigue resistance in mixes subject to thermal aging. This mixture gave the strongest enhancement when tested across several conditions, and improved fatigue life by 53%. A multi-scale fatigue performance assessment revealed the inadequacy of initial stiffness modulus as an index to directly evaluate fatigue performance. In contrast, accurate characterisations of mix fatigue performance pre- and post-aging are achieved using the stable dissipated energy change rate.

In brief, the current study used hydrated lime to modify asphalt mixes, before evaluating fatigue characteristics. Third point bending fatigue testing was carried out to comprehensively assess fatigue characteristics in these mixtures, focusing on fatigue resistance.

2.9 Permanent Deformation (Rutting)

Ruts are depressed areas running lengthways along wheel tracks and are seen in roads' transverse profile. Ruts may allow water to infiltrate unbound subgrades through the asphalt courses, and in more extreme cases where deformation has affected the subgrade, water will be retained where the pavement and subgrade meet, accelerating the pavement's deterioration. In low temperature conditions, water remaining on the pavement's surface due to rutting may form ice sheets, decreasing skid resistance. Hydroplane risk is also enhanced. Environmental conditions and vehicle loading cause rutting, with heavy loads significantly contributing to this process through shear deformations, compaction and abrasion. Climatic factors such as temperature, freezing-thawing events and temperatures may influence the materials used in pavement construction and therefore exacerbate rutting processes. Varied mechanisms lead to different types of rut, with 4 rutting categories put forward by Dawson and Kolisoja (2006) based on wheel shear, subgrade weakness, damaged particles and compaction, for various classes of road and loading conditions. While ruts are produced through complex mechanisms, surface rutting is generally understood to fall into two categories: rutting of the asphalt; and of unbound granular material (UGM). The former includes both rutting through consolidation and through material flow (Kandhal and Cooley, 2003). In consolidation rutting, the material is condensed along one dimension or vertically compressed, with no asphalt shoving taking place, in comparison to material flow in the lateral plane, which is caused by too few air voids or poor shear strength (Witczak, 2007). Where the mixture is thoroughly compacted, densification has a low impact in comparison with shear deformation, meaning that asphalt ruts would generally form due to shear deformation for this pavement (Long, 2001). Creep recovery testing was designed for assessment of resistance to rutting in asphalt mixes through examining creep deformation for mastics and bitumen (Elnasri, Airey and Thom, 2013; Elnasri, Thom and Airey, 2016). Asphalt ruts are formed as permanent deformations build up within the asphalt layers and bitumen base layers. Asphalt concretes have viscoelastic properties, and their stiffness is variable based on the concrete's temperature, falling significantly as temperature rises. In addition, winds increase convection, influencing pavement temperatures. Most asphalt rutting occurs at higher temperatures and is increased under high traffic volumes which pass slowly over the surface. The higher temperatures stemming from climate change could therefore contribute to increased asphalt rutting.

2.10 Assessing Rutting Resistance in Asphalt Mixtures

Material testing aims to replicate conditions which pavements experience in the field. Various testing approaches have been developed which assess pavement rutting. Relevant organisations and research groups have applied several of these test approaches extensively in assessing permanent deformation (Witczak, 2002), including the following:

• Uniaxial stress test: this test applies creeping, repeat or dynamic loads on samples in the form of unconfined cylinders.

• Triaxial stress testing: this test confines sample cylinders by applying creep, dynamic or repeated loads.

• Diametral testing: this is applied to mould samples with creep or repeat loads applied.

• Wheel track tests: these tests apply repeated wheel passes with a specified loading, either on a segment of pavement in the field or on a slab specimen.

2.11 Uniaxial Repeated Load Test

The uniaxial repeated load test is the most frequently applied testing process when assessing rutting within asphalt mix concrete (Nascimento, 2008), and is widely utilised in rating different mixtures in terms of their susceptibility to this issue, although it is unsuitable for use in predicting performance. For this test, compression stress gave a 0.1 s haversine pulse shape with 0.9 s rest afterwards. At 60°C, stresses of 204 and 10.2 kPa were recorded for haversine and resting periods respectively (Witczak, 2002; Nascimento, 2008). The curve showing accumulated permanent deformation (ε_{p}) against cycle number is zoned into three areas. Within the primary zone, there is a higher rate of sample densification, while the secondary zone forms a testing phase, and strain rate is lower at this stage. Finally, sample failure occurs in the curve's tertiary zone. The flow number (FN) indicates the cycle number at which this final zone begins, with a negligible rate of plastic deformation at this point (Witczak, 2002). Testing ceases on reaching the flow number, at a cycle number of 10,000 or at the point where unconfined returns a finding threshold of 2% (Dongré, D'Angelo and Copeland, 2009) .

2.12 Triaxial Test

When bituminous layers within pavements are mechanically damaged, this can either be based on crack or rut formation. The chief cause of such issues is traffic: particularly slow-moving, heavy vehicular traffic. Rutting forms longitudinally based on permanent deformation in the layers of the pavement and makes roads less comfortable to use and more dangerous. Road rutting falls into two categories: rutting with a significant radius size, which is linked to permanent deformations within the subgrade or granular base layer materials; or ruts with smaller radii which are linked with bituminous layer permanent deformation, which generally occurs within or near to wheel paths.

There are three primary challenges involved in the study of bituminous-layer ruts based on permanent deformation. Firstly, loading is a complex factor, occurring locally and dynamically and displaying significant geometric complexity as well as a lack of homogeneity in pressure distribution. Secondly, the bituminous mix materials behave in a complex manner in terms of flow, being based on bitumen as a viscous substance and granular structural components, giving them structural heterogeneity. Considering flow, bitumen-based mixes have properties of viscoelasticity, thermo-susceptibility, and viscoelasticity in their behaviours, with reactions also depending on triaxial loading pathways as well as cyclical loads, as with granular material. Thirdly, the extremely small scale of cyclical strain alongside the extremely long timescales and cycle numbers makes it challenging to reproduce conditions for laboratory-based studies of bituminous concrete.

It is important to define representative triaxial stress pathways for laboratory studies of rutting within bitumen-based mixtures. Load pathways produced through the movement of wheel loading on a pavement present challenge when trying to replicate these in laboratory conditions (Gabet *et al.*, 2011; Perraton *et al.*, 2011), through inducing cyclical, time-developing three-dimensional load pathways which have stress rotations. Accurate simulation of these loads are challenging using thermo-controlled triaxial equipment or other widely-used presses. Therefore, approaches in bituminous mix design emphasise empirical testing and simulation, including French Wheel tracking testing for example. While this type of testing can more realistically replicate load conditions, it is not possible to identify flow properties for materials in this test, because of the lack of homogeneity and complexity of the stress condition within the sample. Therefore, triaxial testing with a homogenous sample is more suited to rheological studies.

Rutting is one of the most common distresses for asphalt pavements (Zhang, Xie and Zhao, 2021). It occurs due to inadequate shear strength within pavements when exposed to high temperatures and repetitive traffic load (Du *et al.*, 2018; Fan *et al.*, 2022). Asphalt concrete mixture design and its composite material modification play the primary role in improving asphalt pavement rutting resistance (Guo and Nian, 2020). In addition, layer structure design and construction also influence the high-temperature performance of asphalt pavement because of their effects on the heat dissipation and retention of the whole structure (Jiang *et al.*, 2021). Modifying asphalt concrete using mineral additives as micro-fillers has been widely adopted and proves to be effective in improving flexible pavement durability. Among the varied functional mineral additives, hydrated lime (HL) has been of particular interest due to its wide availability and economical cost. Previous studies have shown that partial replacement of conventional limestone dust mineral filler using HL at a rate of 2.5% of total aggregate weight produces optimistic improvement in the resistance of HMA concrete to permanent deformation (Al-Tameemi *et al.*, 2016), moisture susceptibility (Al-Tameemi *et al.*, 2019) and fatigue distress (Wang et al., 2022).

The rutting resistance of asphalt concrete is determined by both the bitumen binder rheology and the cohesion force between aggregate particles. Two parameters, called the rutting parameter, $G^*/\sin\delta$, and zero-shear viscosity (ZSV), are commonly used for the binder rheological effect (Laukkanen *et al.*, 2015; Singh and Kataware, 2016). For final asphalt concrete mixtures, the flow number parameter has been proposed to assess their rutting potential (McLean and Monismith, 1974; Islam, Kalevela and Nesselhauf, 2019). Both uniaxial and triaxial penetration tests are commonly used to evaluate the flow number for the performant deformation behaviour of asphalt concrete (Bonaquist, 2012). However, the triaxial repeated load permanent deformation test can not only be used to check the quality of mixture design, but also provide parameters to predict the rutting depth of asphalt pavement (Zhang *et al.*, 2016; Zhu *et al.*, 2016; Huang, Zhang *et al.*, 2018) and the variation of the resilient modulus (Fedrigo *et al.*, 2018) under realistic complex stress conditions. Triaxial testing has also been employed to investigate the thermomechanical behaviours of asphalt concrete (Huang *et al.*, 2019).

In spite of the large number of laboratory and field studies on HL modified asphalt concrete (Sebaaly *et al.*, 2003; Bouron *et al.*, 2021), specific investigation of its rutting behaviour is still insufficient. In particular, the knowledge of the materials' plastic and elastic properties under coupled climatic thermal and traffic complex mechanical conditions is still limited. There is, so far, little experimental research on triaxial tests for HL modified asphalt concrete. Most of the reported work on the characterization for the properties in response to the coupled thermomechanical influence is inadequate to provide specific guidance for pavement design in trying to use HL modified asphalt concrete (Taherkhani and Tajdini, 2019; Lagos-Varas *et al.*, 2022). To contribute more knowledge to bridge this gap, this research reports an experimental study using triaxial tests to compare the elastoplastic behaviour of HMA concrete mixtures under coupled thermal and mechanical loads.

2.13 Thermal Properties

Cracking/distress which is thermally induced is defined through various thermal characteristics, including the Coefficient of Thermal Expansion (CTE), Coefficient of Thermal Contraction (CTC), specific heat capacity (C_P) and thermal conductivity (K). Moreover, the Mechanistic-Empirical Pavement Design Guide (MEPDG) looks at CTC for prediction of low temperature asphalt pavement cracking. The values for C_P and k form main inputs for MEPDG, as well as being applied in temperature prediction and moisture profile prediction for structural and sub-grade parts of pavements across their design lifespan (Chintakunta, 2007; Baus and Stires, 2010). Thermal conductivity (K) is a measure for heat flux which flows within materials at the unit temperature gradient, measured as (W/m K). C_P as the material-specific heat capacity in (J/kg K) measures the energy as heat needed for the unit temperature to be increased for the body's unit mass. Thermal inertia is termed thermal diffusivity ($\boldsymbol{a}$). The thermal diffusivity coefficient describes how rapidly alterations in a material's temperature occur under variable surrounding thermal conditions, being given by:

$$a = \frac{K}{\rho C_P} \qquad \text{Equation (2-1)}$$

Where:

K= Thermal Conductivity, W/m K.

ρ = Density, kg/m3; and

C_P= Specific Heat Capacity, J/kg K.

Among other characteristics, thermal diffusivity is considered in predicting pavement temperatures, capacity for frost to penetrate, thaw settlement and overlay compaction time estimates (Hildebrand, 1986; Luca and Mrawira, 2005). Influences on asphalt's thermal conductivity include the kind of mix used and the aggregate used (Andersland and Ladanyi, 2004), gradation of aggregate (Mirzanamadi, Johansson and Grammatikos, 2018), the denseness of the mix (Hassn et al., 2016), temperature of the mix (Chadbourn et al., 1996) and mix moisture levels (Hassn *et al.*, 2016; Mirzanamadi, Johansson and Grammatikos, 2018). Thus, Hassn *et al.* (2016) identify the potential for thermal conductivity to rise as density rises, due to reductions in air void presence in the mix. Moreover, the variables of moisture and frost can lead to greater thermal conductivity in asphalt, according to Mirzanamadi, Johansson and Grammatikos (2018). At the same time, it has been suggested that thermal conductivity in asphalt could be reduced when at 25° C or over (Chadbourn *et al*., 1996). Thermal conductivity influences the parameters thermal diffusivity and specific heat capacity, with Hassn *et al.* (2016) finding that with increased air void levels in conjunction with reduced thermal conductivity, reductions occur in thermal diffusivity and specific heat capacity.

- **Thermal Conductivity (K).**

The thermal conductivity of a material determines how effectively it conducts heat. When the thermal conductivity is higher, heat flux can be transferred to the sublayer with greater efficiency. In general, common equation applications and laboratory tests are applied to determine values of K and C_P. K can be determined through either steady or non-steady state methods. Steady state testing measures conductivity at a time where equilibrium has been reached, and therefore, enough time is required for materials to reach this condition. In comparison, findings from non-steady state approaches are less time-consuming because the measurement of thermal conductivity is made as materials heat (Crompton, 2006).

The NCHRP provides guidelines for thermal conductivity levels in pavements in their Report 602: Calibration and Validation of the Enhanced Integrated Climatic Model (EICM) for Pavement Design (Zapata and Houston, 2008), summarised as follows: first, acceptable dry thermal conductivity in HMA pavements ranges between 0.44 and 0.81 BTU/(hr•ft•°F) (0.76 - 1.40 W/(m•°C)). For each section, an assumption of 0.67 BTU/(hr•ft•°F) (1.16 W/(m•°C)) was given as a default level. The database does not provide information on dry thermal conductivity for unbound material. Default levels in the EICM stem from AASHTO soil classifications. Default thermal conductivity was presented following Tye and Brazel (1969), Farouki (1982) and Yaws (1997), and are in line with a value of 1.16 for asphalt concrete. Typically, k and C_P values are determined through laboratory testing and numerical analysis. There are several test standards to measure k value, such as the Hot Wire Method (ASTM C1113), Guarded Heat Flow Meter Method (ASTME1530), and Guarded Hot Plate Method (ASTM C177) (Islam and Tarefder, 2014, 2015). Table 2.1 and Table 2.2 offer further published estimations for thermal conductivity, and these are similar in level to those suggested in the EICM. It can be observed that k and C_P value ranges are 0.5-2.890 W/(m K) and 0.63–2.1 kJ/(kg K) respectively.

Numerous studies have demonstrated that the thermal properties of pavement materials have an impact on the temperature of the pavement surface (Chen, Wang and Zhu, 2017; Gui *et al.*, 2007; Wu *et al.*, 2018; ShengYue *et al.*, 2014). The thermal properties of pavement materials that are commonly discussed and have an influence on pavement temperature are primarily related to thermal conductivity and specific heat capacity.

Table 2.1 demonstrates that the thermal conductivity of asphalt concrete is not a constant value. This variability is attributed to the fact that asphalt concrete is a composite or granular material. The thermal conductivity of pavement materials is dependent on various factors, such as the thermal properties of each component material, mass and volumetric composition, presence of air voids, gradations, and even microstructures. Obtaining the thermal properties of pavement materials typically involves experiments or simulations, and a wide range of values has been reported in the literature (Mrawira and Luca, 2002 Côté, Grosjean and Konrad, 2013, Chen, Wang and Li, 2015, Ren *et al.*, 2018). Consequently, inaccurate estimation of these values can result in unforeseen errors when predicting pavement temperature.

The thermal properties of a pavement have an impact on the distribution of temperature within the pavement structure. Research has shown that there is an inverse relationship between the pavement surface temperature and the thermal conductivity of the surface layer. In contrast, the mid-depth temperature is positively correlated with the thermal conductivity of the surface layer (Zhang, Wang and Ren, 2017). In general, lower thermal conductivity of a pavement tends to result in higher surface temperatures during the daytime and lower surface temperatures during the night-time (Stempihar *et al.*, 2012; Hu *et al.*, 2017). By enhancing the thermal conductivity of the pavement, it becomes possible to reduce the maximum surface temperature and the minimum bottom temperature, while increasing the minimum surface temperature and the maximum bottom temperature. This explains why incorporating aggregates with higher thermal conductivity, like quartzite aggregates, in the pavement surface layer can contribute to lowering of the peak temperature of the pavement's surface (Dawson *et al.,* 2012). Moreover, an increase in the thermal conductivity of pavement materials leads to a reduction in the thermal gradient across the depth of the pavement (Denby *et al.*, 2013; Dehdezi, 2014), Similarly, increasing the thermal conductivity of pavement materials also reduces the daily temperature amplitude at the surface of the pavement (Shi *et al.*, 2019). Recent research has demonstrated that the temperature of pavement can be manipulated by employing a specific combination of layer materials with varying thermal conductivities. It has been observed that implementing low-conductivity asphalt in the top layer and high-conductivity asphalt in the bottom layer can effectively lead to significant reductions in maximum temperature (Yinfei, Qin and Shengyue, 2015; Yinfei, Shengyue and Jian, 2015; Chen, Wang and Zhu, 2017).

Table 2.1 AC Pavement Thermal Conductivity Value Reported in Previous Studies.

Thermal Conductivity (W/m. k)	**Reference Source**
0.75	Engineering ToolBox (2016a)
0.896	Carlson *et al.* (2010)
1.16	Zapata and Houston (2008)
1.21	Corlew (1968); Gui *et al.* (2007)
2.00	Chadbourn *et al.* (1998); Gui *et al.* (2007)
2.88	Xu and Solaimanian (2010)
0.800–1.600	Highter (1984); Carlson et al. (2010)
1.620-2.060	Luca and Mrawira (2005)
1.30-01.420	Tan, Low and Fwa (1992)

0.800-1.600	Highter (1984)
2.280-2.880	Kavianipour and Beck (1977)
0.740-2.890	Solaimanian and Bolzan (1993)
1.370-1.750	Wolfe, Heath and Colony (1980)
0.800-1.420	Jordan and Thomas (1976)
1.210	Barber (1957)
1.464	Islam and Tarefder (2014)
1.00-2.50	Qin (2016)
0.500-2.500	Chen, Wang and Xie (2019)
1.133-1.920	Byzyka, Rahman and Chamberlain (2021)
0.740	Acharya, Riehl and Fuchs (2021)
2.742	Sun *et al.* (2022)

- **Specific Heat Capacity**

Specific heat capacity is defined as the energy required to raise the temperature of unit mass of the substance by one degree. This means that lower specific heat capacity can raise pavement temperature with the same amount of heat input (Cengel and Heat, 2003). The association between heat content alteration and temperature alteration in a mass m (kg) can be shown through Equation 2.2.

Table 2.2 shows specific heat capacity values reported in previous studies.

$$\Delta Q = m\ \mathrm{C_P}\ \Delta T \qquad \text{Equation (2-2)}$$

Where:

ΔQ = heat increase or loss, J;

C_P= specific heat capacity, J/kg K; and

ΔT = temperature change measured, K.

Additionally, expression of specific heat capacity may be done using Volumetric Heat Capacity (VHC) (J/m3 K) in the following:

VHC= Density (ρ) × Specific heat capacity ($\mathbf{c_p}$) Equation (2-3)

Table 2.2 AC Pavement Specific Heat Values Reported in Previous Studies

Specific Heat (kJ/(kg.k))	**Reference Source**
0.920	Zapata and Houston (2008)
0.920	ToolBox (2016)
0.921	Cengel and Heat (2003); Gui *et al.* (2007)
0.866	Chadbourn *et al.* (1998); Gui *et al.* (2007)
0.880	Xu and Solaimanian (2010)
1.475-1.853	Luca and Mrawira (2005)
0.800-1.60	Highter (1984)
0.879-0.963	Wolfe, Heath and Colony (1980)
0.920	Barber (1957)
2.110	Islam and Tarefder (2014)

0.700-1.200	Qin (2016)
0.934-2.100	Chen, Wang and Xie (2019)
0.699-1.339	Byzyka, Rahman and Chamberlain (2021)
0.633	Acharya, Riehl and Fuchs (2021)
0.923	Sun *et al.* (2022)

The specific heat capacity of pavement materials also plays a role in predicting temperature outcomes. Research has shown that increasing the heat capacity can result in a decrease in the peak temperature of the pavement surface and a delay in the occurrence of the peak hour (Zhang, Wang and Ren, 2017). Simultaneously, the daily minimum temperature of the pavement can be increased by enhancing the specific heat capacity (Gui *et al.*, 2007). As the thermal diffusivity increases, the temperature variation from the top to the bottom of the pavement decreases. Conversely, lower thermal diffusivity promotes a more stable temperature distribution at shallower depths within the pavement (Dehdezi, 2014). Based on the preceding discussions, factors such as pavement albedo, emissivity, and thermal properties significantly influence the temperature distribution within the pavement. It is essential to exercise caution when determining these parameters to achieve accurate predictions. Randomly selecting these parameters based on typical values can lead to unexpected errors. While the thermal properties of pavement materials can be obtained from the reported typical range in existing literature, this range often lacks the precision required for accurate predictions. There is a lack of practical guidance for selecting material thermal properties based on factors such as material category, gradation, age, water content, and other relevant information. Furthermore, the thermal contact resistance between pavement layers, an important thermal property, has not been thoroughly studied or considered in previous research. Most studies assume perfect thermal contact between pavement layers, which may not reflect the actual conditions accurately.

The accurate determination of thermal properties is crucial for assessing pavement performance and designing effective pavement systems. To achieve this, various factors such as material category, gradation, age, and water content should be considered. However, the existing literature lacks practical guidance on selecting material thermal properties based on these parameters. Additionally, the significance of thermal contact resistance between pavement layers has often been overlooked in previous studies.

Also, the environmental impact on asphalt pavements is a significant concern, particularly with regard to factors such as temperature variation. Various physical and chemical phenomena come into play, causing fluctuations in temperature that affect the performance and condition of asphalt pavements (Buttlar *et al.,* 2006; Souza and Castro, 2012; Xue *et al.,* 2013), moisture diffusion (Luo *et al*., 2018; Najmeddine and Shakiba 2021), and asphalt aging (Cui *et al*., 2020; Omairey *et al*., 2021) can occur in an asphalt pavement and impact its mechanical behaviour under service conditions. Among these environmental effects, the influence of coupled temperature-stress fields appears to be still limited, it is worth noting that there is a lack of studies that have integrated these coupled temperature-stress fields into multiscale modelling approaches, and especially for the hydrated lime-modified asphalt concrete.

The summary in Table 2.3 outlines the published literature that reports estimates for pavement density levels.

Table 2.3 AC Pavement Density Value Reported in Previous Studies.

Density(gm/cm^3)	**Reference Source**
2.238	Corlew (1968); Gui *et al.* (2007)
2.1-2.400	Solutions (2016)
2.15–2.500	Solutions (2016)
2.100	Chadbourn *et al.* (1996); Gui *et al.* (2007)
1.500	Cengel and Heat (2003); Gui *et al.* (2007)
2.110	Islam and Tarefder (2014)
2.100-2.350	Qin (2016)

2.261-2.320	Byzyka, Rahman and Chamberlain (2021)
2.243	Acharya, Riehl and Fuchs (2021)
2.173	Sun *et al.* (2022)

- **Coefficients of Thermal Expansion and Contraction (α-value)**

To calculate thermal strains produced by changing temperatures, the α-value must be identified. Materials lengthen when subject to changing temperatures, and therefore, α-values become longer/shorter along with unit temperature changes, as they represent strain for each degree of temperature alteration.

A number of published studies examine coefficients of thermal expansion (CTE) and contraction (CTC) for asphalt concrete. Stoffels and Kwanda's (1996) study involved patching resistive strain gauges onto specimen cylinders of 51 mm thickness and 152.4 mm diameter and recording how far the diameter of specimens was reduced as the temperature was lowered from zero to -25 °C. Tests were applied to cylinders gathered in the field across several sections of highway. The authors report CTC values of between 1.33x10-5 and 2.97x10-5 per ˚C horizontally (at 90° to compaction orientation). The findings reveal a linear variation in strain by temperature. No significant effect was found for variables including location and direction of the gauges or material used.

Mehta *et al.* (1999) applied Linear Variable Differential Transformers (LVDTs) in their study measuring CTC values to determine the CTC of cylindrical core samples of 150 mm diameter and 50 mm thick from 0˚C to -25 ˚C. The CTC value was reported to be between 1.58x10-5 and 2.33x10-5 per ˚C. The authors used the same methodology as Stoffels and Kwanda (1996), but applied LVDTs and not resistive strain gauges.

A study by Zeng and Shields (1999) involved AC beams 51 mm wide and deep and 340 mm long, for testing at temperatures ranging from -40 to 40 °C. LVDTs were applied external to the environmental chamber. Using one type of asphalt mix, the authors found CTC to be

1.35x10-5 per ˚C, while CTE was 2.62x10-5 per ˚C. On investigating the impact of temperature on the two sets of values, the authors found that these did not support thermally linear values for CTC or CTE.

Mamlouk et al. (2005) prepared specimen beams 50 mm wide and deep by 390 mm thick, both collected from the field and compacted in the laboratory, and tested these within an environmental chamber, with LVDTs attached externally to the chamber via a rubber plug. The samples were tested at temperatures of between 0 °C and 60 °C, finding CTC values of 3.745x10-5 per ˚C and CTE of 3.786x10-5 per ˚C. Various materials were tested, with air void volumes from 3.6 % to 8.0 %. The authors' conclusions were that thermal coefficients were influenced by material used, but changes in CTE and CTC values were not correlated to specific materials, and it is possible that the wide range of air void volumes led to the differences found across results.

Xu and Solaimanian (2008) measured CTC and CTE for specimen cylinders at between -5 ˚C and 40 ˚C. The samples were exposed to temperature fluctuation within an environmental chamber, measuring deformation with an extensometer. The authors produced a finite element model simulating thermal strain and stress within samples to assess recorded values for CTE and CTC, determining these values in the vertical plane.

Various studies have examined types and proportions of aggregates and their impact on CTE and CTC in Portland Cement Concrete (PCC) (Won, 2005; Jahangirnejad, Buch and Kravchenko, 2009; Naik, Kraus and Kumar, 2011), and their findings show significant impacts from both parameters. It follows from this finding that the type of aggregate would also affect CTE and CTC in asphalt cement. For asphalt binders, CTC and CTE are $1.1\text{x}10^{-4}$ per °C, while for rock, the value is between $0.4\ \text{x}10^{-5}$ and $1.3\text{x}10^{-5}$ per °C (Al-Ostaz, 2007; Timm, Turochy and Davis, 2010).

From the above review, it is seen that each study examined CTE and CTC values in a single direction, with most studies assessing values horizontally, at right angles to compaction direction, and only Xu and Solaimanian (2008) measuring these values along the vertical orientation. Moreover, impacts from cross-anisotropy, considering the vertical and horizontal values, remains unclear, as do impacts from aggregate grades and geological properties, and air voids.

Zou et al. (2005) and Bayat and Knight (2010) each assessed thermal strain within an instrumented section of road, but the α-value in the field was not recorded. Moreover, these studies do not present the process used to calibrate the strain gauge. Another problem could arise from non-linear effects of temperature on α-value, with type and grade of aggregate and air voids also having potential impacts on findings. Therefore, these findings are not suitable for use in the current study, as α-value is dependent on the temperature of materials. Based on this, there are no usable findings for CTC and CTE in the field which may be applied in measuring thermal strain across varied temperatures in the field, leaving a gap in the literature.

Islam and Tarefder (2015) measured α-value for both laboratory compacted and field specimens of asphalt across a range of temperatures for use in varying stages, and report that Equations 2-4 and 2-5 below, derived from a best fit curve for the study data, can identify CTE and CTC values in με/°C for various temperatures (in degrees Celsius):

$$CTC = -1.6 \times 10^{-8}T^2 + 9.5 \times 10^{-7}T + 1.7 \times 10^{-5} \quad \text{Equation (2-4)}$$

$$CTE = 4.3 \times 10^{-9}T^2 - 2.3 \times 10^{-7}T + 2.8 \times 10^{-5} \quad \text{Equation (2-5)}$$

Where:

CTC = Coefficients of Thermal Contraction

CTE = Coefficients of Thermal Expansion

T= temperature in °C

2.14 Heat Transfer Theory

Temperature changes in pavements occur as a physical phenomenon in line with heat transfer theory, and it is essential to understand this theory in detail in order to develop predictive modelling for pavement temperatures. Heat transfer theory is also applicable in empirical modelling through statistical analyses, making clear the major variables involved in pavement temperatures. This section describes heat transfer theory as applied in predicting pavement temperatures. Heat is most frequently transferred through radiative, conductive and convective processes (Annaratone, 2010) .

Figure 2.6 illustrates heat transfer within pavements, in which conduction is the primary mechanism. However, transfers between the surface of the pavement and the surrounding medium occur via convection and radiation.

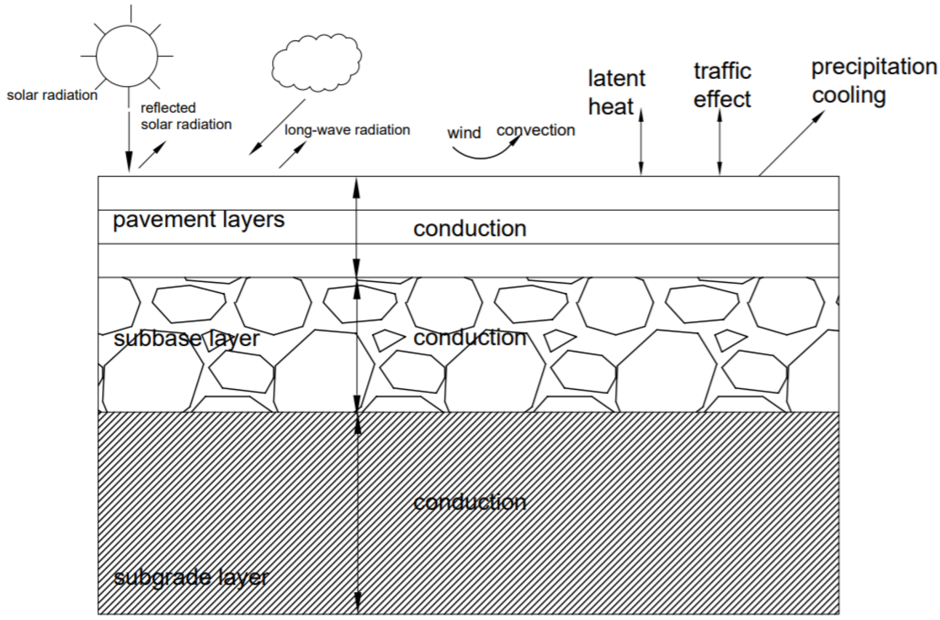

Figure 2.6 Illustration of Heat Transfer in the Pavement-Environment System.

2.14.1 Conduction

Cengel and Heat (2003) define conduction as energy transfer from particles in a material which have greater energy to neighbouring particles with lower energy levels, as these particles interact. Within solids, free electron movement is generally responsible for conducted heat in metals, and molecular vibration within lattices conducts heat in non-metallic solids. Figure 2.7 shows heat conduction rates through a plane layer with Δx thickness, with A as the cross-section, and a difference in temperature of $\Delta T = T_2 - T_1$, being controlled by Fourier's law, as found in the following equation (2-6):

$$Q_{Conduction} = k\,A\frac{T_1 - T_2}{\Delta x} = -k\,A\frac{\Delta T}{\Delta x} \qquad \text{Equation (2-6)}$$

Where:

$Q_{Conduction}$ = rate of heat conduction (w)

A= surface area (m^2)

K = thermal conductivity of the material (w/mk)

$\frac{\Delta T}{\Delta x}$ = temperature gradient in the direction of heat flow for ondimension

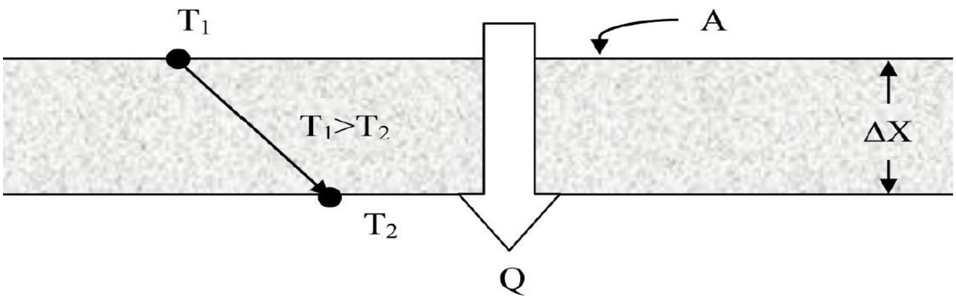

Figure 2.7 Heat Conduction through a Plane Layer

2.14.2 Convection

Cengel and Heat (2003) define convection as the transfer of heat energy between moving liquid/gas and a neighbouring solid material. Newton's law of cooling governs transfer rates, as is shown below:

$q_{Convection}=h_c\ (T_s\text{-}T_{air})$ Equation (2-7)

Where:

$Q_{Convection}$= surface-to-air convective heat transfer for 1 unit area (W/m2).

h_c= convective heat transfer coefficient(w/m^2k)

T_s= surface temperature (k)

T_{air}= temperature of the air at a distance from the pavement's surface (K).

2.14.3 Radiation

Cengel and Heat (2003) describe radiation as emissions of electromagnetic wave energy/photons stemming from alteration in electronic configuration at molecular or atomic level. Radiative heat transfers are different from convective and conductive transfers in that they can travel through a vacuum, without needing material through which to travel. When the temperature of a material leads to electromagnetic emissions from it, this is known as thermal radiation, occurring at any electromagnetic wavelength from 0.1 – 100 μm. The spectrum of thermal radiation encompasses all infrared and visible radiation and part of the ultraviolet spectrum also. Stefan-Boltzmann's law governs the heat emissions of a blackbody/ideal radiator, as shown below:

$$\mathrm{Q_{thermal}} = \sigma \, \mathrm{AT_0^4} \qquad \text{Equation (2-8)}$$

Where:

$\mathrm{Q_{thermal}}$ = rate of heat radiated (w)

$\sigma =$ Stefan Boltzmann Constant $= 5.67e^{-8}$ $(\mathrm{w/m^2\ k^4})$

2.15 Developing A Thermal Model for Pavements

Pavements interact thermally with the surrounding atmosphere in highly complex ways, with heat transferred based on four types of process: phase change through water evaporating and condensing; and convective, radiative, and conductive transfer. Radiative heat exchange occurs between pavements and sky, sun, trees and buildings etc. within the pavement's visual ambit. Pavement-air convective thermal transfer occurs through both forced and natural convective processes, while conductive heat transfer occurs between the layers of the pavement, including subgrade and base. This combined-process thermal interactivity creates pavements' internal temperature profile, as well as governing the quantity of heat released from pavement to atmosphere, and when this occurs.

The temperature profile of a pavement must be taken into account when identifying its structural integrity. In particular, in asphalt pavements, stiffness depends to a great extent upon temperature profile, and this has a bearing on how thick the pavement needs to be to support vehicle loading. For concrete materials, a temperature gradient can lead the slab to curl, which in turn causes incomplete slab-base contact, meaning that the slab may crack when under traffic loads.

The thermal energy which is released by a pavement into the surrounding environment impacts upon local air temperatures, and in urban locations where a large proportion of the land is paved, this factor contributes to the production of urban heat islands (UHIs). The volume of energy released, when it is emitted, and how, as in through radiative or convective heat transfer, each contribute to the total impact of this release on the environment locally.

Pavements undergo 24-hour solar radiation fluctuations based on the sun's cycle, and fluctuations over the course of the year based on the local climate. Both subgrade and pavement layers experience significant changes in thermal conditions seasonally, with the storage and then release of much of the daily sun's energy which has been absorbed. As part of this thermal cycle, a small percentage of the energy radiated onto the pavement each day by the sun in Summer and Autumn is retained and then released through the colder parts of the year. To calculate this unbalanced aspect of the heat transfer cycle, which is termed a transient as it changes over time, it must be modelled mathematically by heat transfer mode, to include the following:

- Conductive heat transfer under the pavement's surface
- Convective heat transfer from the pavement's surface
- Absorbed solar energy.
- Radiative cooling

Moreover, there is another transient variable related to evaporating and condensing water, termed phase change, and this variable must be included at times when the subbase, base and pavement layers are wet. However, water phase change presents significant challenges for modelling, with no approach to including this factor available at present.

Analysis techniques to address problems of transient conduction are given in Liu and Gazis (2001) and Wang (2012), based on an assumption of a sinusoidal boundary temperature on the pavement's top surface which can be applied as an approximation of the cycling of solar radiation over a 24-hour period. This technique can be used to identify characteristic pavement responses: however, it relies on the temperature at the pavement's surface being a function of time, with this data input forming a boundary condition, and the general lack of availability of such data means that the technique often cannot be applied for large problems related to thermal interactions.

Findings from models which are run over shorter timespans, of several days for example, do not show sufficient sensitivity to the lower boundary condition or to the depth of application. Moreover, researchers must be able to estimate the temperature of the pavement within a tolerance of between 3 and 5 °C based on the assumptions made. When models are run over longer timespans, the lower boundary condition must be more precisely considered, based on the tendency to store energy for longer and cumulatively over time deeper in the pavement. Findings by Gui *et al.* (2007) support this, in which there is an assumption of a 33.5 °C starting temperature present consistently from 3 metres beneath the surface upwards. Repetition of a 24-hour heat cycle was first performed for preconditioning of heat storage in the subgrade, and then the model was run for a 72-hour period along with data from experiment. The predicted temperature profile was a very good match with experimental findings when performed following 10-cycle preconditioning. However, accuracy was reduced in 20-cycle preconditioning, and further reduced when a 30-cycle preconditioning run was performed.

Generally, models of convection heat flux coming from the surface of the pavement ($q_{\mathrm{Convection}}$) are based on Newton's Law of Cooling (Equation 2-6). The problem with this approach is that calculating the convective heat transfer coefficient (h_c) presents a significant challenge, as this is variable, and the starting point of both the boundary layers and the momentum are complex to identify. Various modelling approaches exist for identifying the coefficient of convective heat transfer. Solaimanian and Kennedy (1993) assumed h_c to be constant at 3.5 W/(m2•°C), ignoring wind speeds and pavement-air temperature differentials. Gui *et al.* (2007) applied a correlation based upon laminar flows across flat plates, disregarding natural convective forces and based on the assumption that both the thermal and hydrodynamic boundary layer develop at the same time. Yavuzturk, Ksaibati and Chiasson (2005) applied flat plate correlation, with allowances made for laminar flows transforming into turbulent flows to model forced convection, while also using flat plate correlation to model natural convection. Ultimately, selection was made for h_c as the convective coefficient based on which was the greater coefficient; forced or natural convection. Qin and Hiller (2011b) again applied laminar flat plate correlation: however, they added 5.6 W/(m2•°C) as a constant representing natural convection. Various researchers (Hermansson, 2001; Herb *et al.*, 2009; Ho and Romero, 2009) have applied Vehrencamp's (1953) empirical modelling system in some form, in which h_c is determined through the equation which follows:

$$h_c = 698.24\left[0.00144 \times T_m{}^{0.3} \times U^{0.7} + 0.00097 \times (T_s - T_{air})^{0.3}\right] \qquad \text{Equation (2-9)}$$

Where:

h_c= convective heat transfer coefficient(w/m^{2}k)

T_m = the average of the surface temperature and the air temperature (K).

U = wind speed (m/s).

T_s = surface temperature (K).

T_{air} = the air temperature far away from the surface (K).

This model is also adopted by the EICM, with the alteration that an upper limit of 17 W/(m2•°C) is set for h so that the modelling of conduction does not become numerically unstable. Equation 2-10 is used by Hall *et al.* (2012) in calculating the convection coefficient, using temperature data for the pavement from numerous locations to select the best fit.

$$h_c = 5.8 + 4.1\,U \qquad \text{Equation (2-10)}$$

Where:

h_c = convective heat transfer coefficient (w/m^{2}k).

U= wind speed (m/s).

For this simplified convective heat transfer coefficient, notably, Hall *et al.* (2012) manipulate a number of variables in their model at the same time in order to find best fit using a restricted set of data from experiment, and this reduces the strength of the foundation for their approach.

The modelling approach which best approximates real-life findings appears from this to be the Vehrencamp model, on the basis first that it is empirically derived, from correlating data from an experiment conducted for a sizeable Californian dry lakebed. Therefore, this model of convection uses flat-surface convection with a well-established hydrodynamic boundary layer, and this is analogous to physical parameters when considering pavement convection to a greater extent than flat plate correlation, as the latter is based on the assumption that thermal and hydrodynamic boundary layers develop simultaneously. The Vehrencamp approach has the additional advantage that free and forced convection modes are accounted for.

From Equation 2-9, the equation's first term within the brackets represents forced convection contributions, while the second represents free convection. From the way in which the term for forced convection is structured, it is implied that turbulent flow is mostly being modelled here, and on the basis of the hydrodynamic boundary layer being strongly developed, this fits with expectations.

Certain factors related to convective processes in pavements are not effectively matched in the Vehrencamp approach, however. Based on the tendency for pavement surfaces to be hotter than different surface types upwind, it can be anticipated that a new thermal boundary layer develops located at the pavement's forward. This differs from the conditions modelled by the Vehrencamp model, which relates to isothermal surfaces of large size, with strong development of the thermal boundary layer comparable to that of the hydrodynamic boundary layer. This variation should lead the model to underpredict pavement-based heat transfer values. Another point of consideration is that Vehrencamp modelling uses wind speeds taken at two metres above the ground surface, and the technique is often applied using data from weather stations as an input, with wind speeds typically taken at ten metres above surface level. Based on reductions in windspeeds at higher elevations, overprediction of heat transfer rates can be anticipated with this approach. On the other hand, the Vehrencamp model utilises air temperatures taken at two metres above the ground, and this is comparable to the standardised measurements used in weather stations.

Radiation-based pavement-to-air and air-to-pavement exchanges are found at two separate wavelength ranges, with the sun's radiation being almost exclusively at shorter wavelengths, occupying NIR, visible and UV spectra, with 99% of sunlight experienced on Earth being at between 300 nm and 2500 nm. By contrast, surface-to-atmosphere radiative transfer occurs at longer wavelengths in the far infrared spectrum. For any specified wavelength surface, absorption capacity equals emission capacity, with each being a function of wavelength in relation to the specific surface. This means that two models are necessary in order to create an effective model of pavement radiative exchange, respectively addressing radiative cooling processes and absorption of the sun's radiation. For a hypothetical all-wavelength-absorbing or black pavement surface, it would still be necessary to approach thermally based long wavelength and solar short wavelength radiation with separate methods, due to the fact that emissions of radiation from the pavement would be restricted to long wavelengths.

The shortwave solar radiation incident on the pavement's surface depends upon the point of both the daily and seasonal cycles, as well as the location's latitude, the pavement's orientation and a number of variables in the air, including cloud coverage. A proportion of the sun's radiation returns to space after reflecting off the planet's surface, while another proportion is absorbed. Wong and Chow (2001) give a wide-ranging account of available modelling approaches for the prediction of the amount of solar radiation which strikes a surface. The majority of thermal modelling techniques for pavements apply measurements and not predictions of solar radiation, with researchers generally accepting standard methods for applying such data. Where solar irradiance, given as (I), or solar strength by unit area has been determined, the pavement's absorption of solar energy, given as (q abs), can be determined through the following equation (2-11):

$$q_{abs} = (1 - a) \times I \qquad \text{Equation (2-11)}$$

Where:

q_{abs} = solar energy absorption

a = the surface's albedo or solar reflectance.

I = the solar incident irradiation transfer for each area unit area in W/m2.

Longwave radiation exchange also occurs between pavement surfaces and air, as well as with the surface of other structures or objects within the pavement's visual surroundings, when the air is the sole element considered in pavement radiative exchange, temperatures for air and pavement, and the pavement's emissivity. Pavement-air heat transfer through radiation (q"*rad*) can be found through Equation 2 -12.

$$q_{rad} = \varepsilon\sigma\ ({T_s}^4 - {T_{sky}}^4) \qquad \text{Equation (2-12)}$$

Where:

q_{rad} = transfer of radiative energy

ε = pavement material emissivity

σ = Stefan-Boltzmann constant (5.67×10-8 W/(m2•K4))

Ts = temperature at the surface (K)

T_{sky}= sky temperature (k).

Various work has sought to model the temperature of the sky (T_{sky}) effectively. Hermansson (2001) models this factor simply by taking air temperature (T_{air}), but this method is not considered effective. The majority of simpler models which attempt to provide accuracy under clear skies apply a variable to represent water vapour, as seen in Berdahl and Fromberg (1982). A review on the subject by Hall *et al.* (2012) considers the empirically-based Bliss equation to offer the closest match between data from experiments and thermal pavement models for T_{sky}, and this is given below:

$$T_{sky} = T_{air}\ \left(0.8 + 0.004T_{dp}\right)^{0.25} \qquad \text{Equation (2-13)}$$

Where:

T_{sky}= sky temperature (K).

T_{air} = air temperature (K).

T_{dp} = dew point temperature in °C.

the American Society of Heating, Refrigerating, and Air-Conditioning Engineers (ASHRAE, 2003) adopt this equation, as well as Yavuzturk, Ksaibati and Chiasson (2005) and Gui *et al.* (2007). Notably, the derivations presented above quantify heat transfer through conduction, convection, absorption and radiation, but water phase change is omitted. Thus, errors are to be expected in the model due to a failure to consider the wetness of the sub-base, base and pavement layers. It was decided that water phase change as an avenue of heat transfer should be excluded on three grounds. Firstly, accurate measurement of the condition and presence of moisture in each layer of the pavement would require extensive work and is impractical considering the scope of the thesis. Secondly, assumptions of dryness and lack of freeze within the pavement under study, which would exclude water phase changes as a variable, permits prediction of the greatest potential temperature which the pavement could reach, and predicting this condition is central to performance prediction and design processes for pavements. Finally, precise modelling of energy exchanges based on water phase change requires highly complex approaches in comparison to the other modes of heat transfer to be modelled and is outside the feasible scope of this study.

2.16 Temperature at the Lower Surface of Asphalt

The temperature of pavements is identified as strongly correlated with radiation from the sun and the temperature of surrounding air: however, solar radiation measures are not easy to obtain (Shtawi, 1984). Ambient temperature does not have a significant impact on the unbound material layers of the sub-base and sub-grade in comparison to the asphalt concrete, which varies in its elastic and plastic characteristics under different temperatures, based on asphalt cement as the binding material being affected by temperature in its properties, and with alteration in turn of the overall asphalt concrete’s mechanical behaviours.

Before thermal strain can be calculated, the temperature of the pavement must first be identified. Flexible pavements' response to temperature has been the subject of research for over half a century (Domaschuk, Skarsgard and Christianson, 1964; Littlefield, 1967; Jones, Darter and Littlefield, 1968). This research relies upon predictions of changes in temperature within the pavement, and various works have done this, using probabilistic, numerical and statistical approaches with data regarding pavements and climate, mainly gathered as part of the SHRP and placed in the Database for Pavement LTPP. These approaches are flawed however, as there is a tendency for overestimation of low temperatures and underestimation of high temperatures with these techniques.

A predictive algorithm for temperature profile estimation in one dimension for a multiple-layer pavement was given by Wang (2012), based on thermal properties for HMA. This algorithm was based on the vertical dimension of the pavement as well as temperature at the surface. Validations of Wang's findings relied on field data from Kallas' (1966) study and were collected from 1964-5. However, fit values were inadequate at a depth of over 0.15 m, and furthermore, based on developments in the mixes used for HMA as well as techniques for compaction, the data does not have validity when considering currently used asphalts.

A model for thermal transfer was proposed by Khadrawi, Al-Shyyab and Abo-Qudais (2012) for prediction of asphalt concrete's transient thermal behaviours based on the material's thermal characteristics, solar radiation, surrounding air temperature and surface temperature. This approach allowed prediction of the temperature of the pavement to any depth, although in the study, the assumptions were that the asphalt concrete was infinitely deep and had standard thermal characteristics. This model requires field validation prior to applying it to different site contexts.

An analysis by Ksaibati and Yavuzturk (2002) applied a 2D finite modelling approach with the ability to identify hourly temperatures for any selected point within asphalt pavement structures. Their modelling takes into account factors affecting ambient temperatures, including dry bulb temperature, global intensity of solar radiation, wind, and the geometric dimensions and thermal characteristics of the pavement. This presents a challenge in pavement engineering in practice, with multiple factors that can be challenging to collect data on.

The Diefenderfer statistical model (Diefenderfer, 2002) contains two statistical approaches. It was developed from the Virginia road (VSR) instrument section and aims to estimate lowest and highest temperatures at a given pavement depth.

Another model has been put forward by Albayati and Alani (2015) for predicting pavement temperatures as a function of the depth of the point in the pavement beneath the surface and the surrounding air temperature. The authors measured both air temperature in the field and temperature at a range of depth points in an asphalt pavement, and then compared this modelling with modelling approaches by Witczak (1972), which are frequently applied by pavement engineers. The results showed that most temperature findings when applying Witczak's modelling approach gave higher values than were found through field measurement, while the SHRP's Superpave approach gave markedly higher values, overestimating temperatures by approximately 20°C for pavements at 20°C and by approximately 12°C for pavements at around 60°C. Based on these findings, Albayati and Alani (2015) concluded that their developed model gave more accurate results in predicting pavement temperatures.

$$T_{pav} = 1.217 \times T_{air} - 0.354 \times Z \qquad \text{Equation (2-14)}$$

Where:

T_{pav} = design pavement temperature (°C)

T_{air} = design air temperature(°C)

Z = depth of pavement in cm below the pavement surface

Busby (2015) presented extrapolated temperatures from 0 to 5 m depth based on a geological survey on the shallow ground seasonal temperature in the UK, as shown in Figure 2.8.

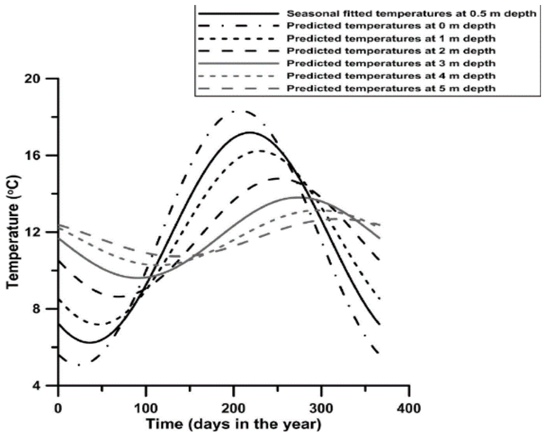

Figure 2.8 Seasonal Soil Temperature Cycles at the Wallingford Met Office Weather Station.

2.17 Pavement temperature

Pavement temperatures are correlated to energetic balance, and energy at the surface of the structure is especially significant. Heat from the sun is absorbed, and this is more or less constant across the pavement's useful lifespan, which is generally between 2 and 4 decades. The surface albedo (reflection coincident) is important to the pavement's absorption of solar energy, and may be the most significant factor in determining maximal temperature (Gui *et al.*, 2007; Li, Harvey and Jones, 2013). A proportion of the energy is emitted from the pavement through convection and radiation, with wind speeds and air temperatures influencing heat losses due to convection. Heat conduction transfers heat from the asphalt to the lower levels of the pavement, and the materials used influence the pavement's temperature profile based on their thermal conductivity and heat capacity (Yavuzturk, Ksaibati and Chiasson, 2005; Hu, Yao and Hua, 2007; Berrang-Ford, Pearce and Ford, 2015).

There is broad agreement among researchers that temperatures have most influence on the asphalt pavement layers, in which these materials become less stiff the hotter they become, thus inhibiting stress-strain responses and reducing load-spreading capacity through the pavement (Thom and Brown, 1987). Moreover, even a reduction in stiffness with no significance when viewed at a daily timescale may have longer-term significance, leading the pavement to show load-based degradation more rapidly. In addition, asphalt material is less resistant to permanent deformations at higher temperatures (Thom, 2008; Dawson *et al.*, 2014). Where extreme conditions mean that temperatures can increase significantly within hours or within a day, permanent deformations may develop more rapidly (AASHTO, 2003; Long, 2001). Temperature rise based on climate change may bring greater thermal stress within the asphalt pavement layers, thus increasing the incidence of thermal cracking (Lytton, Shanmugham and Garrett, 1983; Dave and Hoplin, 2015). Importantly, asphalt/bituminous mixes show sensitivity to changing temperatures in terms of modulus and strength, meaning that a flexible pavement could undergo a range of damage types. Within this, falling temperatures may lead to cracking, while temperature increases could cause rutting as permanent deformations (Wang *et al.*, 2003). Moreover, rising temperatures may lead asphalt mixes to age more rapidly, with increasingly brittle pavements having an increased tendency to crack (Yin *et al.*, 2017; Moreno-Navarro *et al.*, 2018).

A number of researchers have investigated the effect of different climate factors on pavement performance indicators by applying MEPDG (Qin and Hiller, 2013; Yang *et al.*, 2017). This tool predicts pavements' performance, taking into account structural design, materials, and variables in the surrounding environment. Environmental stresses can be investigated through applying the EICM (Zapata *et al.*, 2007), which uses weather parameters to predict the environment of the pavement in terms of moisture and temperature levels. From this, the response of the materials can be predicted, to assess how the pavement will perform in the long term. As pavements generally react non-linearly to climate variables, analyses should be conducted on a case-by-case basis. Despite this, some broader conclusions can be noted. First, temperature tends to have the greatest impact on the performance of pavement (Li, Schwartz and Forman, 2013; Yang *et al.*, 2017). Qiao *et al.* (2020) investigated alterations in pavements' performance in response to climatic factors for three representative sections of highway across three US locations predicted to undergo effects from climate change. The authors found the possibility of impact from the range of temperatures present as well as average annual temperature. Li, Schwartz and Forman (2013) and Yang *et al.* (2017) reached comparable findings in similar studies, while no significant influence was identified from precipitation (Li, Schwartz and Forman, 2013). In contrast, Qiao *et al.* (2020) identified that where ground water levels were high, precipitation could have a similar significance to temperature. Sensitivity to wind speeds and percentage sunshine (absence of cloud cover) has also been identified, although to a lesser extent than temperature (Schwartz *et al.*, 2013; Yang *et al.*, 2017).

2.18 Primary Factors Influencing Pavement Temperature

Changes in the environment are a cause of dissimilarity in pavement temperature. This influence results in a change in the rigidity and shape of the materials forming the pavement. Consequently, this shift affects the functionality of the pavements in service provision. Knowledge of temperature and its effects on pavement functionality has caused keen interest in considering these factors before actualizing a pavement design (Willway *et al.*, 2008; Roffa and Farhat, 2013). For instance, the material bituminous binder is selected based on the region's environmental conditions (Willway *et al.*, 2008; Kumbargeri and Biligiri, 2016). The temperature, in particular, meets practical and construction-based needs. Although environmental conditions are widely considered in the construction of pavements, damage is inevitable (Li, Mills and McNeil, 2011; El-Maaty, 2017). Such damage arises from changes in the area's environmental conditions. Initial studies seeking to ascertain the impact of environmental factors on the functionality of pavements established that factors such as temperature and moisture levels were vital in analysing the response of pavement materials and projections for the continuing performance of the pavement (Al-Abdul Wahhab and Balghunaim, 1994).

The study further reports that temperature changes resulting from the shifting weather and climate of a region cause an increment in the layers of asphalt and eventual cracking of the material due to the heat (Dave and Hoplin, 2015). Furthermore, the quicker aging of asphalt layers can be attributed to the high temperatures the layers are exposed to (Yin *et al.*, 2017; Moreno-Navarro *et al.*, 2018). Additionally, high thermal rates result in fragility of the layers, increasing the chances of pavements cracking. Low temperatures also influence the functionality of pavements. A low temperature may cause the asphalt layers to stiffen. Consequently, cracks may be formed on the surfaces of the pavement. While higher temperatures disrupt the processes, low temperatures hasten the process, causing deformations in the pavements (Basu, Marasteanu and Hesp, 2003; Chen, Wang and Xie, 2019).

2.19 -Temperature Prediction Models for Asphalt Pavements

Studies investigating the history and development of the prediction of temperatures in asphalt layers note that the forecast can be divided into three major stages: numerical and finite element techniques; theoretical and analytical approaches; and statistical and probabilistic models. Research on the impacts of climatic conditions on asphalt pavements dates back many years. Barber was among the first researchers who sought to determine the central temperatures in asphalt roads, basing his research on the available meteorological statistics. Barber conducted this study in 1957 (Barber, 1957). More scholars and researchers studying the temperature behaviour of asphalt pavements concentrated on the spread of temperature in the different levels of the asphalt layers. The researchers employed the thermal conduction model and Finite Difference Model (FDM) as the theoretical framework to imitate the structure of thermal diffusion (Roque *et al.*, 2010).

The following study was conducted in 1987, as the LTPP project was completed from the United States (Hermansson, 2001). This study measured the new trends in the data evaluation of asphalt layers. At this time, a large amount of data was available, ranging from atmospheric temperature to solar radiation, and their existing links to temperatures of asphalt pavements. Additionally, it consisted of necessary information, which is a motivating factor for the research (Diefenderfer, Al-Qadi and Diefenderfer, 2006). This study applied the regression method to develop the models used in predicting asphalt temperatures, and tried to apply the regression method for the prediction model to rectify the existing deviations and miscalculations of the asphalt layers (Chao and Jinxi, 2018). The first stage of work in this area occurred between 1950 and 1990. This stage necessitated the researchers' concentration on the tendency of thermal changes and diffusion. Some researchers chose to apply slope methods in their studies to determine the temperatures of the asphalt pavements. Additionally, in the 1990s, some Canadian and American scholars diverted their research methods to apply a different analysis method in evaluating asphalt pavements. This diversion played a critical role in providing diverse databases and information concerning temperature and radiation, which are used in further studies to date. Despite this change during the second phase, between 1990 and 2000, some researchers still employed the regression method to develop the models used in predicting asphalt temperatures by concentrating on the extreme ends of asphalt temperature as presented in periods of bituminous selection for the super pave method. From these periods, different studies and scholars began daily evaluations of asphalt temperatures to predict the temperature occurrence with minimal variable changes, which has been continually successful in road constructions to date. The third stage occurred between 2000 and the present day. In this stage, researchers widely employ statistical methods to achieve regression prediction models using two models. These models are used to correct deflection measurements using back-calculation modulus in the layers and to imitate temperature change distributions in the asphalt structure. The researchers in the initial stages have strongly inspired the research and researchers in the third stage. The range of this field of study developed significantly following the different research phases. It can be concluded that temperature prediction models have improved in diverse ways because of the comprehensive database progress experienced in the 1990s.

2.20 Methods used to Predict Pavement Temperatures

In the last half of the century, strategies of predicting asphalt temperature and means of improving prediction methods have been on the rise. Recent work applying more advanced statistical methods has involved the engineering sector, owing to the strong statistical methods used (Sun, 2016). Additionally, many researchers aim to develop efficient statistical methods of temperature prediction in asphalt pavements (Wang, Roesler and Guo, 2009; Khan, Islam and Tarefder, 2019). Consequently, three primary approaches have been established. These methods are numerical and finite elements, theoretical and analytical, and statistical and probabilities techniques (Gedafa *et al.*, 2014; Sun *et al.*, 2017; Chao and Jinxi, 2018; Khan *et al.*, 2019).A Partial Differential Equation (PDE) determines the heat conduction in given conditions when using numeric and analytical methods. However, the experimental models originated from the application of statistical analysis (Wang *et al.*, 2009). as illustrated below.

The methods as shown in Table 2.4 were conducted in four stages. The first phase involved developing the controlling equation, which was tasked to regulate thermal conduction in the asphalt layer system. Typically, the equation is usually either 1D or 2D. The PDE clarifies the 2D or 1D thermal transfer. Typically, the controlling equation is set up to determine the conduction of heat in asphalt pavements, which is usually created in the 2D or 1D thermal transmission model, which is constituted by a time-dependent PDE (Khan *et al.*, 2017). The Finite Element Method (FEM) on the other hand, is a numeric process that is applied in a variety of engineering problems. In FEM, the PDE serves differently in different phases. In the first stage, the PDE is changed from a strong to a weakened version (Jeong and Zollinger, 2006; Chen *et al.*, 2019; N. Zhang *et al.*, 2019). In the second phase, the “Dirichlet boundary” is determined (Qin and Hiller, 2011b) or the mixed form connecting climate conditions to the temperature of the asphalt layers in depth is identified. However, the connection can only be established when the energy balance at the top of the layers of the pavement is analysed (Crevier and Delage, 2001). The third phase consists of the detachment of the spatial domain. This phase applies the use of numerical methods, including the finite-difference method and finite-element process. The latter causes an enormous Ordinary Differential Equations (ODEs) system in time (Yavuzturk, Ksaibati and Chiasson, 2005; Qin and Hiller, 2011), Finite Volume Method (FVM) (Wang *et al.*,2009; Chen *et al.*, 2019). and FEM (Hermansson,

2004; Gui *et al.*, 2007). The fourth phase necessitates an appropriate time planimeter to resolve ODEs effectively. Examples of a time planimeter include the linear multistep technique or a Runge-Kutta method (Wang *et al.*, 2009). The compound heat transfer process in numerical analysis is critical because it is applied to ensure the universality of the process, as well as the compatibility of temperature predictions under diverse conditions and in different places. The analytical method provides a range of advantages. However, one of the most significant advantages of the process is its ability to provide quick solutions to current challenges and be used in real-time (Chen *et al.*, 2014). Additionally, calculations on the precision of these models are significantly influenced by a pavement's density as well as the number of elements contained in a model (Chen, Wang and Zhu, 2017). On the other hand, the process is disadvantageous to users because it requires in-depth knowledge in designing FEM and immense expertise to guarantee the intersection of solutions (Sun, Hudson and Zhang, 2003). The temperature of the asphalt pavement obtained by analytical solutions is impacted by heat conduction and the Initial Boundary Value Problem (IBVP). The initial boundary value used by this method is the road surface temperature (Wang, 2013). This simplification impacts climatic factors such as the speed of the wind, air temperature, and solar radiation (Chong, Tramontini and Pivoto Specht, 2009; Wang, Roesler and Guo, 2009; Wang and Roesler, 2014). Numerical analysis is different from regression methods and equations. The difference arises in the manner the two ways apply appropriate assumptions that are strictly aimed at obtaining solutions for the temperatures of the pavement (Chen *et al.*, 2014). Compared to analytical processes, non-numerical procedures are more challenging. There are many numerical methods applied in these studies, including FDM, FEM, and FVM.

Table 2.4 Numerical Models for Predicting Pavement Temperatures

Author, Year, Location	**Influential Factors**	**Results and Summary**
Straub and Przbycien (1968) USA	Pavement temperatures Solar radiation Air temperatures	• There is a greater effect from solar radiation than from air temperature on surface temperature. • Primary input values do not affect predicted maximum surface temperatures, while input temperatures have greater significance, with greater depth for accuracy in predictions.
Dempsey (1969) USA	Short and long wave light Thermal characteristics Air temperatures Physical weight Materials classification	• Advanced equations are sometimes highly complex, with multiple variables applied to predict pavement temperatures. Such models therefore cannot be applied routinely (Asefzadeh, Hashemian and Bayat, 2017).

	Moisture level Thermal capacity Thermal conduction	
Rumney and Jimenez (1970) USA	Pavement temperatures Air temperatures Solar radiation	• Monograph models did not provide accurate findings. • A monograph chart was generated for 50-80 mm depth pavements. • Correlation monographs were created to give pavement temperature predictions for given air temperatures and intensities of solar radiation. • This study focused on high-temperature desert climates to investigate maximum temperatures for asphalt pavements.
Williamson (1972) South Africa	Solar radiation Air temperatures Thermal properties	• The model was validated with data related to asphalt pavement of 20 cm thickness. • Precipitation and moisture impacts were ignored by the model.
Christison and Anderson (1972) Canada	Solar radiation	• This study assessed pavements' performance for a cold climate. • Precipitation and moisture impacts were ignored by the model.

	Air temperatures Wind speeds Physical characteristics	• The study showed how the temperature of pavements differed when white paint was applied compared with unpainted pavement, as well as assessing impacts on surface temperature for a cement-treated base pavement based on shelter from or exposure to natural sunlight (Ksaibati and Yavuzturk, 2002) .
Kondo and Miura (1976) Japan	Air temperatures Pavement temperatures	• The condition was not found in measurements of surface asphalt temperatures. • Low temperatures were ignored in the study, despite being identified as the most significant factor in collapsed asphalt.
Lytton *et al.* (1993) USA	Structure of pavements Material properties	• Model does not give a sufficient explanation of heat transfer dynamics, with other potential deficiencies based on a range of issues. • Estimation of solar radiation was based on a regression equation despite the possibility of gaining estimates with greater reliability from other channels. • The EICM model ignores impacts from variation in radiation characteristics by season at the surface of the pavement for a given site (Ghayoomi, Dave and Mousavi, no date; Hermansson, 2004; Salem *et al.*, 2004).
Minhoto et al. (2006) Portugal	Solar radiation Pavement temperature	• Accurate temperature prediction compared to the actual pavement temperature measured throughout the year.

	Daily wind speed	• The models are not suitable for field use. Statistical methods are useful for creating a simple prediction equation (Asefzadeh, Hashemian and Bayat, 2017).
Lufs de Picado-Santos Portugal(2016)	Maximum air temperatures by month Minimum air temperatures by month Asphalt layer temperature by hour	• Hour-by-hour weather data was applied to establish damage caused hourly, and a validated model was applied, calculating distribution of pavement temperatures (Andersland and Ladanyi, 2004). • Characterising pavement design conditions more effectively produces findings with greater reliability. • The model structures from the study are suitable for rapid adoption in other locations. • The work to model behaviours of pavement materials to for applications in design is at an early stage and there are many challenges ahead.
Mammeri et al. (2015) France	Pavement temperatures Air temperatures, Humidity, Depth, Solar radiation	• Comparisons of numerically and experimentally reached findings point to the need to include night-time cooling when modelling surface temperatures, and particularly for arid regions. • FEM is complex, while most engineers tend to select simpler approaches to analysis (Alavi, Pouranian and Hajj, 2014).

- **Theoretical and Analytical Approaches**

The history of analytical studies in prediction of pavement temperatures can be traced to the 1950s, when Barber derived pavement temperature metrics through the usage of climate data (Barber, 1957). As shown in Table 2.5, numerous studies have attempted to predict pavement temperatures using analytical techniques. Pavement temperature modelling can be defined by its central tenets, mainly climatic parameters such as meteorological and geographical data. As aforementioned above, analytical methods have been used in statistical temperature or numerical models (Dong, 2016). Regardless, analytical methods do not necessarily require spatial uniqueness of the real-time or field in developing time-dependent temperature models that can eliminate the computational problems attached to a numerical method, such as mathematical stability and truncated errors (Wang, 2010). However, the analytical approach can be criticized as concerns are raised over the multi-layer pavement system (Wang, Roesler and Guo, 2009). In addition, complexity is encountered in the process of deriving closed-form analytical fluid (Alavi, Pouranian and Hajj, 2014; Asefzadeh, Hashemian and Bayat, 2017).

Table 2.5 Models for Predicting Pavement Temperatures Based on Analytical Approaches.

Author, Year, Location	Influential Factors	Results and Summary
Barber (1957) USA	Pavement temperatures Wind Precipitation Air temperatures Solar radiation Thermal property coefficients	• Modelling was used with 6.35 cm thick asphalt paving. • Comparisons were made of findings from modelling and actual measurements of temperature: based on the findings, max temperature error is generally around 3 °C, rising to over 5 °C at times (Chao and Jinxi, 2018). • The model was capable of calculating max temperature and predicting min temperature (Arangi and Jain, 2015; Pan et al., 2015).
Solaimanian and Kennedy (1993) USA	Maximum air temperatures Solar radiation by hour	Modelling failed to consider winter conditions, as the research focused on maximum temperatures (Hermansson, 2004).
Highter (1984) USA	Thermal conductivity in asphalt pavement temperatures for various specific densities	• A typically used recycling procedure applying heat externally to the asphalt pavement was used. • Thermal conductivity spread in the surface and base limestone courses differed significantly, and this was attributed to gradient as well as aggregate total size. • Correlation monographs were created with pavement temperature predictions at given intensities of solar radiation and given air temperatures. • Maximum temperatures for asphalt pavements were studied using high-temperature desert conditions.

Liang and Niu (1998) USA	Surrounding air temperatures Temperatures at the pavement's surface	• Non-linear temperature distributions by depth were identified, and in particular taking into account temperature variation daily. • For temperature distributions, an analytical solution was used for a system of 3 layers, with simple boundary conditions solely accounting for surface-surrounding air 2-way heat transfer.
Liu and Yuan (2000) USA	Surrounding air temperatures Pavement's surface temperature Depth Time	• This analytical solution may be extended to investigate/estimate temperature distributions for an asphalt pavement in durations of weeks/months.

- **Statistical and Probability Techniques**

The empirical models can be categorized into linear regression, neural network, and non-linear regression (Chen *et al.*, 2019). The linear regression model is considered the most viable approach in developing empirical models as it can predict maximum or minimum temperature levels at a certain depth (Chong *et al.*, 2009; Al-Abdul Wahhab and Balghunaim, 1994; Ramadhan and Wahhab, 1997; Bosscher *et al.*, 1998; Alavi *et al.*,2014). Notably, linear regression models comprise numerous parameters that are helpful in real-time scenarios in predicting surface temperature (Kršmanc, Slak and Demšar, 2013). Use of the linear regression method has a major disadvantage due to the complexity and non-linear pavement temperatures that flow through the depth (Sherif and Hassan, 2004). The approach is not viable in predicting pavement temperatures as it depends on time as the sole independent factor. Due to timely variation in the expected pavement temperature, advanced empirical approaches involve sine terms in their metrics.

However, statistical analysis methods are primarily used to develop large amounts of field data on climate databases and asphalt pavement details in most instances (Ovik, Birgisson and Newcomb, 1999; Park, Buch and Chatti, 2001). These may consider meteorological and geographical variables such as ambient temperature, solar radiation, wind speed, and location (Jia, Sun and Yu, 2008; Yin *et al.*, 2019), as shown in Table 2.6. The regression method is credited due to its ability to establish a quantitative relationship between the asphalt pavement and temperature variation data (Li, Liu and Sun, 2018). The formulas applied are essential in computing mathematical solutions to express the link between the available quantities and solving real-world problems. The main benefit of using mathematical models is the facilitation of interpretation and analysis of data observed through description and comparison of the evolution law statistically (Khraibani *et al.*, 2012).

Notably, statistical methods are presumed essential in providing reliable projections of temperature with input data involving the original pattern of the required databases. Therefore, the approach is instrumental in evaluating and analysing pavement temperatures through predictive models without involving inputs such as analytical deviation and numerical computation (Chen *et al.*, 2019). The SHRP history can be traced in the US and Canada in 1987. The 20-year-old study focuses on the most viable approaches in improving the onsite performance description of temperature pavements (Robertson, 1997). Also, the study introduced a new concept of a bitumen classification system known as PG (Qiao *et al.*, 2020). The GP is helpful to civil engineers in determining the maximum and minimum temperatures selected relative to a given pavement. Thus, the choice of a bituminous binder is viable as it helps prevent the cracking and rutting of pavement in cold and hot temperatures (Yusoff *et al.*, 2011). In addition, the newly introduced design manual of temperature in pavements, referred to as Mechanistic-Empirical Pavement Design Guide, has been fundamental in helping to prove the benefits of adoption and utilization of the PG classification system and utilizing the actual weather record.

Table 2.6 Models for Predicting Pavement Temperatures Based on Analytical Approaches.

Author, Year, Location	Influential Factors Modelled	Results and Summary
SHRP (1987) USA	$1331\alpha\tau a.\cos z \frac{1}{\cos z} + \varepsilon\delta T_a^4 - h_c(T_s - T_a) - 164k - \epsilon\delta T_S^4 = 0$ In which α represents pavement surface absorptivity, while the heat conduction coefficient of air is given by ta, Z represents 20° latitude, pavement surface emissivity is ε, s represents the Stefan-Boltzman constant (5.7x 10^{-8}W/m2), hc = the heat transfer surface coefficient (W/m2 ℃), the heat conduction coefficient (W/m2 ℃) is k, air temperature (K) is Ta, and surface temperature (K) is Ts.	• This model assumes that there is energy balance at the maximum temperatures, while this is not the case. • Energy was not balanced even where wind speeds, atmospheric conditions and solar radiation were stable.
Wahhab, Asi and Ramadhan (2001) Saudi Arabia	$T(d) = 3.714 + 1.006T(a) - 0.146d$ In which T(d) represents pavement temperature in ℃ for depth d, T(a) = air temperature in ℃, and depth in cm beneath the surface of the pavement is d.	• This model is predictive of min/max temperature, as is crucial in asphalt pavement design. • Saudi Arabia has a desert climate, with little variation in temperatures across the year.
Park, Buch and Chatti (2001) USA	$T(d) = T_s(-0.3451d - 0.0432d_2 + 0.00196d_3\ ) \times \sin(0.35_\tau)\ + 5.967$ where Td is the temperature of pavement (℃), Ts is the surface. temperature (℃), d is depth (mm), and τ is the coefficient associated with time.	• Verification of the model was done at temperatures from 28.4 - 53.7 °C with depths of between 14 cm and 27.7 cm.
Diefenderfer et al. (2003) USA		• The model may be applied across every season and in various

	$$T_{pmax} = 3.2935 + 0.6356T_{max} + 0.1051Y - 27.795P_d$$ $$T_{pmin} = 1.6472 + 0.6\,504T_{min} + 0.\,0861Y + 7.2385d_{db}$$ In which T_{pmax} represents prediction of maximum temperature in ℃, maximum daily temperature in °C is Tmax, minimum daily temperature in °C is T_{pmin}, minimum daily temperature in °C is given as T_{min}, Y is a single day within the year, numbered 1-365, and depth in metres beneath the surface is db.	climatic regions once the equation is confirmed by applying US SMP site data (Wang, Roesler and Guo, 2009; Khan, Islam and Tarefder, 2019).
Hassan *et al.* (2008) Oman	$$T_{surf} = -1.437 + 1.121T_{air}$$ $$T_{20mm} = 3.160 + 1.319T_{airx}$$ In which T_{surf} represents the pavement's minimum temperature in ℃, minimum and maximum air temperatures in °C are $T_{air\ and}\ T_{airx}$ respectively, and temperature of the pavement in ℃ at 20 mm is T_{20mm}.	• The formulae used can be applied experimentally for temperature predictions for given depths of pavement.
Jia, Sun and Yu (2008) China	$$T_p = P_1 + \left(P_2T_{a5} + P_3\ (Q_5)^2 \right) + H(P_4T_a + P_5Q) + (P_6H + P_7H^2 + P_8H^3) + P_9T_M$$ In which the temperature of the pavement at h cm is T_p, solar radiation in kW per m2 is Q, air temperature averaged over the past 5 h is T_{a5}, solar radiation in kW per m2 averaged over the past 5 h is Q5, prediction point depth in centimetres is H, P1–P8 represent undetermined regression coefficients in the predictive model, and the monthly average for air temperature over the previous 2 decades is Tm.	• This model is not practical for use in the field due to its multi-variable design. Improvements in the model could allow it to be used in the field in predicting asphalt collapse, however.
Tabatabaie, Ziari and Khalili (2008) Iran	$$T = 0.94Sur + 0.94\sin(2\pi t/24) - 2.99\log(d) - 0.02comp + 0.2Air + 0.32BP + 0.17BT - 0.34$$ In which the temperature of the asphalt in °C is T, the temperature of the air in ℃ is air, surface temperature is S and t represents the time based on the 24-hour clock and depth in centimetres is d. Compaction by no. of blows is given as comp, bitumen contents as BP, and type of bitumen is BT (using 1 as 40/50 and 2 as 60/70).	• The model has the disadvantage that minimum/maximum temperatures for the asphalt cannot be predicted, and this is a vital element in designing asphalt pavements.

		• There is a linear relation between climatic factors and asphalt temperatures.
Zheng, Cai and Zhang (2011) China	$$T_{pave-rising} = 1.170\ T_{air-rising} - 0.50h + 3.55$$ $$T_{pave-falling} = 1.085\ T_{air-falling} - 0.07h + 4.3$$ $$T_{pave} = 1.118\ T_{air} - 0.023h + 4.1$$ In which the asphalt pavement's temperature in °C at h depth when temperatures are rising is given as Tpave-rising, air temperature rising periods are Tair-rising, while pavement depth in centimetres is h. The pavement's temperature in °C when temperature is dropping is Tpave-falling and dropping air temperature in °C is Tair-falling, and Tair represents the temperature of the air.	• The models offer simplicity and practicality. A high level of accuracy is shown when comparing predictions with measurements. The model is not suitable for use across all regions.
Al-Hamed and Maryam (2011) Iraq	$$T_{pave} = 3.175 + 0.04866Z + 0.946\ T_{air}$$ In which the temperature of the pavement in °C is shown by Tpave, and depth beneath the surface of the pavement in centimetres is Z.	• The linear regression modelling here offers practicality and simplicity but has not been validated.
Matić *et al.* (2013) Serbia	$$Y_{max} = 0.963288\, x_{max} - 0151137X_d + 4.452996$$ $$Y_{min} = 1.004801x_{min} - 0.1992731\ X_d + 0.051532$$ In which maximum pavement and maximum air temperatures in °C are Y_{max} and x_{max} respectively, minimum pavement and air temperatures in °C are Y_{min} and x_{min} respectively, and depth in centimetres is represented as xd.	• This is an uncomplicated, first-order linear equation model, which is applicable in the field, and is frequently selected for road design engineering. • Serbia is a European country with low temperatures occurring year-round, and the model is not suitable for other regions.

Salem-Hassan (2015) Libya	$T_{maxpav,d} = 7.059 + 0.7764246\ T_{maxsur\ d} + 0.054628 Day - 0.000141 Day2 + 0.000006 CumSR - 0.053402\ TL_{at}$ $T_{minpav,,d} = 9.8364 + 0.668591\ T_{minsur\ d} + 0.259098 d + 0.099289 Day + 0.000261 Day2 - 0.000025 CumSR - 0.053402\ TL_{at}$ In which maximum daily pavement temperature in °C is $T_{maxpav,d}$, max daily surface temperature in °C is $T_{maxsur\ d}$, distance in centimetres from the surface is d, day of the year, and the square of day of the year is Day2. Cumulative solar radiation in W/m2 is $CumSR$, latitude of a section in degrees is $L_{at,}$ minimum daily pavement temperature in °C at d distance from the surface is $T_{minpav,,d}$, while min daily surface temperature in °C is represented by $T_{minsur\ d}$.	• The data used is not extensive and covers a limited duration, reducing its reliability for model development. • Libya is a multi-climate country, having both coastal and desert areas, with substantially differing air temperatures. Therefore, it is not possible to integrate asphalt pavement responses within a single standardised model.
Ariawan, Subagio and Setiadji (2015) Indonesia	$T_{.00} = 10.813 + 0.919 RH$ $T_{.20} = 6.898 + 0.687\ T.Air + 0.640\ T_{.00}$ $T_{.70} = 1.965 + 0..755\ T.Air + 0.331\ T_{.00}$ In which RH = humidity, air temperature in °C is T.Air, surface temperature in °C is T.00 , and temperatures at 20 mm and 70 mm depths are given in °C as T.20 and T.70 respectively.	• Indonesia's tropical climate includes high levels of precipitation, solar radiation and humidity year-round. • This model shows accuracy, simplicity and practicality: however, it can only be used to model temperature at the depths the equations refer to, and not to different depths.

Experimental work was conducted in addition to numerical analysis to investigate mechanisms for storing heat among a range of pavements, as well as how heat was exchanged and transferred between sublayers, upper pavement layers and the air. The findings of these experiments and analyses were also used to consider the role played by pavements in influencing temperature conditions in the surrounding environment (Asaeda and Ca, 1993, 2000; Asaeda et al., 1996). Gui et al. (2007) proposed a model of mathematical analysis for calculating temperature close to the surface of pavements using data measuring air temperatures, wind speeds, solar radiation and dew-point temperatures.

Temperature amplitude and maximal temperatures for the pavement surface have been widely studied empirically and numerically, with various models developed for prediction of how temperatures will develop in a pavement and estimation of surface temperature fluctuations, as well as to consider impacts from the thermophysical characteristics shown by pavement materials on temperature at the surface (Thompson *et al.*, 1987). Examples of such models are the enhanced integrated climatic model and the long-term pavement performance model (Mohseni, 1996), as well as various empirical models (Bosscher *et al.*, 1998; Hermansson, 2000). Each model considers fluctuations in temperature at the pavement's surface to be dependent upon the temperature of the surrounding air and latitude, in addition to further regressed empirical coefficients: however, the models do not include solar radiation, and this represents a weakness, as this factor drives temperature fluctuations below the surface of the pavement. Moreover, such modelling does not account for the thermal characteristics of pavements, including volumetric heat capacity and thermal conductivity, leading to inaccuracy in predicting pavement performance in practice. Therefore, the model put forward in the current study includes within it the thermal characteristics of the pavement.

Applications of FEM for asphalt pavements have included simulating temperature distribution for different climatic conditions, as well as simulating interactions with traffic loads (Hadi and Bodhinayake, 2003; Hermansson, 2004; Akbulut and Aslantas, 2005; Minhoto *et al.*, 2005; Yang and Liu, 2007; Melaku and Qiu, 2015; Li *et al.*, 2018; Han *et al.*, 2018). The current study proposes an initial 2D finite element model for use in finite element analysis of an asphalt pavement. There is a need for the modelling in this study firstly to allow for simulations of heat flows in asphalt mixes to address cool repair boundary problems. Additionally, these models may have future applications for designing and calibration of asphalt for different climatic conditions, different characteristics of asphalt and varied rehabilitation states.

2.21 Theory of Thermal Mechanical Problems

2.21.1 Conservation of Momentum

Newton's Second Law of Motion is now known as the Conservation of Momentum. The current understanding of the above is as follows (Malvern 1969): the vector sum of all external forces that act on the particles of a particular set equals the temporal rate of change of the overall momentum of the set. It is worth noting that the above law applies to both linear and angular momentum. The traction vector, t, acts on an area, dS, on the body's boundary, S, as indicated in the diagram. There are also body forces per unit mass, f, that act on a volume, dV, in the body's interior, V.

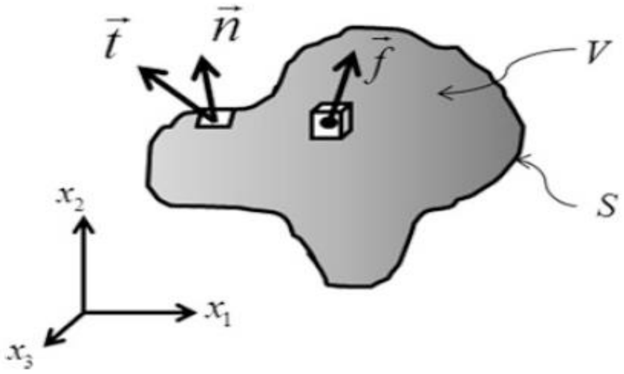

Figure 2.9 Depiction of a continuous body with forces acting both on the interior and exterior (Little *et al.*, 2018)

$$\int_S \vec{t} ds + \int_V \rho \vec{f} \, dV = \frac{d}{dt} \int_V \rho \, \vec{v} \, dV \qquad \text{Equation (2-15)}$$

Where the derivative $\frac{d}{dt}$ is the material derivative (Malvern 1969) and $\vec{v}$ is the velocity vector, given by $\vec{v}_i = \frac{\boldsymbol{du}}{\boldsymbol{dt}}$

$$\int_S t_i ds + \int_V \rho f_i \, dV = \frac{d}{dt} \int_V \rho v_i \, dV \qquad \text{Equation (2-16)}$$

Substituting Cauchy's formula, $t_i = \sigma_{ji} n_j$ into Equation 3-3 and applying the Divergence Therom $\int_v f_{i,i} dV = \int_S f_i n_i \, dS$ as well as the consevation of mass Equation (3-1), in addition to the Reynolds Transport Theorem $\frac{d}{dt}\int_V \rho F \, dV = \int_V \rho \frac{dF}{dt} dV$ will result in

$$\int_V \left[\sigma_{ji,j} + \rho f_i - \rho \frac{dv_i}{dt}\right] dV = 0 \qquad \text{Equation (2-17)}$$

The conservation of linear momentum in the body V +S is stated globally in Equation 3-4.

Because of the arbitrary nature of the volume, Equation 3-4 also suggests that,

$$\sigma_{ij\ j} + \rho f_i = \rho \frac{dv_i}{dt} \qquad \text{Equation (2-18)}$$

The Cauchy Equations of Motion (Equation 3-5) give a local expression of linear momentum conservation for all points in the body (Cauchy, 1822; Little, Allen and Bhasin, 2018) when the loads are delivered to the body slowly enough that the rate of change of velocity (acceleration) $\frac{dv_i}{dt}$, is insignificantly small. So, Equation 3-5 reduce this to the differential equations of equilibrium.

$$\sigma_{ij\ j} + \rho f_i = 0 \qquad \text{Equation (2-19)}$$

The strain and stress of the solid material are shown in Equations 3-20 and 3-21 respectively.

$$\varepsilon_{ij} = \frac{1}{2}\left(\frac{\partial u_i}{\partial x_j} + \frac{\partial u_j}{\partial x_i}\right) \qquad \text{Equation (2-20)}$$

$$\sigma_{ij} = \lambda \varepsilon_{kk} \delta_{ij} + 2\mu \varepsilon_{ij} - \alpha(3\lambda + 2\mu)\Delta T \delta_{ij} \qquad \text{Equation (2-21)}$$

Where:

$\lambda = \frac{vE}{(1-2v)(1+v)}$ and $\mu = \frac{E}{2(1+v)}$ are the Lamé parameters.

$\lambda = K - \frac{2G}{3}$ $\qquad$ $K = \frac{E}{3(1-2v)}$

$$\mu = G \qquad\qquad G = \frac{E}{2(1+v)}$$

Where:

K = Bulk Modulus

G = Rigidity Modulus

α = Thermal expansion/contraction coefficient

ΔT = Temperature change which, in the modelling work for this study, is linked to a reference temperature of 10°C for the scenario of the UK climate.

For an isotropic solid material, its deformation follows Navier's equations, which can be written in the form below:

$$\frac{E}{2(1+v)}\left(\frac{1}{(1-2v)}\nabla(\nabla \cdot \mathrm{u}) + \nabla^2 \mathrm{u}\right) + \mathrm{f} = \rho \frac{\partial^2 \mathrm{u}}{\partial t^2} \qquad \text{Equation (2-22)}$$

where:

u =The vector of displacement in space (u_x u_y u_z)

f = Body force per unit volume

E = Lagrange modulus

v= Poisson ratio

ρ =Density.

2.21.2 CONSERVATION OF ENERGY

The conservation of energy is an essential issue in the context of flexible pavements and is critical to a thorough knowledge of pavement performance. This is owing to the fact that a pavement dissipates energy in a variety of ways during the course of its life. This can be caused by heat flux, crack formation, chemical changes, and material waste. The rules of thermodynamics must be applied in order to comprehend and anticipate the consequences of such events. The First Law of Thermodynamics, which defines the following (Clausius 1850), is known as The Conservation of Energy:

The difference between the work done by the system and the heat accrued by it equals the increase in internal energy in a thermodynamic process concerning a closed system. The following is a mathematical statement of the preceding:

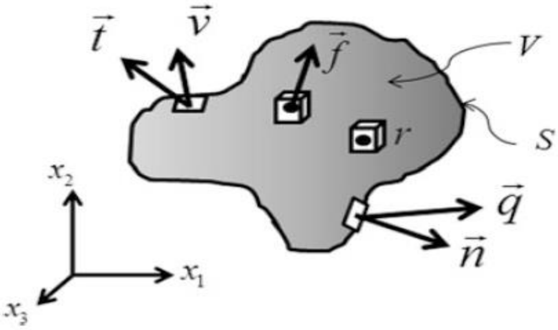

Figure 2.10 Depiction of a continuous body subjected to various forms of energy (Little *et al.*, 2018)

$$\frac{dU}{dt} = \frac{dQ}{dt} + \frac{dW}{dt} \qquad \text{Equation (2-23)}$$

Where:

U is the internal energy of the body, Q is heat contained within the body, W is work performed on the body, $\vec{q}$ is the heat flow per unit area, and r is the internal heat source per unit mass, in order to apply Equation 3-10 to an arbitrary (Figure 2.10). When Equation 3-10 is applied for the object, V+S, the following equation is obtained:

$$\frac{d}{dt}\int_V \rho u dV = -\int_S q_i n_i dS + \int_V \rho r dV + \int_S t_i\, v_i\, dS + \int_V \rho f_i v_i\, dV \qquad \text{Equation (2-24)}$$

Where:

u is the internal energy per unit mass, by employing the Divergence Theorem, The Cauchy Equations of Motion Equation (3-5) and the Reynolds Transport converting Equation 3-11 to Equation 3-12.

$$\int_V \left(\rho \frac{du}{dt} + q_{i,i} - \rho r - \sigma_{ij} \frac{d_{\varepsilon ij}}{dt}\right) dV = 0 \qquad \text{Equation (2-25)}$$

Equation 3-12 is a general formulation of energy conservation in the body, V+S. Due to the arbitrary nature of the volume, Equation 3-12 also suggests that:

$$\rho \frac{du}{dt} = \sigma_{ij} \frac{d_{\varepsilon ij}}{dt} - q_{i,i} + \rho r \qquad \text{Equation (2-26)}$$

Equation 3-13 is a local energy conservation statement that applies to all points in the body.

When exposed to a heat transfer process, the solid material satisfies the thermal energy conservation condition as shown in Equation 3-14.

$$\rho c_p \frac{dT}{dt} = \nabla(k \nabla T) + \rho r - \alpha(3\lambda + 2\mu) T \frac{d\varepsilon_{kk}}{dt} \qquad \text{Equation (2-27)}$$

Where:

cp = Specific heat capacity

k = Thermal conductivity

r = Heat source per unit mass

In this study, the heat source r and thermal energy, due to the deformation strain rate ($\frac{d_{\epsilon kk}}{dt}$), are neglected.

2.22 Summary

The literature review demonstrates that there is extensive evidence that hydrated lime is an effective additive in designing asphalt concrete pavements to better resist their main distress mechanisms, including rut formation, degradation based on moisture, and fatigue cracking. The development of coupled thermal-mechanical loading analytical approaches to enhance pavement design processes and analyses is a challenge to this field. The process of designing flexible pavement is necessarily iterative, with factors to be managed including vehicle load configurations, material properties, climate conditions, modelling of performance etc., in order to fulfil the criteria, set for effective performance. The previously more limited capacity for computation meant that pavement design was mainly based on empirical research, with available data covering only a narrow range of local conditions and materials. Based on this background, developing a model for coupled thermal-mechanical analysis to inform flexible pavement design represents a positive contribution towards progress in this field. Finally, this chapter has outlined the notational and mathematical methods needed in order to model the flexible pavement. Variables and field variables to model pavement performance have also been presented. In addition, several field equations are presented which are needed for prediction of that performance. Among material properties, mass density is considered to be already determined.

CHAPTER 3 - EXPERIMENTS FOR THERMAL AND FATIGUE PROPERTIES

3.1 Introduction

A previous PhD project (Al-Tameemi, 2017) at Salford had investigated conventional mechanical properties of hydrated lime modified HMA concrete at 6 different contents, i.e.: 0, 1.0, 1.5, 2.0, 2.5, and 3.0% by total aggregate weight. The previous study identified that HMA concrete samples of 2.5% HL addition generated an optimum performance in terms of resilient modulus, permanent deformation under three temperatures, namely 20°C, 40°C, and 60°C, and moisture susceptibility and fatigue performance at a temperature of 20°C. The current project is a continuing study from the previous project. For this reason, the investigation and comparison will focus on the optimum 2.5% HL content and control mixes with 0% HL content.

3.2 Materials

The materials used for the asphalt concrete mixes are identical to those used in the earlier study, including mineral filler, aggregate and asphalt cement materials. Routine testing was used to characterise the materials using specifications provide by the American Society of Testing and Materials (ASTM).

3.2.1 Asphalt Cement

The asphalt cement for the experiment comes from the Aldorah refinery to the South-west of Baghdad and has a penetration grade of 40/50. The material's main physical characteristics and adherence to the ASTM-D946 were identified through various tests, and these characteristics are provided in Table 3.1.

Table 3.1 Physical Characteristics for 40/50 Penetration Grade Asphalt Cement

Property	ASTM Designation	Penetration Grade 40-50	
		Test Result	ASTM specification
Penetration At 25C,100 gm,5 sec. (0.1mm)	D5	42	40-50
Softening Point (Ring & Ball) (°C)	D36	49	……
Ductility at (25 °C, 5cm/min) (cm)	D113	>100	>100
Flash Point, (Cleveland open cup) (°C)	D92	293	Min.232
Specific Gravity (25 °C)	D70	1.041	……
Residue from thin film oven test (ASTM D1754)			
Penetration At 25C,100 gm,5 sec. (0.1mm)	D5	25	Min 55% of original
Ductility at (25 C, 5cm/min) (cm)	D113	80	Min 25

3.2.2 Mineral Filler

The study used a non-plastic mineral filler which passes through sieve number 200, with a diameter of 0.075 mm. Two types of mineral filler were used in the study, they are limestone dust and hydrated lime. For each material, physical characteristics are given in Table 3.2 while chemical characteristics are given in Table 3.3.

Table 3.2 Physical Characteristics for Hydrated Lime and Limestone.

Material property	Hydrated lime	Limestone dust (filler)
Specific gravity(gm./cm^3)	2.43	2.71
Specific surface (m^2/Kg)	394	246
Passing No. 100 Mesh (150 μm), %	100	100
Passing No. 200 Mesh (75 μm), %	99	87

Table 3.3 Chemical Characteristics of Hydrated Lime and Limestone

Chemical components	Hydrated lime	Limestone filler
% CaO	56.1	68.3
% SiO2	1.38	2.23
% Al2O3	0.72	N/A
% Fe2O3	0.12	N/A
% MgO	0.13	0.32
% SO3	0.21	1.2
% Loss on Ignition (L. O. I.)	40.65	27.3

3.2.3 Aggregate

Crushed quartz was employed as the aggregate. Both coarse and fine aggregates, obtained after sieving, were measured, and reintegrated in the correct proportion for base, levelling and wearing layer grades according to the ASTM-D3515. Traditional testing methods were applied to assess the aggregate's physical characteristics. Table 3.4 provides the aggregate's physical characteristics, while asphalt mix specifications for the base, levelling and wearing grades are shown in Table 3.5 whereas the requirement for the asphalt concrete mixture graduations and the selected aggregate gradations for the pavement asphalt concrete layers (wearing, levelling and base) are also presented in Table 3.5.

Table 3.4 Physical Characteristics of Aggregates

Properties	Coarse Aggregate	Fine Aggregate	ASTM SPECIFICATION
Bulk specific gravity (g/cm^3) (ASTM C127 and C128)	2.52	2.643	N/A
Apparent specific gravity (g/cm^3) (ASTM C127 and C128)	2.55	2.68	N/A
Percentage water absorbed (ASTM C127 and C128)	0.13	0.52	N/A
Percentage wear (Los-Angeles Abrasion) (ASTM C131	19		50 Max
Percentage fractured fragments D5821	96		90 Min
Percentage sand equivalent (ASTM D 2419)		59	45 Min
Percentage soundness loss through sodium sulphate solution (C-88)	4.12		N/A

Table 3.5 Asphalt Concrete Mixture Grading (ASTM-D3515)

Sieve size	mm	% Passing by Weight of Total Aggregate + Filler					
		Base Course D-3		Leveling Course D-4		Wearing Course D-5	
		Selected Gradation	Specification Limit	Selected Gradation	Specification Limit	Selected Gradation	Specification Limit
1.5 in	37.5	100	100				
1	25.0	95	90 - 100	100	100		
0.75	19.0	83	76 - 90	95	90-100	100	100
0.5	12.5	68	56 - 80	80	76 - 90	95	90 - 100
⅜	9.5	61	48 - 74	68	56 - 80	83	76 - 90
No. 4	4.75	44	29 - 59	50	35 - 65	59	44 - 74
No. 8	2.36	32	19 - 45	36	23 - 49	43	28 - 58
No. 50	0.3	11	5 - 17	12	5 - 19	13	5 - 21
No. 200	0.075	5	1 - 7	6	2-8	7	2-10

3.3 Preparing Mixtures

Control mixes were prepared using limestone dust as the only mineral filler with a content of 7, 6, and 5% of the total weight of the mixes. The three percentages are in the midrange suggested by ASTM-D3515 for the three types of applications, i.e.: D-5, D-4, and D-3 for wearing, levelling, and base course, respectively. Other sample mixes took five different hydrated lime percentages by the total weight of the aggregates, namely 1.0, 1.5, 2.0, 2.5, and 3.0%. The hydrated lime was used to replace the same weight of limestone dust filler. Dry hydrated lime was added into the mixtures following the normal procedure. Each mixture had the same aggregate gradation to avoid variation in physical and mineralogical characteristics. Table 3.6 gives the hydrated lime content for the mixtures of the wearing, levelling, and base course.

Table 3.6 Hydrated Lime Replacement of Mineral Filler within Mixes for the Various Pavement Layers

Hydrated lime content (%)	Wearing course		Levelling course		Base course	
	Mixture	**Limestone content (%)**	**Mixture**	**Limestone content (%)**	**Mixture**	**Limestone content (%)**
0	CW	7	CL	6	CB	5
1	H1W	6	H1L	5	H1B	4
1.5	H1.5W	5.5	H1.5L	4.5	H1.5B	3.5
2	H2W	5	H2L	4	H2B	3
2.5	H2.5W	4.5	H2.5L	3.5	H2.5B	2.5
3	H3W	4	H3L	3	H3B	2

3.3.1 Measuring Particle Grade

Aggregates were sampled in the laboratory and graded for particle size. The samples of the different materials were quartered, in line with guidance in the ASTM-D3515. In this process, the material is turned to form a pile with even distribution, before dividing the sample in half with a cross piece. This is repeated to create a pile of the correct mass. This is then used for the grading process, in which it is firstly dried in an oven of controlled temperature 110 ±5°C to reach constant weight, which involves repeated checks on the sample's weight and replacing in the oven over the course of several hours, until that the weight alters below 0.1%. Thereafter, samples were left for cooling and then washed in a sieve No.200 (75)-micron diameter mesh to retain fines such as silt until the wash water draining through ran clear. The materials remaining within the sieve were recovered Figure 3.1.

Figure 3.1 Washing of a Sample with a Guard and 75-Micron Sieve, with all Particles Remaining in the Sieve Washing back through to the Sample

Thereafter, sieve analysis was conducted, as shown in Figure 3.2. The grades of aggregate specified for wearing course, levelling course and base course are given in Figure 3.3, Figure 3.4 and Figure 3.5 respectively. Aggregate grades are in the specified range for the wearing course layer, levelling course layer and base course layer respectively .

(a) Sieve analysis

(b) prepared Raw Materials

Figure 3.2 Material preparation

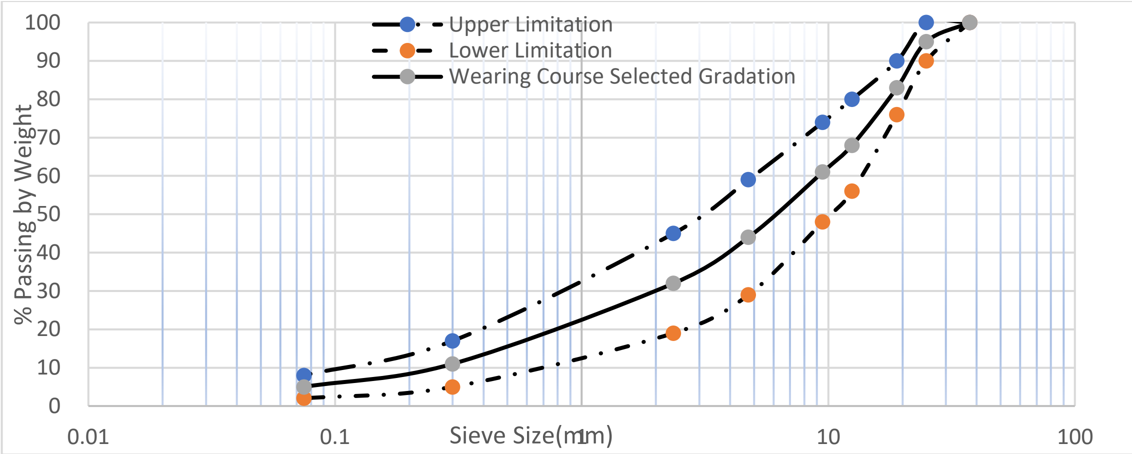

Figure 3.3 Grade for Mineral Filler/Aggregate for the Wearing Course

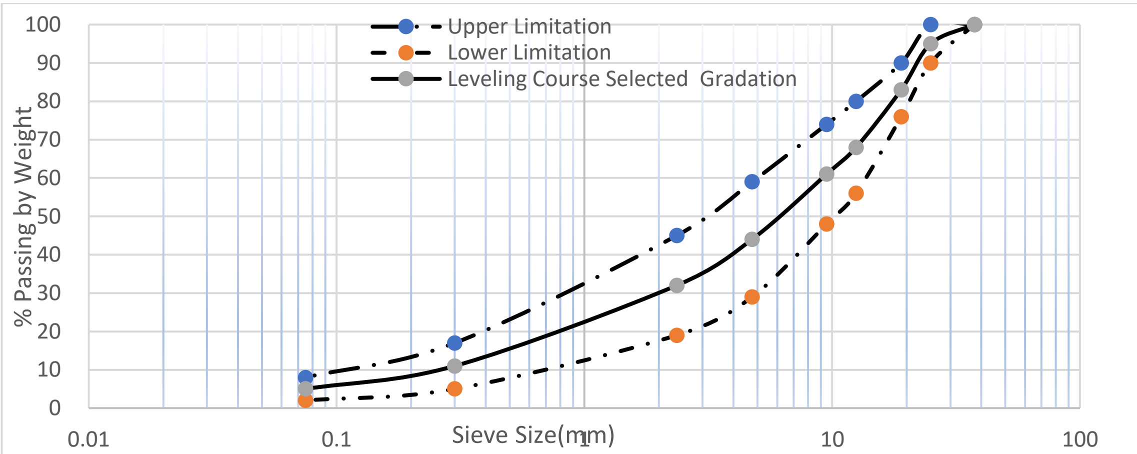

Figure 3.4 Grade for Mineral Filler/Aggregate for the Wearing Course

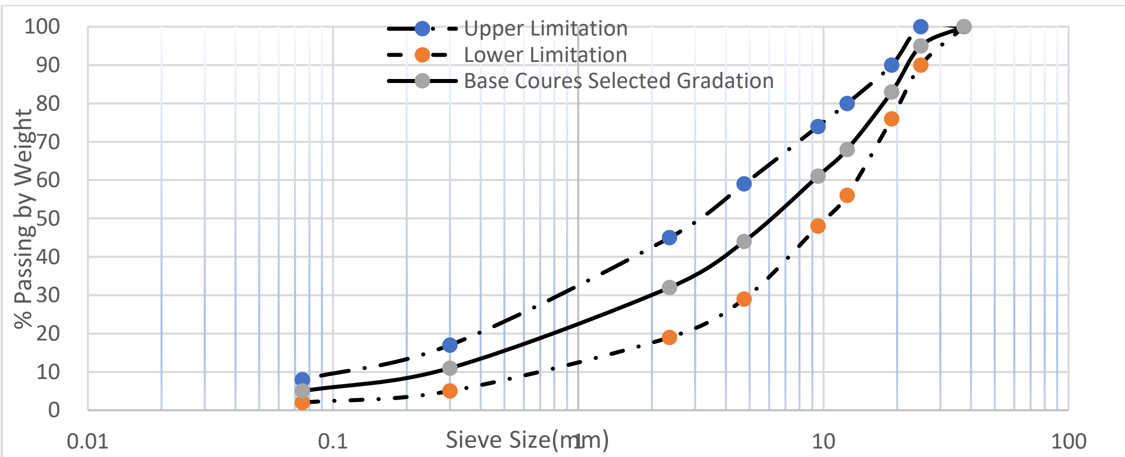

Figure 3.5 Grade for Mineral Filler/aggregate for the Base Course

3.3.2 Mix Designs

Marshall Mix Design (ASTM D6926-2010a) was performed in mixture preparation, which is the accepted process for asphalt concrete sample preparation using Marshall equipment. Moreover, the Asphalt Institute's MS-2 guide to mix design was also referred to. Sample preparation began with the production of batch aggregate fractions, involving weighing out aggregate fractions following the particular design for the type of sample to be created, ensuring the appropriate batch weight was reached when combining these. The aggregates were heated in an oven together with the asphalt cement, to reach the correct temperature to be mixed to create the hot mix asphalt mixture required. The Brookfield Rotational Viscometer was used to measure viscosity at two temperatures, i.e., 135°C and 165°C, the appropriate temperature for compacting the mix. Viscosity was measured after the mixes had reached an even temperature for 30 minutes. This involved rotating a size-27 spindle at 20rpm for 10 minutes and taking averaged measurements from the final 5 minutes of this period to calculate apparent viscosity. A lower temperature-viscosity relation is applied to determine mixing temperature and compaction temperature, as shown in Figure 3.6, which were identified respectively as 160°C and 150°C. After checking aggregates and mixing temperatures were at the required level, asphalt was mixed into the aggregates.

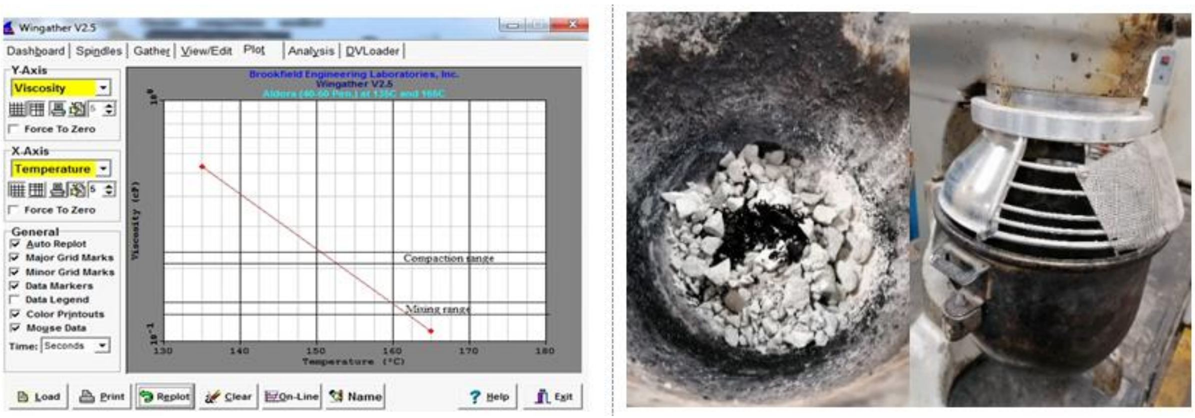

Figure 3.6 Viscosity Temperature Chart and Addition of Asphalt to Aggregates Occurs before the Bowl is Positioned on the Mixing Unit

The asphalt cement percentages by the total weight of the specimens were in the range of 4.3–5.5 for the W course, 4.0–5.2 for the L course, and 3.7–4.9 for the B course. Mixes with an interval of 0.3% in each range were studied. Three specimens were made for each percentage. The property results took the average value of the three tests. The preparation and testing of specimens were conducted according to the standard ASTM D6926-10 (ASTM 2010;ASTM 2004). Cylindrical specimens of 101.6 mm (4 in.) in diameter and 63.5 mm (2.5 in.) in height were first manufactured and the cured for 0.50 to 0.75 h in a water bath at 60°C. Afterward, they were compressed by their side surface under a constant loading rate of 50.8 mm/min (2inch/min) until they failed. The result of each test was plotted in terms of the percentage of asphalt (by total weight of the mix) on a linear scale. Each point shown on the plot is an average result of the tests of the three specimens of a specific mixture. Thereafter, the optimum asphalt content (OAC) was determined by taking the average of the three asphalt contents of the mixtures of a certain hydrated lime content, which achieved the following three criteria:

- Maximum unit weight (density).
- Maximum stability; and
- 4% air voids.

Optimum asphalt content mixes with their specific unit weight, stability and percentage of air voids are given in Table 3.7.

Table 3.7 Marshal Design Preparation for all Layers: Wearing Course, Leveling Course and Base Course

Mixture	OAC (%)	Density (g/cm3)	GMM (g/cm3)	Stability (KN)	Flow (mm)	AV (%)	VMA (%)	VFA (%)
Control CW	4.9	2.34	2.44	11.6	3.25	4.02	14.22	71.74
H1W	4.9	2.34	2.44	12.13	3	4.01	14.18	71.7
H1.5W	5	2.33	2.44	12.14	2.8	4.08	14.4	72.4
H2W	5.2	2.33	2.43	14.14	3	4.14	14.68	72.74
H2.5W	5.3	2.32	2.42	13	2.8	4	15.2	71.47
H3W	5.3	2.31	2.41	12	2.6	4.1	15.4	71.2
Control CL	4.6	2.32	2.43	10.57	3.25	4.02	13.14	69.36
H1L	4.7	2.32	2.43	10.31	3.1	4.3	13.5	66
H1.5L	4.8	2.32	2.43	10.25	2.8	4.3	13.3	67
H2L	4.9	2.32	2.42	11.19	3	4.35	13.36	67.4
H2.5L	5	2.3	2.42	11.5	3	4.5	13.7	67
H3L	5	2.3	2.41	11	2.5	4.6	14	67
Control CB	4.3	2.31	2.42	8.9	2.92	4.29	14	69.35
H1B	4.3	2.31	2.42	8.77	2.7	4.28	13.99	69.39
H1.5B	4.4	2.31	2.41	9	2.5	4.5	14.3	69
H2B	4.5	2.305	2.41	9.6	2.4	4.2	14.39	70
H2.5B	4.6	2.297	2.4	10.7	2.45	4.39	14.67	70.06
H3B	4.7	2.29	2.4	9	2.3	4.55	15	70.1

AV refers to air voids; VFA refers to void in aggregate filled with asphalt; VMA refers to voids in mineral aggregates; GMM is the theoretical maximum specific gravity for the loose mix and excluding air voids; and Flow represents deformation in mm for a sample, measuring from test initiation to the point of greatest stability.

For each specimen used, calculations were made for percentage of air voids (ASTM D3203), bulk density, specific gravity (ASTM D2726) and GMM (ASTM D2041). A brief summary of calculations for air voids (AV), bulk specific gravity (G_{mb}), and maximum theoretical specific gravity (G_{mm}) is given below:

• Bulk Specific Gravity (G_{mb}): specimens are weighed at 25°C in water, air and saturated with the surface dried. Calculations are made as in the equation below:

$$G_{mb} = \frac{W_a}{W_{ssd}+W_w} \qquad \text{Equation (3-1)}$$

Where:

G_{mb} = The bulk specific gravity for the specimen following compaction,

W_a = The weight in grams of the dry specimen,

W_{ssd} = The weight in grams of the saturated, surface-dried specimen; and

W_w = The weight in grams of the specimen in water.

- The maximum specific gravity (G_{mm}) obtained at the laboratory is calculated as follows:

$$G_{mm} = \frac{A}{A+B-C} \qquad \text{Equation (3-2)}$$

Where:

G_{mm} = The maximum specific gravity for the loose pavement mix,

A = The dry specimen’s weight in grams in air,

B = The water-filled flask’s weight in grams at 25°C, and

C = The water-filled flask's weight with the specimen in grams at 25°C.

• Air voids are measured as the overall air pocket content of the compacted mixture by volume, with these voids occurring all through a specimen as spaces separating coated aggregates. The AV measurement is calculated firstly by finding the sample's maximum theoretical specific gravity, and then finding the difference between this value and bulk density, expressed in % of theoretical density, in line with the relation below:

$$AV = \frac{G_{mm} - G_{mb}}{G_{mm}} \qquad \text{Equation (3-3)}$$

Where:

AV = The void percentage in the overall sample of mixture,

G_{mm} = The maximum theoretical specific gravity (gm/cm3), and

G_{mb} = The bulk specific gravity (gm/cm3) in the compacted sample.

3.4 Exploring the impacts of hydrated lime through experiment

For this experimental exploration of the impacts of hydrated lime, firstly, the optimal proportion of asphalt was calculated for each asphalt concrete mixture by applying the Marshall mix design procedure. Following this, mixtures were produced to conform to these optimised content ratios, followed by testing to assess thermal and engineering characteristics. Assessment of permanent fatigue and permanent deformation parameters was carried out through triaxial testing as well as repeat flexural beam testing.

3.4.1 Asphalt cement testing

Various testing approaches have been developed to assess stiffness and consistency in bituminous materials such as asphalt cement, which is primarily used for its ability to bond together particles of aggregates to create asphalt concrete mixes. The more significant of these testing approaches, as adopted by most relevant bodies and standards in flexible pavement design, are the softening point and penetration tests. A summary of the two test types is given below.

3.4.2 Penetration Test

Penetration here refers to the extent to which a standard-dimension needle penetrates in the vertical direction an asphalt specimen which has been subject to melting and cooling processes within specific and controlled temperatures, loads and durations. This is measured in 10ths of a millimetre. Penetration tests are applied to measure consistency under ASTM D5 (ASTM Vol. 04.03, 2004), with greater penetration measures pointing to greater softness in the material. An illustration of this test as applied to asphalt cement is given in Figure 3.7.

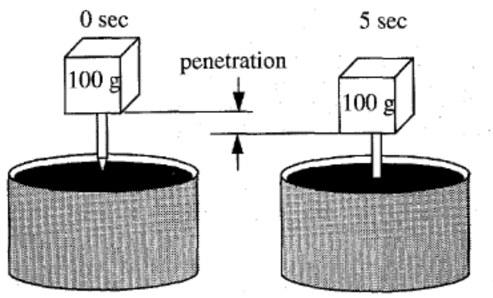

Figure 3.7 Penetration test applied to a bituminous specimen (McGennis et al., 1995)

3.4.3 Softening Point Test

The ring and ball, or softening point test, measures the temperature reached in order for a fixed-weight steel ball lying on top of a sample of asphalt cement to drop vertically by 1 inch (25.4 millimetres). As temperature rises incrementally, and the asphalt cement becomes softer, the ball drops into the mixture in a gradual manner. This occurs as a result of the increased internal flows of the cement as it becomes hotter. This test is illustrated for an asphalt cement specimen in Figure 3.8. The softening point test is performed in accordance with ASTM D36, where the test procedure is given in detail.

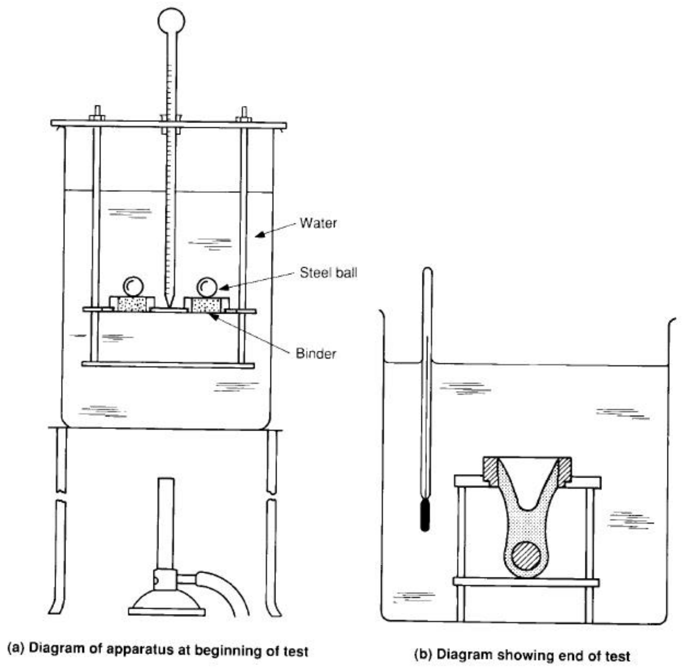

Figure 3.8 Softening point test as applied to bituminous material (Millard, 1993)

3.5 Testing for Thermal Properties

A previous project at Salford has investigated the main conventional mechanical properties of all the designed mixes and has concluded that the mix with 2.5% HL addition produced the optimum performance. This study focused on measuring and comparing the thermal properties of the 2.5% HL mixes and 0% HL control mixes used for three different layer purposes.

3.5.1 Measurement Apparatus

Two methods can be used to determine thermal conductivity, namely steady-state and non-steady-state approaches. When thermal conductivity is measured with steady-state approaches, this occurs while the materials are in a steady thermal condition. The other approach, including use of the Quick Thermal Conductivity Meter (QTM500) applied here, allows for more rapid results, with thermal conductivity being recorded as the materials heat up (Crompton, 2006).

3.5.2 Quick Thermal Conductivity Meter and Principles for Measurements

Using the QTM-500, measurement of samples of various materials can be done through a simple process which involves applying a probe with a sensor to the sample's surface, and pushing 'start', with the results shown 60 seconds later. The probe consists of a heater wire and thermocouple, and when constant electric current is applied, exponential heating of the heater wire occurs. The curve for linear temperature increase is shown in Figure 3.9, in which the axis for time is subject to a logarithmic scale. The greater the rise angle of the line, the lower the thermal conductivity of the sample, with a smaller angle of rise seen in material which has a higher Caterforce. Materials' thermal conductivity can be determined using the temperature curve's angle of increase.

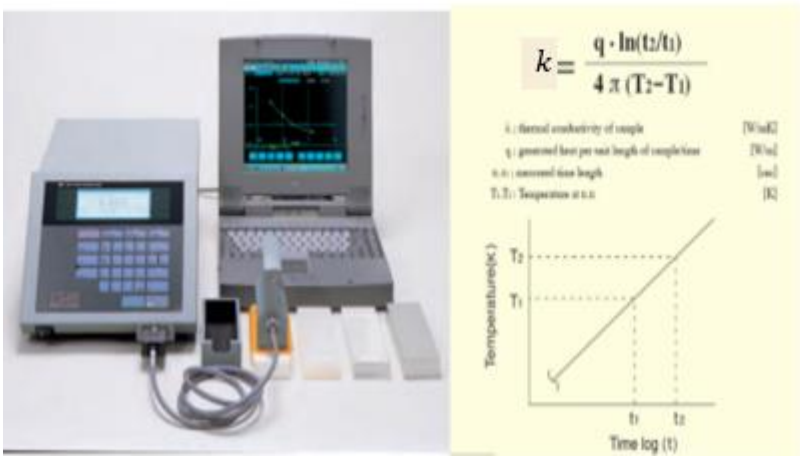

Figure 3.9 Principles in Measuring Parameters

3.5.3 Preparing Samples for Measuring Thermal Characteristics.

To measure thermal conductivity through the QTM-500, the guidance states that samples should be a minimum of 5 inches (127 mm) in diameter. This study utilised cylindrical moulds of a dimension of 6 inches (152.4 mm) in diameter and 2.5 inches (63.5 mm) in height. The asphalt concrete samples were designed for the application of wearing, levelling and base course, respectively. Two types of mixes were made for each specific layer (see Table 4.7). One is the control mix, which used limestone dust only for the mineral filler, and the other one is based on the control sample but with partial replacement of the limestone filler, using HL at 2.5% of the total weight of aggregate.

After production of the asphalt mixture batches, they were maintained, together with the moulds, under the temperature specified for compaction, which for the 40/50 asphalt mixes used here was 150 $\pm$5°C. Thereafter, the mixtures were loaded into the moulds placed on a balance, with the temperature checked before starting to compact the mixture in the mould. If the mixture in mould was found to be below the temperature limit, it would be replaced in an oven to reheat, while if above the limit, it was left for further cooling. When the specified temperature was reached, compaction was conducted through applying 114 blows to each end of the mixture in a cylindrical mould, using a 4.536 kg hammer which fell from a 457.2 mm height, to make the sample blocks for testing. The mix in the moulds was topped with a paper disc so that none of the materials became stuck to the compaction footing. Following compaction and removal of the paper disc, the sample blocks were left for cooling and then demoulded. The demoulded samples were left for another 24 hours at ambient room temperature for further cooling prior to testing (see Figure 3.10).


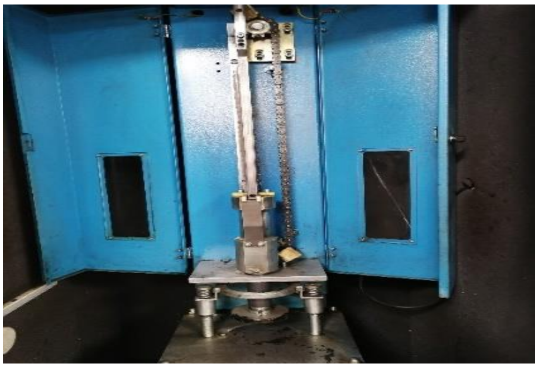

Figure 3.10 Checking the Temperature of the Asphalt Sample (Left) before Compacting it (Right) Using an Impact Compactor.

(a) Samples Ready for Testing

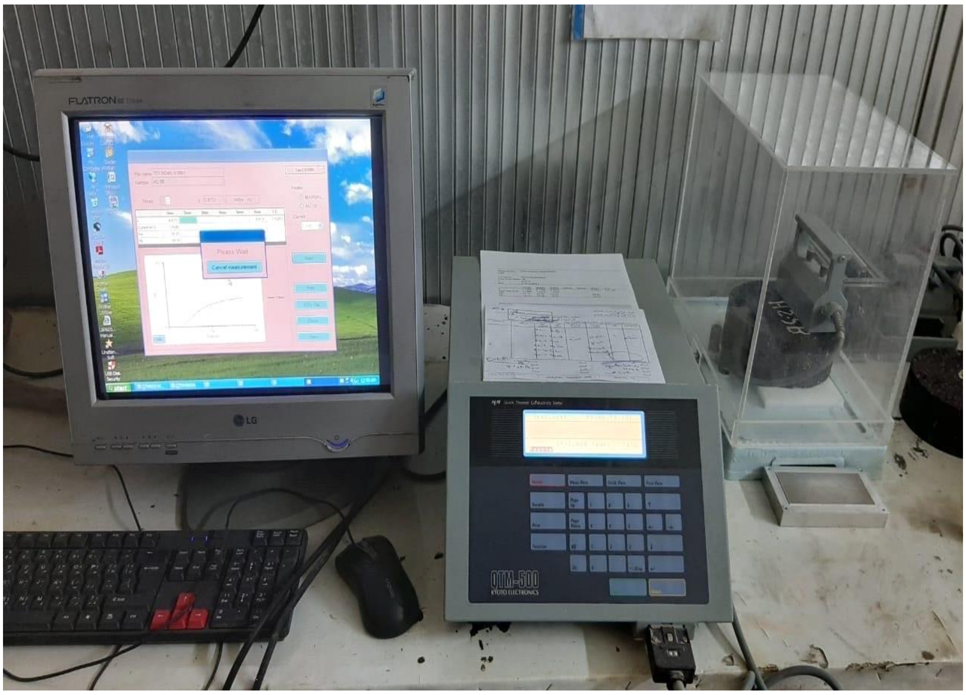

(b) Experimental setup

Figure 3.11 Thermal Conductivity Testing

3.5.4 Determining Thermal Conductivity, k

All samples were tested using the QTM500. In Figure 3.11, the method of measurement called hotwire method allows k of the sample to be obtained by the following procedure:

1. Connect the probes directly on top of the sample by simply placing the probe on a smooth surface of the sample to easily measure its thermal conductivity.

2. Through pushing the measurement button, the recorded measurement values are displayed. This also allows various and necessary pieces of information like graphs to be displayed quickly. The average calculation of measured values, as well as the room temperature characteristics of the sample, can be displayed, making it easy to analyse results, as shown in Figure 3.12.

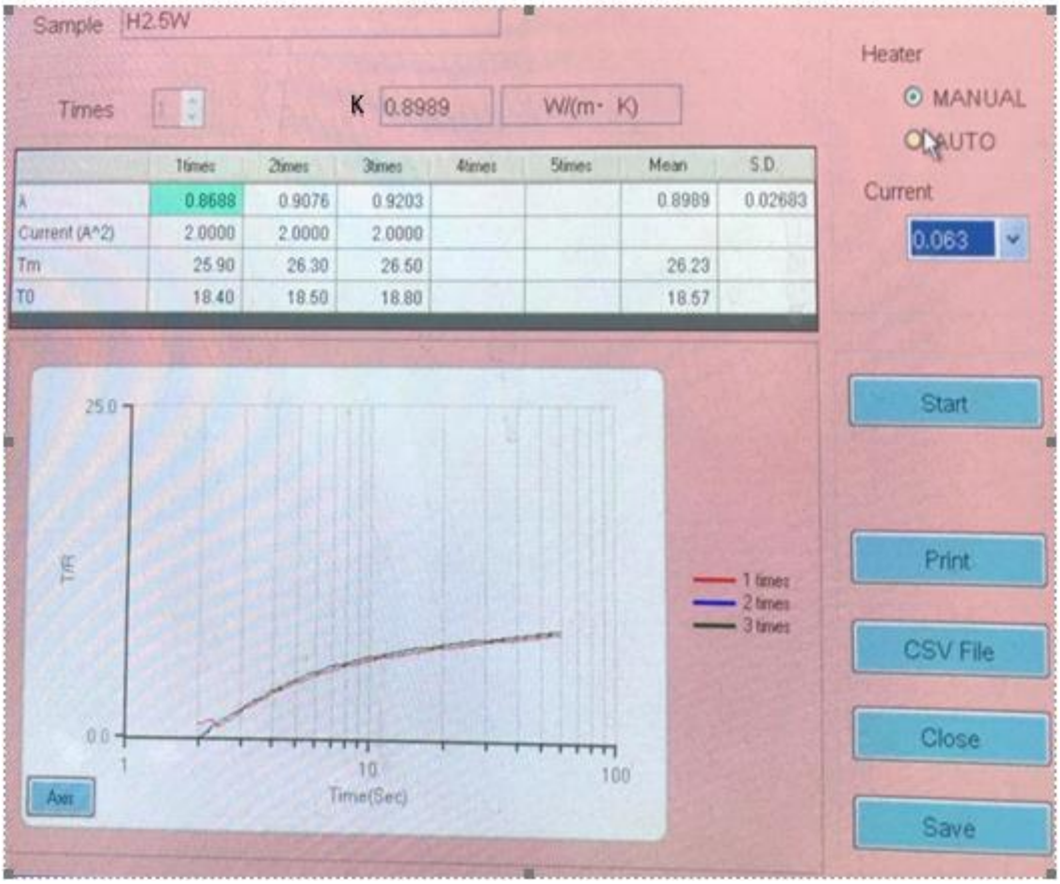

Figure 3.12 Output of the QTM

3.6 Experimental Results

Equation 3-4 was used to calculate per-unit heat production, Equation 2-2 determined specific heat capacity, and Equation 2-1 identified thermal diffusivity.

$$Q = \frac{K\,4\pi(T_2 - T_1)}{.\ln(t_2/t_1)} \qquad \text{Equation (3-4)}$$

Where:

Q = Generated Heat per unit length of sample (W/m).

K = Thermal Conductivity (W/m K).

t_1, t_2 = Duration given in seconds

T_1, T_2 = Temperature for t_1, t_2 (K).

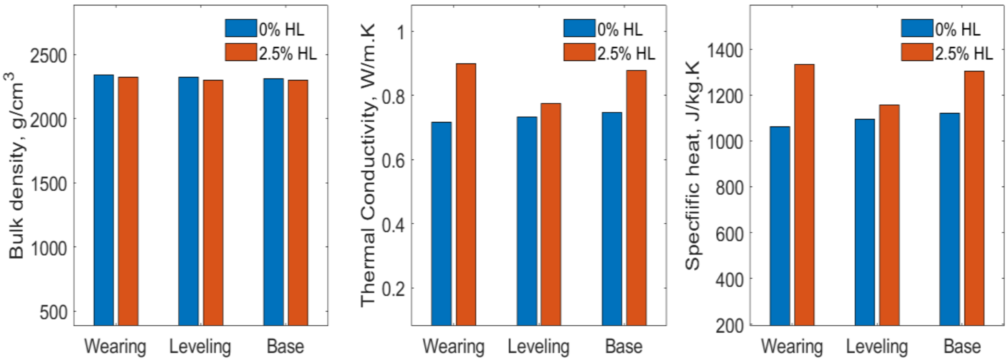

Figure 3.13 Comparing Thermal Characteristics of Mixtures with 0% and with 2.5% HL

Figure 3.13 compares the measured bulk density and two thermal properties between the control mixes and those with 2.5% HL addition. It can be seen that HL addition has a very small influence on the bulk density, but significantly increases the thermal conductivity and thermal capacity (specific heat). Specifically, the increase in thermal conductivity is 27% for the wearing mix, 7% for the levelling mix, and 17% for the base mix. The increase in specific heat is 25% for the wearing mix, 6% for the levelling mix, and 16% for the base mix. Theoretically, a high magnitude of thermal properties will help crack healing. The data shown in Figure 3.13 indicate that the mixtures with added hydrated lime appear to have a higher asphalt content than the control mixture. The mixtures of 2.5%HLW, 2.5% HLL, and 2.5HLB have OAC values of 5.3%, 5%, and 4.4%, respectively, which are higher than that of the mixtures with less hydrated lime content. The three control samples for the W, L, and B course have the lowest OAC values, which are 4.9%, 4.6%, and 4.3%, respectively. The increase in asphalt cement for the hydrated lime modified mixtures can be attributed to the relatively high specific surface area of hydrated lime, which is about 1.6 times of that of limestone dust. The high surface area attracts more asphalt cement particles to achieve a more thorough hydration process (Al-Suhaibani, Al-Mudaiheem and Al-Fozan, 1992; Shahrour and Saloukeh, 1992)

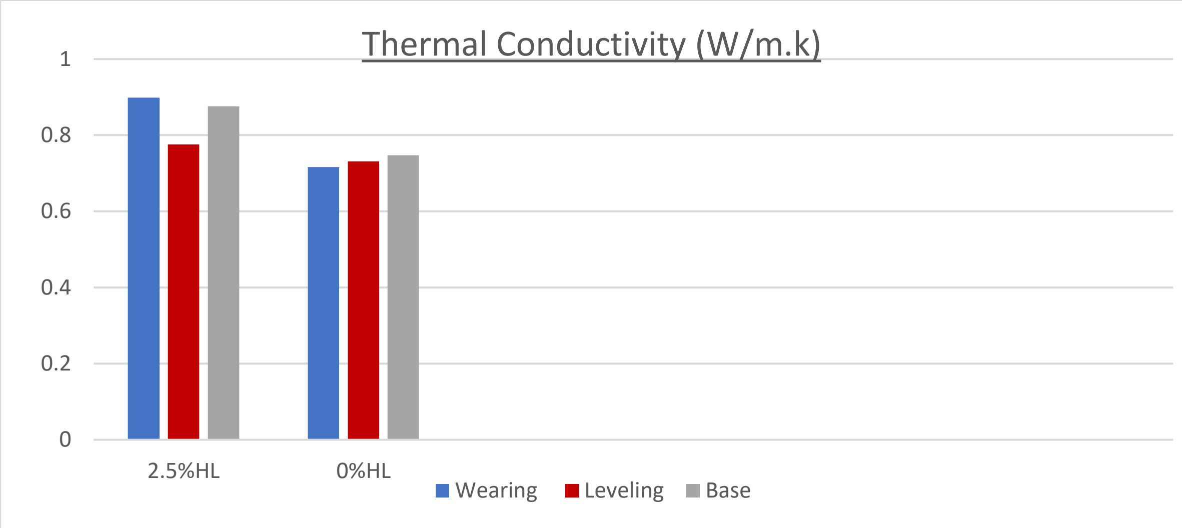

Figure 3.14 Findings from the Thermal Conductivity Test

Figure 3.14 provides the findings produced by thermal conductivity tests of both 2.5% HL samples and control samples without HL, recorded in W/ (m.k). The results on the left are for wearing, levelling and base course samples with a 2.5% addition of hydrated lime, while on the right are the results for wearing, levelling and base course samples without HL. Each set of findings was recorded using the QTM-500. Thermal conductivity values for 2.5% HL samples were between ~0.7757 and ~0.898 W/(m.k), in comparison to 0% HL sample values of between ~0.7161 and ~0.7471 W/(m.k).

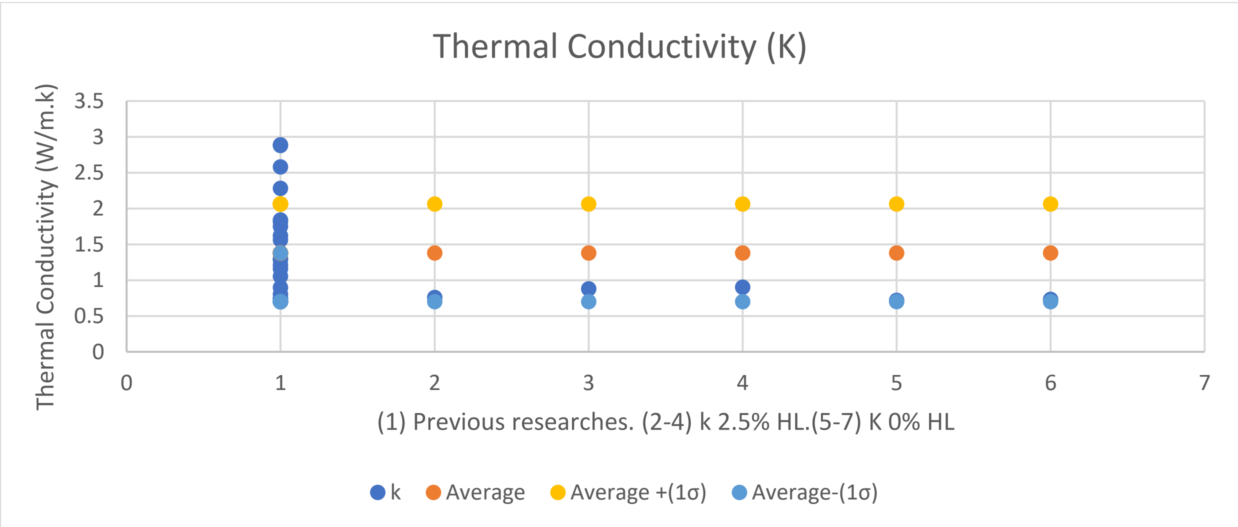

Figure 3.15 Results for Thermal Conductivity Shown against Published Values

In Figure 3.15, the values for thermal conductivity are further compared to results reported in other works, as discussed in Chapter Two's literature review. Location 1 provides AC findings from previous work, and 2-4 represent the findings for the 2.5% HL samples in the current study, while 5-7 present the results for the control samples without hydrated lime. Using the orange averaged line at 1.380, along with plus/minus-one sigma lines respectively in yellow 2.0608 and in light blue at 0.6993, showing values in previously published works. It is clear that the values from the current study are in general lower than averaged values, but with every value being higher than the minus one sigma line. Overall, the values obtained here can reasonably be compared to 0.99 w/mk as recommended by the EICM.

In addition, specific heat was tested across both 2.5% hydrated lime and control specimens, and the findings are shown in Figure 3.16 in kJ/(kg.k). The 3 bars on the left of the chart represent results for wearing, levelling and base course samples modified with hydrated lime, while the bars to the right show findings for the control samples, with no hydrated lime added. Each set of values was calculated using Equation 2.2. Specific heat values for the 2.5% HL samples were between ~1.1555 and ~1.3335 kJ/(kg.k), with control samples giving values between ~1.0626 and ~1.1211 kJ/(kg.k).

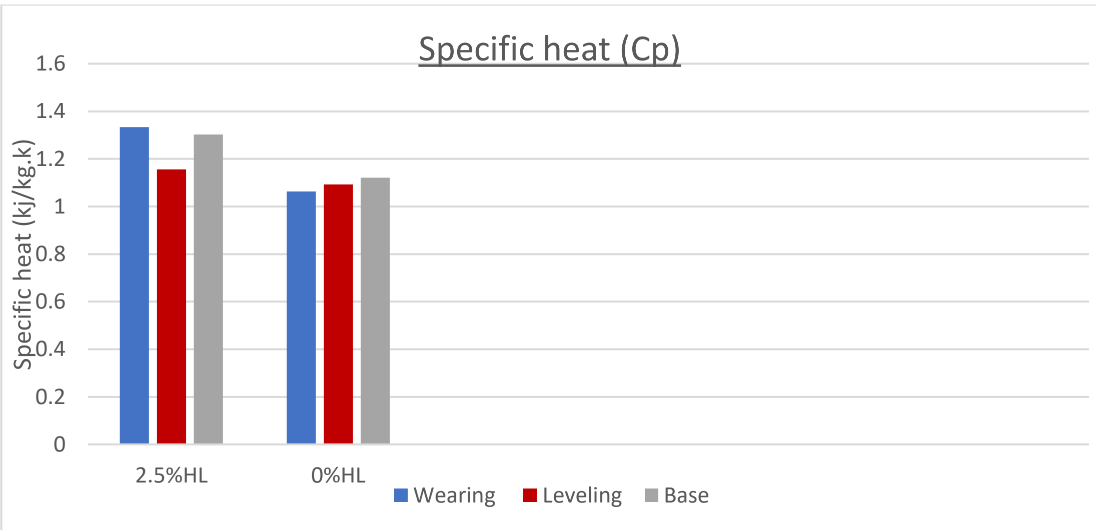

Figure 3.16 Findings for Specific Heat Tests

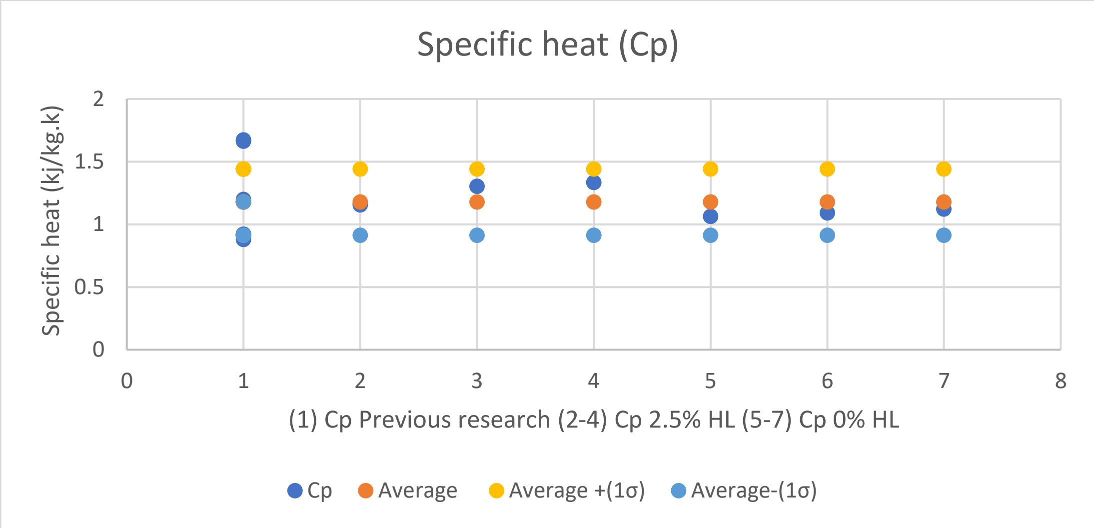

Figure 3.17 Findings for Specific Heat against Findings from Literature

Figure 3.17 shows the link between specific heat values in this study and those in other published work, as discussed in the literature in Chapter Two, with location 1 representing findings from previous work, 2-4 representing the findings for the 2.5%HL specimens in this study, and 5-7 representing the control samples without hydrated lime. The orange points show the average values at 1.172, while yellow shows the plus-one sigma at 1.4409, and minus-one sigma is shown in pale blue at 0.91350 based on previous studies. Viewing the results, the findings from this study are partly above the average value and partly close to or just below this average, while remaining higher than the minus-one sigma level. At the same time, inconsistency in these patterns was identified when comparing with recommended EICM values, with specific heat findings for each mixture exceeding 0.92 w/mk as the EICM recommendation.

The findings given below relate to density in both control specimens and 2.5% HL samples, and are presented in gm/cm^3 in Figure 3.18. To the left of the figure, the bars represent the results for the wearing, levelling and base course samples modified with hydrated lime, while the bars to the right show findings from the control mixtures for each course. For the 2.5% HL specimens, findings were between ~2.297 and ~2.320 gm/cm^3, and for controls were between ~2.310 and ~2.340 gm/cm^3

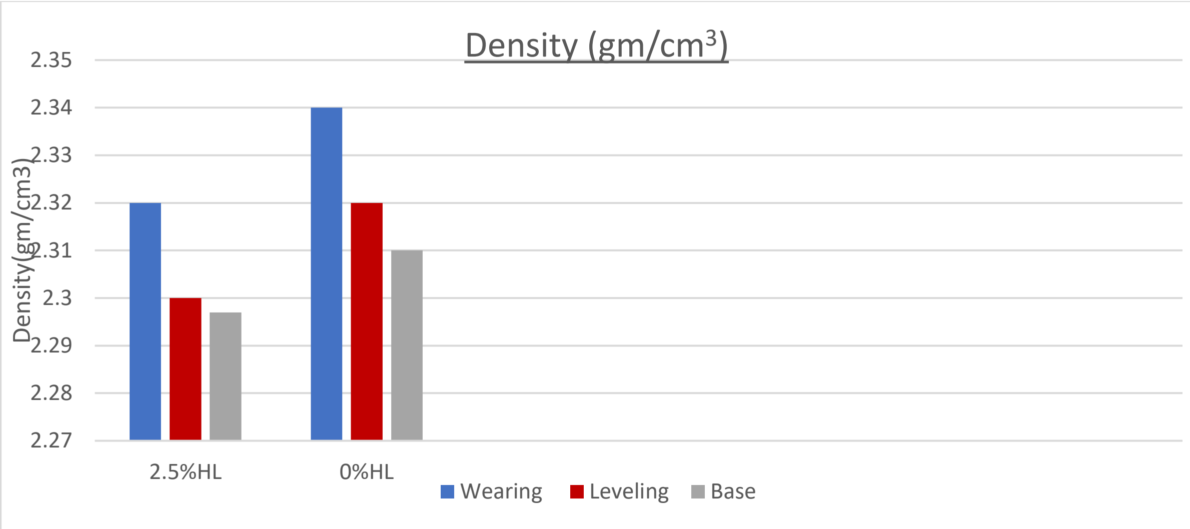

Figure 3.18 Findings for Density

Figure 3.19 again compares this study's findings with those of previous works discussed in Chapter Two (shown in location 1 in the Figure), but here for density. Locations 2-4 display the findings for the 2.5% HL specimens in this study, with 5-7 representing the control samples. The orange points show the average values at 2.2430 gm/cm^3, yellow shows the plus-one sigma at 2.4993 and minus-one sigma is shown in pale blue at 1.9867 based on the literature. From the Figure, the density of specimens in the current study has a tendency to exceed average values.

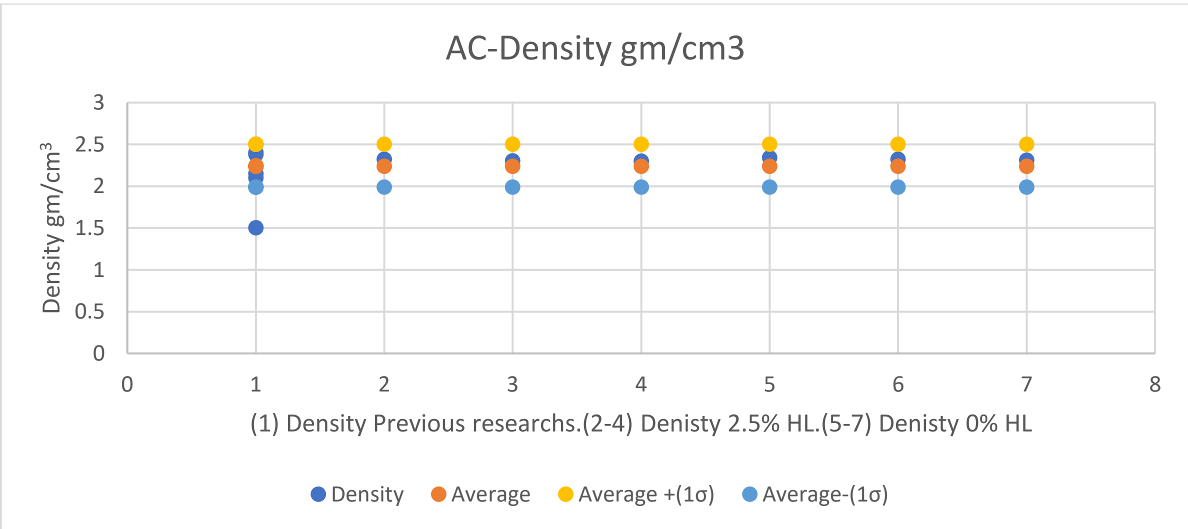

Figure 3.19 Findings for Density Shown against Values from Literature

3.7 Flexural Fatigue Cracking

3.7.1 Preparing Specimens

Cuboid beams of dimensions 381×76×76 mm^3, were produced as specimens of the 6 HMA concrete mixes designed for wearing course application. The control mix used limestone dust for the mineral filler at 7% of the total weight of aggregates. The five other mixes used HL to replace the limestone dust in the control mix at a rate of 1, 1.5, 2, 2.5 and 3% respectively by total of weight of aggregate. Four specimens were prepared for each mix. First, the prepared loose mixes were loaded into preheated steel moulds, at approximately 5450 gm of mix for each mould. The mixture was shovelled prior to compaction and then pressed using a compressive machine with a gradually applied static load of 65771 Kg for 2 minutes, in line with ASTM-D1074-96. The mould was made "free floating" by using a "double plunger" arrangement. The applied load, 65771 Kg, which was tested and selected prior the cast of specimens, was determined to give the specimens a density above a Marshall Density of 2.3 gm/cm^3. In general, a compression temperature of 150°C is used to achieve a more homogenous mix. The final stage was to extract specimens by gripping them tightly with the compressive equipment machine and freeing them from their mould 24 hours later. Figure 3.20 illustrates the moulds for the specimens, the compressive procedure, the process of extracting specimens and specimens prepared for testing.

(a) Flexural beam specimen mould

(b) Compaction of beam specimen

(c) Extraction of specimen

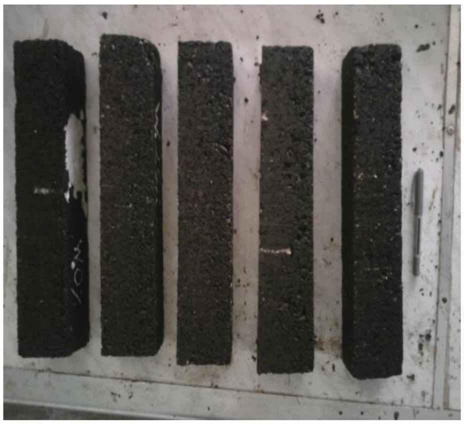

(d) Beam specimens

Figure 3.20 Preparation of Specimens for Fatigue Cracking Test

3.7.2 Flexural Beam Fatigue Testing

Third point loading for flexural beams was adopted for fatigue testing as illustrated in Figure 3.21. This approach was applied to achieve a pure bend at the middle third area of the beam. Fatigue life as the number of cycle repetitions of loads (P) applied to the beam up to total breakage of the beam, a moment frequently accepted as an indication of the complete failure of the beam and commonly considered as an indicator of fatigue cracking potential (Huang, 2004). Testing was carried out in stress-controlled mode, and flexural was imposed at 2 Hz, using 0.1 seconds of loading to 0.4 seconds unloaded, and utilising a rectangular waveform. A total of four different loads (P) were applied, namely 223, 310, 402 and 490 N. The loads were chosen to allow each specimen to reach failure at between 100 and 100,000 repetitions. All tests were performed under three controlled temperatures, which were 15, 20 and 25°C. Test beam specimens were put into test chambers temperature controlled at 15, 20 and 25°C for 6 hrs to ensure an even temperature distribution throughout the specimens. In the tests, loading was applied via a Pneumatic Repeated Load System (PRLS), while deflection at the mid-span point was recorded using a digital camera up to the failure point. An aluminium steel rod in contact with the Linear Variable Differential Transducer (LVDT) was placed at the middle point of the beam's top surface to detect local vertical deflection. The LVDT was connected to a data acquisition system which stored deflection data across different time points and analysis was conducted to determine strain for any required cycle number and in each test. Specimen testing was carried out in line with SHRP standards, for a beam specimen with a length of 381 mm and a height and width of 76 mm. For fatigue testing, initial tensile strain was identified at approximately 200 repetitions through Equation 4-7, as given below. A plot of initial strain against repetitions to failure was made for the S-N curve for fatigue analysis, with beam failure specified as the point where the beam broke down. Equations for general use in analysing beams with simple supports are listed below (Huang, 2004):

$$\sigma = \frac{3\, \mathrm{p}_a}{\mathrm{bd}^2} \qquad \text{Equation (3-5)}$$

$$\mathrm{E_s} = \frac{\mathrm{p}_a\ (3\mathrm{L}^2 - 4a^2)}{4\mathrm{bd}^3\Delta} \qquad \text{Equation (3-6)}$$

$$\varepsilon_\mathrm{t} = \frac{\sigma}{\mathrm{E_s}} = \frac{12\mathrm{h}\Delta}{3\mathrm{L}^2 - 4a^2} \qquad \text{Equation (3-7)}$$

Where:

ε_t = Tensile strain

σ = Flexural stress

Es = Stiffness modulus based on centre deflection of beam specimen.

h = Height of the beam

Δ = Dynamic deflection at the centre of the beam.

L = Length of span between supports.

a = Distance from support to the load point (L/3)

As reported previously, within the controlled fatigue test, cracking is initiated, with a minimal propagation phase following before complete failure is reached. This differs markedly from a controlled strain modality, in which the propagation phase is far lengthier, leading to a new definition (Hopman, Kunst and Pronk, 1989). Therefore, the fatigue life, N_f, against initial strain, ε_t, provides the material fatigue characteristic, which is defined using the following power equation (3-8) (Monismith, Kasianchuk and Epps, 1967):

$$\mathrm{N_f} = \mathrm{K_1}(\, \varepsilon_\mathrm{t})^{-\mathrm{K_2}} \qquad \text{Equation (3-8)}$$

Where:

N_f = Number of repetitions to failure

K_1= fatigue constant, value of Nf when εt = 1

ε_t = initial tensile strain   at about the 200th repetition

K_2= inverse slope of the straight line in the logarithmic relationship

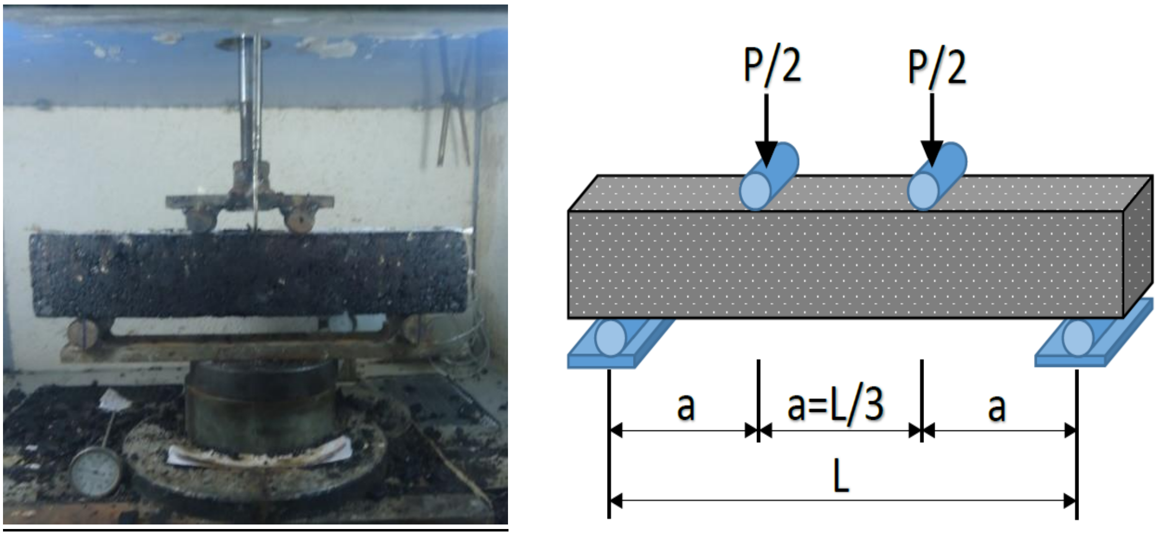

Figure 3.21 Schematic of Loading Configuration of the Beam

3.8 Hydrated Lime's Influence on Fatigue Cracking

The impacts of hydrated lime on resistance to fatigue cracking were assessed through applying flexural testing as described above. The relation of strain (ε_t) to loading repetition number to failure (N_f) follows the model of Equation 3-8. This equation contains parameters $k_1$and k_2. Equation 3-9 displaces as a straight line in a log-log scale plot, in which log(k_1) stands for the intercept of log (N_f) and the k_2 stands for the slope of the linear trend of the log (N_f) against log (ε_t).

$$\log N_f = \log k_1 - k_2 \log \varepsilon_t \qquad \text{Equation (3-9)}$$

3.8.1 Initial Tensile Strain-Fatigue Failure Life Relationship

Figure 3.22 shows the temperature effect on the measured strain at the 200th cycle under the four applied loads. The control mix displaces the lowest initial strain at temperatures of 15 ℃ & 25 ℃, but nearly the highest at 20 ℃. However, the 2.5 % HL mix is the opposite, with the highest initial strain at 15 ℃ & 25 ℃, but the lowest at 20 ℃. Such little correlation between the initial strain and temperature may be explained due to the initial microstructure adjustment of the mixes in their fresh state. Figure 3.22 shows that at 20℃, the mixes of 0% and 1% have better fatigue life than the others at high initial strain level (> 200th). The results can be explained by the suggestion that hydrated lime helps the fatigue resistance at temperatures away from the room temperature range, but has no impactive benefit for mixes in room temperature conditions. However, at a lower strain condition (<200th), HL addition shows promising improvement on fatigue resistance for the three temperature conditions.

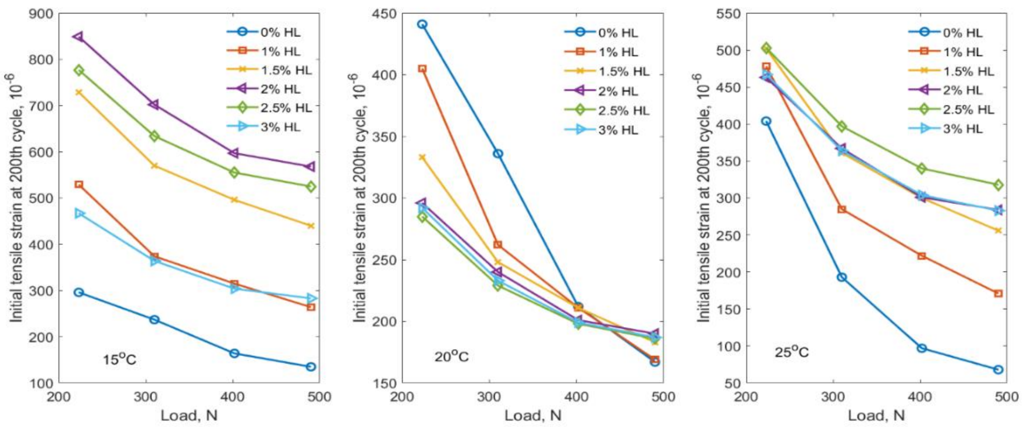

Figure 3.22 Initial strain at the 200th loading cycle vs the loads applied.

Figure 3.23 shows the fatigue test results, the S-N curves. It can be seen from Figure 3.23(b), showing a linear trend at the log-log scale, that the mix of 2.5 % HL at the three temperatures has the smallest slope. Meanwhile, at the same initial strain, the 2.5 % HL mix has the highest load repetition number (N_f) before failure at temperature 25 ℃, and at the other two temperatures, 15 ℃ & 20 ℃, and when the initial strain is less than 270 micro-strains. The result confirms and strengthens the conclusions in other previous studies (Al-Tameemi, Wang and Albayati, 2016; Al-Tameemi *et al.*, 2019; Al Ashaibi *et al.*, 2022) that 2.5 % HL addition can be an optimum rate for HMA concrete to obtain a compromise material property improvement when exposed to both mechanical loading and thermal influence.

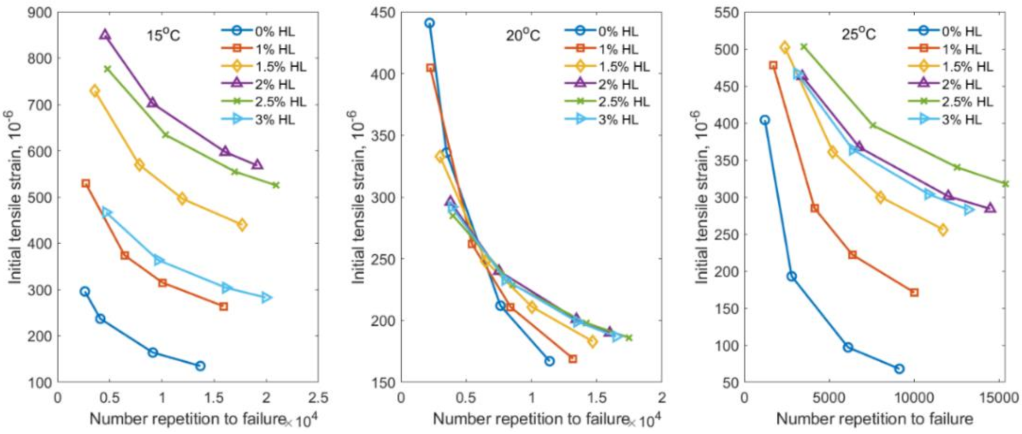

(a) In Normal Scale

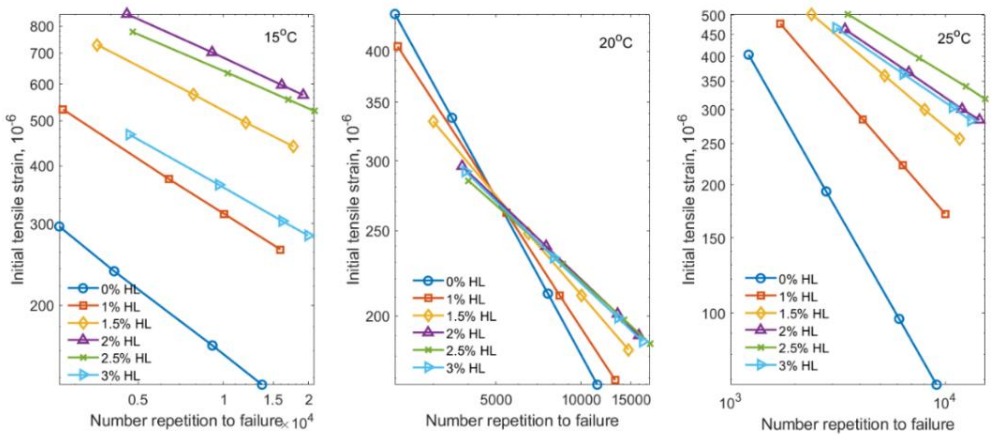

(b) In Log-log Scale

Figure 3.23 Fatigue Test Result of the 6 Mix for Wearing Course Application

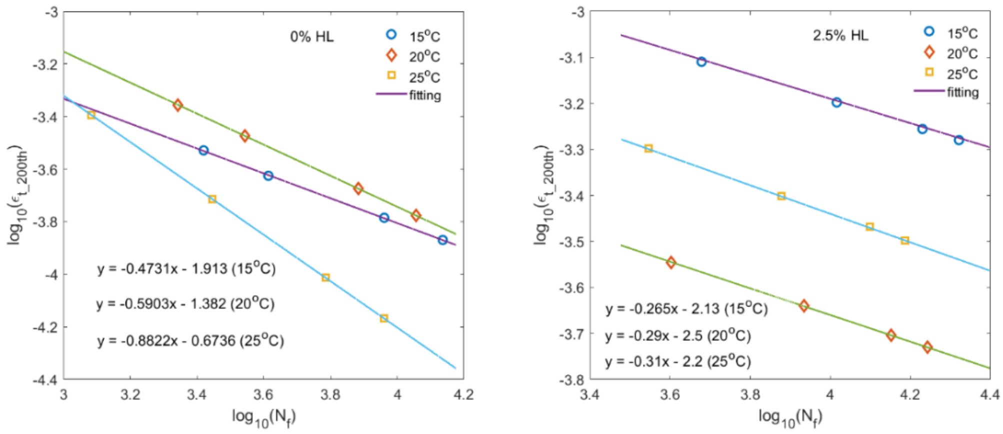

Figure 3.24 The S-N curve of the mix of 2.5% HL under three temperatures and fitting at log-log scale

Figure 3.24 provides a comparison of results for the mix with 2.5% HL and the control mix (0% HL) in Figure 3.23. A power function, $\varepsilon_{t\_200th} = k_1 {N_f}^{k_2}$, which is generally used to represent the S-N curves of materials, has been adopted to fit to the data. The fitting results are shown in log-log scale presentation, which gives a good representation. This function in a relationship for fatigue tests Equation 4-8 of the form (Monismith, Kasianchuk and Epps, 1967) .

Figure 3.25 plots the two fitting parameters obtained, k_1 and k_2, against temperature, where the relation between the two parameters and temperature is well represented using two polynomials, from which temperature's effect on the S-N curve of the wearing mixes of 0 % HL and 2.5 % HL addition can be written into the form of Equations 3-10 and 3-11:

- For 0% HL addition:

$$\varepsilon_{t\_200th} = (2.83 \times 10^{-3}T^2 - 9.30 \times 10^{-2}T){N_f}^{(-4.09\times10^{-2}T+0.17)} \quad \text{Equation (3-10)}$$

- For 2.5 % HL addition:

$$\varepsilon_{t\_200th} = (1.48 \times 10^{-4}T^2 - 6.03 \times 10^{-3}T + 6.46 \times 10^{-2}){N_f}^{(-4.50\times10^{-3}T-0.20)} \quad \text{Equation (3-11)}$$

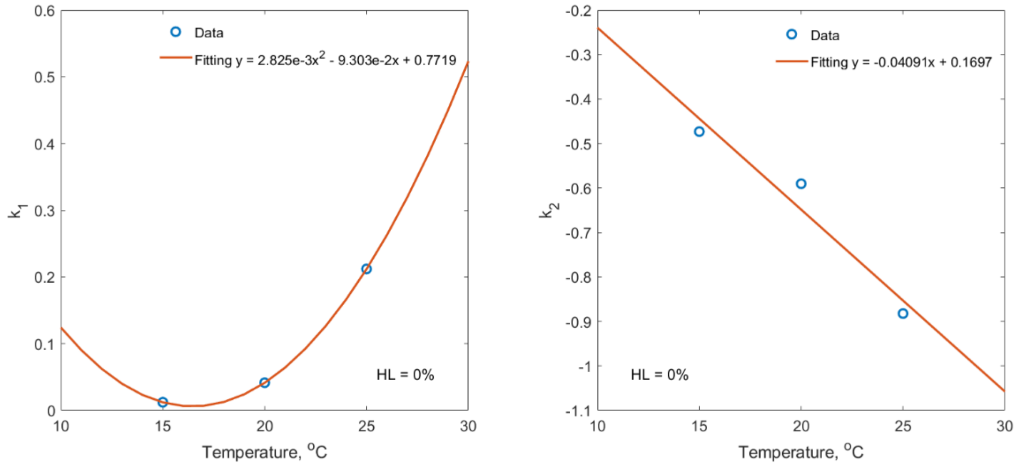

(a) 0% HL

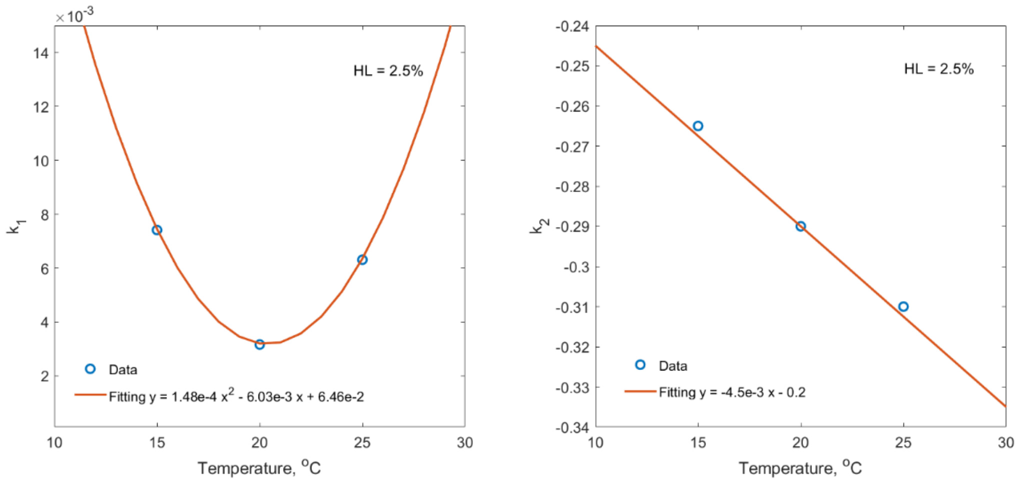

(b) 2.5% HL

Figure 3.25 Characterization of K_1 and K_2 variation with Temperature

The plots demonstrate that in the case of 2.5 %HL, the average absolute value of k_2 in the range of temperatures is much less than that in the case of 0 %HL. This means that the S-N curve of the 2.5 %HL mix is much flatter than that of the 0 %HL mix in the log-log scale. Therefore, under the same stress conditions, the 2.5 %HL mix has a higher fatigue life in the range of temperature variation. The mechanism for improving fatigue resistance is due to the high porosity and chemical reactivity of HL particles. High porosity enhances the contact surface between the mineral filler and the asphalt cement particles, which make the mixes have higher density and stiffness. Chemical reactivity improves bitumen–aggregate adhesion (Blažek et al.,

2000) and slows down bitumen aging (Little and Petersen, 2005) because of the pozzolanic reaction activated by the HL.

3.8.2 Effects of Hydrated Lime on Variables within Fatigue Equations

The 2.5% replacement of mineral filler with hydrated lime for the asphalt concrete mixtures investigated has affected both intercept (K_1) and inverse slope (K_2) within the fatigue equations in relation to initial tensile strain (ε_t), as well as cycle numbers to fracture (N_f). Figure 3.25 illustrates the respective effects of temperature addition on k_1 and K_2 as variables in fatigue equations. The K_1 parameter is $2.83 \times 10^{-3}T^2 - 9.30 \times 10^{-2} + 0.77$ for the wearing control mix, and this is reduced to its smallest value when 2.5% HL is added. This reduction in the value of K_1 follows a polynomial equation, showing a good fit. When viewing the value of K_2 across mixtures, inverse slope value also decreases with 2.5% addition of HL, and this is fitted to a polynomial equation. The outputs generated by the equations linking hydrated lime with fatigue parameters as given in these figures may be used in describing the impacts exerted by HL on fatigue repetition numbers as well as tensile strain through direct substitution of equations with K_1 and K_2 with hydrated lime within the principal fatigue equation.

3.9 Summary

Optimum asphalt content was adopted for the preparation of mixtures for each hydrated lime content (as a partial substitute for limestone dust) for the proposed asphalt concrete layers, wearing, levelling and base in various specimen dimensions and for different criteria and testing purposes. Firstly, a continuing experiment-based test process was reported which investigated thermal characteristics for both mixtures: the control mix (0% HL); and the optimised mixtures containing hydrated lime (2.5 %HL). The Quick Thermal Conductivity Meter (QTM500) was applied for all mixes' specimens with a diameter of 152.4 mm (6 inches) and height of 63.5 mm (2.5 inches). Secondly, experimental work conducted with cuboid beams of dimensions 381×76×76 mm^3 under the PRLS at different rates of stress and temperatures to compare fatigue life of unmodified asphalt concrete mixes and those with added hydrated lime was described. Testing was performed at three temperatures: 15℃, 20℃ and 25℃. The temperature effect has been characterized by mathematical expressions for the parameters of the S-N curve formulation.

The findings from these experiments will be applied in the modelling put forward in later chapters to characterise thermal-fatigue properties in asphalt mixtures.

A summary of mixture design and testing procedures conducted in this research are presented in Table 3.8.

Table 3.8 Summary of Experiments, Specimen Dimensions, and Purpose of Testing

Tests	Dimensions	Testing purpose	Mix type	Hydrated lime content
Marshal Mix Design 60°C (30 to 45min) loading rate 50.8mm/min.	Diameter 101.6mm Height 63.5mm	Optimum asphalt content (OAC) as well as volumetric properties	Wearing Leveling Base	0% 2.5%
Thermal Properties Using Quick Thermal Conductivity Meter (QTM500)	Diameter 152.4mm Height 63.5mm	Measured Thermal properties	Wearing Leveling Base	0% 2.5%
Flexural Fatigue Cracking Stress levels 223N, 310N, 402N and 490 N Temperature 15°C, 20°C, 25°C. Duration 0.1s load period 0.4 without load	Length 381mm Depth 76mm Width 76mm	Fatigue cracking	Wearing	0% 1% 1.5% 2% 2.5% 3%
Triaxial repeated load test Temperature levels 20◦C, 40◦C, and 60◦C, and three deviatoric stress 10 (68.9) psi (kPa) , 20 (137.9) psi (kPa), and 30 (206.9)psi (kPa), Duration 0.1s load period 0.9 without load	Diameter 101.6mm Height 152.4mm	Permanent deformation	Wearing Leveling Base	0% 2.5%

CHAPTER 4 - MODELLING THERMOMECHANIC RESPONSE OF PAVEMENT USING HYDRATED LIME MODIFIED CONCRETE

4.1 Introduction

As mentioned in Chapter Two, little research has been reported for the thermal physics and thermal property characterization of HL modified asphalt concrete (Mirzanamadi, Johansson and Grammatikos, 2018). However, information on the thermal response of the HL modified asphalt concrete is required as the essential parametric input at the stage of pavement design (Han *et al.*, 2018; Li, Liu and Sun, 2018). In this chapter, the results of the experimental work conducted to determine the thermal properties of different asphalt concrete mixes with and without HL modification are implemented to analyse the thermal and mechanical behaviour of a pavement structure using the asphalt concretes under a scenario of coupled traffic loading and environmental temperature variation.

Pavement analysis is increasingly utilising mechanistic analysis as opposed to solely empirical techniques. The most frequent mechanistic approach is finite element analysis, which overcomes issues associated with restrictions to a given set of materials- and environment-based parameters. In order to be valid, designs must address the relevant parameters, and if these are altered, a design becomes inapplicable. The effectiveness of finite element analysis relies upon how far predictions of strain and stress responses of the pavement materials are accurate. In this chapter, a modelling assessment is undertaken for pavements containing hydrated lime asphalt concrete, in which various parameters are evaluated: load configurations; mechanical properties for three asphalt concrete mixtures; experimentally-derived thermal characteristics established in the work covered in Chapter 4, including the coefficient of thermal expansion (CTE) and coefficient of thermal contraction (CTC); and the interactive thermal relationships between pavements and the surrounding air and conditions. The aim of this is to produce a modelling which is as close to real-world data as possible. The chapter considers the impacts of adding HL to asphalt concrete mixes by analysing temperature profiles as well as thermally induced strains and stresses and how these are distributed through the pavement. Here, coupled thermo-mechanical effects are applied to identify how far the pavement's surface is displaced vertically, as well as the greatest stress values within the pavement across the year.

4.2 Necessary parameters in designing and analysing flexible pavements.

Structural design of flexible pavement must consider predictions for a range of parameters, which are discussed in the sub-sections which follow:

4.2.1 Loading Configuration and Dimensions

The design of a pavement relies on traffic load identified through numbers of standard axle load passes, broadly assumed as 18-kip (80kN) single-axle loading as transferred to pavement through a double dual-tyre set (see Figure 4.1). This measurement is generally referred to as the equivalent single axle load (ESAL) (Garber and Hoel, 2008). The axle load equivalence factor has been applied to estimate the effect of a given axle loading, and represents how much the pavement is damaged every time this load passes over it in comparison to the effect of an axle loading set as standard (Moussa and El-Hamrawy, 2003).

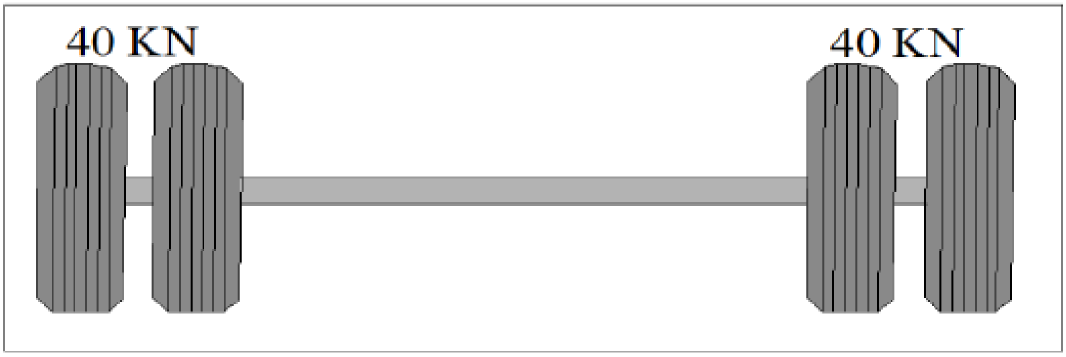

Figure 4.1 80 kN (18-kip) ESAL Configuration

4.2.2 Tyre-pavement Contact Area

The area of contact between tyre and pavement forms a significant parameter in analysing pavement performance, and forms a challenging problem, because different types of tyres will have different contact areas. Various works have studied approaches to representing the region of contact between tyre and pavement (Muniandy *et al.*, 2014). However, when comparing studies in this area, inconsistent data collection is identified across the studies (Helwany, Dyer and Leidy, 1998). Despite this uncertainty, an assumption can be made that the region of contact is in the form of 2 semi-circles joined by a region in the shape of a rectangle (see Figure 4.2), which Huang (2004) suggests can be made simpler, making a form with an area equivalent to 0.5227 Lc^2 and 0.6 Lc width (Huang, 2004).

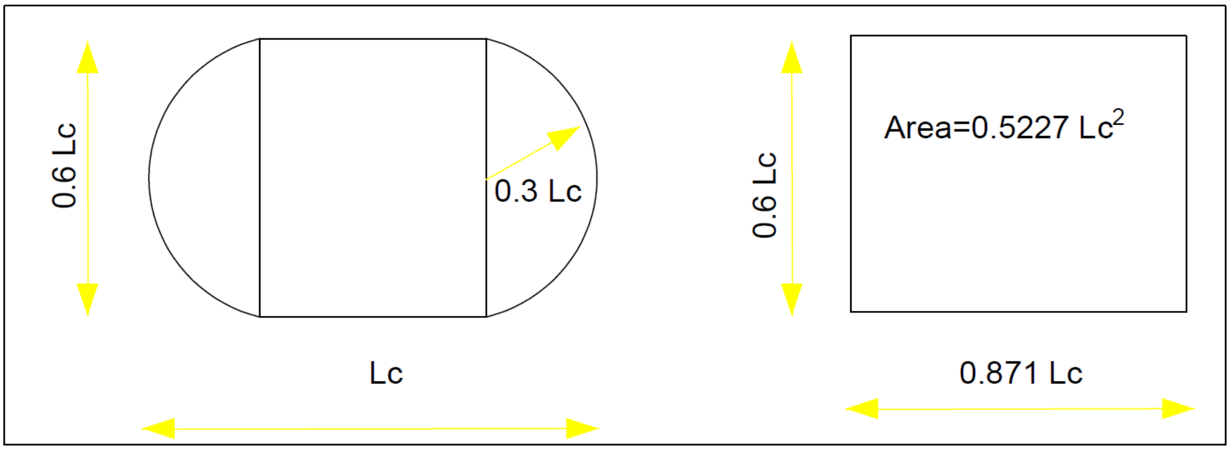

(a) Real contact surface of tyre

b) Equivalent contact surface

Figure 4.2 Tyre-pavement Contact Area (Huang, 2004)

4.2.3 Tyre pressure

Tyre pressure significantly influences the development of pavement stresses, and particularly in the upper layers, including surface layers, and on base layers (Suh, Cho and Mun, 2011). Notably, while tyre pressure in lorries in the 1960s was around 555 kPa, by the mid-1990s, it had risen to almost 750 kPa (Li, 2009), chiefly due to developments in the technologies used in tyre manufacture. Tyres have increased in strength and thickness, which increases the inflation pressures they can withstand and enables them to carry higher loads.

4.3 Material Response Characteristics

In structural design and analysis of asphalt pavements, whether using finite element analysis or any approach, Poisson's ratio and resilient modulus must be identified for the materials used to determine their stiffness. It is necessary to identify these characteristics in order to calculate strain, stress and deflection responses when traffic and thermal loads are applied to pavements. Response characteristics with respect to the subgrade, subbase and each asphalt concrete layer of the pavement are calculated as discussed in the sections which follow:

- **Asphalt Concrete Layers**

  Repeated load testing is used with the modified mixes and controls to establish their resilient modulus (Al-Tameemi *et al.*, 2019).

Secondly, the Poisson ratio (ν) is the proportion of lateral to axial strain and is determined based on calculation of these two values in testing the resilient modulus. This is a lesser factor in assessing and predicting how a pavement will perform, and thus is generally based on assumed values and not identified based on testing in practice (Southgate *et al.*, 1976). Table 4.1 gives ranges and representative values for the Poisson ratio of different materials used in pavements, and in this work, assumptions for Poisson ratio values made for subgrade material, subbase and asphalt concrete layers used the typical values in the table:

Table 4.1 Poisson Ratios for Different Paving Materials (Southgate *et al.*,1976)

Material	Range	Typical Value
Asphalt concrete	0.30 - 0.40	0.35
Unstabilized granular subbase and base	0.30 - 0.45	0.4
Silty subgrade	0.35 - 0.45	0.45
Clay subgrade	0.4 – 0.5	0.5

- **Subbase**

  Research staff for Shell Oil (Claessen *et al.*, 1977) put forward an approach to estimating resilient modulus in granular materials of the subbase which assumes that this parameter is a function of subgrade resilient modulus based on the relation shown below:

$$M_{R(Subbase)} = K \times M_{R(Subgrade)} \qquad \text{Equation (4-1)}$$

  Where:

  $K = 0.2h^{0.45}$

  h = Depth in millimetres of the subbase layer

  MR = Resilient modulus, given in psi

  This relation can be applied where 2 < k < 4.

- **Subgrade**

  As with the subbase layer, the estimation made for the resilient modulus of the subgrade is based on a relation put forward by research done by Shell (Claessen *et al.*, 1977). This relation derives from the way in which dynamic in-situ testing of resilient modulus for this layer correlates to the appropriate California Bearing Ratio (CBR) finding from laboratory measurements. ASTM D-1883 standard testing may be used to determine the soil of the subgrade's CBR value, through the following relation:

$$M_{R(Subgrade)} = 1450\ CBR \qquad \text{Equation (4-2)}$$

  Where:

  M_R= Resilient Modulus of Subgrade in psi

  CBR=Value for the subgrade soil, given in percentage terms.

4.4 Modelling Evaluation for the Pavement Constructed using HL Asphalt Concrete

4.4.1 Finite Element Analysis

The FEA approach to creating models has significantly contributed to current capacity for modelling any physical phenomenon which involves structures which are complex. This is due to this modelling system replacing a real, continuous domain with a model which is analogous but contains separate elements and connecting nodes. By breaking down structures to form finite quantities of components or elements, it becomes easier to understand how the model behaves as compared to studying the continuous system.

In the current study, a 2D FEA approach is applied through COMSOL Multiphysics® version 5.6 to model a flexible pavement section. This modelling mainly comprises pavement layer dimensions, material properties, each element and node, configurations of loads and boundary parameters, and different factors used in describing the pavement system in physical terms. A finite element modelling analysis is conducted to evaluate the beneficial effect on a constructed pavement structure using HL-modified asphalt concrete under a service scenario exposed to coupled traffic loading and typical seasonal temperature variation experienced in the UK. A classical thermomechanical model (Little, Allen and Bhasin, 2018) was adopted, which is established based on a motion equation and thermal energy conservation as briefed below:

4.4.2 Mesh generation

Figure 4.3 illustrates the geometric features of the FEM model following meshing. Finer meshes are generally applied close to load regions in order to model stress gradients, with meshes being larger at a greater distance from this area. Mesh sensitivity analysis allowed the finer mesh to be optimised in terms of element size. The smallest size of element measures 0.6” (15 mm), determined on the basis of this analysis. The areas transitioning from finer to coarser meshes were smoothed using an edge-biased structure meshing pattern.

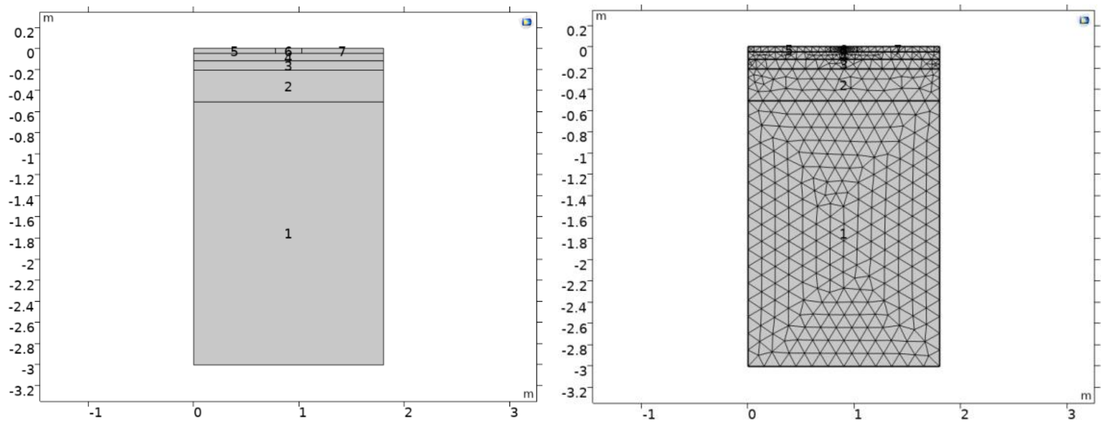

Figure 4.3 Pavement geometry and FE mesh used in the structural analyses.

4.4.3 Boundary condition

Restraint is applied to the lower boundary in the vertical and horizontal direction. This means that deflections will not occur in the horizontal or vertical direction within this plane. Vertical boundary movement is restricted solely horizontally. Interfaces between layers are assumed to be completely bonded.

4.4.4 Motion equation

For an isotropic solid material, its deformation follows Equation 2-22. The strain and stress of the solid material are shown in Equations 2-20 - 2-22 and 2-27.

4.4.5 Energy equation

When exposed to a heat transfer process, the solid material satisfies the thermal energy conservation condition, as shown in Equation 2-27.

Equations 2-20 - 2-22 and 2-27 closely describe the thermomechanical state of a structural system. They were applied to analyse a pavement structure of three asphalt layers using the mixes investigated in the experiment described in Chapter Three.

4.4.6 Pavement Structure

Figure 4.4 illustrates a constructed five-layer single carriageway pavement structure. Finite element analysis modelling was conducted for half of the symmetric structure. A wheel pressure was applied on the surface, representing traffic loading. The geometric information is presented in Table 4.2. The traffic load was set at a scenario of an Equivalent Single Axial Load (ESAL) of 70 kN, referring to a statistical traffic condition. The load magnitude, which gives a wheel load pressure of 0.772 MPa on an estimated contact area of 9.073×10^{-2} m2 (Al-Tameemi *et al.*, 2019) , was deliberately increased for this study to compare with the thermal effect. Equations 2-22– 2-27 were solved using the partial differential equation module of a commercial FEA software package (COMSOL Multiphysics).

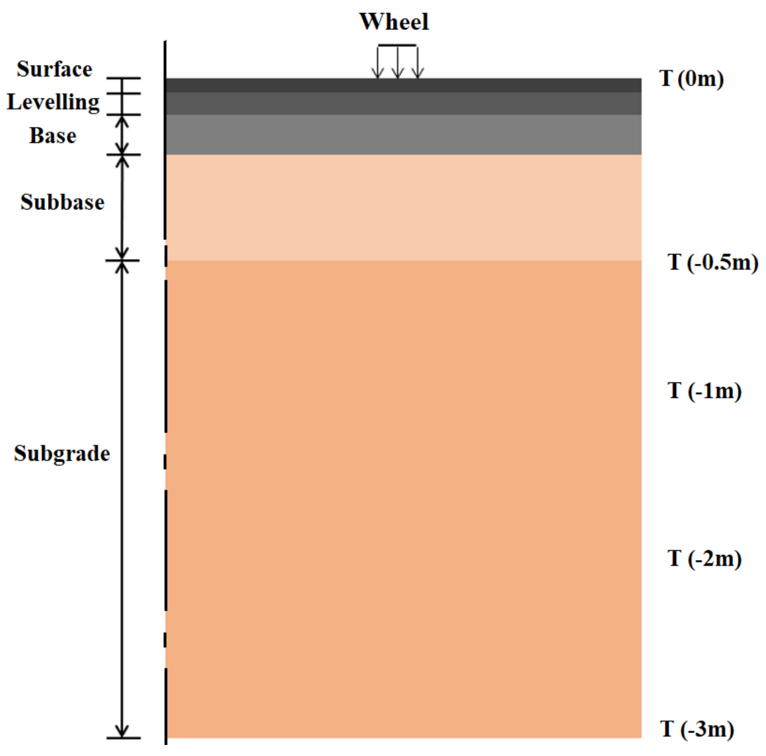

Figure 4.4 FE Geometric Model

Table 4.2 FE Geometric Data

	Surface/Wearing	Binder/Levelling	Base	Subbase	Subgrade	Wheel
Thickness (mm)	50	70	90	300	2500	-
Width (mm)	1800	1800	1800	1800	1800	250

Table 4.3 lists the mechanical properties of the mixes for three pavement layers which were reported in a previous study (Al-Tameemi, Wang and Albayati, 2016), and the thermal properties from this study. The data for the two foundation layers (subbase and subgrade) refer to another published work (Ishikawa and Miura, 2015). A thermal deformation model based on a laboratory study on a newly constructed asphalt pavement (Islam and Tarefder, 2015) was adopted to estimate the bulk material temperature effect on the coefficient of thermal expansion (CTE) and contraction (CTC). They are two quadratic polynomials in the form of Equation 2-4 and Equation 2-5.

Table 4.3 Material Properties for FE Analysis

Property	HL content	Pavement layer				
		Wearing	Levelling	Base	Subbase	Subgrade
Modulus E (MPa)	0%	$0.2819T^2 - 41.53T + 2090$	$0.3877T^2 - 46.41T + 1929$	$0.3404T^2 - 40.41T + 1649$	170	65
	2.5%	$0.1898T^2 - 43.03T + 2623$	$0.5248T^2 - 63.3T + 2527$	$0.3359T^2 - 41.12T + 1803$	170	65
Poisson ratio v	0%	0.35	0.35	0.35	0.4	0.4
	2.5%	0.35	0.35	0.35	0.4	0.4
Density ρ (g/cm^3)	0%	2.34	2.32	2.31	1.76	1.29
	2.5%	2.32	2.30	2.297	1.76	1.29
Thermal Conductivity k (W/m/K)	0%	0.7161	0.7318	0.7471	1.3	0.28
	2.5%	0.8989	0.7757	0.8763	1.3	0.28
Thermal Capacity c_p (J/kg/K)	0%	1062.6	1092.79	1121.12	837	800
	2.5%	1333.48	1155.49	1303.09	837	800
Thermal deformation coefficient α	0%	CTE Equation (2-4) CTC Equation (2-5)			3.32e-6	3.4e-5
	2.5%				3.32e-6	3.4e-5

* The temperature in the relevant formula is given in °C

The thermal interaction between the pavement and the atmospheric environment is a complex process dominated by heat transfer in the form of conduction, radiation, and convection at the pavement's surface and surrounding ground conditions. Under special climatic conditions, other physics such as the latent heat flux due to ice melting or moisture evaporation are involved as well (Chen, Wang and Xie, 2019). The heat exchange mechanism in the pavement–climate system has been part of topical research for a long time (Qiao *et al.*, 2020). Characteristic models for the details of the underlining physics have been proposed and developed (Qin and Hiller, 2011; Qin, 2015; Wu *et al.*, 2018). In this study, the UK climate and environment are set as a scenario for the modelling case study. As the primary purpose is to evaluate the effect of HL-modified asphalt concrete on pavement behaviour, a simplified Dirichlet temperature boundary condition is adopted for the pavement structure based on a geological survey of the shallow ground seasonal temperature in the UK (Busby, 2015). Figure 4.5 shows a characterization model using a sine function to fit the shallow ground temperature variation at five depths, i.e., 0, −0.5, −1, −2, and −3 m. The data are from reference (Busby, 2015). Figure 4.5 provides temperature variation information by day. However, the daily weather temperature change in the UK, in general, would be about 10 ℃ for a year-round time. Based on this assumption, a daily weather temperature variation is assumed to take a sine wave form in a 24 h period and is embedded in the data curves of Figure 4.5, as shown by Figure 4.6 a. Combining the daily weather temperature variation with the yearly variation curve for 0 m depth, an annual pavement surface temperature variation by hour is shown in Figure 4.6b & c.

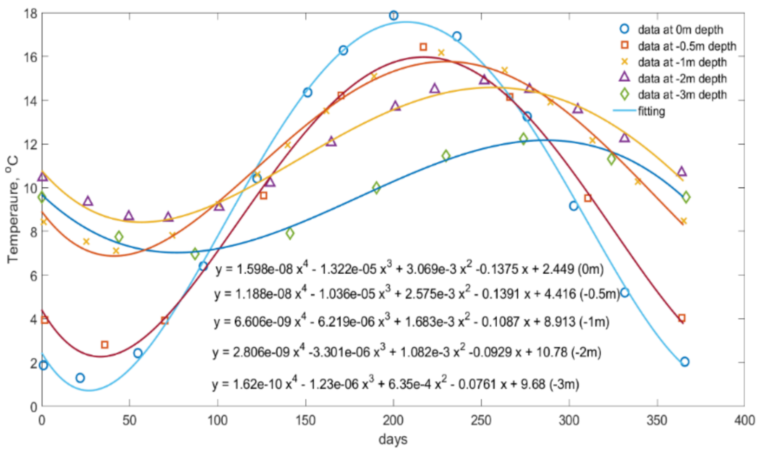

Figure 4.5 Characterization Modelling for Year-round UK Shallow Ground Temperature Variation (Busby, 2015)

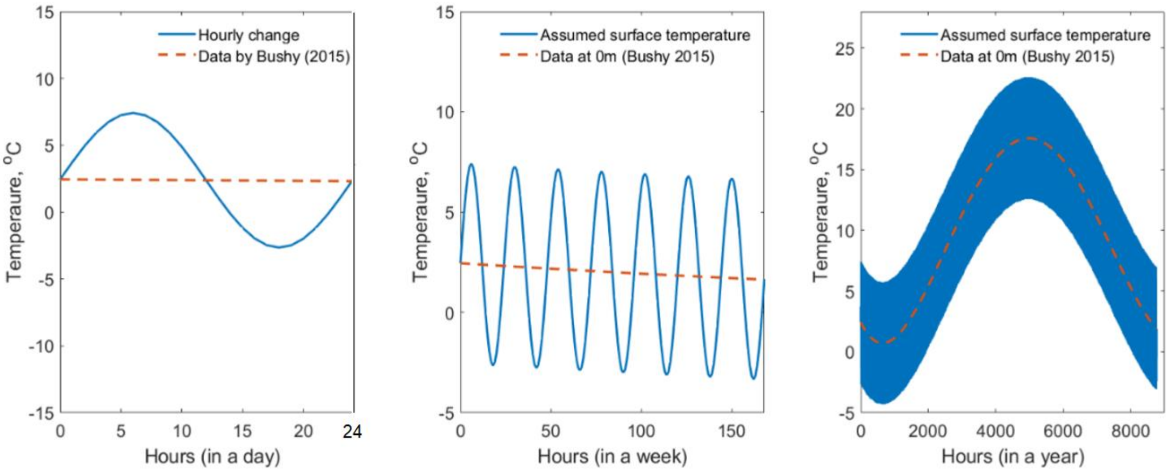

(a) Temperature over 24 h (b) Temperature over150 h (c) Temperature in a year

Figure 4.6 Assumed Seasonal Temperature Condition at the Pavement Surface

The pavement surface temperature was set as the seasonal temperature at a depth of 0 m, i.e., T (0 m). The bottom surface temperature was set at T (−3 m). The other boundary conditions are a thermal isolation along a left symmetric vertical line and the temperature of the right vertical edge, which is interpolated according to the annual belowground temperature variation data using the fitting curves in Figure 4.6 b at the corresponding depth, illustrated in Figure 4.4. It also assumes that there is no horizontal displacement for the vertical edges of all layers and no vertical displacement at the bottom of the subgrade. The initial temperature condition in the whole structure is assumed to have a value of 8.7 °C, the mean value of the seasonal temperature at depth −0.5 m, when solving the energy equation, Equation 2-27.

4.5 Modelling Results and Comparison

4.5.1 Temperature Profile and Thermal Strain & Stress Distribution

Numerical computing was performed at an hourly time step starting from 0 h on the 1st day in January. Figure 4.7 shows the temperature profile at the time in four typical seasons. A modelling time of 720 hrs occurred in February, 2880 hrs in May, 5040 hrs in August, and 7200 hrs in November. It can be seen that the degree of annual temperature variation in the pavement decreases with depth downward. February and August have a large temperature variation from the top of wearing course to the bottom of the subgrade. May and November have a small vertical temperature variation. The wearing course has the highest temperature variation gradient all year round.

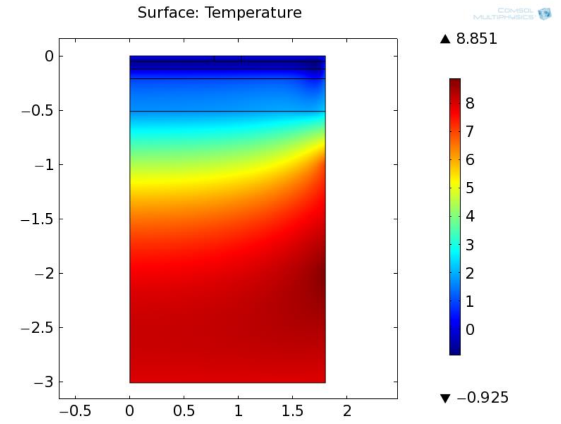

720 hrs (Feb)

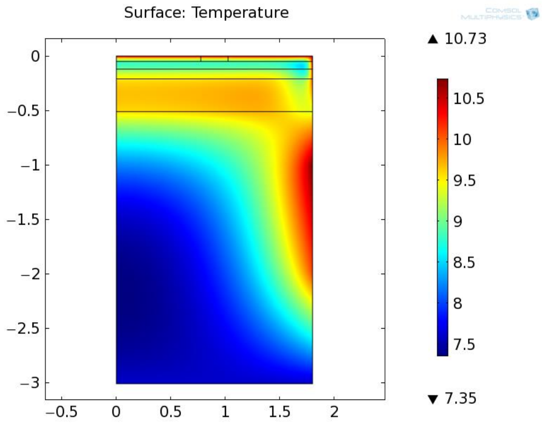

2880 hrs (May)

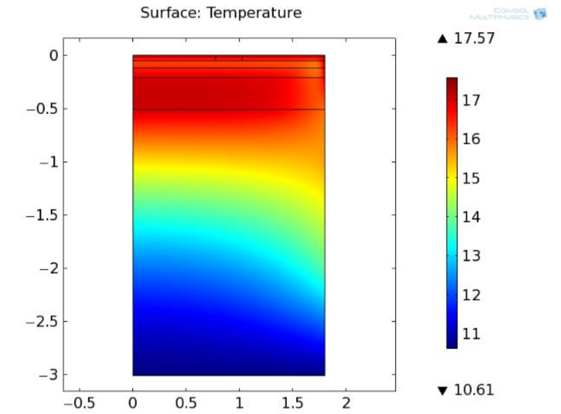

5040 hrs (Aug)

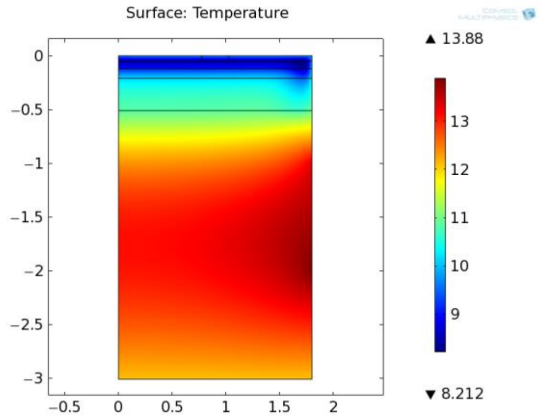

2700 hrs (Nov)

Figure 4.7 Seasonal Temperature Profile in the Pavement Structure

Figure 4.8 compares the vertical temperature distribution along the central symmetric line (Figure 4.4) between the pavements with 2.5% HL and 0% HL. It shows that although the HL-modified asphalt concrete narrows the temperature variation range along the three asphalt layers and the subbase, and particularly in the month of February, the difference is very small. The highest local temperature difference is less than 1 °C at the wearing layer.

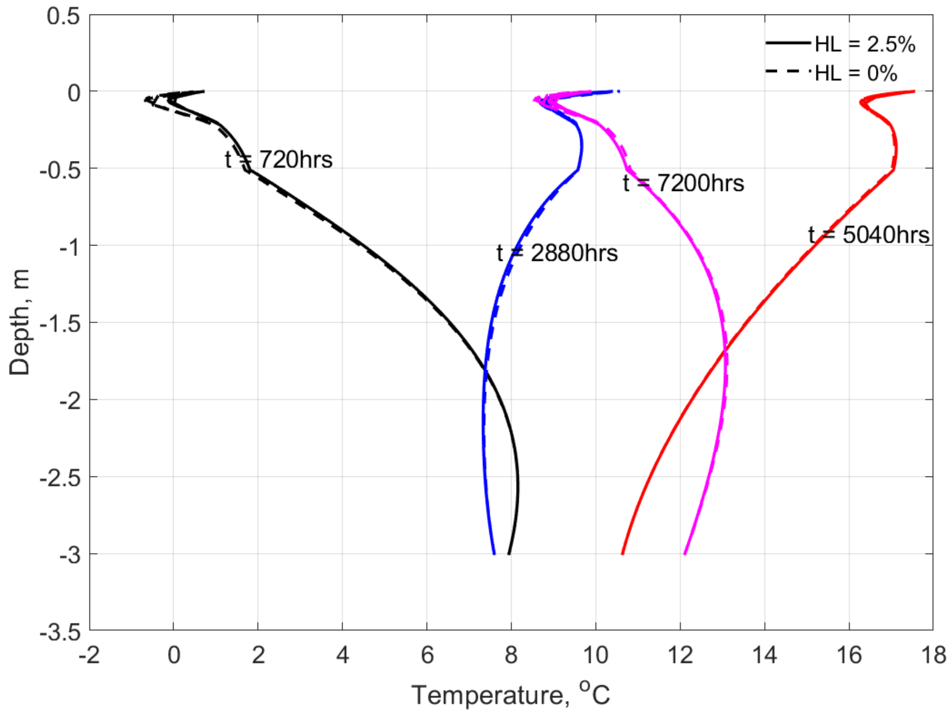

Figure 4.8 Vertical Temperature Profile along the Symmetric Centre of the Pavement.

Figure 4.9 shows the vertical distribution of the thermal strain ($\alpha\Delta T$) and stress ($(3\lambda + 2\mu)\ \alpha\ \Delta T$) along the central symmetric line. It can be seen that the highest inconsistent thermal strain exists at the interface between the subbase and the subgrade. However, the biggest thermal stress happens at the surface of the wearing course.

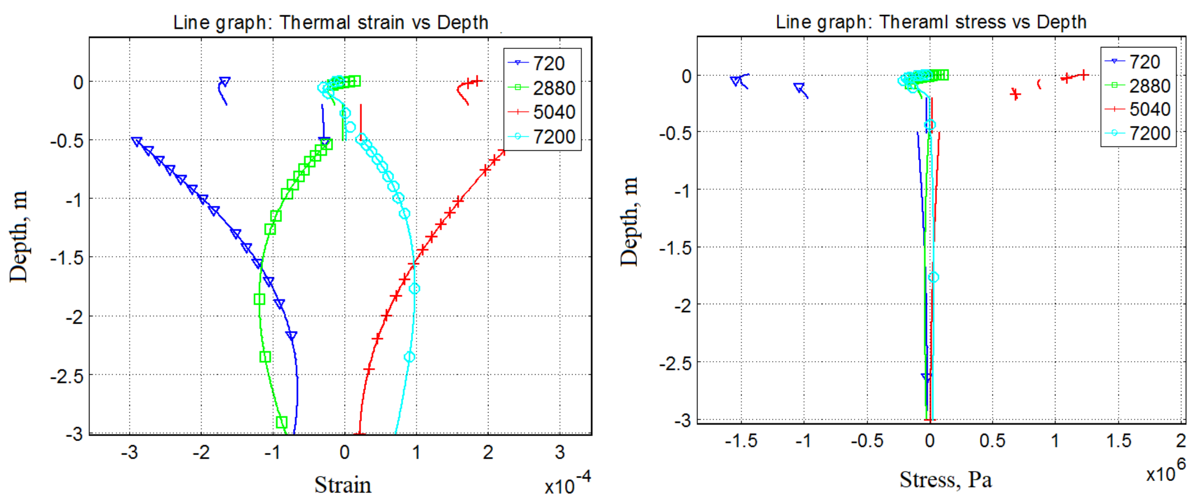

2.5 % HL

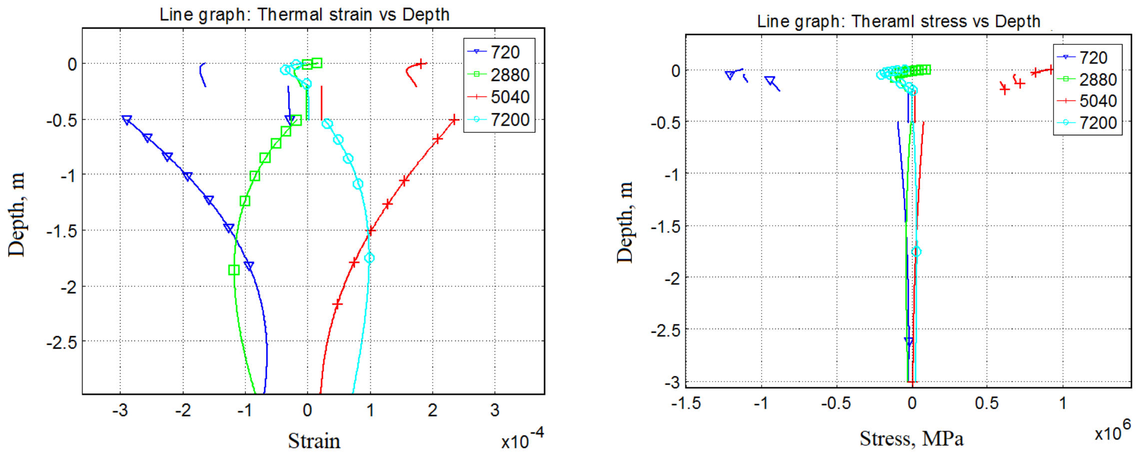

0 % HL

Figure 4.9 Thermal Strain and Stress in the 0% HL& 2.5%HL Pavement

4.5.2 Coupled Thermomechanical Effect

Figure 4.10 compares the vertical displacement of the pavement surface in a coupled thermomechanical situation. It shows that pavements with 2.5% HL and 0% HL are very similar in their response to environmental temperature variation. However, the HL pavement has less vertical deformation under all year-round under traffic loading. In the centre of the pavement (x = 0), under the coupled thermomechanical condition, pavement using no HL has a higher vertical displacement for all four times. Comparing the maximum vertical displacement at the position of the wheel load, the 2.5% HL pavement is about 1.5% less than that of the control 0% HL pavement. This result highlights the benefit of HL on long-term fatigue life and rutting of the pavement under repetitive loads. The two mixes, with 2.5% hydrated lime, and the control mix, show only minor differences when vertical displacement is calculated for one vehicle, but with multiple vehicles loads across the asphalt pavement's lifespan, this translates into significantly different deterioration levels for the mixes.

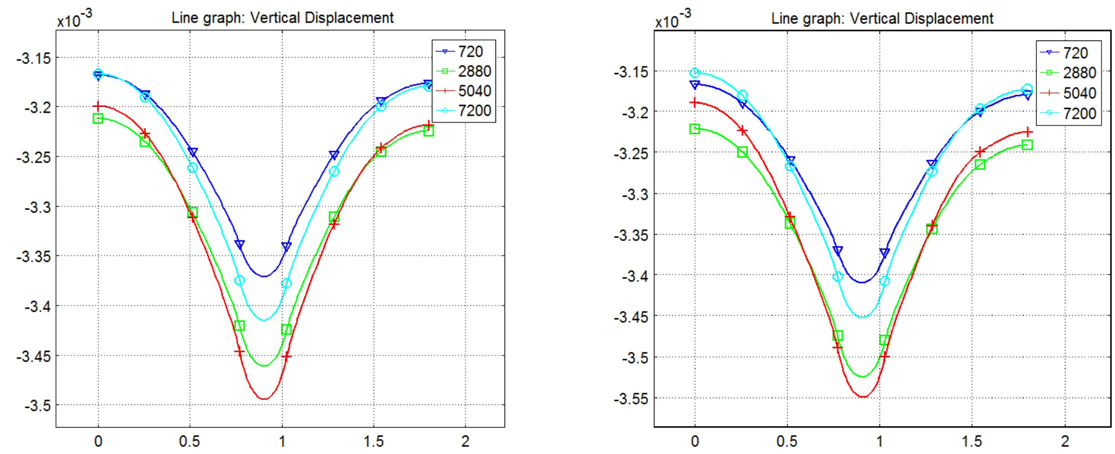

2.5% HL   0% HL

Figure 4.10 Vertical Displacement of the Pavement Surface

Figure 4.11 shows the sum of the two principal stresses, in Equation 4-3, due to traffic loading. It is undisputable that the maximum value is in the wearing course at the edge of the contact region with wheels. It can be seen that the traffic stress is dominant in the three layers of the asphalt pavement.

$$\sigma_{max/min} = \frac{\sigma_{xx} + \sigma_{yy}}{2} \pm \sqrt{\left(\frac{\sigma_{xx} - \sigma_{yy}}{2}\right)^2 + \left(t_{xy}\right)^2} \qquad \text{Equation (4-3)}$$

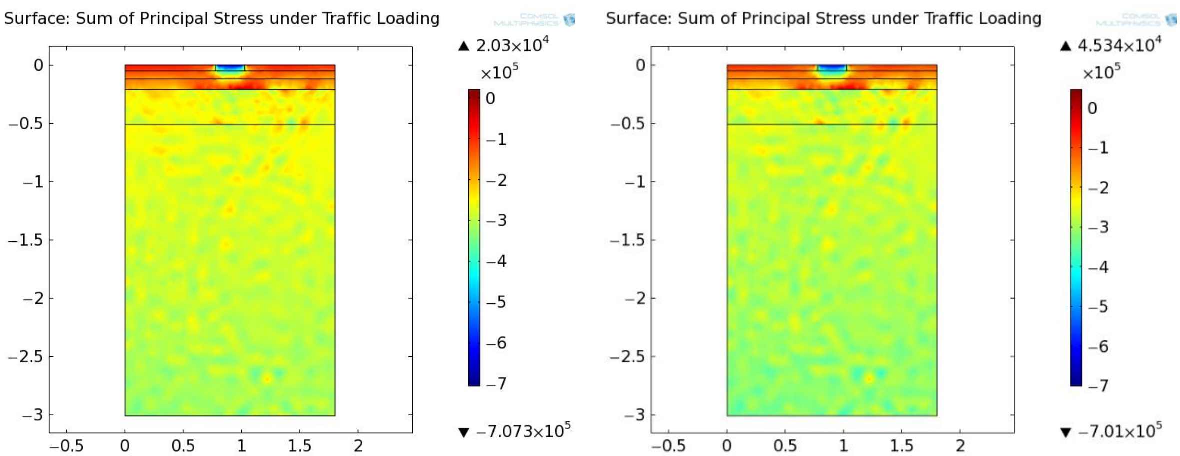

2.5% HL   0% HL

Figure 4.11 Sum of the 1st and 2nd Principal Traffic Stress at Time 720 hrs

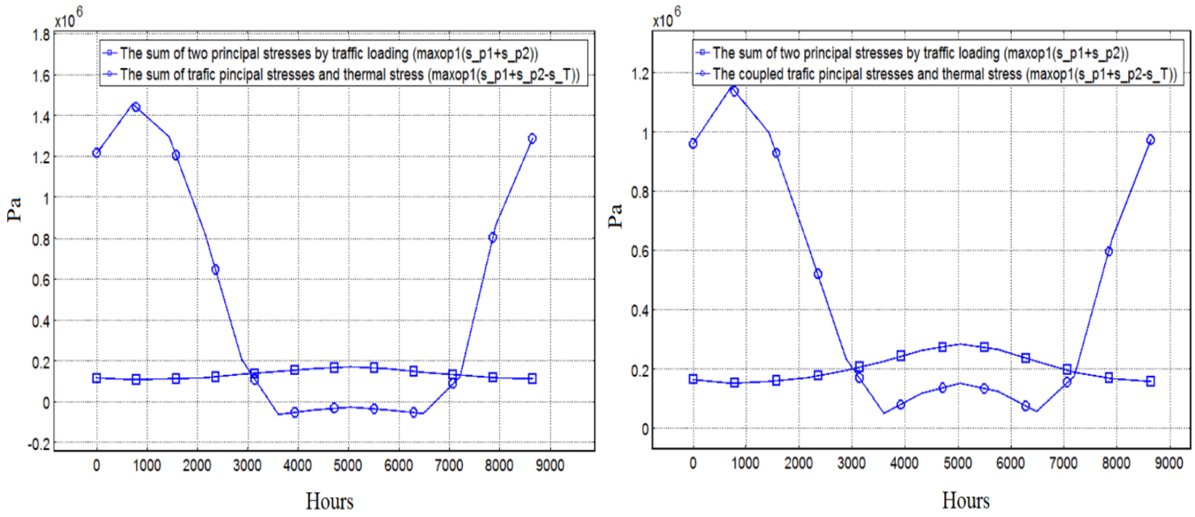

2.5% HL 0% HL

Figure 4.12 Maximum Stress Value in the Pavement Year-round

Figure 4.12 compares the maximum value of the sum of the two principal traffic stresses, and the maximum coupled stress of the sum of the two principal traffic stresses and the thermal stress for a year-round time. Referring to Equation 3-8, coupled stress is defined as: $\sigma_{max} + \sigma_{min} - \alpha\,(3\lambda + 2\,\mu)\,\Delta T$. It shows that the HL pavement has a lesser internal stress level under traffic loading only. However, the thermal effect, particularly at low temperatures (during the winter season), causes more internal tensile stress level in the HL pavement than in the pavement with no HL. In the two pavement structures, the thermal effect outweighs the traffic effect in the winter season, between 0~2500 h, and from 7500 h to the end of the year. The maximum sum of the principal traffic stress is 0.17 MPa at 5000 h and the maximum couple stress is 1.46 MPa at about 720 h for the HL pavement, while the two maximum values for the control pavement are 0.28 MPa and 1.15 MPa. The results indicate that the benefit of HL on only traffic stress reduction is about 39%, but the thermal effect on the maximum internal tensile stress is 26% higher in the HL pavement. This result explains why there is an optimum content of HL for asphalt concrete modification when exposed to temperature variation (Al-Tameemi, Wang and Albayati, 2016; Al-Marafi, 2021) .

Figure 4.13 shows the coupled stress ($\sigma_{max} + \sigma_{min} - \alpha\,(3\lambda + 2\mu)\,\Delta T$) profile in the pavement at time 720 hrs in the winter season. For the HL pavement, the highest tensile stress is located predominantly in the wearing course, while for the pavement with no HL, high tensile stress is not only located in the wearing course but also at the bottom of the base course.

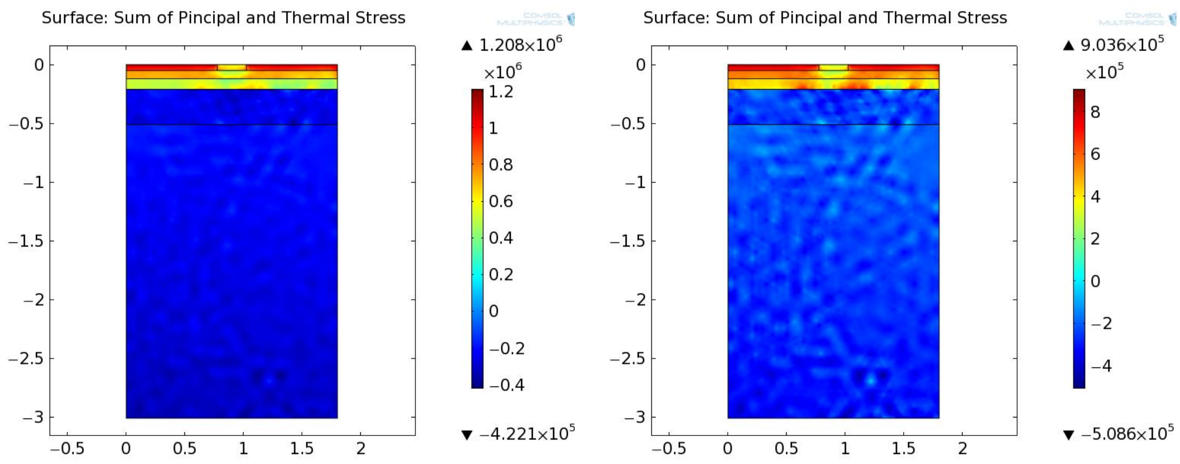

2.5% HL 0% HL

Figure 4.13 Coupled Thermomechanical Stress

4.6 CONCLUSION

Chapter Four draws on data from the experiments reported, to provide thermal characteristics for the optimised asphalt mixtures modified with hydrated lime. This data, along with the results of previous experimental work, is used for the characterisation of thermos-mechanical constitutive relationships for the optimised HL mixes. Once the thermal and mechanical characteristics were acquired, numerical modelling was conducted to analyse environmental thermal influence and coupled thermomechanical effects on the behaviour of the constructed pavement structures. The following conclusions can be drawn.

- The 2.5% addition of HL to replace the equivalent weight of limestone dust filler enhances the thermal properties of the modified asphalt concrete, with increased magnitudes of thermal conductivity (27% for wearing mix, 7% for levelling mix, 0.17% for base mix) and specific heat (25% for wearing mix, 6% for levelling mix, 0.16% for base mix). For the HL modified mix, there is no correlation between thermal properties and either the optimum asphalt cement or mineral filler content.
    - Between the pavement using HL concrete and that not using HL concrete, there is a very small difference between the local temperature profiles within the structural layers.

Correspondingly, the difference in the thermal strain and stress profiles within the two pavements is very small as well.

- The thermal effect is pronounced under the coupled thermomechanical conditions for pavements exposed to both traffic and climatic impacts because of the temperature effect on the mechanical properties, such as the modulus and deformation coefficient of the mixes.
- The modelling analysis shows that the HL pavement has about 1.5% less deformation than the control pavement at the site under the direct traffic loading. This result highlights the benefit of HL for long-term fatigue and rutting resistance.
- The modelling results indicate that the benefit of HL on traffic-only stress reduction is about 39%, but the thermal effect increases maximum total internal tensile stress level by 26% in the HL pavement in the winter season. This explains why there is an optimum HL content for asphalt concrete modification when exposed to temperature variation.
- The modelling results have shown that for the HL asphalt concrete pavement, the local maximum tensile stress predominates in the surface region: i.e., the wearing layer. This will help reduce the workload involved in crack repair and in the long-term, help in saving cost and effort on maintenance.

CHAPTER 5 – MODELLING FATIGUE LIFE OF PAVEMENT USING HYDRATED LIME CONCRETE

5.1 Introduction

Climate change and economic sustainability have posed major challenges for road infrastructure. Directly exposed to atmosphere and traffic, pavement surfaces are subject to a prominent combined deteriorating mechanism caused by coupled traffic loading, atmospheric and surrounding environmental temperature variation, and direct solar radiation (Sun *et al.*, 2020; Du *et al.*, 2021), for which fatigue deterioration is the most common form. Modifying asphalt concrete using mineral additives as a micro-filler has been widely adopted and proves to be effective to improve flexible pavement durability. Among the varied functional mineral additives, hydrated lime (HL) has been, for some time, of particular interest due to its outstanding effectiveness, wide availability, and economical cost (Lesueur, Petit and H.-J. Ritter, 2013; Bouron *et al.*, 2021). Although many experimental studies have reported significant improvement in the mechanical properties of asphalt mixes using HL as an additive (Kollaros, Kalaitzaki and Athanasopoulou, 2017; Iwański, 2020) and an optimum rate of addition (Zhou and Sun, 2020), so far, few experimental studies have been undertaken on temperature's influence on the fatigue life of HL modified asphalt concrete (Kakade, Reddy and Reddy, 2016; Zhou *et al.*, 2021). Meanwhile, there has been little reported work on computational analysis for climatic thermal impact on the fatigue life of pavement structures constructed using HL-modified asphalt concrete (Kai and Fang, 2011; Chen, Wang and Xie, 2019). As an effort to increase knowledge in these aspects, a series of experiments have been performed. A previous publication (Al Ashaibi *et al.*, 2022) has reported experimental tests for thermal properties of asphalt concrete with and without HL modification, and numerical modelling which compared the thermomechanical response of pavement structures using the two materials when exposed to an environmental temperature condition. In this chapter, the experimental data establish a characterization model for the temperature effect on the tensile fatigue life of HMA concrete. To demonstrate its practical meaning, numerical modelling was performed to analyse the stress and strain status of a pavement structure exposed to traffic loading and environment impact. Different from previous modelling work (Al Ashaibi *et al.*, 2022), in this research, set within a geo-climatic scenario, the modelling refers to a real climatic condition by taking into account direct solar radiation, to illustrate a practical-meaning case investigation of coupled thermomechanical conditions on pavements using and without using HL. In line with previous studies, the work contributes new data and knowledge regarding the material and its applications.

5.2 Experiment on Thermal Effects on Fatigue Life

As mentioned in Chapter three, an experiment was performed to study temperature effects on six different mixes designed for wearing course application, following ASTM D6926-2010a. Specifications and in depth information about the mix design, sample preparation, experimental setup, and test procedure, etc. have been detailed in Chapter Three of this research work.

5.3 Modelling Coupled Thermomechanical Effects on Pavement Structures

5.3.1 Governing equations

A classical thermomechanical model (Little, Allen and Bhasin, 2018) is adopted to describe the coupled thermomechanical effect on pavement structures and to compare the predicted fatigue life for pavements using asphalt concrete with 0% and 2.5% HL addition, respectively.

5.3.2 Motion equation

For an isotropic solid material, deformation follows Navier's Equations 2-22 -2-27.

5.3.3 Energy equation

The thermal energy conservation of solid materials follows Equation 2-27:

5.4 Material properties

Solving the system of Equations 2-20 - 2-22 and 2-27 needs the materials’ physical, thermal, and mechanical properties, and their variation at different temperatures. Table 4.3 gives the relevant properties for the asphalt concrete mixes with 0% and 2.5% HL addition, which are primarily from a previous study conducted at the same research laboratory (Al Ashaibi *et al.*, 2022; Al-Tameemi, Wang and Albayati, 2016). However, for the thermal deformation coefficient, a model based on a laboratory study on a newly constructed asphalt pavement (Islam and Tarefder, 2015) was adopted, which used two quadratic polynomials in the form of the Equations 2-4 and 2-5, to estimate the coefficients of thermal expansion (CTE) and contraction (CTC) for their variation with temperature. The data for the two foundation layers (subbase and subgrade) are from other published work (Ishikawa and Miura, 2015).

5.5 Modelling the Climatic Thermal Effect on a Pavement Structure

5.5.1 A Pavement Finite Element Model

A single lane carriageway pavement structure of five layers was modelled using FEM. The coupled thermomechanical model for Equations 2-20-2-22 and 2-27 was implement using the partial different equations module of the COMSOL Multiphysics software. Figure 5.1 shows only half of the symmetric pavement structure. A wheel represents the traffic. Table 4.2 lists the geometric information.

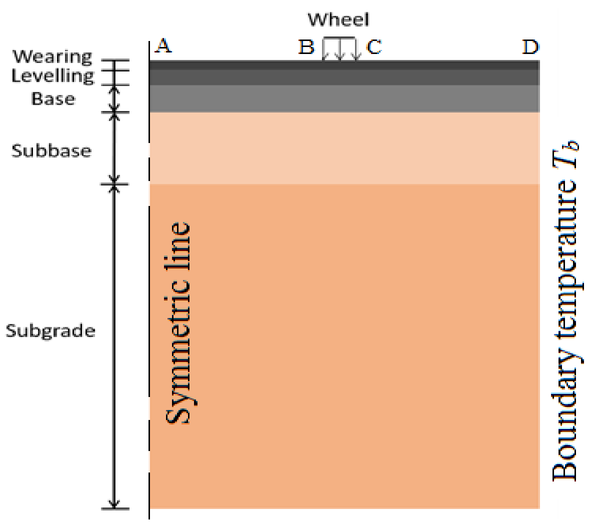

Figure 5.1 FE geometric model (A, B, C & D are four positions on the pavement surface).

5.5.2 Climatic thermal conditions

The thermal interaction between the pavement and the local atmospheric environment has been a topic of interest in pavement engineering and urban environment research. The thermal exchange at the pavement's surface consists of three physical mechanisms, i.e., solar irradiation adsorption, pavement emission and interfacial air convection (Bouron *et al.*, 2021; Wu *et al.*, 2018; Chen, Wang and Xie, 2019). which decide the vertical thermal flux at the pavement surface, which can be described using Equation 5-1:

$$q_T = (1 - a)I - \varepsilon\sigma(T_s^4 - T_a^4) - h_c(T_s - T_a) \qquad \text{Equation (5-1)}$$

Where:

q_T = Stands for the vertical thermal flux at the pavement surface(W/m^2)

a = Albedo coefficient of the pavement material

I = Solar incident irradiation (W/m^2)

ε = Pavement material emissivity

T_s = Surface temperature (K)

T_a = Atmospheric air temperature (K)

σ = Stefan-Boltzmann constant, 5.67×10^{-8} W/m^2/K^4

h_c = Heat convection coefficient (W/m^2/K)

For climatic thermal effect analysis, this study differs from a previous study in Chapter Five (Al Ashaibi *et al.*, 2022) which used an assumed temperature condition. In this study, by setting a scenario at a location in Greater Manchester in the northwest of England, a database of the UK Global Horizontal Irradiance (GHI) (Palmer *et al.*, 2017) has been utilised to determine the thermal boundary condition for FE modelling of the pavement structure. The GHI database records the annual hourly incident irradiation around the UK. To characterise these data for FE modelling parametric input, first, an average daily variation by hour in each month was calculated. Figure 5.2 gives the results for the data at the location set (GHI_tmy_MIDAS X_394936,Y_392020 2008_2017 (Palmer and Bettsl., 2018), which is a site in the northwest of England, in the greater Manchester area. A Gaussian distribution (Equation 5-2) is employed to represent the average hourly GHI in a day for each month over a period of one year. The red curve in Figure 5.2 shows the results for this GHI. Table 5.1 provides the obtained Gaussian parameters. Thereafter, the three representative Gaussian parameters, a, b and c are characterized for their monthly variation using a sum sine function, as illustrated in Figure 5.3.

Table 5.1 Gaussian parameters

Month	**January**	**February**	**March**	**April**	**May**	**June**	**July**	**August**	**September**	**October**	**November**	**December**
a	287.2	251.6	205	119.5	110.9	159.2	119.5	350.1	253.2	298.6	300.8	319.6
b	13.47	13.32	14.28	15.41	16.03	15.61	15.41	14.92	14.36	14.58	12.75	13.25
c	5.357	5.89	7.162	10.28	12.79	11.62	10.28	6.837	8.712	6.462	5.721	5.251

$$GHI = a \times \exp\left(-\left(\frac{t-b}{c}\right)^2\right) \qquad \text{Equation (5-2)}$$

where:

t = Time in hours

a, b and c = Three parameter constants.

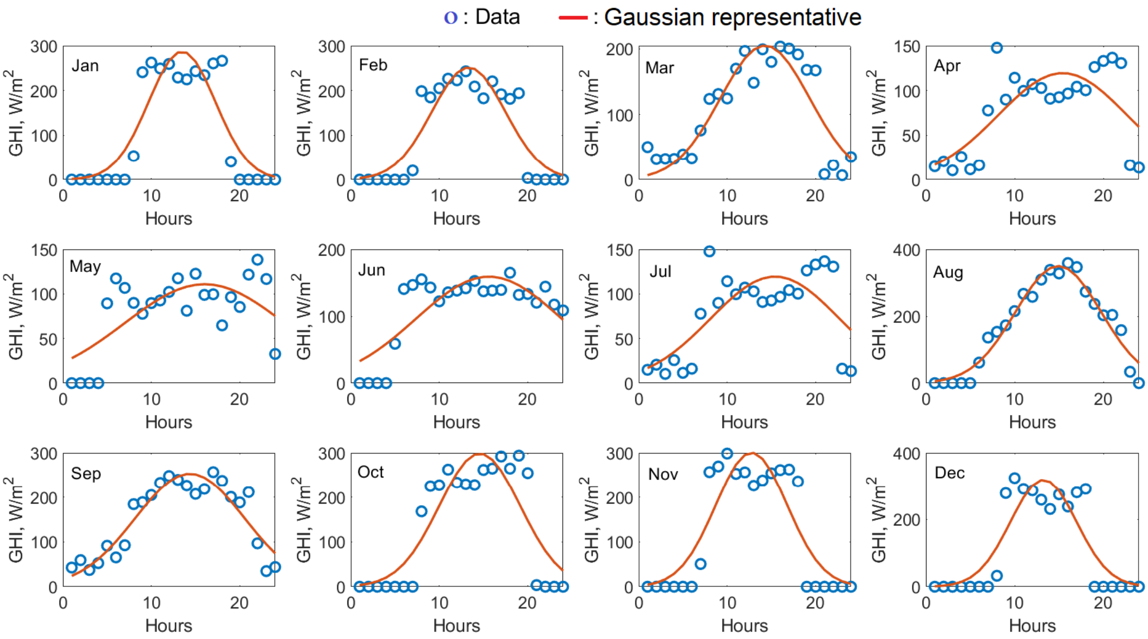

Figure 5.2 Annual monthly average daily Global Horizontal Irradiance at the location in Greater Manchester UK

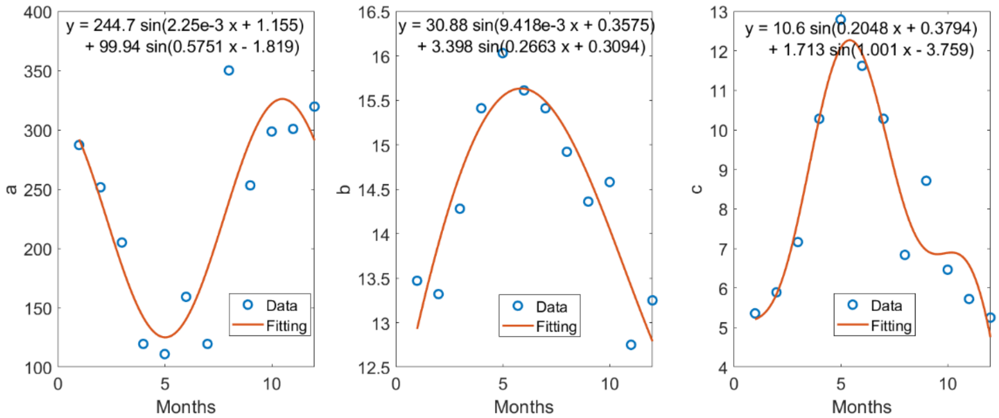

Figure 5.3 Characterized Gaussian representative parameters

To determine the q_T through Equation 5-1, it is necessary to know the atmospheric air temperature T_a, for which data from the UK weather forecast record is adopted here. Figure 5.4 (a) shows the annual monthly temperature variation in the region of Manchester and a representative curve fitting to the average of Low and High. Figure 5.4 (b) shows the variation of amplitude: the difference between the Average and the Low or High, and a representative curve fitting to the data of the amplitude. On the data and representatives in Figure 5.4, the hourly atmospheric air temperature is characterised using Equation 6-3. Figure 5.5 illustrates the modelled temperature condition across one year.

$$T_a = T_{mean} + DT \times \sin(2pt/24) \qquad \text{Equation (5-3)}$$

Where:

T_{mean} = Average curve in the Figure 5.4(a)

$DT = \frac{High-Low}{2}$ is the variation magnitude against the average and represented by the curve in the Figure 5.4 (b).

t = Time in hours

The x in Figure 5.4(a) and Figure 5.4(b) is the time in months, i.e., x = t/30/24.

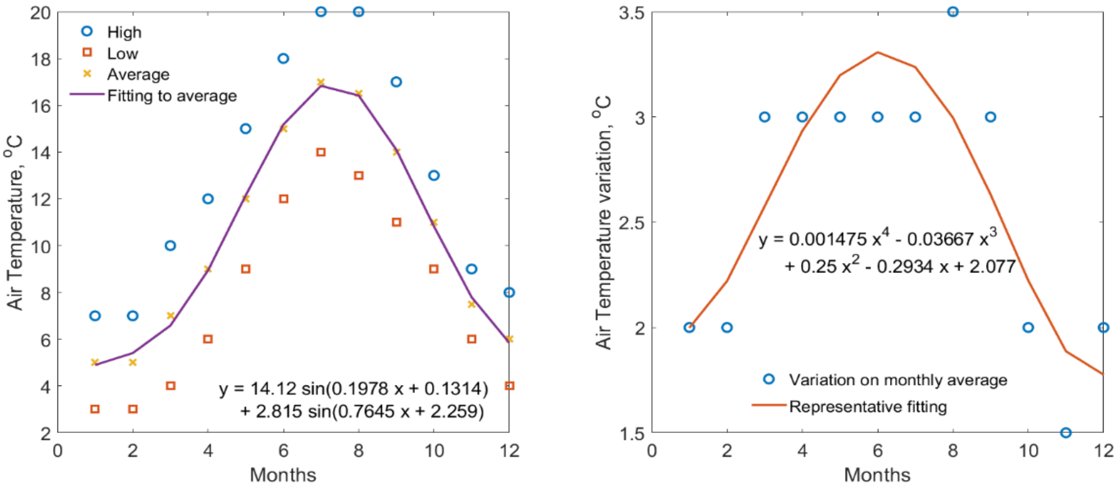

(a) (b)

Figure 5.4 UK Manchester area annual temperature variation

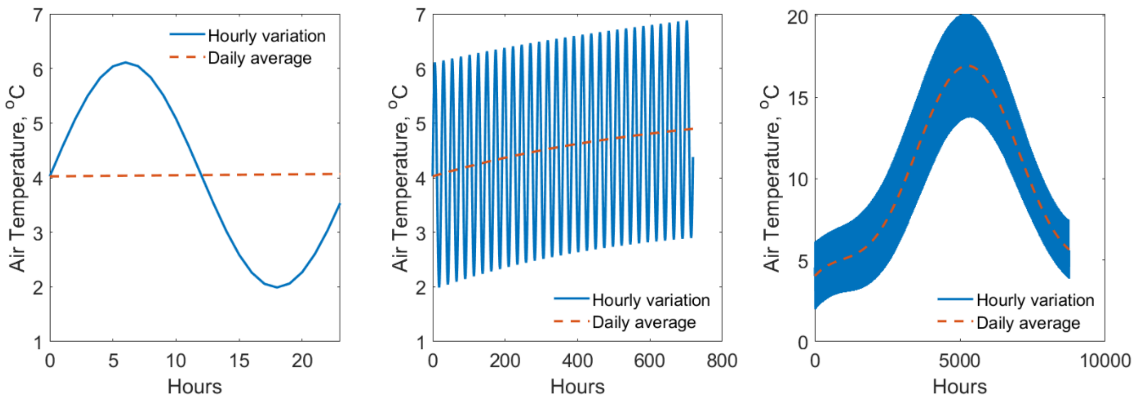

Figure 5.5 Characterized hourly air temperature variation in one year time

A number of heat convection models have ever been proposed for the h_c in Equation 5-1 (Chen, Wang and Xie, 2019). h_c directly relates to the local atmospheric weather state, including temperature, humidity and wind (Dempsey, Herlache and Patel, 1986; Bentz, 2000). As it is not a key topic of this study, a constant value, 13.5 W/m^2/°C drawn from data provided by Qin and Hiller (2011) was assumed.

To solve the energy equation, Equation 2-27, the thermal boundary condition must be defined. A thermal insulation condition is applied at a symmetric line. For the boundary temperature T_b, a geological survey on the shallow ground seasonal temperature in the UK (Busby, 2015) is assumed for the surrounding ground condition for this work.

Figure 5.6 (a) shows the data and characterization fitting curves for temperature variation at five depths underground: i.e., 0, -0.5, -1, -2 and -3m.

Figure 5.6 (b) shows a left boundary temperature at 720hrs, 2880hrs, 5040hrs and 7200hrs. The initial temperature condition in the structure is assumed to be 10 °C, referring the mean value at depth -0.5m.

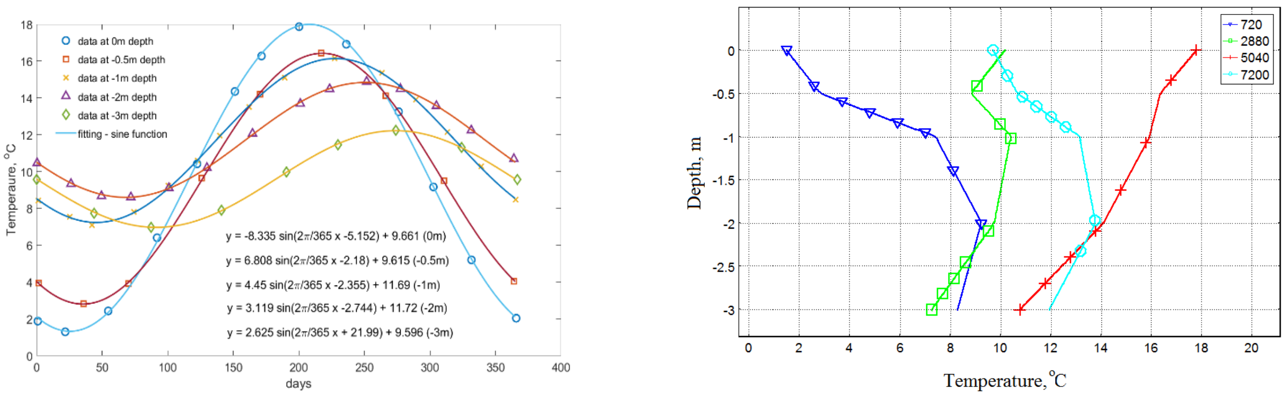

(a) Year-round UK shallow ground temperature variation (Busby, 2015)

(b) Vertical temperature profile on the righthand side

Figure 5.6 Temperature boundary condition

5.5.3 Traffic condition

A wheel pressure applied on the surface represents the traffic loading. An equivalent single wheel load of 70kN (Al Ashaibi *et al.*, 2022) is set for the modelling work, which gives a wheel load pressure of 0.772 MPa on an estimated contact area of 9.073×10^{-2} m^2 (Al-Tameemi *et al.*, 2019). The boundary condition to solve the motion equation, Equation 2-22, assumes that there is no horizontal displacement for the vertical edges of all layers, and no vertical displacement at the bottom of the subgrade.

5.6 Modelling Results

5.6.1 Temperature, Deformation and Strain

Figure 5.7 shows the calculated pavement surface temperature variation at the four positions A, B, C & D in Figure 5.1. It can be seen that the surface hourly temperature variation is almost identical for the two mixes, with the biggest variation amplitude at the edge of the pavement. The surface temperature presents a similar patten to the atmospheric air temperature shown in Figure 5.5. The calculated annual average surface temperature is 10.3°C at positions A, B & C, and 9.8 °C at D for both pavements. The annual maximum temperature at position A, B, C is about 1.5°C lower, but at position D is about 2°C higher than that of the air atmospheric temperature shown in Figure 5.5. The predicted local surface temperature variation justifies the informative advance of the thermal boundary condition adopted by this study compared to the previous study (Al Ashaibi *et al.*, 2022), which used a uniform pavement surface temperature condition.

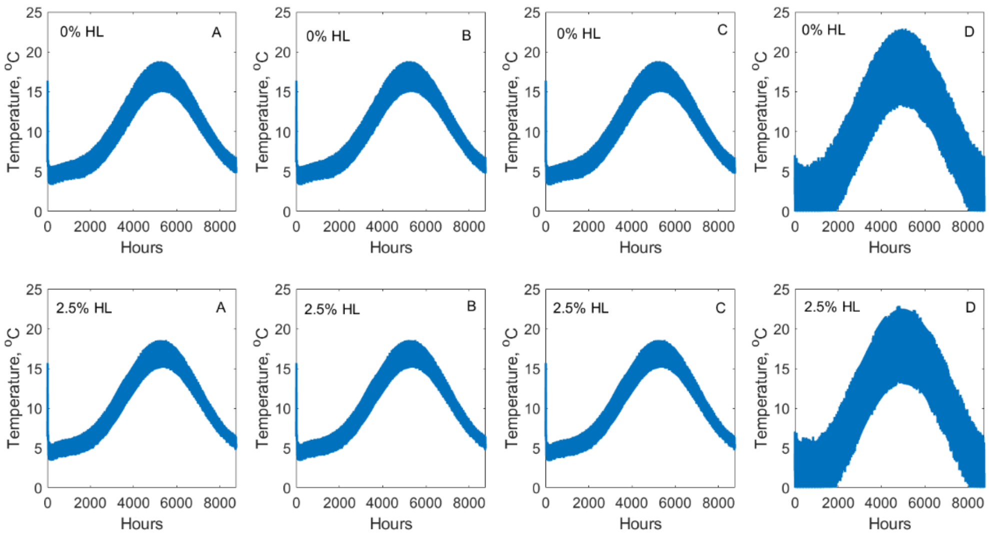

Figure 5.7 Pavement surface temperature variation year-round

Figure 5.8 compares vertical deformation at the pavement's surface at four different seasonal times in a year (720 hrs in February (Winter), 2880 hrs in May (Spring), 5040hrs in August (Summer), and 7200hrs in November (Autumn)). It can be seen that the pavement with 2.5% HL addition has up to 1% less deformation at the position bearing traffic loading. The result is similar to that predicated based on assumed surface temperature conditions (Al Ashaibi *et al.*, 2022). In addition, both of the boundary conditions are in agreement that the biggest vertical deformation at the surface happens in the summertime (5040 hrs). However, compared with the vertical displacement prediction in Al Ashaibi *et al.* (2022), Figure 5.8 shows a much smaller difference in vertical displacement in the other seasons: i.e., Winter, Spring and Autumn. The results highlight the importance of accurate boundary condition description.

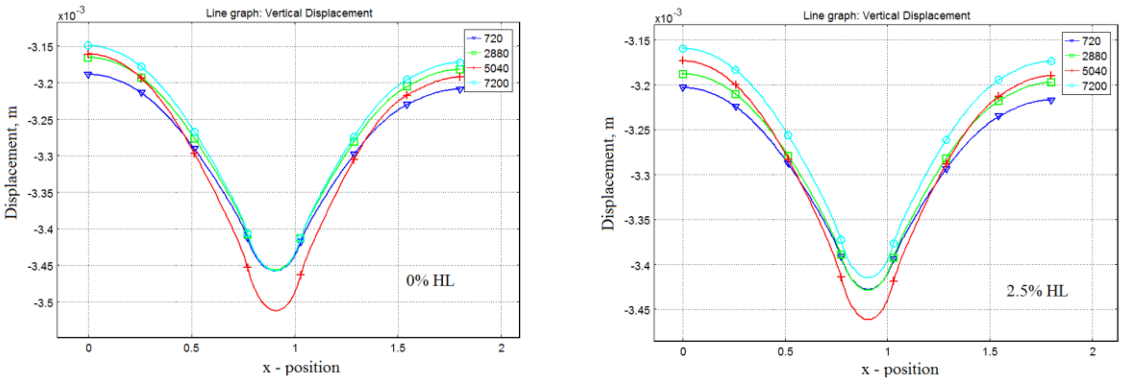

Figure 5.8 Comparison of the vertical deformation of the pavement surface

Figure 5.9 illustrates the vertical temperature profile of the pavement structure at position A at a time in four seasons. It shows that, in year-round time, the biggest temperature variation is at the surface. The seasonal temperature variation decreases downwards, and the vertical temperature profiles of the HL pavement and that using no HL are very close, with very small differences, less than 0.5 ℃, at the surface. Based on the results, the rest of the study will primarily focus discussions on the surface layer of the pavement. The results in Figure 5.9 are also closely similar to those predicted using a temperature boundary condition (Al Ashaibi *et al.*, 2022).

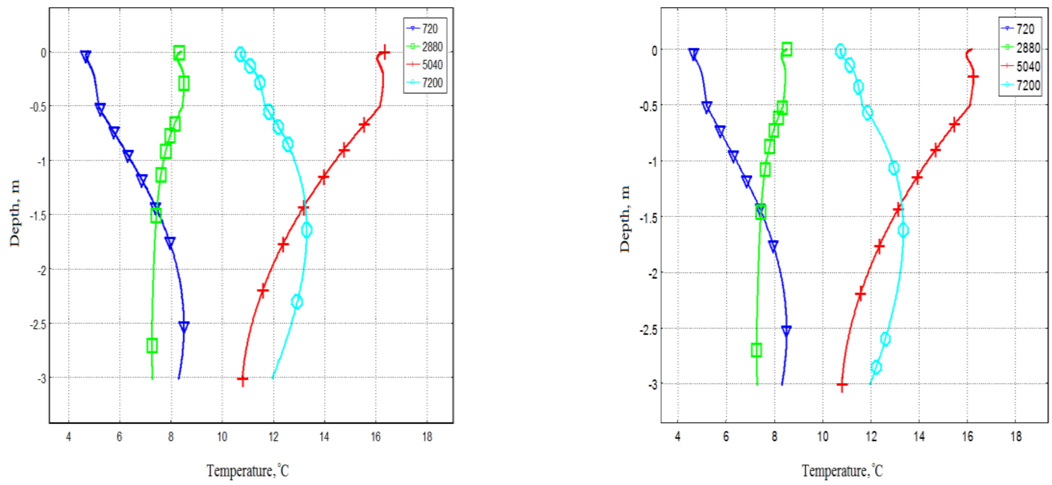

0% HL 2.5% HL

Figure 5.9 Pavement vertical temperature at position A

Figure 5.10 compares the maximum thermal strain and the two principal mechanical strains due to traffic load only in the pavement structure across a year. It shows that the annual maximum thermal strain ($e_t = \alpha\Delta T$) profiles of the pavements using HL are much higher than that of no use of HL. The maximum difference is about 100 times. The maximum 1st principal mechanical strain ($\varepsilon_{max} = \frac{\varepsilon_{xx}+\varepsilon_{yy}}{2} + \sqrt{\left(\frac{\varepsilon_{xx}-\varepsilon_{yy}}{2}\right)^2 + \left(\varepsilon_{xy}\right)^2}$) is in tension (positive), which is higher than thermal strain in the 0% HL pavement, but much lower than thermal strain in 2.5% HL pavement. Meanwhile it is shown that the 2nd principal strain ($\varepsilon_{min} = \frac{\varepsilon_{xx}+\varepsilon_{yy}}{2} - \sqrt{\left(\frac{\varepsilon_{xx}-\varepsilon_{yy}}{2}\right)^2 + \left(\varepsilon_{xy}\right)^2}$) in the pavements is very small and is in compression (negative). For this reason, this study only discusses the coupled effect of thermal strain and the 1st principal mechanical strain, based on the assumption that the tensile strain plays the principal role in fatigue cracking.

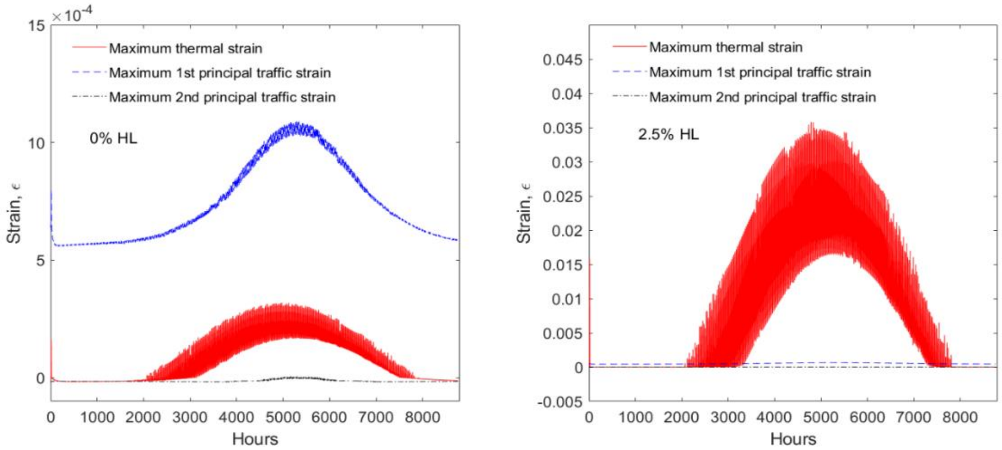

Figure 5.10 Maximum thermal strain and mechanical strain in pavement structure

Figure 5.11 compares the hourly variation in thermal strain and 1st principal mechanical strain of the pavement surface at four positions (A, B, C and D in Figure 5.1) across a year. Figure 5.11 (a) shows that the HL pavement has a much higher thermal strain at the surface than the pavement using no HL in the two warm seasons, Spring and Summer (3000–7000 hrs). The coupled resultant strain, which is defined as $e_{max} - e_T$ in terms of Equation 3-8, is also high in this period, but in compression for the HL pavement. Figure 5.11 (b) highlights the tensile states across the period of a year. It is not a surprise that the highest value is at the position directly bearing traffic (B & C), where the local tensile stress level in the 2.5 % HL pavement is lower than that in the 0 %HL by 13 % or more. Particularly, in Summer, the whole surface strain state is in compression for the pavement with 2.5 %HL. This result indicates that the pavement is exposed to the most severe conditions in winter. The annual average coupled resultant strains are, 3.99×10^{-5}, 1.897×10^{-4}, 1.851×10^{-4}, 5.82×10^{-5}, at A, B, C and D, for the 2.5 %HL pavement, and 3.99×10^{-5}, 3.738×10^{-4}, 3.575×10^{-4}, 5.81×10^{-5} for the 0%HL pavement. At positions B and C, the annual average for the 2.5 %HL pavement is about 50 % lower than that of the 0 %HL pavement.

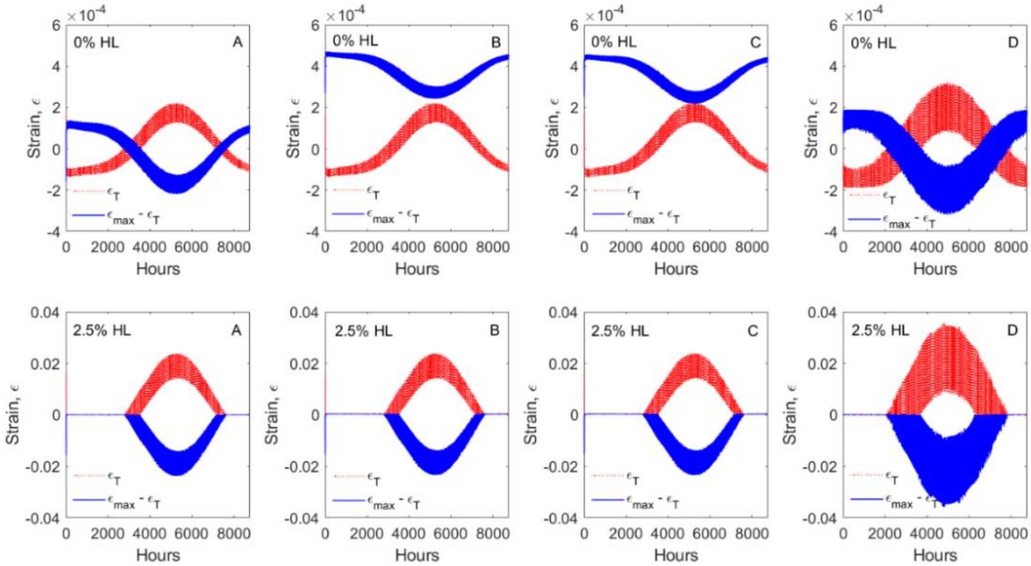

(a) Thermal strain, ε_T and coupled strain, $\varepsilon_{max} - \varepsilon_T$

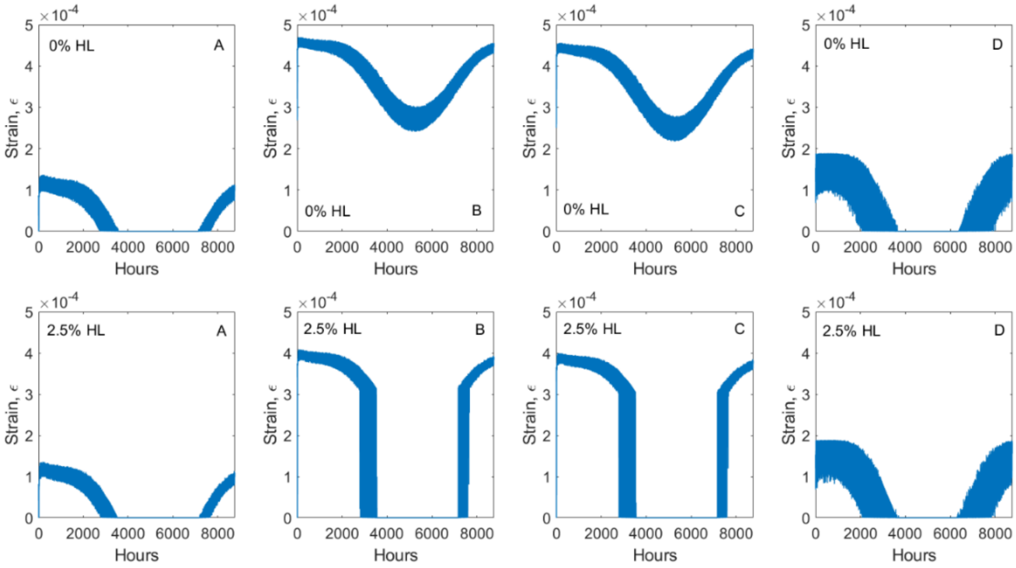

(b) Coupled strain in tensile state, $\varepsilon_{\text{max}} - \varepsilon_{\text{T}} >= 0$

Figure 5.11 The coupling of thermal & 1st principal mechanical strain at the pavement surface

5.7 Pavement Fatigue Life Estimation in Terms of Tensile Stress

The fatigue life of asphalt pavement not only depends on the cyclic traffic loading and temperature, but also on the thermal variation history of the asphalt binder (Ding, Qiu and Rahman, 2020). A parameter of complex modulus, $G^*sin\delta$, is used as the criteria for the fatigue of asphalt binder, which however has received considerable criticism. For this reason, a time sweep using the Dynamic Shear Rheometer (DSR) has been proposed (Planche *et al.*, 2004). For asphalt concrete mixtures specifically, a D^R failure criterion has also been proposed (Wang, Keshavarzi and Kim, 2018). The variable D^R is defined as the average loss of integrity per cycle throughout the service life of an asphalt mixture. The higher the D^R value, the greater the ductility of the asphalt mixture (Wang, Keshavarzi and Kim, 2018). As the main purpose is to compare the HL effect, this study simply uses structural strain information and the results of tensile fatigue tests to evaluate the fatigue life of pavement under coupled climatic and traffic conditions. Using a classical linear cumulative-damage theory (or the Palmgren-Miner rule), a rate of fatigue life consumed, or loss is defined in Equation 5-4:

$$R_f = \sum_{i=1}^{k} \frac{n_i}{N_f(\varepsilon_i)} \qquad \text{Equation (5-4)}$$

Where:

N_f (ε_i) = The fatigue life of the material subjected to a strain ε_i under the load *I;*

k = The total number of different loads applied; and

n_i = The number of cycles of each respective load *i*.

The value of N_f is estimated using Equations 2-23 and 2-24, where εt_200th simply takes the value of the coupled resultant stain, i.e., $e_t = e_{max} - e_T$. By this method, the rate of fatigue life consumed in the period of a year can be approximated by integrating the $1/N_f$ curves obtained. Since the temperature variation is in a daily cycle, fatigue life is simply evaluated based on the daily average values of the surface temperature and the coupled resultant strain at position B. Figure 5.12 shows their average value in days, which only shows the tensile strain, as compressive strain is considered to have a negligible effect on fatigue in this study, referring to a bending test.

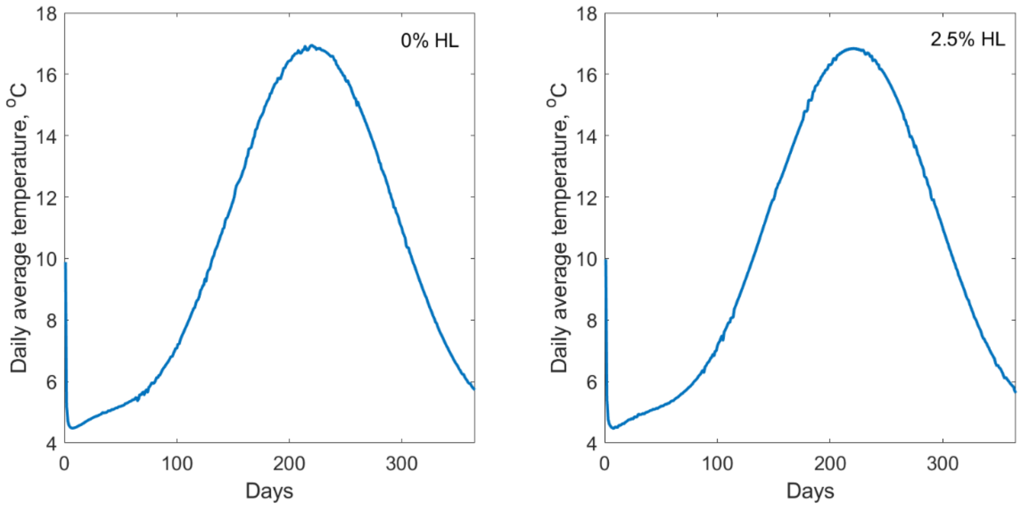

(a) Average temperature

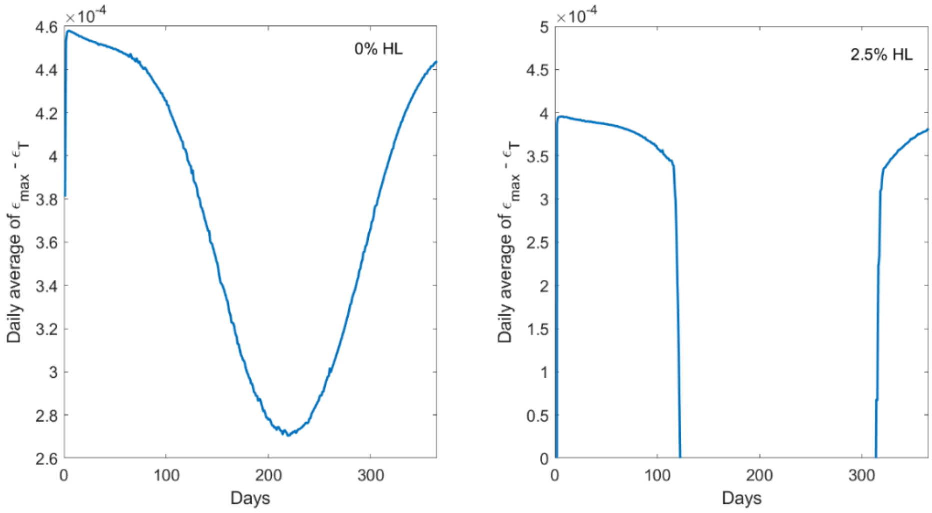

(b) Average tensile strain

Figure 5.12 Daily average surface temperature and coupled resultant strain at position B.

Figure 5.13 shows the $^{1}/_{N_f}$ calculated at position B on the pavement's surface using Equations 2-23 and 2-24 and the daily data in Figure 5.12. It is seen that the pavement using the 2.5% HL asphalt concrete has a much lower fatigue life consumption than the pavement using the concrete with no HL modification. Figure 5.13(a) illustrates that the main fatigue life consumption for 0% HL pavement would be under hot temperatures in summer, while Figure 5.13(b) illustrates that the 2.5% HL pavement has its major fatigue life consumption under cold temperatures in late autumn and winter. Compared with the surface deformation results in Figure 5.8, an interesting finding is that the highest fatigue consumption and the largest deformation happen in opposite seasonal temperature conditions for the pavement using HL. Overall, the modelling analysis further confirms that HL asphalt concrete offers an outstanding improvement in pavement performance when exposed to coupled thermomechanical loading.

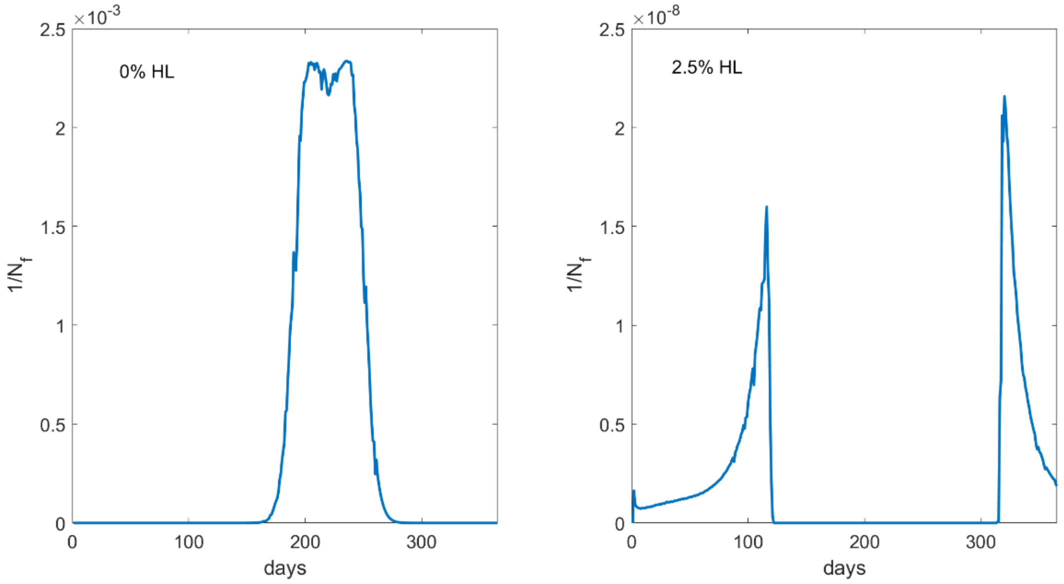

Figure 5.13 The calculated fatigue life loss, 1⁄(N_f), given strain in year-roud time

5.8 Conclusion

This chapter has applied the findings from experimental work related to the tensile fatigue life of HMA concrete mixes designed for wearing layer application, as reported in Chapter Three, comparing fatigue life across asphalt concrete mixes both modified with HL as a partial mineral filler, and in unmodified mixes. Based on the experimental data produced regarding temperature effects, a case study of numerical modelling was performed to estimate seasonal climatic effects on the constructed pavement and the benefits of hydrated lime asphalt concrete.

From the study, and the modelling developed, the following conclusion can be drawn.

• The reported experiment has confirmed that the 2.5% replacement of conventional limestone filler using hydrated lime will generate an optimum increment of fatigue life for the wearing course mix under three different temperatures. The results and conclusion are in line with what has been found in the study of other mechanical properties.

• The case study for numerical modelling highlights the advantage of the heat transfer boundary condition over a temperature boundary to give more informative predictions.

• The modelling results illustrate the interesting finding that pavements using and not using HL modified asphalt concrete have quite different thermomechanical strain states in different seasons. HL modified pavement has a higher rate of fatigue life loss under cold conditions, such as in winter, while the pavement using no HL has a higher fatigue life loss under hot conditions, such as in summer.

• For pavements using HL, the largest deformation and the highest fatigue consumption happen in opposite different climatic seasons.

• In line with the material experiment, the modelling has further confirmed that HL asphalt concrete gives outstanding improvements in pavement durability when exposed to coupled thermomechanical loading.

CHAPTER 6 - TRIAXIAL TESTS AND MODELLING OF PERMANENT DEFORMATION IN THE PAVEMENT

6.1 Introduction

Asphalt pavements are subject to a number of challenges, and rutting forms one of the most severe of these issues, with significant impacts on the safety and comfort of road users. Rutting occurs where the pavement has inadequate shear strength when exposed to high temperatures and loads, leading to permanent plastic deformations (Xie and Yang, 2019; Guo and Nian, 2020). Studies demonstrate that as rutting forms, dilatancy is also present (Muraya, Molenaar and Van de Ven, 2009), in which the volume of the pavement material expands when subject to shear activity. Shear deformation is described as a response to frictional forces from the aggregates, interlocking particle effects and cohesion exerted by the mortar, leading to dilatancy behaviours (Bolton, 1986). Song and Pellinen (2007) report dilatancy behaviour as an essential factor in asphalt pavement rut formation. Work by Zhang *et al.* (2015, 2016) investigated associations between variations in load times and temperature and axial, radial and volumetric strain, as well as stress change for an asphalt mix, and performed analysis of dilatant deformation laws and variables impacting asphalt mixes. As research has advanced in this area, dilatancy behaviour has become more established as a factor in rutting. Evidence from studies has led triaxial testing to be commonly applied compared to other testing approaches, due to its accuracy in simulation of mechanical conditions (Feng *et al.*, 2018; Zhang *et al.*, 2019). Present use of triaxial testing includes examinations of brittle material, e.g. rock and concrete, with few discussions of this type of test as applied to modified asphalt mixes (Zhao *et al.*, 2021). The most frequently applied tests used with asphalt mixtures at present are split tensile testing and single-indicator flexural testing (Cerni *et al.*, 2017; Cheng *et al.*, 2020). Extensive research has used standard triaxial testing to investigate asphalt concrete's mechanical properties in the context of core walls in hydraulic structures (Wang *et al.*, 2005; Yang *et al.*, 2014; Xia Zhan and Wang, 2019). Xie *et al.* (2019) investigated asphalt concrete's triaxial failure properties using a specially designed confining pressure triaxial testing approach, successfully establishing 3D criteria for failure. Standard triaxial testing however is capable of applying confining and axial pressures only to a sample, with no capability for achieving triaxial loads, and therefore, intermediate principal stress impacts affecting asphalt concrete strength cannot be examined (Su, Hossiney and Tia, 2013; Zheng and Huang, 2015). Enhancements to asphalt matrix materials can result in better-performing mixes: for example through making them more resistant to cracking under cool temperature conditions, or more resistant to rutting under hotter conditions (Abdi *et al.*, 2021; Moniri *et al.*, 2021).

The triaxial test has the capability to control and apply deviatoric stress, which is responsible for deformation shape. This chapter describes the triaxial experiment used in this research and presents the experiments conducted and results from these experiments for three temperatures, 20℃, 40℃, and 60℃, and three deviatoric stress levels: 10 (68.9) psi (kPa) , 20 (137.9) psi (kPa), and 30 (206.9)psi (kPa). Triaxial testing forms the third objective of the research, which is fully addressed in this chapter.

6.2 Experimental Design and Materials for Triaxial Testing

The same materials, mix design, and procedures used to prepare specimens to determine thermal properties and flexural fatigue in this research were also followed to prepare the samples for the triaxial test. Two mixtures were prepared: a hydrated lime modified 2.5% HL mix; and an unmodified mix with 0%. HL.

Asphalt concrete mixes were prepared with the optimum asphalt content obtained by Marshall properties, stability and flow, air content, density, voids in mineral aggregate (VMA), and voids filled with asphalt (VFA). The optimum asphalt content took a value determined for the hydrated lime modified flexible pavement in a previous study (Al-Tameemi, 2017) and which was adopted for all of the mixes in this study. The compete process of specimen preparation from mixing and compaction was carried out in accordance with the respective AASHTOT307 Triaxial Cyclic Compression test.

6.2.1 Experiment Design

In this study for prediction of permanent deformation for hydrated lime-modified asphalt concrete, four variables were accounted for as representing impacts on permanent deformation on asphalt concretes in practice, from mix characteristics, vehicle loads and conditions in the environment. The study therefore focused on:

1. Testing temperatures;
2. Load conditions (deviator stresses);
3. Mix characteristics; and
4. Proportion of hydrated lime.

This factorial experiment is designed as illustrated in Table 6.1, which shows that the repeat loading test contains four factors, namely mixture type, temperature and stress, for which 3 levels are included, and hydrated lime, for which 2 levels are used. This creates the need for 18 samples (3^3 x 2^1) to be used, as shown in Figure 6.1.

Figure 6.1 All Samples for Both Mixes

Table 6.1 Factorial Design of the Experimental Work

<table>
<tr><th colspan="5">Triaxial repeated load test</th></tr>
<tr><td>Factor</td><td>Temperature</td><td>Stress level</td><td>Mix type</td><td>Hydrated lime content</td></tr>
<tr><td>Level</td><td>3</td><td>3</td><td>3</td><td>2</td></tr>
<tr><td colspan="5"></td></tr>
<tr><td rowspan="4">Variables</td><td>20℃</td><td>68.9(kPa)</td><td>Wearing</td><td rowspan="2">0%</td></tr>
<tr><td rowspan="2">40℃</td><td rowspan="2">137.895 (kPa)</td><td rowspan="2">Leveling</td></tr>
<tr><td rowspan="2">2.5%</td></tr>
<tr><td>60℃</td><td>206.89 (kPa)</td><td>Base</td></tr>
</table>

Asphalt concrete mixes were made following the design standards ASTM D 6926-10 and ASTM-D-1559for three pavement course layers, i.e., wearing, leveling and base courses. The control mixes use limestone dust only for the mineral filler. The particle size of the limestone duct is less than 0.075 mm (passed through sieve No. 200). The mineral filler (MF) contents are 7, 6, and 5% by total weight of the mix, respectively, for the wearing, leveling and base applications. Other three mixes are designed to use hydrated lime to replace the limestone dust of each control mix by 2.5% of the total weight of the aggregates of the control mixes. Table 3.7 gives out three key Marshall design properties for these mixes: i.e., optimum asphalt cement (OAC) content, bulk density, and air void (AV) content (Al-Tameemi, Wang and Albayati, 2016). Each of the six prepared mixes were casted into cylindrical specimens, which are in triplicate and the size of 101.6 mm (4 inch) in diameter and 152.4 mm (6 inch) in height, for the triaxial tests as shown in Figure 6.1.

6.2.2 Triaxial test

The specimens are dried for at least eight hours to a constant weight to ensure that they are dry for this test. The top and bottom surfaces of the specimens are checked for any blemishes and to make sure that they are level so that they do not rock on the plates. Figure 6.2 presents the triaxial experiment setup. Siting in the airtight pressure cell, specimens are designed to be subject to a peripheral confining pressure on the cylindrical side surface and a vertically axial compressive loading on the top. At first, the pressure cell and the specimen in it were put into an environment chamber at a set temperature. They were left there for two hours to reach a uniform temperature distribution within the specimen.

(a) Airtight pressure cell

(b) Specimen testing in PRLS

Figure 6.2 Triaxial experiment setup

Thereafter, the triaxial test was performed by applying repetitive compressive loading in the form of a rectangular wave and a frequency of 1Hz, which exerts a certain loading force for 0.1 seconds followed by a rest without loading for 0.9 seconds. Each test had a total load repetition number of up to 10,000. The deformation in the axis direction of the specimen was recorded using two linear variable differential transducers (LVDTs). The triaxial tests were conducted under three different temperatures, they are 20°C, 40°C and 60°C. Axial compressive loading (load stress) and confining pressure (confining stress), which was applied by the air pressure inflated in the pressure cell, are listed in Table 6.2.

Table 6.2 Triaxial test load conditions

Deviator Stress psi (kPa)	Confining Stress psi (kPa)	Axial Load Stress psi (kPa)
10 (68.9)	0 (0)	10 (68.9)
20 (137.9)	10 (68.9)	30 (206.8)
30 (206.9)	10(68.9)	40 (275.8)

6.3 Experiment Results & Discussion

Both permanent and elastic deformation have been recorded for the number load repetition at 1, 2, 10, 100, 500, 1000, 2000, 3000, 4000, 5000, 6000, 7000, 8000, 9000 and 10000. Figure 6.4 shows the measured axial permanent strain and resilient (elastic) strain under a uniaxial load of 10 psi (68.9 kPa). Temperature presents a large influence on both permanent and resilient deformation. The higher the temperature, the larger the permanent and resilient deformation. The results in Figure 6.4(a) demonstrate that increasing mineral filler content improves rutting resistance, since the permanent deformation displaces that wearing layer mix (7% MF) > levelling layer mix (6% MF) > base layer mix (5% MF). For the mixes with lower MF addition, such as the mixes for leveling and base layers, the HL modification has a more distinct effect on stability improvement, in which the modified mixes have much less permanent deformation compared to the counterpart control mixes. At the low temperature (20°C), the unconfined permanent deformation (ε_p) takes on an almost ideally linear increase with the load repetition number in the log-log scale, which can be well represented using the power function (see Equation 6-1 below). However, the linear trend becomes disrupted at higher temperatures.

$$\varepsilon_p = aN^b \qquad \text{Equation (6-1)}$$

Where:

N= number of repetitions, and a and b are two constant parameters relating to the y-axis interception and the slope of the linear trend.

Findings for permanent deformation are generally expressed as a relation linking permanent strain to loading repetitions. Broadly speaking, this relation can be classified into primary, secondary and tertiary regions (Walubita et al., 2013). There have been numerous models developed to date to characterise permanent deformation in layered asphalt concrete pavements. For the present work, the characterisation of permanent deformation for the secondary region is based upon the power relationship linking cumulative permanent strain and loading repetitions. This characterisation is given in Equation 6-1, as first put forward by Barksdale (1972) and Monismith *et al.* (1975). See Figure 6.3.

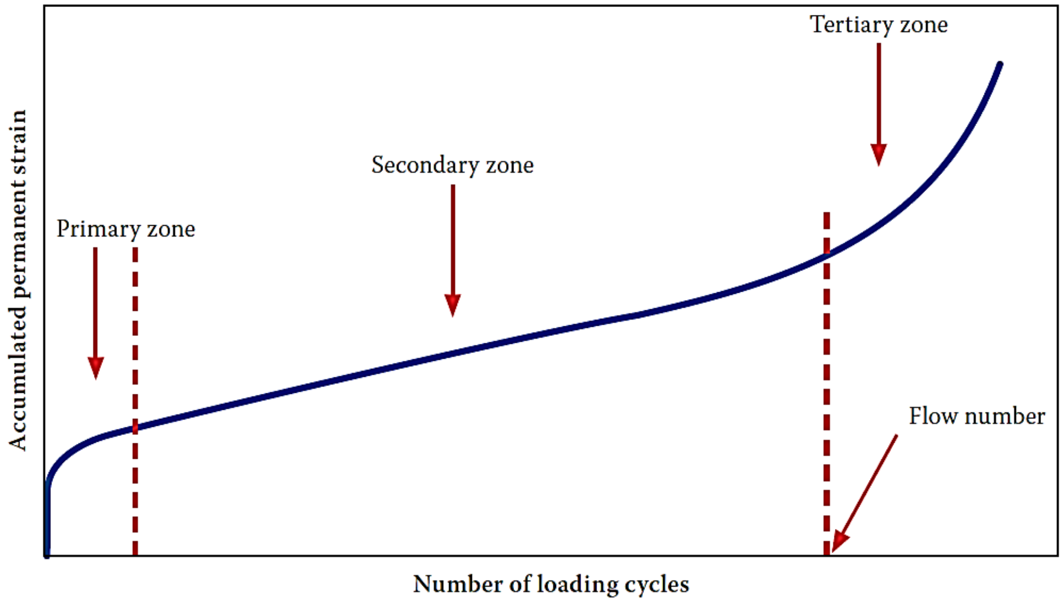

Figure 6.3 Typical relationship between permanent strain and number of load repetitions (Walubita *et al.*, 2013)

Most of the curves in Figure 6.4 (b) show two or three distinctive horizontally linear sections. The resilient strains are a little higher after being exposed to initial repetitions. The result demonstrates an initial shakedown of the mixes: a phenomenon in which elastic-plastic structures subjected to cyclic or repeated loads can respond in a resilient manner when the load applied is above the yield limit but lower than a critical load limit (Yu and Wang, 2012; Liu *et al.*, 2022) aligned with permanent deformation. An interesting fact is that the elastic modulus decreases very little with the initial number of repetitions. This might be explained due to the local aggregate rearrangement in the flow of asphalt matrix in line with accumulated plastic deformation. However, the shakedown limits decrease with increasing temperature, as the resilient strain curves become more horizontally straight at the temperature 60°C.

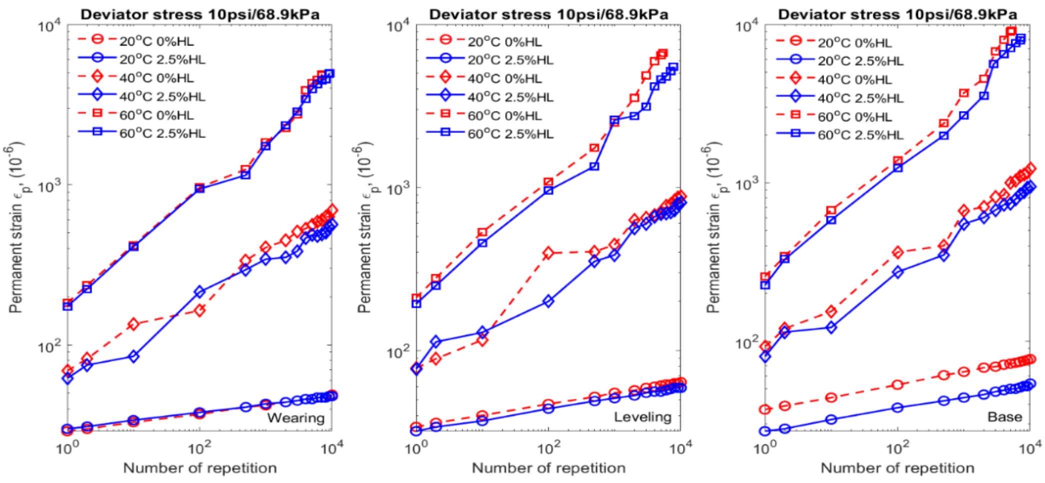

(a) Permanent deformation

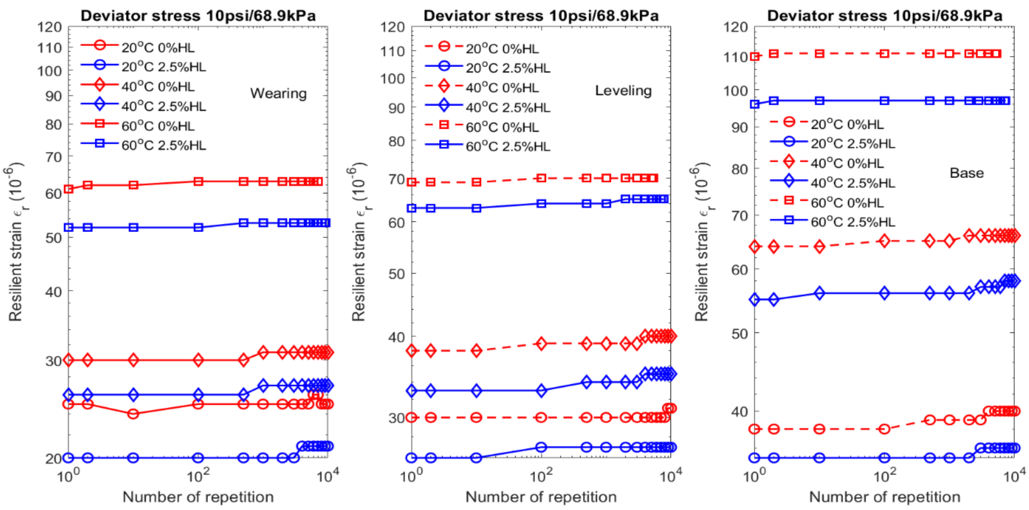

(b) Elastic deformation

Figure 6.4 Results at 10 psi deviator stress

Figure 6.5 shows the measured axial permanent strain and elastic (resilient) strain under a triaxial load of 20 psi (137.9 kPa) deviator stress: i.e., 30 psi (206.8) axial stress and 10 psi (68.9) confining stress. Similar to that noticed in Figure 6.4, at the low temperature of 20°C, permanent deformation shows an ideal linear trend in log-log scale with the number of load repetitions. For each of the three kinds of mixes, HL modification reduces both the permanent and elastic deformation at the three temperatures. In particular, Figure 6.5(a) shows that the most obvious improving effect in rutting resisting occurs for the wearing layer mix and levelling layer mix, probably due to the higher filler content in the two mixes.

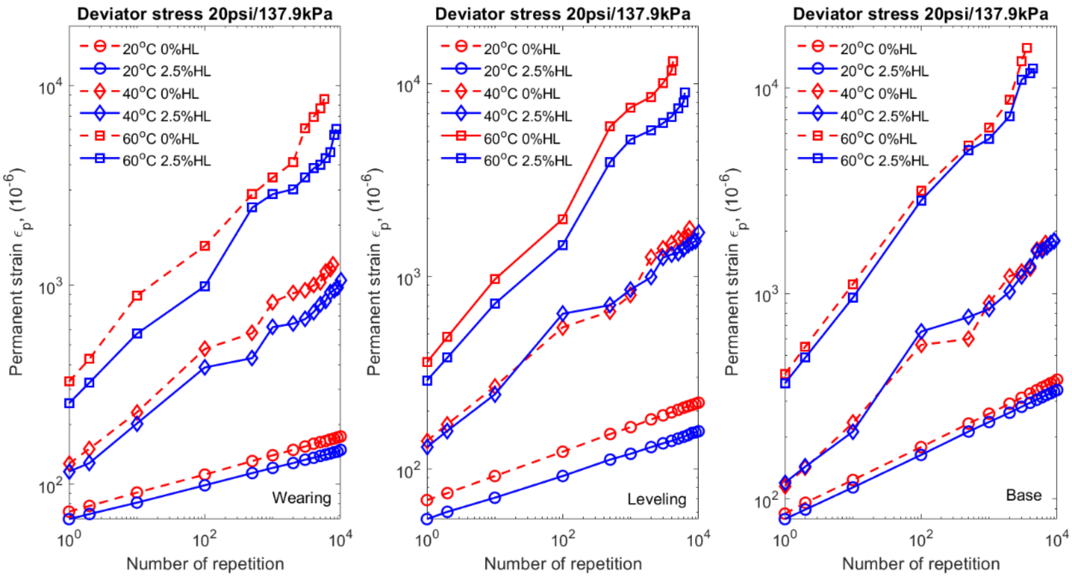

(a) Permanent deformation

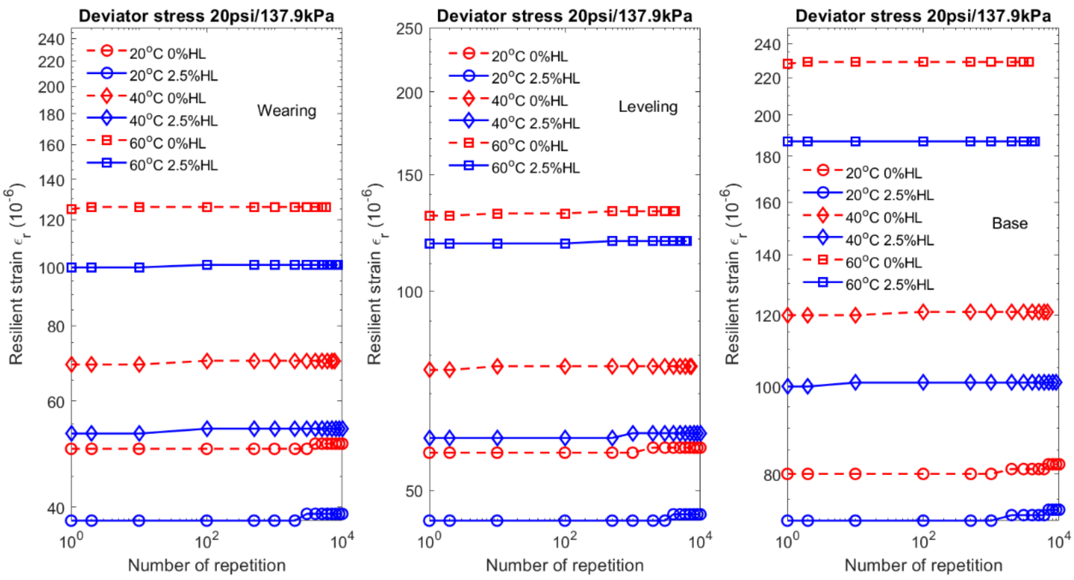

(b) Elastic deformation

Figure 6.5 Results at 20 psi deviator stress

Figure 6.6 shows the measured axial permanent and resilient strain under the triaxial deviatoric stress of 30 psi (206.8 kPa). The results in Figure 6.6 (a) are comparable with those in Figure 6.5 (a). An ideal linear relationship between permanent strain and number of repetitions is maintained at 20°C, while the HL effect is particularly highlighted in the wearing and levelling layer mixes, which have a higher content of mineral filler.

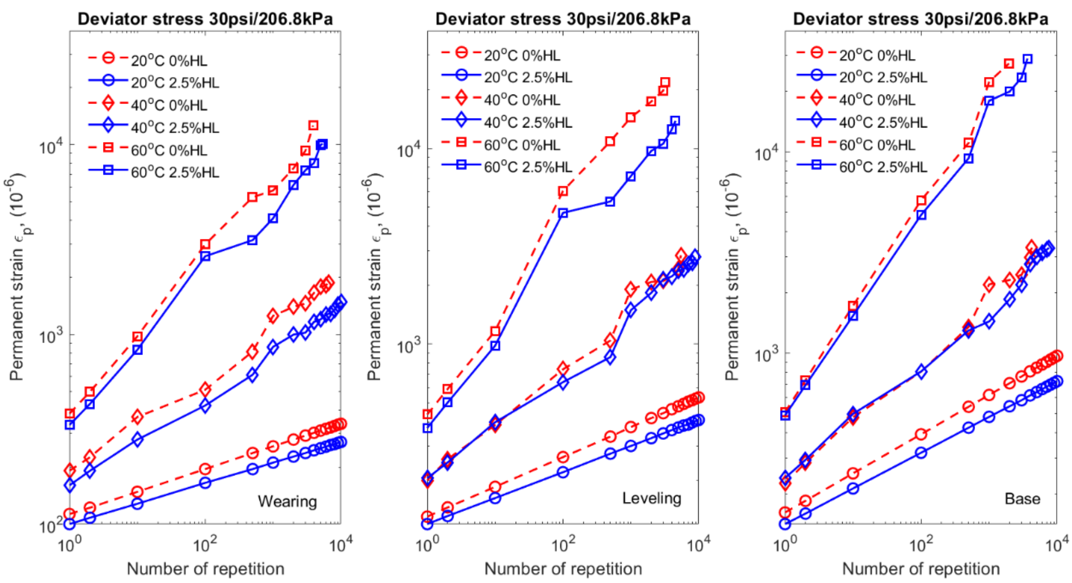

(a) Permanent deformation

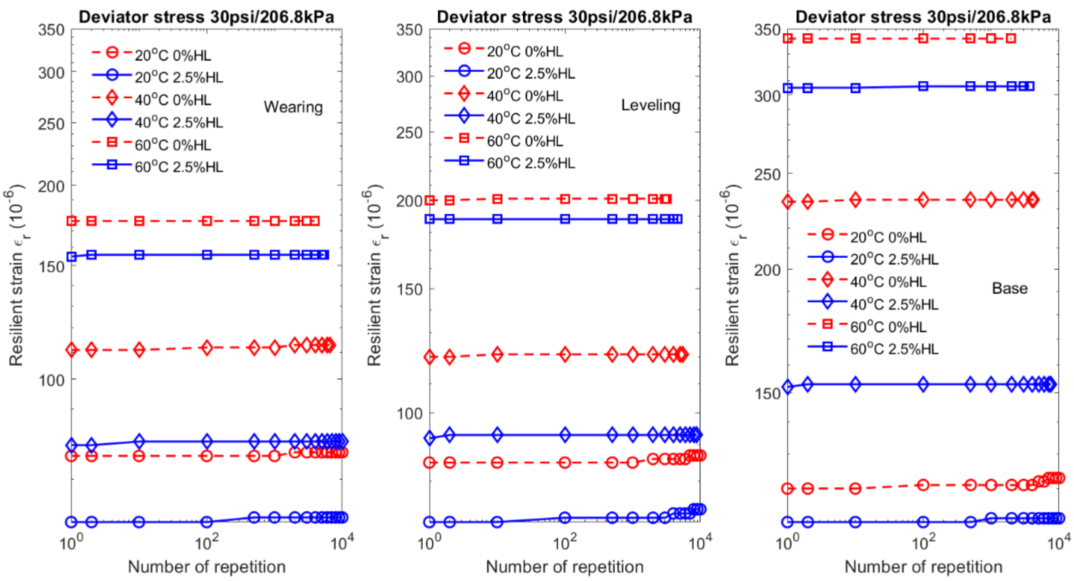

(b) Elastic deformation

Figure 6.6 Results at 30 psi deviator stress

Comparing the plots (b) in Figures 6.4 - 6.6, it is noticed that, under each specific triaxial load condition, the base layer mix has a much higher axial resilient strain than the mixes for the other two layers. The difference in the resilient strain with and without HL is smaller for the wear and levelling mixes than for the base mix. The result highlights the influence of the total content of mineral filler, which exists as an optimum value as well in line with the HL additive content. Another important observation is that, while HL modification shows an impressive improvement in rigidity for all the mixes, the resilient strain is considerably different under different stress deviations for the same mix. This means that the resilient modulus of asphalt concrete depends on the stress condition. The triaxial resilient modulus in general increases with confining and deviatoric stresses, as has also been reported by other researchers, and is possibly explained due to density increase and strain hardening (Fedrigo, Núñez *et al.*, 2018).

6.4 Triaxial Result Characterization

Both the relationships of permanent strain and elastic strain vs number of load repetitions can be characterized using the power function (Equation 6-1), with good representation. Figure 6.7 and Figure 6.8 illustrate the characterization results.

Table 6.3 and Table 6.4 list the parameters determined using Equation 6-1 to fit the permanent strain data, which are illustrated and compared in Figure 6.9.

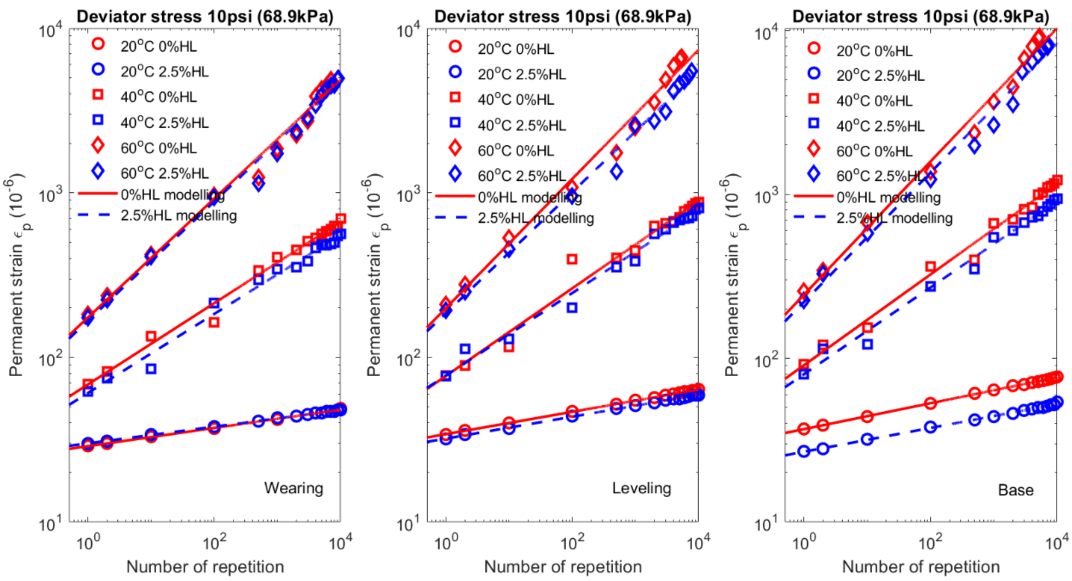

(a) For the test of 10 psi (68.9 kPa) deviator stress

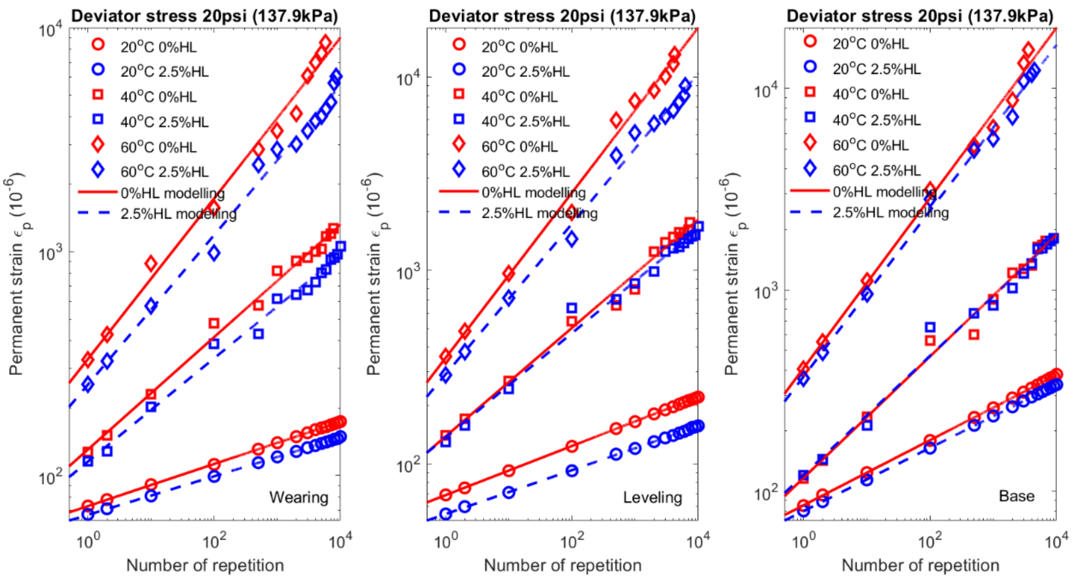

(b) For the test of 20 psi (137.9 kPa) deviator stress

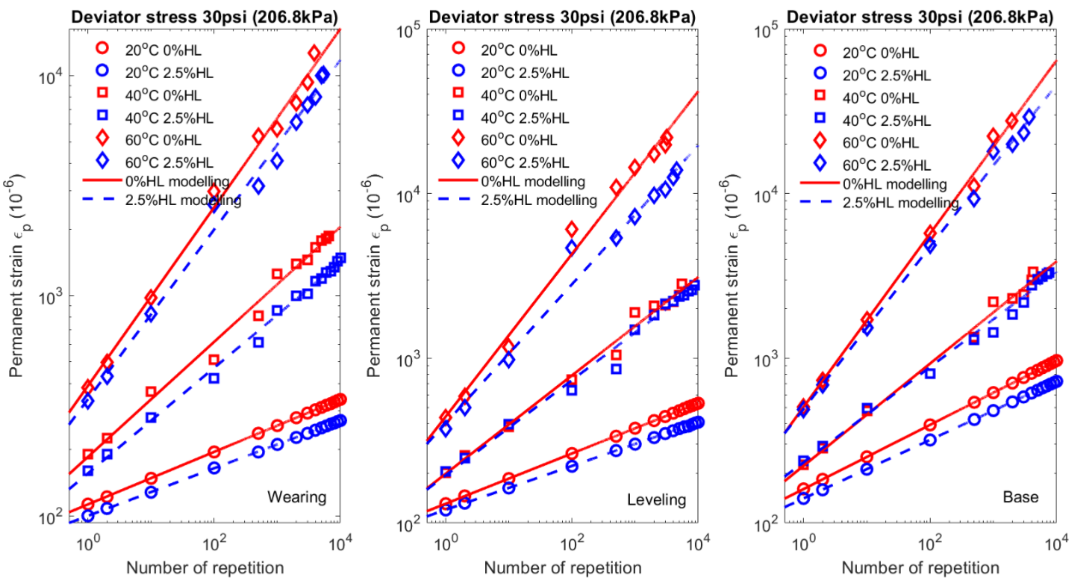

(c) For the test of 30 psi (206.8 kPa) deviator stress

Figure 6.7 The characteristic representation for permanent strain using Equation (6-1)

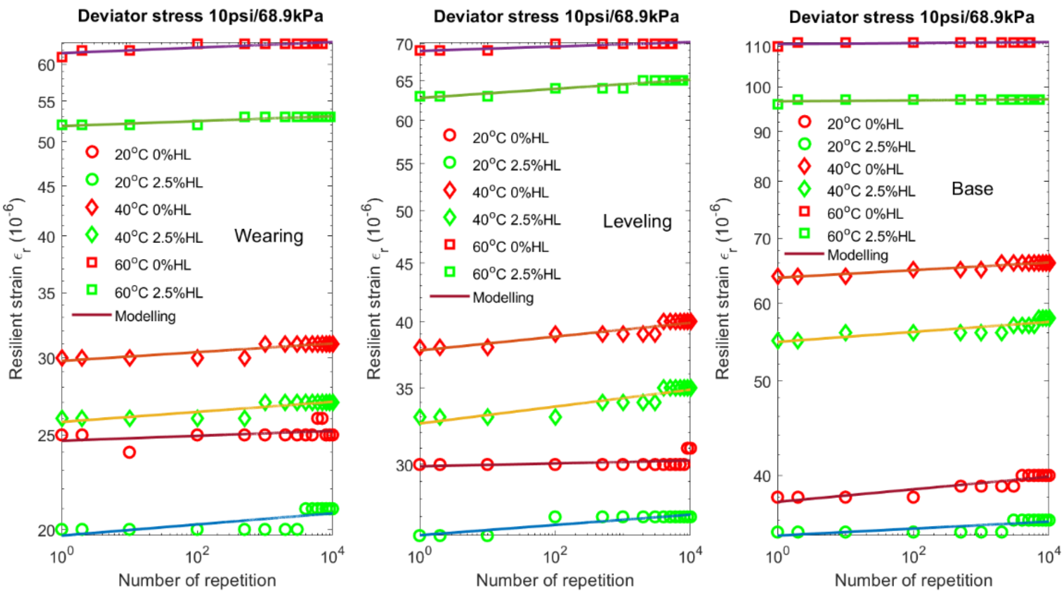

(a) For the test of 10 psi (68.9 kPa) deviator stress

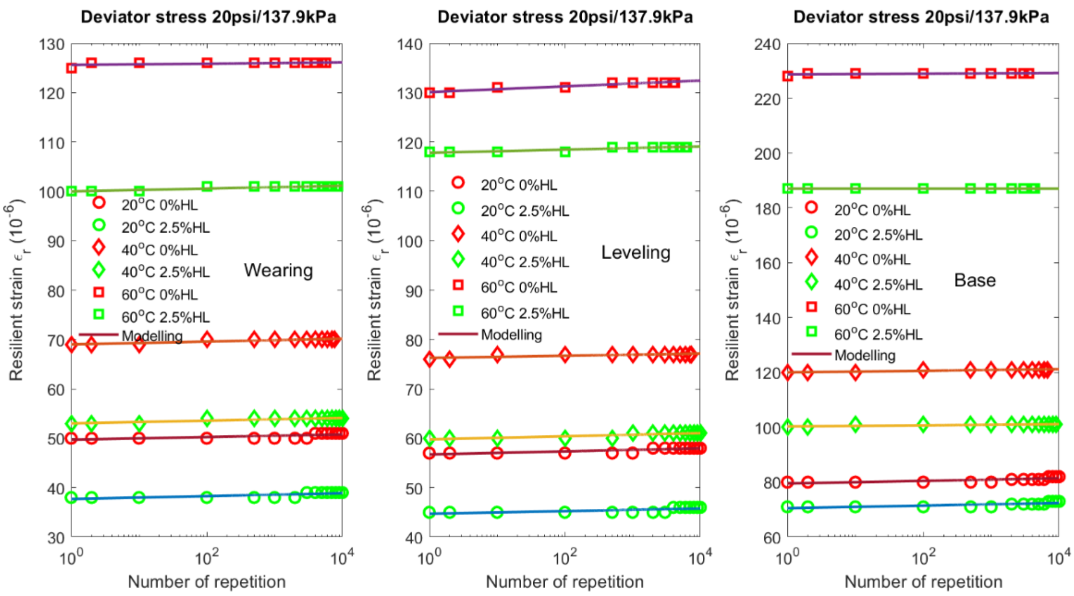

(b) For the test of 20 psi (137.9 kPa) deviator stress

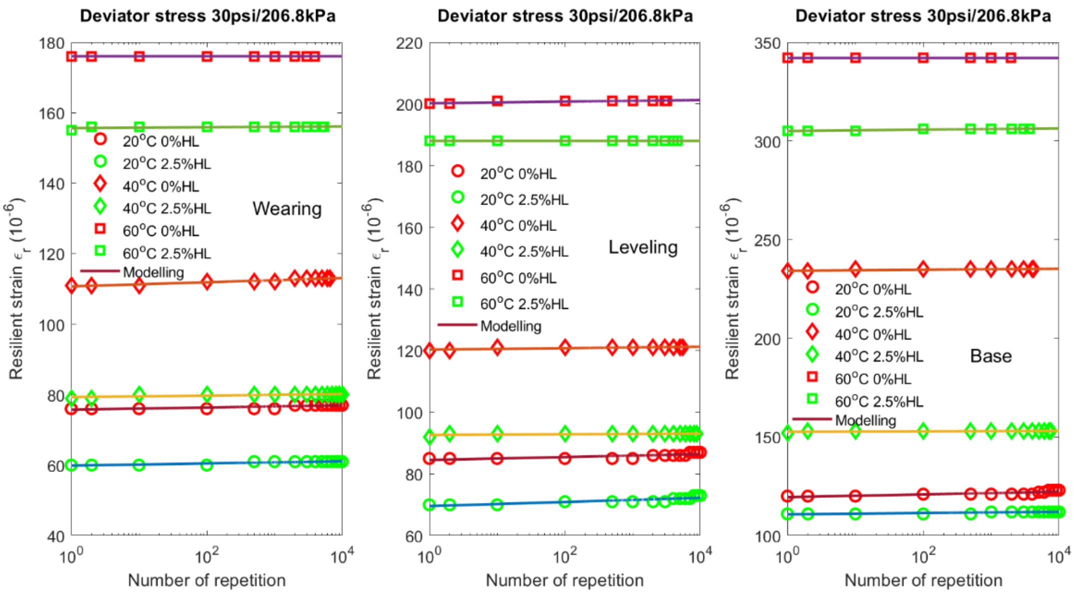

(c) For the test of 30 psi (209.8 kPa) deviator stress

Figure 6.8 Characteristic representation for elastic strain using Equation (6-1)

Table 6.3 Parameters determined in Equation 6-1 to represent permanent strain for the control mixes

Deviator stress psi	Temperature °C	Mixes	a	b
Control mixes of 0% HL				
10	20	Wearing	28.9068	0.0553
		Levelling	34.1979	0.0678
		Base	36.8978	0.0790
	40	Wearing	68.5488	0.2469
		Levelling	77.2681	0.2658
		Base	90.5733	0.2771
	60	Wearing	174.9847	0.3611
		Levelling	199.5262	0.3923
		Base	243.7811	0.4068
20	20	Wearing	72.9458	0.0941
		Levelling	68.8652	0.1269
		Base	85.3100	0.1617
	40	Wearing	130.6171	0.2511
		Levelling	138.6756	0.2802
		Base	116.6810	0.3018
	60	Wearing	331.1311	0.3588
		Levelling	353.1832	0.4266
		Base	409.2607	0.4227
30	20	Wearing	112.7197	0.1193
		Levelling	130.9182	0.1525
		Base	160.6941	0.1948
	40	Wearing	185.3532	0.2613
		Levelling	199.0673	0.2984
		Base	222.3310	0.3104
	60	Wearing	389.9420	0.4055
		Levelling	442.5884	0.4935
		Base	505.8247	0.5263

Table 6.4 Parameters determined in Equation 6-1 to represent permanent strain for the HL mixes

Deviator stress psi	Temperature °C	Mixes	a	b
Mixes of 2.5% HL				
10	20	Wearing	30.0608	0.0508
		Levelling	32.1366	0.0665
		Base	26.8534	0.0727
	40	Wearing	60.8135	0.2402
		Levelling	77.6247	0.2506
		Base	79.7995	0.2650
	60	Wearing	167.1091	0.3621
		Levelling	185.7804	0.3676
		Base	220.2926	0.3951
20	20	Wearing	66.6807	0.0861
		Levelling	54.9541	0.1134
		Base	79.7995	0.1572
	40	Wearing	115.3453	0.2308
		Levelling	137.0882	0.2691
		Base	120.5036	0.2962
	60	Wearing	254.6830	0.3339
		Levelling	290.4023	0.3887
		Base	371.5352	0.4121
30	20	Wearing	100.0000	0.1331
		Levelling	120.2264	0.1777
		Base	140.9289	0.2398
	40	Wearing	155.9553	0.2889
		Levelling	194.5360	0.2893
		Base	233.3458	0.3855
	60	Wearing	338.8442	0.4215
		Levelling	403.6454	0.4925
		Base	492.0395	0.1331

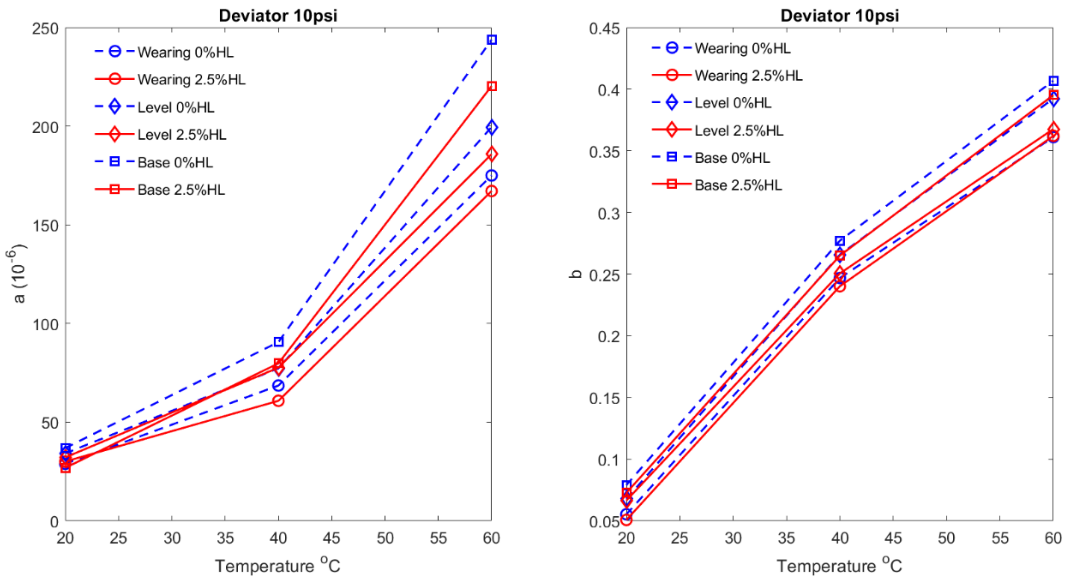

(a) Deviator stress 10 psi (68.9 kPa)

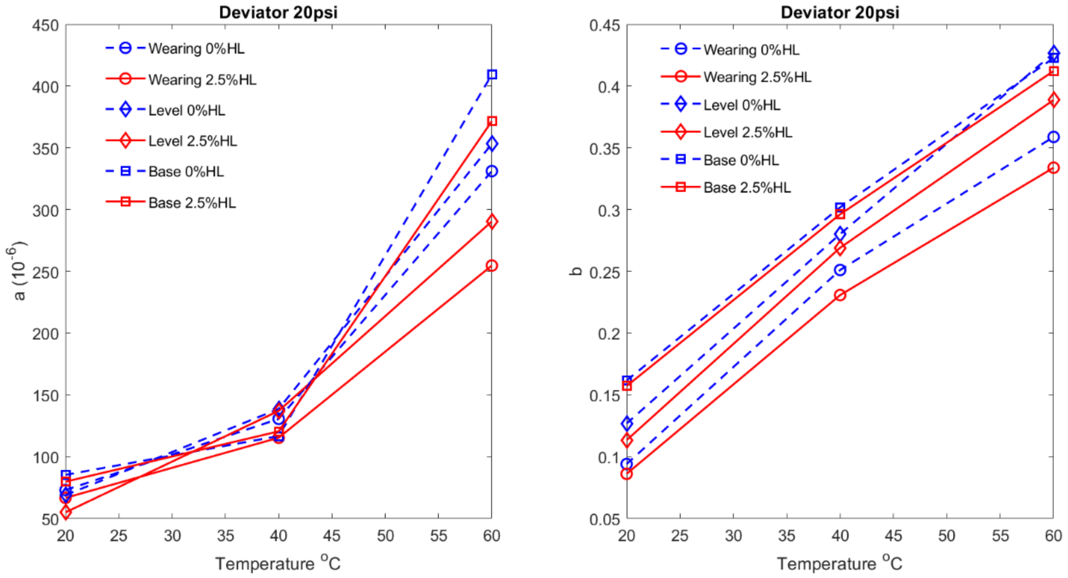

(b) Deviator stress 20 psi (137.9 kPa)

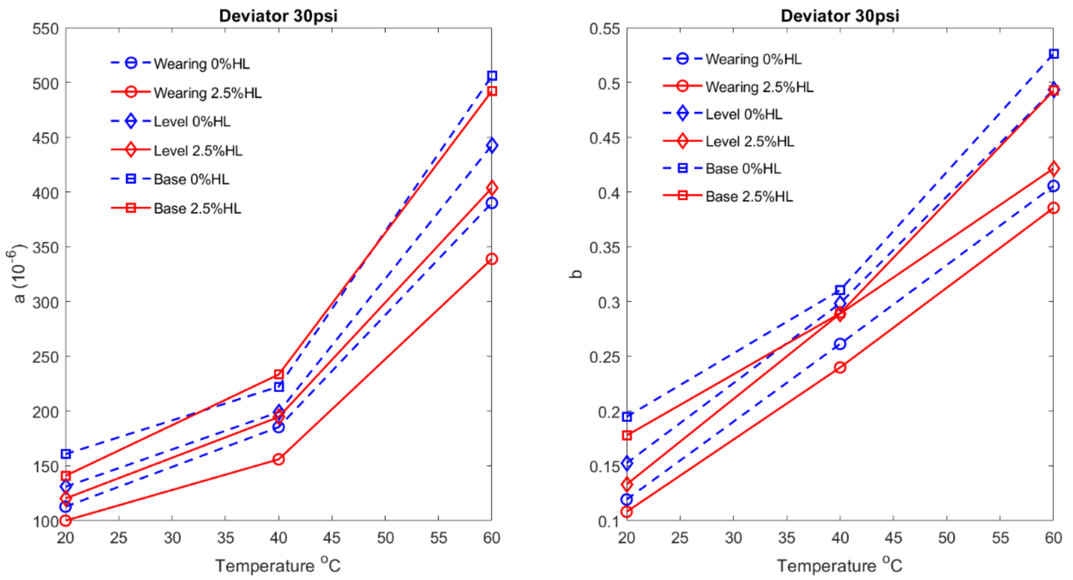

(c) Deviator stress 30 psi (209.8 kPa)

Figure 6.9 Illustration of the parameters in the Tables 6-3 and 6-4.

To develop a comprehensively integrated characteristic model for permanent deformation under complex stress conditions, the data in

Table 6.3, Table 6.4 and Figure 6.9 are further represented in 3D space based on a plane of load stress and confining stress. The characteristic surface of *a* and *b* is represented using a formulated exponential function as shown in Table 6.5, and Figure 6.10 and Figure 6.11 show the *a* and *b* surfaces obtained for the control mixes and the mixes using HL. Figure 6.12 and Figure 6.13 compare the modelling accuracy of the *a* and *b* at the 9 data positions, and demonstrate that characteristic surfaces represent permanent deformation well for all of these mixes under complex, stressed thermal conditions. These models can be used to predict and compare surface rutting deterioration for pavement structures constructed using and without using HL as an additive.

Table 6.5 The characteristic surfaces of parameters, a and b

Control mixes (x: deviator stress, y: temperature)	
Wear layer	a = 14.23 exp (0.03672 x) exp (0.03759 y) b = 0.06014 exp(0.006766 x) exp(0.02866 y)
Levelling layer	a = 14.54 exp (0.03783 x) exp (0.03855 y) b = 0.06371 exp (0.01165 x) exp (0.02845 y)
Base layer	a = 15.58 exp (0.03643 x) exp (0.04033 y) b = 0.07511 exp (0.01348 x) exp (0.02553 y)
Mixes of 2.5% HL (x: the deviator stress, y: temperature)	
Wear layer	a = 13.27 exp(0.03607 x) exp(0.03621 y) b = 0.05704 exp (0.004048 x) exp(0.02978 y)
Levelling layer	a = 14.49 exp(0.03959 x) exp(0.03594 y); b = 0.06665 exp (0.008448 x) exp(0.02712 y)
Base layer	a = 14.07 exp (0.04114 x) exp(0.03918 y) b = 0.07333 exp (0.01152 x) exp (0.02592 y)

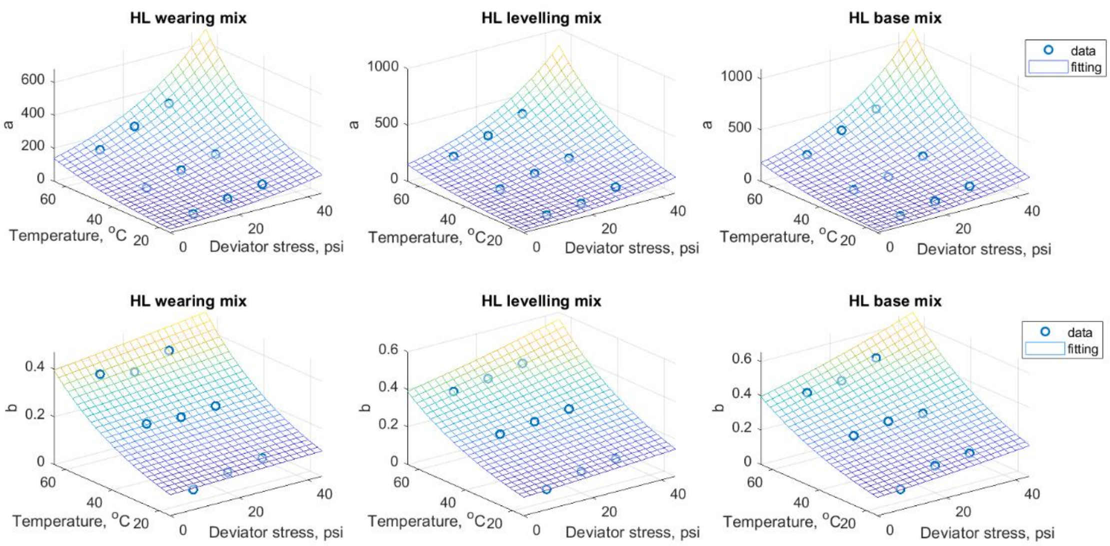

Figure 6.10 Parameters a and b characteristic surface for mixes with 2.5% HL addition

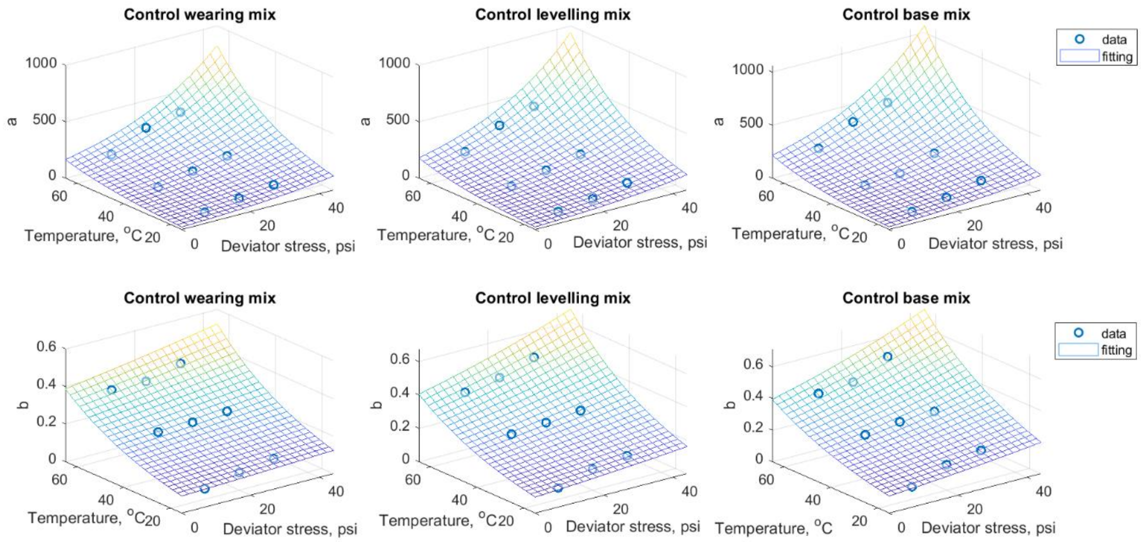

Figure 6.11 Parameter a and b characteristic surface for control mixes

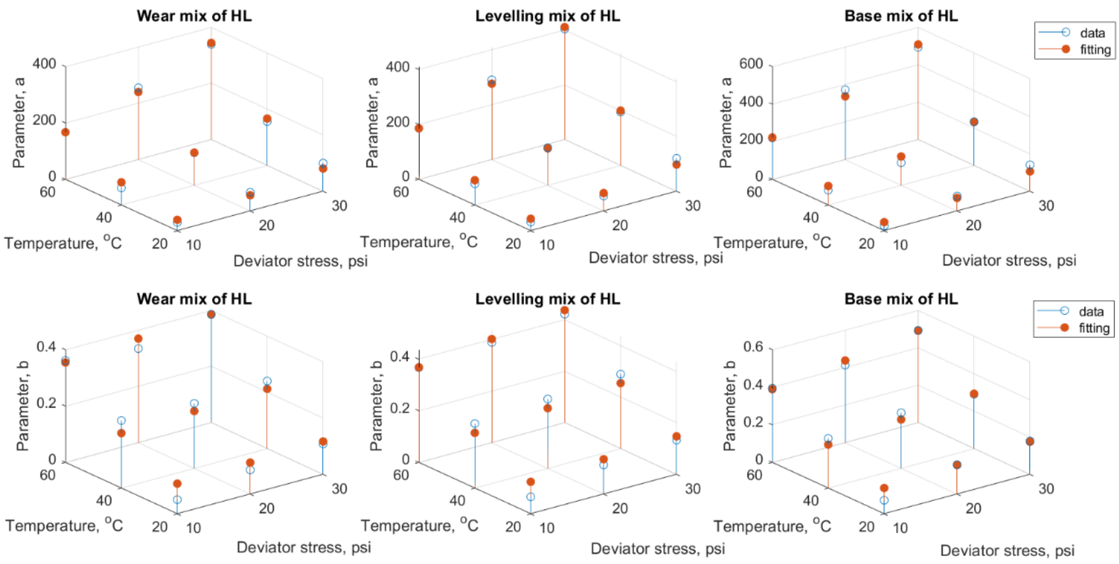

Figure 6.12 Comparison of the characteristic fitting with a and b for mixes of 2.5% HL

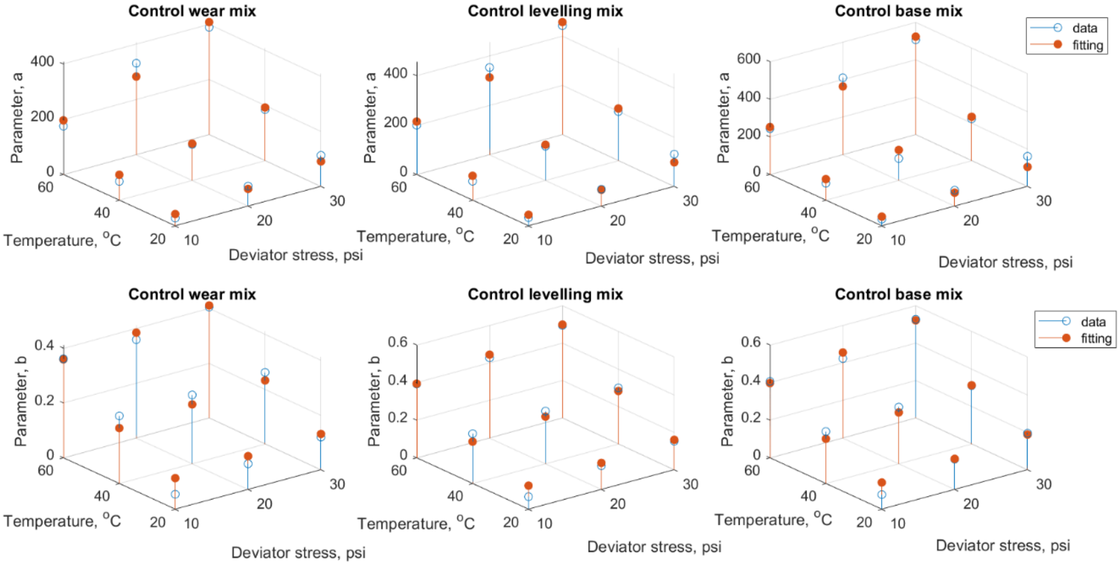

Figure 6.13 Comparison of the characteristic fitting result with the a and b data for control mixes

6.5 Modelling Case Study of Pavement Rutting Prediction

Using the material properties characterised from the triaxial test results, numerical modelling was conducted to compare the rutting resistance of pavement structures using HL modified asphalt concrete with that with no use of HL. A finite element pavement model created before (Al Ashaibi *et al.*, 2022; Wang, Al Ashaibi, Albayati and Haynes, 2022) was adopted. The mechanical and thermal boundary conditions, as illustrated in Figure 6.14, are the same as those in a study by Wang, Al Ashaibi, Albayati and Haynes, 2022). The finite element modelling results in the work of Wang, Al Ashaibi, Albayati and Haynes (2022) were used to predict permanent strain and rutting deformation of the pavement in terms of the above triaxial experiment and the parameters characterised in Table 6.5 for Equation 6-1. As rutting primarily happens under repeated traffic loading, rutting prediction is focused on the permanent deformation along the central vertical line at the middle point of the wheel load. Figure 6.15 shows the results for the principal stresses, which is defined by Equation 6-2. θ_p is the direction angle of the σ_{p1}.

$$\sigma_{p1} = \frac{1}{2}(\sigma_x + \sigma_y) + \sqrt{\tau_{xy}^2 + \frac{1}{4}(\sigma_x - \sigma_y)^2}$$ Equation (6-2a)

$$\sigma_{p2} = \frac{1}{2}(\sigma_x + \sigma_y) - \sqrt{\tau_{xy}^2 + \frac{1}{4}(\sigma_x - \sigma_y)^2}$$ Equation(6-2b)

$$\tan(2\theta_p) = \frac{2\tau_{xy}}{\sigma_x - \sigma_y}$$ Equation (6-2c)

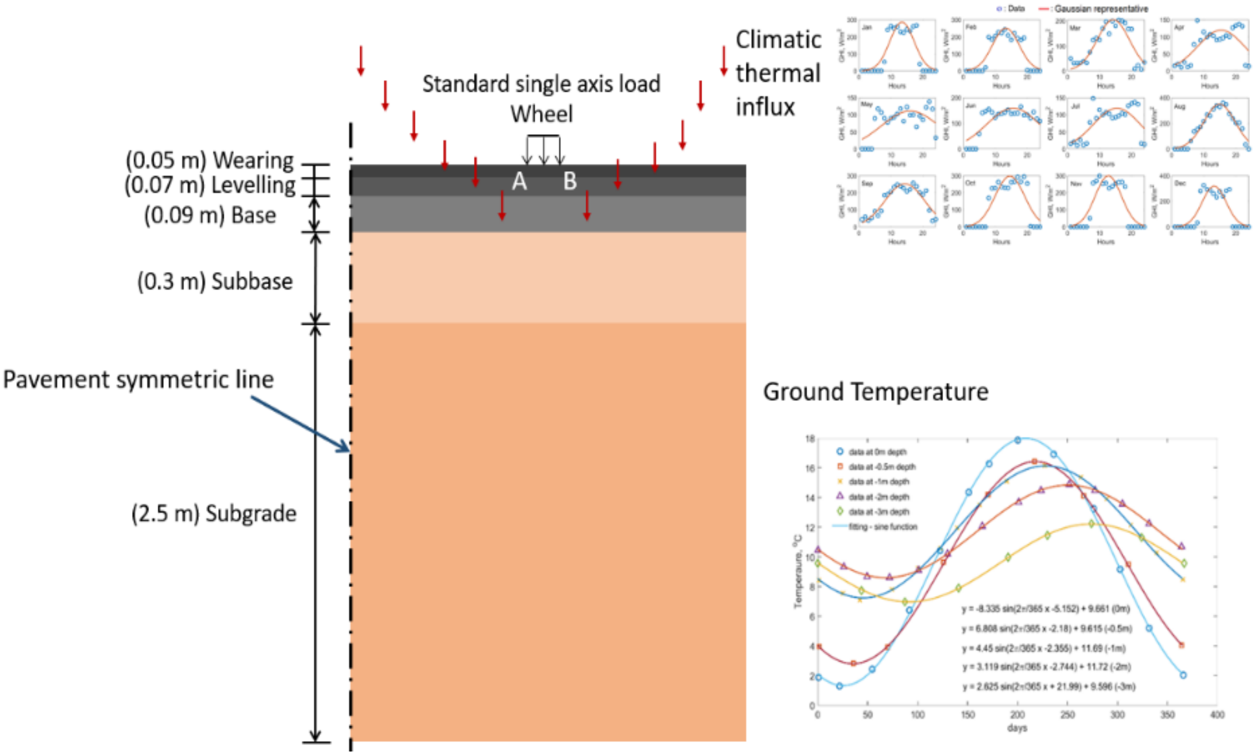

Figure 6.14 FE pavement model (Wang, Al Ashaibi, Albayati and Haynes, 2022).

Figure 6.15(a) indicates that the asphalt layers are mostly under tensile stress in the 1st principal stress direction, but in compression in the 2nd principal stress. The largest deviator stress happens at the contact points at the two sides of the wheel (A and B in Figure 6.14). Figure 6.15(b) compares the variation of deviator stress along the vertical lines under the contact point A, at four different seasonal times (Winter (720 hrs), Spring (2880 hrs), Summer (5040 hrs) and Autumn (7200 hrs)). It can be seen that temperature variation does not have much impact on deviator stress variation.

Pavement using control mixes | Pavement using 2.5% HL mixes

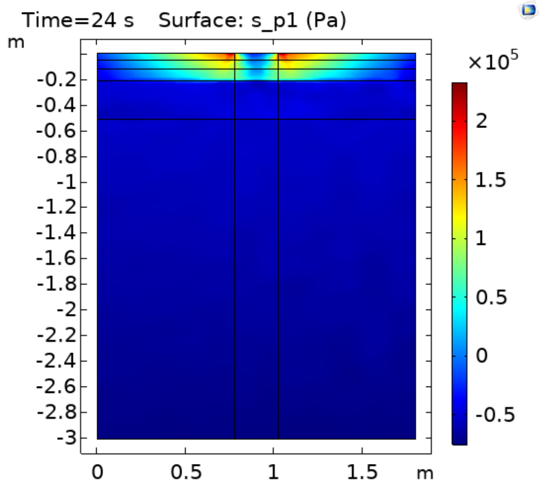

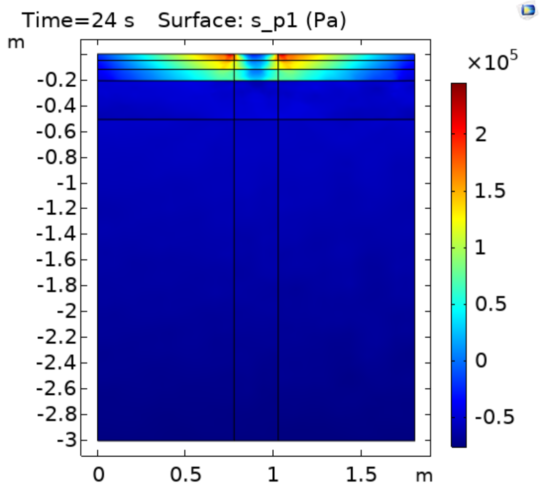

1st principal stress, σ_{p1}

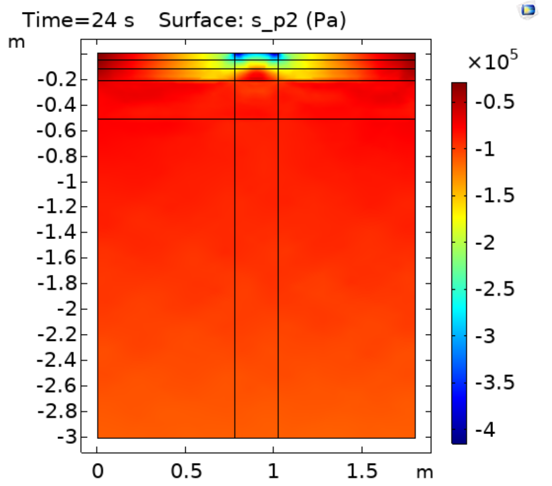

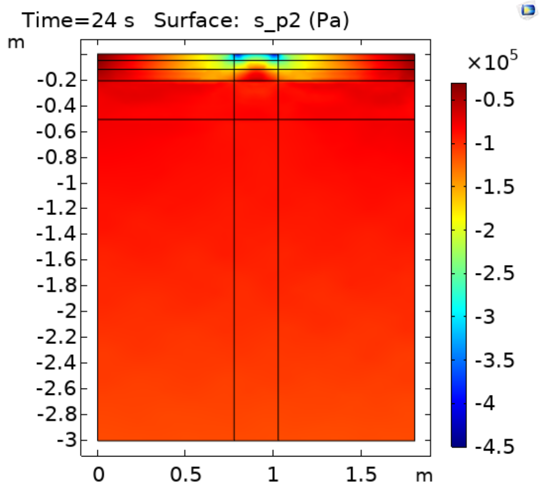

2nd principal stress, σ_{p2}

Figure 6.15 The FE modelling results of the mechanical principal stress distribution

Figure 6.16 shows the FE modelling results of the resilient deformation along the vertical line under the position A. It can be seen that the deformation in horizontal direction ux, is quite severe when the local x displacement changes direction in different climatic seasons. Such direction change of deformation will cause significant thermal fatigue, as discussed in a previous study (Al Ashaibi *et al.*, 2022). The modelling result indicates that thermal fatigue particularly influences the levelling and base layers. The comparison between the control and HL pavement shows that the structure using HL clearly has less elastic deformation and seasonal variation in both x and y direction in all layers. Particularly, using HL largely reduces the deformation in summertime (5040 hours): i.e., pavement performance in a high weather temperature condition.

avement using control mixes	Pavement using 2.5% HL mixes

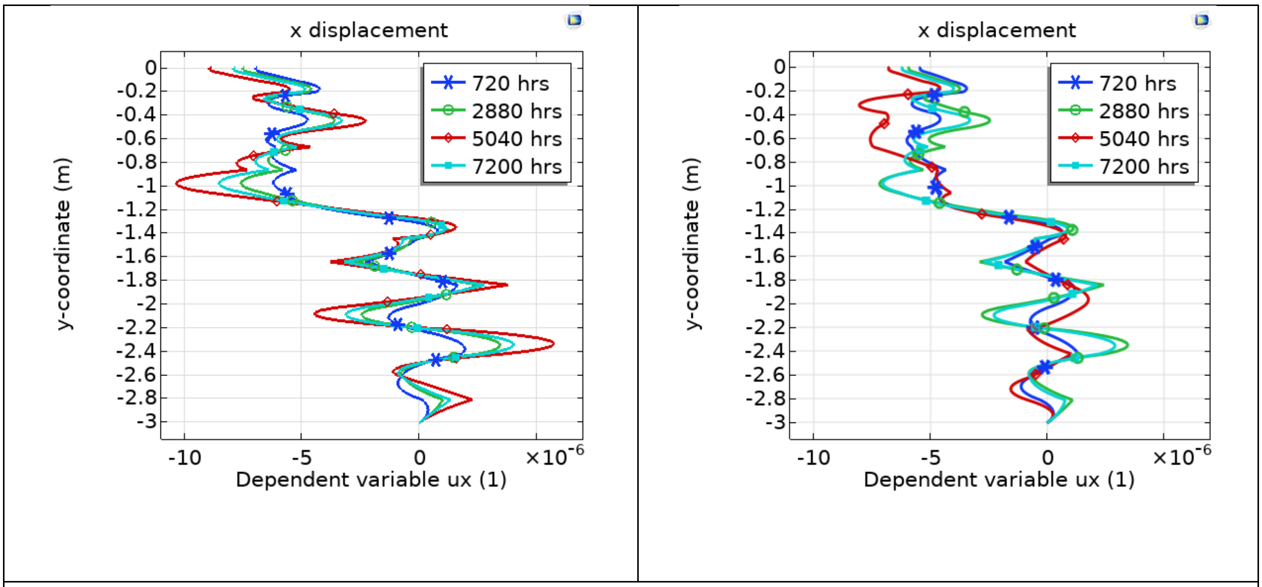

(a) Horizontal elastic displacement

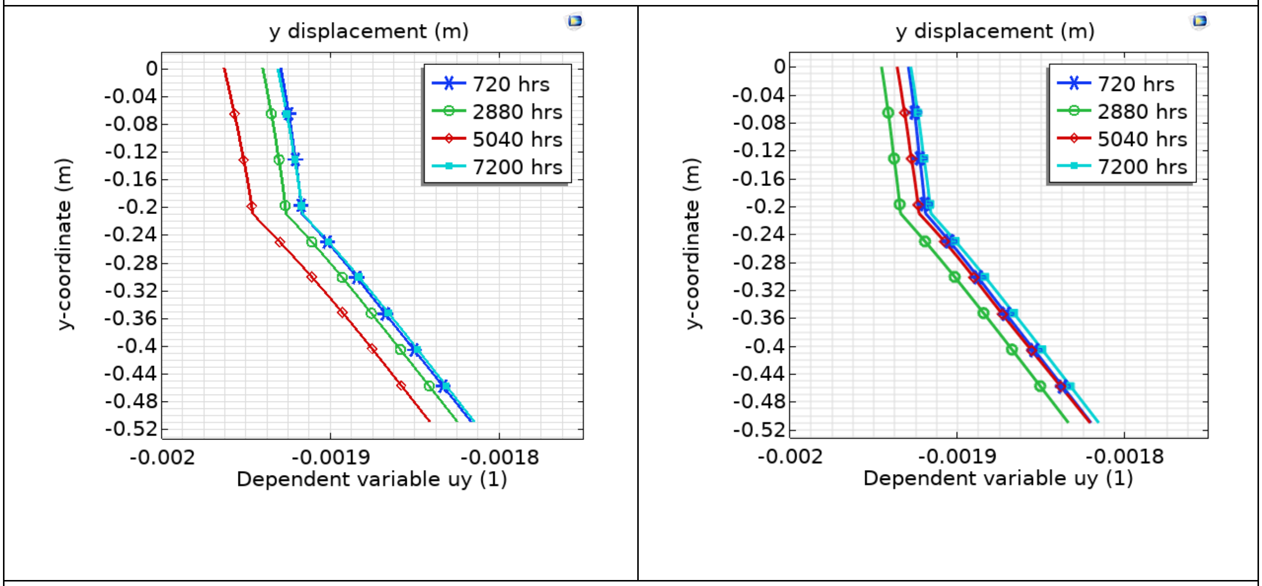

(b) Vertical elastic displacement

Figure 6.16 The FE modelling results of the resilient deformation

Figure 6.17 shows thermal stress in the asphalt and subbase layers under position A. It can be seen that HL has significant influence on thermal stress in Spring (2880 hours), which changes from compression to tensile, and Autumn (7200 hours) with increase in tensile. The thermal stress in the subbase is negligible.

<table>
<tr><th>Pavement using control mixes</th><th>Pavement using 2.5% HL mixes</th></tr>
<tr><td>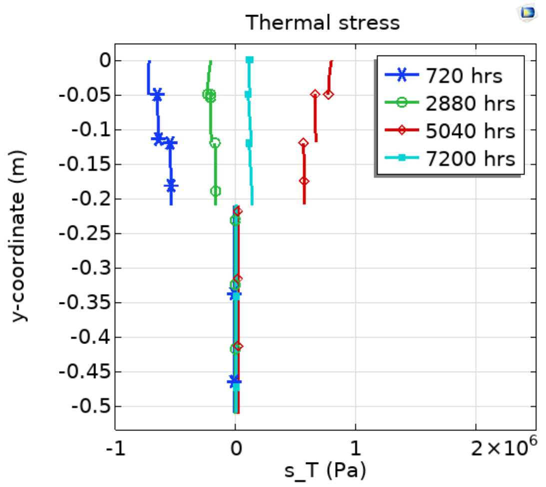
</td><td>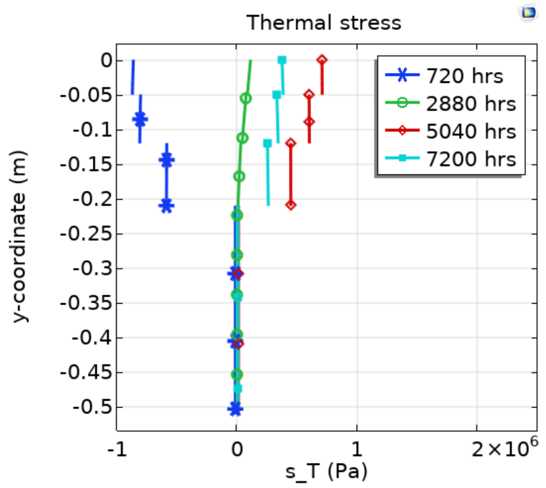
</td></tr>
</table>

Figure 6.17 Thermal stress in asphalt layers and subbase

Figure 6.18 shows the sum of the local principal stresses and thermal stress in three asphalt layers under the position A. Comparing the stress in the 1st principal direction, it is noticed that the average stress in tension conditions is less for the HL pavement across three seasons (2880, 5040 and 7200 hours). Tension condition only exist in summer (5040 hours) and autumn (7200 hours) for the pavement using no HL. For stress in compression in winter (720 hours), the HL pavement shows higher levels than the pavement with no use of HL. In the 2nd principal direction, the control pavement is in compressive state in three seasons, while the HL pavement is in this state in the Winter (720 hours) and Spring (2880 hours) only, while the compressive stress is slightly higher in winter.

Pavement using control mixes	Pavement using 2.5% HL mixes

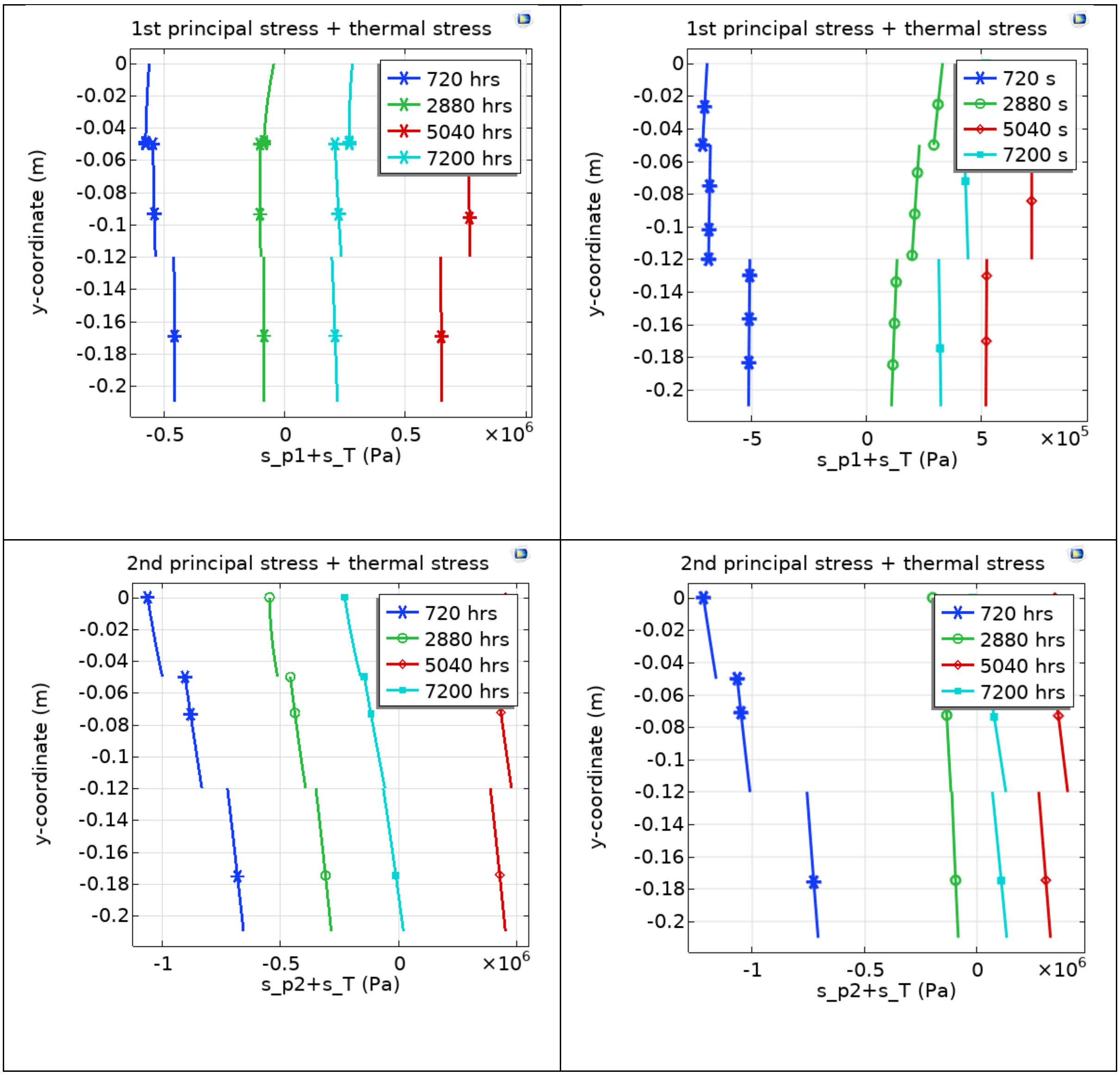

Figure 6.18 Sum of principal stresses and thermal stress

As asphalt concrete is assumed to be weak under tension states, to estimate the rutting deformation, only situations under compression are considered. The local compressive deviator stress is derived from the two principal stress directions. which are defined by Equation 6-3.

$$\sigma_{dev} = \left(\sigma_{p2} + \sigma_T\right) - \left(\sigma_{p1} + \sigma_T\right) \qquad \text{Equation (6-3)}$$

Where:

σ_{p1}, σ_{p2} and σ_T are the 1st, 2nd and thermal stresses, respectively. The σ_{dev} considers that confining stress is in the 1st principal direction. For the situation under tension, i.e., $(\sigma_{p2} + \sigma_T) > 0$ or $(\sigma_{p1} + \sigma_T) > 0$, either the loading or confining stress is taken as none. Figure 6.19 shows the deviator stress, the direction of the 1st principal stress, θ_p, and the temperature along the vertical line under position A in the range of the depth of three asphalt layers. The results indicate that deviator stress in the HL pavement is less than that in the control pavement for the two seasons Spring and Autumn. The HL pavement also has less temperature variation across the year.

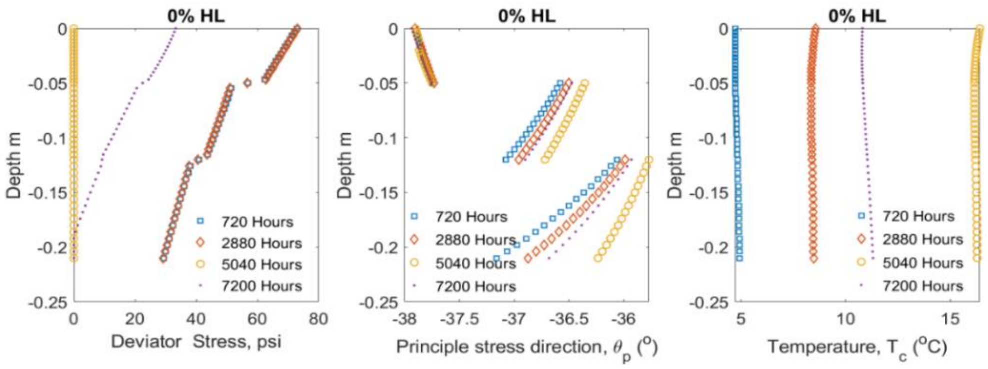

(a) Control mixes

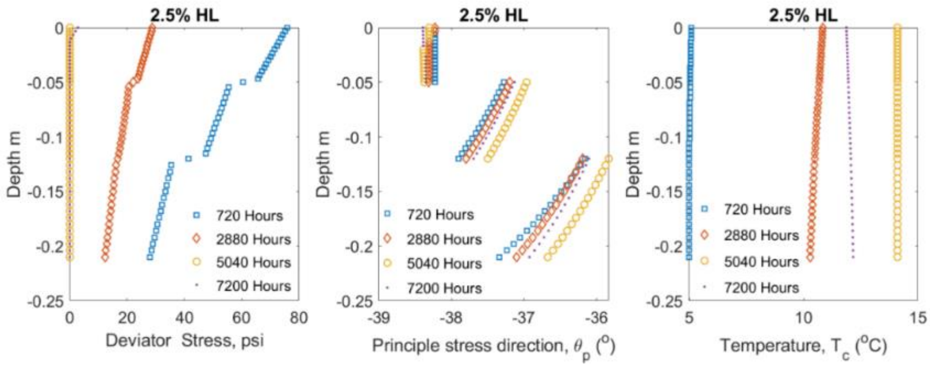

(b) 2.5% HL mixes

Figure 6.19 Deviator stress, direction of principle stress and temperature in asphalt layers under the wheel

Figure 6.20 shows the computed vertical permanent strain along the vertical line under position A, which is estimated by Equation 6-4:

$$\varepsilon_{py} = \varepsilon_p \cos(\theta_p) \qquad \text{Equation (6-4)}$$

Where:

ε_{py} stands for the vertical permanent strain,

ε_p stands for the permanent strain in the primary principal compressive direction, which is taken as σ_{p2}, and the θ_p is the 1st principal stress. ε_p is estimated using Equation 6-1 and the parameter characterization in the Table 6.5. The traffic repetition number, N, takes an assumption of 2 million equivalent single axis loads, which has been evenly allocated to the four different seasons. So, the accounted traffic repetition number is 2×N/4 for each season. The ε_{py} results in Figure 6.20 show that HL significantly reduces permanent strain in Spring and Autumn. In Winter, the HL levelling layer produces the largest permanent deformation. Finally, rutting deformation is estimated by integrating the local permanent strain along the depth under position A, i.e., $R_y = \int_{-0.21}^{0} \varepsilon_{py} dy$. The result shows that the total accumulated rutting deformation in the HL pavement is only about half of that in the control pavement.

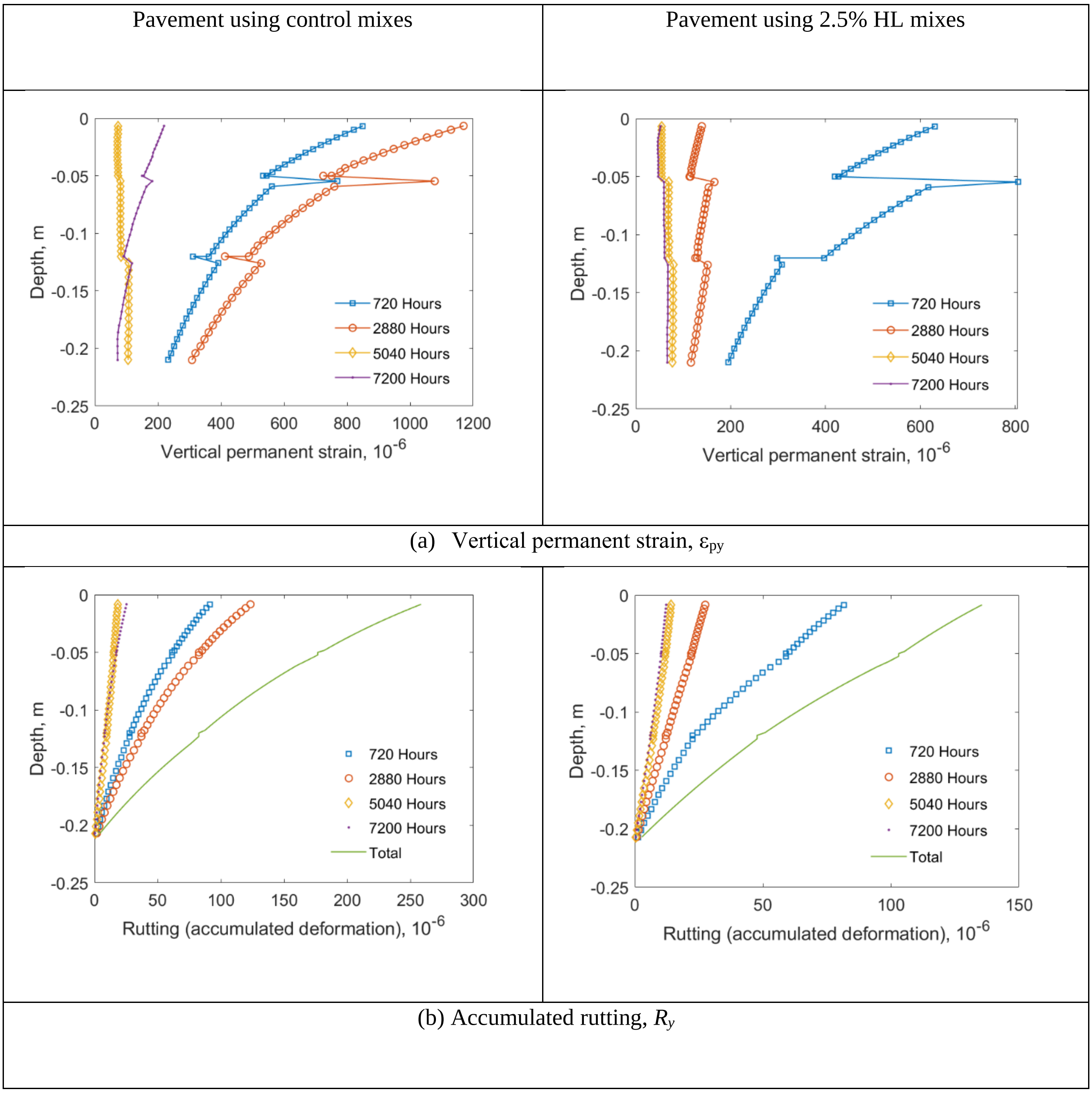

Figure 6.20 Estimated vertical permanent strain and accumulated rutting under the wheel

6.6 Conclusions

This chapter has reported research involving triaxial tests to characterise the permanent deformation of hydrated lime modified hot mix asphalt concrete mixes under complex stress conditions, and to compare these with mixes with no HL modification. Thereafter, a numerical modelling case study was conducted to compare the rutting resistance of pavements constructed using the two different types of mixes. From the study, the following conclusions can be drawn.

- HL as an additive helps the permanent resistance of HMA concrete. Its effect is particularly highly pronounced for mixes which have a higher content of total mineral filler, and accordingly, higher HL content.
- The elastic resilient modulus for fresh HMA displays a small decrease when exposed to initial hardening. This is probably due to aggregate arrangement in the asphalt matrix and the optimistic distribution of the asphalt paste between aggregates. This assumption is supported by the finding that HL addition enhances the elastic deformation resistance of mixes, particularly at higher temperatures, because HL improves the rigidity of the asphalt paste.
- The triaxial test results with respect to deviator stress and temperature conditions can be well characteristically represented using a formulated exponential mathematical model.
- The numerical modelling for coupled thermos-mechanical influence on the constructed pavements shows that HL helps reduce elastic deformation and its seasonal variation in all layers, which benefits fatigue resistance. In addition, the HL pavement has less annual average compressive stress deviation in two principal stress directions.
- The numerical modelling using the permanent deformation model based on the triaxial tests has demonstrated that using a 2.5% HL addition to modify the asphalt mixes designed for different pavement layers, the constructed pavement has almost halved the rutting deformation in the created case study setting in specific geo-climatic conditions.
- The rutting assessment in the study only provides an approximate estimation. However, the model and methodology proposed in this study can be further implemented together with adaptive mesh technology to provide more accurate analysis for pavement rutting deformation.

CHAPTER 7 - CONCLUSIONS AND RECOMMENDATIONS

Based on the materials studied, the tests conducted, and examination of the findings and numerical models, various conclusions are drawn, leading to recommendations and directions for further investigation.

7.1 Conclusions

In conclusion, this comprehensive study has provided compelling evidence regarding the effectiveness of hydrated lime as an additive in asphalt concrete mixes. The incorporation of hydrated lime at a 2.5% ratio, partially replacing limestone dust, has yielded significant enhancements in the performance of asphalt concrete pavements. The findings from experiments and numerical models have shed light on various aspects of this topic, leading to the following notable conclusions:

Thermal Characteristics:

- The substitution of 2.5% limestone dust with hydrated lime has resulted in improved thermal properties of asphalt concrete.
- Significant increases in thermal conduction (27%, 7%, and 0.17%) and specific heat (25%, 6%, and 0.16%) have been observed in wearing, levelling, and base mixes, respectively.
- The optimal proportion of mineral filler and its association with thermal characteristics were not found to be correlated in the mixes containing hydrated lime.
- Negligible differences in local temperatures and thermal stress-strain profiles were observed between hydrated lime-modified and unmodified pavement mixes.

Fatigue Performance and Climate Effects:

- Hydrated lime modification, specifically replacing 2.5% limestone filler, has demonstrated favourable changes in the fatigue life of asphalt concrete mixtures across various temperature conditions.

- A numerical model considering climate effects showcased significant variations in thermomechanical strain between hydrated lime-modified and unmodified pavements, with different susceptibility to fatigue deterioration in cold and hot seasons.
- Hydrated lime-modified pavements exhibited improved durability under coupled thermomechanical loads, making them highly advantageous for long-term performance.

Rutting Resistance and Permanent Deformation:

- The addition of hydrated lime in hot mix asphalt concrete has contributed to permanent resistance against rutting, particularly in mixtures with higher mineral filler content and increased hydrated lime content.
- Elastic resilient modulus and displacement under initial hardening exposure were effectively controlled by hydrated lime, making the asphalt more resistant to elastic deformation, especially in elevated temperatures.
- Mathematical modelling based on triaxial testing accurately characterized the impact of temperature and deviator stress on the mixture.
- Hydrated lime played a crucial role in reducing elastic deformation and promoting uniformity across seasons, thus enhancing fatigue resistance in layered pavements.
- The implementation of 2.5% hydrated lime in each layer of asphalt mixture resulted in a substantial reduction (nearly 50%) in rutting deformation for a given climate condition, as demonstrated by the numerical model.

In summary, the findings underscore the remarkable benefits of incorporating hydrated lime in asphalt concrete mixes. The study's comprehensive approach, integrating experiments, numerical models, and advanced analytical techniques, has contributed to a deeper understanding of the complex interplay between materials, climate effects, and mechanical performance in pavements. This research offers valuable insights for the design and construction of more resilient, fatigue-resistant, and rutting-resistant asphalt concrete pavements, ultimately leading to reduced maintenance efforts and costs.

7.2 Recommendations for Future Study

The results and conclusions from this research point to the need for future research which addresses further related areas, as follows:

1 – Investigate rheology-related material properties, including stress-strain against thermoviscoelastic properties and thermoviscoelastic properties.

2 - Investigate dynamic behaviours and responses across a range of temperatures (stress-strain properties-kinetic Harding).

3 - Thermal aging.

4 - While this research involved 2D analysis of asphalt concrete pavements, this could be examined in 3 dimensions in further work.

5 - Investigate the impact of HL additions on vulnerability to moisture and study the impact of various factors such as aging processes, the freeze-thaw cycle, degradation from moisture, and healing.

6 - Future work is needed to test asphalt concrete damage behaviours in the field based on variables from the environment. Moreover, monitoring of thermal fatigue could be done by applying laboratory-based acoustic emissions tests across various cycles on temperature-conditioned specimens.

7 - Future thermomechanical studies may be required to identify optimal thicknesses for AC pavements in relation to the impact of HL additions combined with various further additives, such as carbon fibre and aluminium, with various kinds of aggregates, asphalt cement and mineral fill.

REFERENCES

AASHTO (1993) 'Guide for Design of Pavement Structures, American Association of State Highway and Transportation Officials. Washington, D.C., USA.', in.

Abdi, A. *et al.* (2021) 'Economic analysis based on the unit weight of hot mix asphalt', *Engineering Solid Mechanics*, 9(1), pp. 93–100.

Acharya, T., Riehl, B. and Fuchs, A. (2021) 'Effects of albedo and thermal inertia on pavement surface temperatures with convective boundary conditions—A CFD Study', *Processes*. Multidisciplinary Digital Publishing Institute, 9(11), p. 2078.

Adlinge, S. S. and Gupta, A. K. (2013) 'Pavement deterioration and its causes', *International Journal of Innovative Research and Development*, 2(4), pp. 437–450.

Al-Abdul Wahhab, H. I. and Balghunaim, F. A. (1994) 'Asphalt pavement temperature related to arid Saudi environment', *Journal of materials in civil engineering*. American Society of Civil Engineers, 6(1), pp. 1–14.

Al-Bayati, H. K. A., Oyeyi, A. G. and Tighe, S. L. (2020) 'Experimental assessment of mineral filler on the volumetric properties and mechanical performance of HMA mixtures', *Civil Engineering Journal*, 6(12), pp. 2312–2331.

Al-Marafi, M. N. I. (2021) 'Effects of Hydrated Lime on Moisture Susceptibility of Asphalt Concrete', *Advances in Science and Technology. Research Journal*. Polish Society of Ecological Engineering (PTIE), 15(2), pp. 13–17.

Al-Ostaz, A. (2007) *Effect of moisture content on the coefficient of thermal expansion of concrete*. Mississippi. Dept. of Transportation.

Al-Qadi, I. L., Elseifi, M. A. and Yoo, P. J. (2005) 'Characterization of pavement damage due to different tire configurations', *Journal of the Association of Asphalt Paving Technologists*, 74, pp. 921–962.

Al-Qadi, I. L., Hassan, M. M. and Elseifi, M. A. (2005) 'Field and theoretical evaluation of thermal fatigue cracking in flexible pavements', *Transportation research record*. SAGE Publications Sage CA: Los Angeles, CA, 1919(1), pp. 87–95.

Al-Suhaibani, A., Al-Mudaiheem, J. and Al-Fozan, F. (1992) ‘Effect of filler type and content on properties of asphalt concrete mixes’, *Effects of aggregates and mineral fillers on asphalt mixture performance*. American Society for Testing and Materials, Philadelphia, Pa, pp. 107–124.

Al-Tameemi, A. F. *et al.* (2019) ‘Moisture Susceptibility and Fatigue Performance of Hydrated Lime–Modified Asphalt Concrete: Experiment and Design Application Case Study’, *Journal of Materials in Civil Engineering*. American Society of Civil Engineers, 31(4), p. 4019019.

Al-Tameemi, A. F. M. (2017) *Implementation of mechanistic-empirical approach for structural design of hydrated lime modified flexible pavement*. University of Salford (United Kingdom).

Al-Tameemi, A. F., Wang, Y. and Albayati, A. (2016) ‘Experimental study of the performance related properties of asphalt concrete modified with hydrated lime’, *Journal of Materials in Civil Engineering*. American Society of Civil Engineers, 28(5), p. 4015185.

Alae, M. *et al.* (2020) ‘Effects of layer interface conditions on top-down fatigue cracking of asphalt pavements’, *International Journal of Pavement Engineering*. Taylor & Francis, 21(3), pp. 280–288.

Alavi, M. Z., Pouranian, M. R. and Hajj, E. Y. (2014) ‘Prediction of asphalt pavement temperature profile with finite control volume method’, *Transportation Research Record*. SAGE Publications Sage CA: Los Angeles, CA, 2456(1), pp. 96–106.

Anandakumar, K. (1999) ‘A study on the partition of net radiation into heat fluxes on a dry asphalt surface’, *Atmospheric Environment*. Elsevier, 33(24–25), pp. 3911–3918.

Andersland, O. B. and Ladanyi, B. (2004) ‘Frozen ground engineering. Hoboken’. New Jersey: John Wiley and Sons, Inc.

Anderson, K. O. and Epps, J. A. (1983) *Asphalt concrete factors related to pavement cracking in west Texas*. Texas Transportation Institute, Texas A & M University System.

Angela L. P, K. (2006) *Methodology and calibration of fatigue transfer functions for mechanistic empirical flexible pavement design*.

Annaratone, D. (2010) *Engineering heat transfer*. Springer Science & Business Media.

Arangi, S. R. and Jain, R. K. (2015) ‘Review paper on pavement temperature prediction model for Indian climatic condition’, *Int. J. of Innovative Research in Adv. Engineering*, 2(8), pp. 1–9.

Ariawan, I. M. A., Subagio, B. S. and Setiadji, B. H. (2015) ‘Development of asphalt pavement temperature model for tropical climate conditions in West Bali region’, *Procedia Engineering*. Elsevier, 125, pp. 474–480.

Asefzadeh, A., Hashemian, L. and Bayat, A. (2017) ‘Development of statistical temperature prediction models for a test road in Edmonton, Alberta, Canada’, *International Journal of Pavement Research and Technology*. Elsevier, 10(5), pp. 369–382.

Al Ashaibi, A. *et al.* (2022) ‘Thermal properties of hydrated lime-modified asphalt concrete and modelling evaluation for their effect on the constructed pavements in service’, *Sustainability*. MDPI, 14(13), p. 7827.

Bagampadde, U., Isacsson, U. and Kiggundu, B. M. (2004) ‘Classical and contemporary aspects of stripping in bituminous mixes’, *Road materials and pavement design*. Taylor & Francis, 5(1), pp. 7–43.

Bahia, H., Tabatabaee, H. and Velasquez, R. (2012) ‘Asphalt thermal cracking analyser (ATCA)’, in *7th RILEM international conference on cracking in pavements*. Springer, pp. 147–156.

Baig, M. G. and Wahhab, H. I. A.-A. (1998) ‘Mechanistic evaluation of hedmanite and lime modified asphalt concrete mixtures’, *Journal of Materials in Civil Engineering*. American Society of Civil Engineers, 10(3), pp. 153–160.

Barber, E. S. (1957) ‘Calculation of maximum pavement temperatures from weather reports’, *Highway Research Board Bulletin*, (168).

Bari, J. and Witczak, M. W. (2005) ‘Evaluation of the effect of lime modification on the dynamic modulus stiffness of hot mix asphalt: use with the new mechanistic–empirical pavement design guide’, *Transportation Research Record*. SAGE Publications Sage CA: Los Angeles, CA, 1929(1), pp. 10–19.

Barksdale, R. D. (1972) 'Laboratory evaluation of rutting in base course materials', in *Presented at the Third International Conference on the Structural Design of Asphalt Pavements, Grosvenor House, Park Lane, London, England, Sept. 11-15, 1972.*

Basu, A., Marasteanu, M. O. and Hesp, S. A. M. (2003) 'Time-temperature superposition and physical hardening effects in low-temperature asphalt binder grading', *Transportation research record*. SAGE Publications Sage CA: Los Angeles, CA, 1829(1), pp. 1–7.

Baus, R. L. and Stires, N. R. (2010) *Mechanistic-empirical pavement design guide implementation*. University of South Carolina. Dept. of Civil & Environmental Engineering.

Bayat, A. and Knight, M. A. (2010) *Measurement and analysis of flexible pavement thermal-induced strains*.

Bentz, D. P. (2000) 'A computer model to predict the surface temperature and time-of-wetness of concrete pavements and bridge decks'.

Berdahl, P. and Fromberg, R. (1982) 'The thermal radiance of clear skies', *Solar energy*. Elsevier, 29(4), pp. 299–314.

Bergman, P. *et al.* (2011) 'Detection of interstellar hydrogen peroxide', *Astronomy & Astrophysics*. EDP Sciences, 531, p. L8.

Berrang-Ford, L., Pearce, T. and Ford, J. D. (2015) 'Systematic review approaches for climate change adaptation research', *Regional Environmental Change*. Springer, 15(5), pp. 755–769.

Blažek, J. *et al.* (2000) 'Effect of hydrated lime addition on properties of asphalt'.

Bolton, M. D. (1986) 'The strength and dilatancy of sands', *Geotechnique*. Thomas Telford Ltd, 36(1), pp. 65–78.

Bonaquist, R. F. (2012) *Evaluation of Flow Number (FN) as a discriminating HMA mixture property*. Wisconsin Highway Research Program.

Bouron, S. *et al.* (2021) 'Improving the durability of asphalt mixtures with hydrated lime: Field results from highway A84', *Case Studies in Construction Materials*. Elsevier, 14, p. e00551.

Brovelli, C. *et al.* (2014) 'Assessment of fatigue resistance of additivated asphalt concrete incorporating fibers and polymers', *Journal of materials in civil engineering*. American Society of Civil Engineers, 26(3), pp. 554–558.

Busby, J. (2015) 'UK shallow ground temperatures for ground coupled heat exchangers', *Quarterly Journal of Engineering Geology and Hydrogeology*. Geological Society of London, 48(3–4), pp. 248–260.

Byzyka, J., Rahman, M. and Chamberlain, D. A. (2021) 'A laboratory investigation on thermal properties of virgin and aged asphalt mixture', *Construction and Building Materials*. Elsevier, 305, p. 124757.

Carlson, J. D., Bhardwaj, R., Phelan, P. E., Kaloush, K. E., and Golden, J. S. (2010) 'Determining Thermal Conductivity of Paving Materials Using Cylindrical Sample Geometry. Journal of Materials in Civil Engineering, 22(2), 186–195. doi.org/10.1061/(ASCE)0899-1561(2010)22:2(186).'

Carpenter, S. H. (1983) *Thermal cracking in asphalt pavements: an examination of models and input parameters*. US Army Corps of Engineers, Engineer Research and Development Center, Cold ….

Carpenter, S. H. and Lytton, R. L. (1977) *Thermal Pavement Cracking in West Texas*. Texas Transportation Institute, Texas A & M University.

Carpenter, S. H., Lytton, R. L. and Epps, J. A. (1974) *Environmental Factors Relevant to Pavement Cracking in West Texas*. Texas Transportation Institute, Texas A & M University.

Cengel, Y. and Heat, T. M. (2003) *A practical approach*. New York, NY, USA: McGraw-Hill.

Cerni, G. *et al.* (2017) 'Correlation between asphalt mixture stiffness determined through static and dynamic indirect tensile tests', *Arabian Journal for Science and Engineering*. Springer, 42(3), pp. 1295–1303.

Chachas, C. V (1971) 'Use of Hydrated Lime in Bituminous Mixtures to Decrease Hardness of the Asphalt Cement'.

Chadbourn, B. A. *et al.* (1996) 'Consideration of hot mix asphalt thermal properties during compaction', in *Quality management of hot mix asphalt*. ASTM International.

Chadbourn, B. A. *et al.* (1998) 'An asphalt paving tool for adverse conditions'.

Chao, J. and Jinxi, Z. (2018) 'Prediction model for asphalt pavement temperature in high-temperature season in Beijing', *Advances in Civil Engineering*. Hindawi, 2018.

Chatti, K., Salama, H. and El Mohtar, C. (2004) 'Effect of heavy trucks with large axle groups on asphalt pavement damage', in *Proceedings 8th International Symposium on Heavy Vehicle Weights and Dimensions*.

Chen, J. *et al.* (2014) 'Solution of pavement temperature field in "Environment-Surface" system through Green's function', *Journal of Central South University*. Springer, 21(5), pp. 2108–2116.

Chen, J., Wang, H. and Xie, P. (2019) 'Pavement temperature prediction: Theoretical models and critical affecting factors', *Applied Thermal Engineering*. Elsevier, 158, p. 113755.

Chen, J., Wang, H. and Zhu, H. (2017) 'Analytical approach for evaluating temperature field of thermal modified asphalt pavement and urban heat island effect', *Applied Thermal Engineering*. Elsevier, 113, pp. 739–748.

Cheng, H. *et al.* (2020) 'Experimentally based parameters applied to concrete damage plasticity model for strain hardening cementitious composite in sandwich pipes', *Materials and Structures*. Springer, 53(4), pp. 1–17.

Chintakunta, S. R. (2007) 'Sensitivity of thermal properties of pavement materials using mechanistic-empirical pavement design guide'. Digital Repository@ Iowa State University, http://lib. dr. iastate. edu/.

Chong, W., Tramontini, R. and Pivoto Specht, L. (2009) 'Application of the Laplace transform and its numerical inversion to temperature profile of a two-layer pavement under site conditions', *Numerical Heat Transfer, Part A: Applications*. Taylor & Francis, 55(11), pp. 1004–1018.

Christison, J. T. and Anderson, K. O. (1972) 'The response of asphalt pavements to low temperature climatic environments', in *Presented at the Third International Conference on the Structural Design of Asphalt Pavements, Grosvenor House, Park Lane, London, England,* *Sept. 11-15, 1972*.

CivilWeb Spreadsheets - Engineering Calculations & Spreadsheets - Equivalent Single Wheel Load (no date). Available at: https://civilweb-spreadsheets.com/road-pavement-design/equivalent-single-wheel-load/.

Claessen, A. I. M. *et al.* (1977) 'Asphalt pavement design--the shell method', in *Volume I of proceedings of 4th International Conference on Structural Design of Asphalt Pavements, Ann Arbor, Michigan, August 22-26, 1977*.

Corlew, J. S. (1968) 'Methods for calculating temperature profiles of hot mix asphalt concrete as related to the construction of asphalt pavements'. Colorado School of Mines.

Crevier, L.-P. and Delage, Y. (2001) 'METRo: A new model for road-condition forecasting in Canada', *Journal of applied meteorology*, 40(11), pp. 2026–2037.

Crompton, T. R. (2006) *Polymer reference book*. iSmithers Rapra Publishing.

Das, A. K. and Singh, D. (2021) 'Evaluation of fatigue performance of asphalt mastics composed of nano hydrated lime filler', *Construction and Building Materials*. Elsevier, 269, p. 121322.

Dave, E. V and Hoplin, C. (2015) 'Flexible pavement thermal cracking performance sensitivity to fracture energy variation of asphalt mixtures', *Road Materials and Pavement Design*. Taylor & Francis, 16(sup1), pp. 423–441.

Dawson, A. (2008) *Water in road structures: movement, drainage & effects*. Springer Science & Business Media.

Dawson, A. *et al.* (2014) 'Energy harvesting from pavements', in *Climate Change, Energy, Sustainability and Pavements*. Springer, pp. 481–517.

Dawson, A. and Kolisoja, P. (2006) 'Managing rutting in low volume roads', *An Executive summary of study conducted by European Union.< http://www. roadex. org/..../Managing% 20Rutting_English. pdf>(Mar. 28, 2012)*.

Dempsey, B. J. (1969) *A Heat-transfer Model for Evaluating Frost Action and Temperature Related Effects in Multilayered Pavement Systems*. University of Illinois at Urbana-Champaign.

Dempsey, B. J., Herlache, W. A. and Patel, A. J. (1986) *Climatic-materials-structural pavement analysis program*.

Diao, H. *et al.* (2023) 'Multiscale Fatigue Performance Evaluation of Hydrated Lime and Basalt Fiber Modified Asphalt Mixture', *Materials*. MDPI, 16(10), p. 3608.

Diefenderfer, B. K. (2002) *Moisture content determination and temperature profile modeling of flexible pavement structures*. Virginia Polytechnic Institute and State University.

Diefenderfer, B. K., Al-Qadi, I. L. and Diefenderfer, S. D. (2006) 'Model to predict pavement temperature profile: development and validation', *Journal of Transportation Engineering*. American Society of Civil Engineers, 132(2), pp. 162–167.

Ding, H., Qiu, Y. and Rahman, A. (2020) 'Influence of thermal history on the intermediate and low-temperature reversible aging properties of asphalt binders', *Road Materials and Pavement Design*. Taylor & Francis, 21(8), pp. 2126–2142.

Domaschuk, L., Skarsgard, P. S. and Christianson, R. H. (1964) 'Cracking of Asphalt Pavements Due to Thermal Contraction', *Canadian Good Roads Association Proc*.

Dongré, R., D'Angelo, J. and Copeland, A. (2009) 'Refinement of flow number as determined by asphalt mixture performance tester: Use in routine quality control–quality assurance practice', *Transportation Research Record*. SAGE Publications Sage CA: Los Angeles, CA, 2127(1), pp. 127–136.

Du, C. *et al.* (2021) 'Coupled Thermomechanical Damage Behavior Analysis of Asphalt Pavements Using a 2D Mesostructure-Based Finite-Element Method', *Journal of Transportation Engineering, Part B: Pavements*. American Society of Civil Engineers, 147(2), p. 4021012.

Du, Y. *et al.* (2018) 'A review on solutions for improving rutting resistance of asphalt pavement and test methods', *Construction and Building Materials*. Elsevier, 168, pp. 893–905.

El-Maaty, A. E. A. (2017) 'Temperature change implications for flexible pavement performance and life', *International Journal of Transportation Engineering and Technology*. Science Publishing Group, 3(1), pp. 1–11.

Elnasri, M., Airey, G. and Thom, N. (2013) ‘Experimental investigation of bitumen and mastics under shear creep and creep-recovery testing’, in *Airfield and highway pavement 2013: Sustainable and efficient pavements*, pp. 921–932.

Elnasri, M., Thom, N. and Airey, G. (2016) ‘Experimental Study of Binder–Filler Interaction Using the Modified Multiple Stress–Strain Creep Recovery Test’, *Materials and Infrastructures 1*. Wiley Online Library, 5, pp. 87–100.

Engineering ToolBox (2016) ‘Solids – Specific Heats. www.engineeringtoolbox.com/specific-heat-solids-d_154.html.’

Epps, A. L. (1999) ‘An approach to examine thermal fatigue in asphalt concrete’, *Journal of the association of asphalt paving technologists*, 68.

Fabb, T. R. J. (1974) ‘The influence of mix composition, binder properties and cooling rate on asphalt cracking at low temperatures’, in *Association of Asphalt Paving Technologists Proc*.

Fan, J. *et al.* (2022) ‘Investigation on triaxial numerical test method and dilatancy behavior of asphalt mixture’, *Construction and Building Materials*. Elsevier, 316, p. 125815.

Farouki, O. T. (1982) ‘Thermal properties of soils relevant to ground freezing. Design techniques for their estimation’, in *In CRREL Proc. of the 3d Intern. Symp. on Ground Freezing*, pp. 139–146.

Fedrigo, W. *et al.* (2018) ‘A study on the resilient modulus of cement-treated mixtures of RAP and aggregates using indirect tensile, triaxial and flexural tests’, *Construction and Building Materials*. Elsevier, 171, pp. 161–169.

Feng, X.-T. *et al.* (2018) ‘A novel true triaxial apparatus for studying the time-dependent behaviour of hard rocks under high stress’, *Rock Mechanics and Rock Engineering*. Springer, 51(9), pp. 2653–2667.

Gabet, T. *et al.* (2011) ‘French wheel tracking round robin test on a polymer modified bitumen mixture’, *Materials and structures*. Springer, 44(6), pp. 1031–1046.

Garber, N. J. and Hoel, L. A. (2008) *Traffic & highway engineering*. Cengage Learning.

Garbowski, T. and Gajewski, T. (2017) ‘Semi-automatic inspection tool of pavement condition from three-dimensional profile scans', *Procedia Engineering*. Elsevier, 172, pp. 310–318.

Garbowski, T. and Pożarycki, A. (2017) 'Multi-level back calculation algorithm for robust determination of pavement layers parameters', *Inverse Problems in Science and Engineering*. Taylor & Francis, 25(5), pp. 674–693.

Gedafa, D. S., Hossain, M. and Romanoschi, S. A. (2014) 'Perpetual pavement temperature prediction model', *Road materials and pavement design*. Taylor & Francis, 15(1), pp. 55–65.

Gerritsen, A. H. and Jongeneel, D. J. (1988) 'Fatigue properties of asphalt mixes under conditions of very low loading frequencies', in *Association of Asphalt Paving Technologists Technical Sessions, 1988, Williamsburg, Virginia, USA.*

Ghayoomi, M., Dave, E. and Mousavi, S. (no date) 'Mechanistic Load Restriction Decision Platform for Pavement Systems Prone to Moisture Variations'.

Grabowski, W. and Wilanowicz, J. (1997) 'Struktura wypełniaczy wapiennych a ich właściwości usztywniające w zaczynach asfaltowych', *Drogownictwo,* (12), pp. 378–382.

Grabowski, W., Wilanowicz, J. and Sobol, T. (2009) 'Structural and functional properties of mineral fillers modified with hydrated lime', in *Sixth International Conference on Maintenance and Rehabilitation of Pavements and Technological Control (MAIREPAV6) International Society for Maintenance and Rehabilitation of Transportation Infrastructure Transportation Research Board*.

Gui, J. *et al.* (2007) 'Impact of pavement thermophysical properties on surface temperatures', *Journal of materials in civil engineering*. American Society of Civil Engineers, 19(8), pp. 683–690.

Guo, R. and Nian, T. (2020) 'Analysis of factors that influence anti-rutting performance of asphalt pavement', *Construction and Building Materials*. Elsevier, 254, p. 119237.

Hall, M. R. *et al.* (2012) 'Influence of the thermophysical properties of pavement materials on the evolution of temperature depth profiles in different climatic regions', *Journal of materials in civil engineering*. American Society of Civil Engineers, 24(1), pp. 32–47.

Han, D. *et al.* (2018) 'Dynamic simulation analysis of the tire-pavement system considering temperature fields', *Construction and Building Materials*. Elsevier, 171, pp. 261–272.

Hanson, D. I., Graves, R. E. and Brown, E. R. (1994) 'Laboratory evaluation of the addition of lime treated sand to hot mix asphalt', *Transportation Research Record*, (1469).

Hassan, H. F. *et al.* (2008) 'Development of asphalt binder performance grades for Omani climate', *Construction and Building Materials*. Elsevier, 22(8), pp. 1684–1690.

Hassn, A. *et al.* (2016) 'Effect of air voids content on thermal properties of asphalt mixtures', *Construction and Building Materials*. Elsevier, 115, pp. 327–335.

Helwany, S., Dyer, J. and Leidy, J. (1998) 'Finite-element analyses of flexible pavements', *Journal of Transportation Engineering*. American Society of Civil Engineers, 124(5), pp. 491–499.

Herb, W. *et al.* (2009) 'Simulation and characterization of asphalt pavement temperatures', *Road materials and pavement design*. Taylor & Francis, 10(1), pp. 233–247.

Hermansson, Å. (2001) 'Mathematical model for calculation of pavement temperatures: comparison of calculated and measured temperatures', *Transportation Research Record*. SAGE Publications Sage CA: Los Angeles, CA, 1764(1), pp. 180–188.

Hermansson, Å. (2004) 'Mathematical model for paved surface summer and winter temperature: comparison of calculated and measured temperatures', *Cold regions science and technology*. Elsevier, 40(1–2), pp. 1–17.

Hesami, S. *et al.* (2013) 'Evaluate the mechanism of the effect of hydrated lime on moisture damage of warm mix asphalt', *Construction and Building Materials*. Elsevier, 47, pp. 935–941.

Hicks, R. G., & Scholz, T. V (2003) 'Life cycle costs for lime in hot mix asphalt (Vol. 3). Arlington, VA: National Lime Association. Retrieved from http://www.lime.org/LCCA/ LCCA_Vol_I.pdf, http://www.lime.org/LCCA/LCCA_Vol_II.pdf, http://www.lime.org/ LCCA/LCCA_Vol_III.pdf.'

Hicks, R. G. (1991) *Moisture damage in asphalt concrete*. Transportation Research Board.

Highter, W. (1984) 'Thermal properties of some asphaltic concrete mixes', in *International Air Transportation Conference*, p. 1598.

Hildebrand, E. E. (1986) ‘Prediction of thaw settlement and surface roughness for highways in permafrost areas.’

Hiller, J. (2011) ‘Field evaluation of built-in curling levels in rigid pavements’, *Minnesota Department of Transportation, Minnesota, USA*.

Hiller, J. E. and Roesler, J. R. (2010) ‘Simplified nonlinear temperature curling analysis for jointed concrete pavements’, *Journal of Transportation Engineering*. American Society of Civil Engineers, 136(7), pp. 654–663.

Ho, C.-H. and Romero, P. (2009) ‘Low Design Temperatures of Asphalt Pavements in Dry–Freeze Regions: Predicting by Means of Solar Radiation, Transient Heat Transfer, and Finite Element Method’, *Transportation research record*. SAGE Publications Sage CA: Los Angeles, CA, 2127(1), pp. 60–71.

Hopman, P. *et al.* (1999) ‘Effects of hydrated lime on the behaviour of mastics and on their construction ageing’, in *Proceedings of The Durable and Safe Road Pavements, V International Conference, Held Kielce, Poland, 11-12 May 1999. Volume 1*.

Hopman, P. C., Kunst, P. and Pronk, A. C. (1989) ‘A renewed interpretation method for fatigue measurements-verification of Miner’s rule’, in *Proceedings of The 4th Eurobitume Symposium, Madrid*, pp. 557–561.

Hu, W., Yao, L. G. and Hua, Z. Z. (2007) ‘Parallel point interpolation method for three-dimensional metal forming simulations’, *Engineering analysis with boundary elements*. Elsevier, 31(4), pp. 326–342.

Huang, S.-C. *et al.* (2002) ‘Effect of hydrated lime on long-term oxidative aging characteristics of asphalt’, *Transportation Research Record*. SAGE Publications Sage CA: Los Angeles, CA, 1810(1), pp. 17–24.

Huang, S.-C. *et al.* (2005) ‘Impact of lime modification of asphalt and freeze–thaw cycling on the asphalt–aggregate interaction and moisture resistance to moisture damage’, *Journal of materials in civil engineering*. American Society of Civil Engineers, 17(6), pp. 711–718.

Huang, T. *et al.* (2019) ‘Shear properties of asphalt mixtures under triaxial compression’, *Applied Sciences*. MDPI, 9(7), p. 1489.

Huang, X. *et al.* (2020) 'Effects of Different Pre-processing Methods on Dry Anaerobic Fermentation of Sugarcane Leaves and Pig Manure', in *E3S Web of Conferences*. EDP Sciences, p. 2065.

Huang, Y. H. (2004) 'Pavement Analysis and Design Pearson Education', *Upper Saddle River, NJ, USA*.

Ishikawa, T. and Miura, S. (2015) 'Influence of moving wheel loads on mechanical behavior of submerged granular roadbed', *Soils and Foundations*. Elsevier, 55(2), pp. 242–257.

Islam, M. R. (2015) *Thermal fatigue damage of asphalt pavement*. The University of New Mexico.

Islam, M. R., Kalevela, S. A. and Nesselhauf, S. K. (2019) 'Sensitivity of the flow number to Mix factors of Hot mix Asphalt', *Infrastructures*. MDPI, 4(2), p. 34.

Islam, M. R. and Tarefder, R. A. (2014) 'Determining thermal properties of asphalt concrete using field data and laboratory testing', *Construction and Building Materials*. Elsevier, 67, pp. 297–306.

Islam, M. R. and Tarefder, R. A. (2015) 'Coefficients of thermal contraction and expansion of asphalt concrete in the laboratory', *Journal of Materials in Civil Engineering*. American Society of Civil Engineers, 27(11), p. 4015020.

Islands, R. U. H. (2008) 'Compendium of Strategies—Cool Pavements', *US Environmental Protection Agency*.

Iwański, M. M. (2020) 'Effect of Hydrated Lime on Indirect Tensile Stiffness Modulus of Asphalt Concrete Produced in Half-Warm Mix Technology', *Materials*. Multidisciplinary Digital Publishing Institute, 13(21), p. 4731.

Iwański, M. M., Maciejewski, K. and Ramiączek, P. (2015) 'Influence of hydrated lime on the properties of filler-bitumen composite', *Structure and Environment*, 7(2).

Izadi, A. *et al.* (2018) 'Effect of aging conditions on the fatigue behavior of hot and warm mix asphalt', *Construction and Building Materials*. Elsevier, 188, pp. 119–129.

Jackson, N. M. and Vinson, T. S. (1996) 'Analysis of thermal fatigue distress of asphalt concrete pavements', *Transportation research record*. SAGE Publications Sage CA: Los

Angeles, CA, 1545(1), pp. 43–49.

Jahangirnejad, S., Buch, N. and Kravchenko, A. (2009) ‘Evaluation of coefficient of thermal expansion test protocol and its impact on jointed concrete pavement performance’, *ACI Materials Journal*. American Concrete Institute, 106(1), p. 64.

Jeong, J.-H. and Zollinger, D. G. (2006) ‘Finite-element modeling and calibration of temperature prediction of hydrating Portland cement concrete pavements’, *Journal of materials in civil engineering*. American Society of Civil Engineers, 18(3), pp. 317–324.

Jia, L., Sun, L. and Yu, Y. (2008) ‘Asphalt pavement statistical temperature prediction models developed from measured data in China’, in *Plan, Build, and Manage Transportation Infrastructure in China*, pp. 723–732.

Jiang, Y. *et al.* (2021) ‘Laboratory investigation on the heat dissipation regularity and road performance of different pavement structure combinations by double-layer paving’, *Construction and Building Materials*. Elsevier, 284, p. 122785.

Johansson, L. S. and Isacsson, U. (1998) ‘Effect of filler on low temperature physical hardening of bitumen’, *Construction and Building Materials*. Elsevier, 12(8), pp. 463–470.

Jones, G. M., Darter, M. I. and Littlefield, G. (1968) ‘Thermal expansion-contraction of asphaltic concrete’.

Jordan, P. G. and Thomas, M. E. (1976) *Prediction of cooling curves for hot mix paving materials by a computer program*.

Kai, L. and Fang, W. (2011) ‘Computer modeling mechanical analysis for asphalt overlay under coupling action of temperature and loads’, *Procedia Engineering*. Elsevier, 15, pp. 5338–5342.

Kakade, V. B., Reddy, M. A. and Reddy, K. S. (2016) ‘Effect of aging on fatigue performance of hydrated lime modified bituminous mixes’, *Construction and Building Materials*. Elsevier, 113, pp. 1034–1043.

Kallas, B. F. (1966) ‘Asphalt pavement temperatures’, *Highway Research Record*, (150).

Kandhal, P. S. and Cooley, L. A. (2003) *Accelerated laboratory rutting tests: Evaluation of the asphalt pavement analyzer*. Transportation Research Board.

Kavianipour, A. and Beck, J. V (1977) ‘Thermal property estimation utilizing the Laplace transform with application to asphaltic pavement’, *International journal of heat and mass transfer*. Elsevier, 20(3), pp. 259–267.

Kennedy, T. W. (1983) ‘Evaluation of methods for field applications of lime to asphalt mixture’, in *Association of Asphalt Paving Technologists*, pp. 508–529.

Ketcham, S. *et al.* (1996) *Manual of practice for an effective anti-icing program: a guide for highway winter maintenance personnel*. United States. Federal Highway Administration.

Khadrawi, A. F., Al-Shyyab, A. and Abo-Qudais, S. A. (2012) ‘Transient Thermal Behavior of Hot–Mix Asphalt Pavement’, in *Applied Mechanics and Materials*. Trans Tech Publ, pp. 400–407.

Khan, M. U. *et al.* (2017) ‘Estimating pavement’s flood resilience’, *Journal of Transportation Engineering, Part B: Pavements*. American Society of Civil Engineers, 143(3), p. 4017009.

Khan, Z. H., Islam, M. R. and Tarefder, R. A. (2019) ‘Determining asphalt surface temperature using weather parameters’, *Journal of Traffic and Transportation Engineering (English Edition)*. Elsevier, 6(6), pp. 577–588.

Khattak, M. J. and Kyatham, V. (2008) ‘Viscoelastic behavior of hydrated lime-modified asphalt matrix and hot mix asphalt under moisture damage conditions’, *Transportation Research Record*. SAGE Publications Sage CA: Los Angeles, CA, 2057(1), pp. 64–74.

Khodaii, A., Tehrani, H. K. and Haghshenas, H. F. (2012) ‘Hydrated lime effect on moisture susceptibility of warm mix asphalt’, *Construction and Building Materials*. Elsevier, 36, pp. 165–170.

Kliewer, J. E., Zeng, H. and Vinson, T. S. (1996) ‘Aging and low-temperature cracking of asphalt concrete mixture’, *Journal of Cold Regions Engineering*. American Society of Civil Engineers, 10(3), pp. 134–148.

Kollaros, G., Kalaitzaki, E. and Athanasopoulou, A. (2017) ‘Using hydrated lime in hot mix asphalt mixtures in road construction’, *American Journal of Engineering Research (AJER)*, 6(7), pp. 261–266.

KONDO, Y. and MIURA, Y. (1976) ‘On the Prediction of Temperature in Pavement Structures’, in *Proceedings of the Japan Society of Civil Engineers*. Japan Society of Civil Engineers, pp. 123–132.

Ksaibati, K. and Yavuzturk, C. (2002) *Assessment of temperature fluctuations in asphalt pavements due to thermal environmental conditions using a two-dimensional transient finite difference approach*.

Kumbargeri, Y. S. and Biligiri, K. P. (2016) ‘Rational performance indicators to evaluate asphalt materials’ aging characteristics’, *Journal of Materials in Civil Engineering*. American Society of Civil Engineers, 28(12), p. 4016157.

Lackner, R. *et al.* (2005) ‘Is low-temperature creep of asphalt mastic independent of filler shape and mineralogy?—arguments from multiscale analysis’, *Journal of Materials in Civil Engineering*. American Society of Civil Engineers, 17(5), pp. 485–491.

Lagos-Varas, M. *et al.* (2022) ‘Viscoelasticity modelling of asphalt mastics under permanent deformation through the use of fractional calculus’, *Construction and Building Materials*. Elsevier, 329, p. 127102.

Laukkanen, O.-V. *et al.* (2015) ‘Creep-recovery behavior of bituminous binders and its relation to asphalt mixture rutting’, *Materials and Structures*. Springer, 48, pp. 4039–4053.

Lesueur, D. (2010) ‘Hydrated lime: A proven additive for durable asphalt pavements–Critical literature review’, *Brussels: European Lime Association (EuLA) Ed*.

Lesueur, D. and Little, D. N. (1999) ‘Effect of hydrated lime on rheology, fracture, and aging of bitumen’, *Transportation Research Record*. SAGE Publications Sage CA: Los Angeles, CA, 1661(1), pp. 93–105.

Lesueur, D., Petit, J. and Ritter, H.-J. (2013) ‘The mechanisms of hydrated lime modification of asphalt mixtures: a state-of-the-art review’, *Road materials and pavement design*. Taylor & Francis, 14(1), pp. 1–16.

Lesueur, D., Petit, J. and Ritter, H. (2013) ‘The mechanisms of hydrated lime modification of asphalt mixtures: a state-of-the-art review’, *Road materials and pavement design*. Taylor & Francis, 14(1), pp. 1–16.

Lesueur, D. and Youtcheff, J. (2014) 'Asphalt pavement durability', *Environmental degradation of advanced and traditional engineering materials*. CRC Press Boca Raton, FL.

Li, H., Harvey, J. and Jones, D. (2013) 'Cooling effect of permeable asphalt pavement under dry and wet conditions', *Transportation research record*. SAGE Publications Sage CA: Los Angeles, CA, 2372(1), pp. 97–107.

Li, K. S. (2009) 'Local hauliers want axle-load limits increased to 30pc', *Business Times*.

Li, Q., Mills, L. and McNeil, S. (2011) 'The implications of climate change on pavement performance and design'. University of Delaware. University Transportation Center.

Li, R., Schwartz, C. W. and Forman, B. (2013) 'Sensitivity of predicted pavement performance to climate characteristics', in *Airfield and Highway Pavement 2013: Sustainable and Efficient Pavements*, pp. 760–771.

Li, Y., Liu, L. and Sun, L. (2018) 'Temperature predictions for asphalt pavement with thick asphalt layer', *Construction and Building Materials*. Elsevier, 160, pp. 802–809.

Liang, R. Y. and Niu, Y.-Z. (1998) 'Temperature and curling stress in concrete pavements: Analytical solutions', *Journal of transportation engineering*. American Society of Civil Engineers, 124(1), pp. 91–100.

Little, D. N., Allen, D. H. and Bhasin, A. (2018) *Modeling and design of flexible pavements and materials*. Springer.

Little, D. N., Epps, J. A. and Sebaaly, P. E. (2006) 'Hydrated lime in hot mix asphalt', *National Lime Association, Arlington, VA*. Citeseer.

Little, D. N. and Petersen, J. C. (2005) 'Unique effects of hydrated lime filler on the performance-related properties of asphalt cements: Physical and chemical interactions revisited', *Journal of Materials in Civil Engineering*. American Society of Civil Engineers, 17(2), pp. 207–218.

Littlefield, G. (1967) 'Thermal expansion and contraction characteristics-utah asphalt concretes', in *Assoc Asphalt Paving Technol Proc*.

Liu, C. *et al.* (2020) 'Analysis and comparison of different impacts of aging and loading frequency on fatigue characterization of asphalt concrete', *Journal of Materials in Civil*

Engineering. American Society of Civil Engineers, 32(9), p. 4020240.

Liu, C. and Gazis, D. C. (2001) 'Heat conduction waves in bilayer cement concrete structures', *Journal of engineering mechanics*. American Society of Civil Engineers, 127(11), pp. 1195–1198.

Liu, C. and Yuan, D. (2000) 'Temperature distribution in layered road structures', *Journal of transportation engineering*. American Society of Civil Engineers, 126(1), pp. 93–95.

Long, F. M. (2001) 'Permanent deformation of asphalt concrete pavements: A nonlinear viscoelastic approach to mix analyses and design'.

Luca, J. and Mrawira, D. (2005) 'New measurement of thermal properties of superpave asphalt concrete', *Journal of Materials in Civil Engineering*. American Society of Civil Engineers, 17(1), pp. 72–79.

Luxemburk, G. F. (1996) 'Lime Hydrate as an Additive to Improve the Adhesion of Bitumen to the Aggregates. In Proceedings of the II International Conference Durable and Save Road Pavements, Kielce, Poland, 15–16 May 1996; pp. 296–302.'

Lv, S. *et al.* (2020) 'Laboratory investigation of fatigue parameters characteristics of aging asphalt mixtures: A dissipated energy approach', *Construction and Building Materials*. Elsevier, 230, p. 116972.

Lytton, R. L. *et al.* (1993) 'An integrated model of the climatic effects on pavements'.

Lytton, R. L., Shanmugham, U. and Garrett, B. D. (1983) *Design of asphalt pavements for thermal fatigue cracking*.

Mahboub, K. C., Liu, Y. and Allen, D. L. (2004) 'Evaluation of temperature responses in concrete pavement', *Journal of transportation engineering*. American Society of Civil Engineers, 130(3), pp. 395–401.

Mamlouk, M. S. *et al.* (2005) 'Determination of thermal properties of asphalt mixtures', *Journal of Testing and Evaluation*. ASTM International, 33(2), pp. 118–126.

Mantalovas, K. and Di Mino, G. (2020) 'Integrating circularity in the sustainability assessment of asphalt mixtures', *Sustainability*. MDPI, 12(2), p. 594.

Marasteanu, M. *et al.* (2012) ‘Investigation of low temperature cracking in asphalt pavements national pooled fund study–phase II’. Minnesota Department of Transportation.

Matić, B. *et al.* (2013) ‘A model for the pavement temperature prediction at specified depth’, *Metalurgija*. Hrvatsko Metalursko Društvo (HMD), 52(4), pp. 505–508.

McLean, D. B. and Monismith, C. L. (1974) ‘Estimation of permanent deformation in asphalt concrete layers due to repeated traffic loading’, *Transportation research record*, (510).

Mehta, Y. A., Stoffels, S. A. and Christensen, D. W. (1999) ‘Determination of coefficient of thermal contraction of asphalt concrete using indirect tensile test hardware’, in *Proceedings of the Association of Asphalt Paving Technologists*. Association of Asphalt Paving Technologist, pp. 349–368.

Mello, L. G. R., Kaloush, K. E. and Farias, M. M. (2010) ‘Damage theory applied to flexural fatigue tests on conventional and asphalt rubber hot mixes’, *Road materials and pavement design*. Taylor & Francis, 11(3), pp. 681–700.

Meng, F. *et al.* (2020) ‘Fatigue Performance Test and Life Calculation of Fiber-Reinforced Asphalt Concrete’, in *Annales de Chimie-Science des Matériaux*, pp. 133–139.

Mfinanga, D. A., Ochiai, H. and Yasufuku, N. (1996) ‘Traffic loading and environmental effects on asphalt pavement rutting’.

Miller, J. S. and Bellinger, W. Y. (2003) *Distress identification manual for the long-term pavement performance program*. United States. Federal Highway Administration. Office of Infrastructure ….

Mirzanamadi, R., Johansson, P. and Grammatikos, S. A. (2018) ‘Thermal properties of asphalt concrete: A numerical and experimental study’, *Construction and Building Materials*. Elsevier, 158, pp. 774–785.

Mohammad, L. N. *et al.* (2000) ‘Mechanistic evaluation of hydrated lime in hot mix asphalt mixtures’, *Transportation Research Record*. SAGE Publications Sage CA: Los Angeles, CA, 1723(1), pp. 26–36.

Mondal, A., Islam, S. S. and Ransinchung RN, G. D. (2022) ‘Synergistic effect of hydrated lime and warm mix asphalt additive on properties of recycled asphalt mixture subjected to laboratory ageing', *International Journal of Pavement Research and Technology*. Springer, pp. 1–15.

Moniri, A. *et al.* (2021) 'Laboratory study of the effect of oil-based recycling agents on high RAP asphalt mixtures', *International Journal of Pavement Engineering*. Taylor & Francis, 22(11), pp. 1423–1434.

Monismith, C. L., Kasianchuk, D. A. and Epps, J. A. (1967) 'Asphalt mixture behavior in repeated flexure: a study of an in-service pavement near Morro Bay, California'.

Monismith, C. L., Ogawa, N. and Freeme, C. R. (1975) 'Permanent deformation characteristics of subgrade soils due to repeated loading', *Transportation research record*, (537).

Montávez, J. P., Jiménez, J. I. and Sarsa, A. (2000) 'A Monte Carlo model of the nocturnal surface temperatures in urban canyons', *Boundary-layer meteorology*. Springer, 96(3), pp. 433–452.

Moreno-Navarro, F. *et al.* (2018) 'Fatigue cracking in asphalt mixtures: the effects of ageing and temperature', *Road Materials and Pavement Design*. Taylor & Francis, 19(3), pp. 561–570.

Moussa, G. K. M. and El-Hamrawy, S. (2003) 'Load equivalence factors as function of axial loads and tire pressure for design of flexible pavement.', *Alexandria Engineering Journal*, 42(4), pp. 443–451.

Muniandy, R. *et al.* (2014) 'Characterization of effective tire contact area for various tread patterns', *Instrumentation Science & Technology*. Taylor & Francis, 42(1), pp. 15–26.

Muraya, P. M., Molenaar, A. A. A. and Van de Ven, M. F. C. (2009) 'Contribution of asphalt mix components to permanent deformation resistance', in *8th international conference on the bearing capacity of roads, railways and airfields, Champaign, IL*, pp. 259–268.

Naik, T. R., Kraus, R. N. and Kumar, R. (2011) 'Influence of types of coarse aggregates on the coefficient of thermal expansion of concrete', *Journal of Materials in Civil Engineering*. American Society of Civil Engineers, 23(4), pp. 467–472.

Nam, K. and Bahia, H. U. (2004) 'Effect of binder and mixture variables on glass transition behavior of asphalt mixtures (with discussion)', *Journal of the Association of Asphalt Paving Technologists*, 73.

Nascimento, L. A. H. do (2008) 'Nova abordagem da dosagem de misturas asfálticas densas com uso do compactador giratório e foco na deformação permanente', *Disserta-ção de Mestrado. Universidade Federal do Rio de Janeiro. Rio de Janeiro, RJ. Disponível em: http://www. coc. ufrj. br*.

NCHRP (2004) '"Mechanistic-Empirical Design of New and Rehabilitated Pavement Structures," NCHRP Project 1-37A Draft Final Report, Transportation Research Board, National Research Council, Washington, D.C.', in.

Nikolaides, A. (2014) *Highway engineering: pavements, materials and control of quality*. CRC Press.

Palmer, D. *et al.* (2017) 'Interpolating and estimating horizontal diffuse solar irradiation to provide UK-wide coverage: Selection of the best performing models', *Energies*. Multidisciplinary Digital Publishing Institute, 10(2), p. 181.

Park, D.-Y., Buch, N. and Chatti, K. (2001) 'Effective layer temperature prediction model and temperature correction via falling weight deflectometer deflections', *Transportation Research Record*. SAGE Publications Sage CA: Los Angeles, CA, 1764(1), pp. 97–111.

Perraton, D. *et al.* (2011) 'Rutting of bituminous mixtures: wheel tracking tests campaign analysis', *Materials and structures*. Springer, 44(5), pp. 969–986.

Petersen, J. C. (2009) 'A review of the fundamentals of asphalt oxidation: chemical, physicochemical, physical property, and durability relationships', *Transportation Research Circular*, (E-C140).

Petersen, J. C., Plancher, H. and Harnsberger, P. M. (1987) 'Lime treatment of asphalt to reduce age hardening and improve flow properties', in *Association of Asphalt Paving Technologists Proceedings Technical Sessions, 1987, Reno, Nevada, USA*.

Pilat, J., Radziszewski, P. and Kalabiska, M. (2000) 'The analysis of visco-elastic properties of mineral-asphalt mixes with lime and rubber powder', in *proceedings of the papers submitted for review at 2nd Eurasphalt and Eurobitume Congress, held 20-22 September*

2000, Barcelona, Spain. Book 1-Session 1.

Planche, J.-P. *et al.* (2004) 'Evaluation of fatigue properties of bituminous binders', *Materials and Structures*. Springer, 37(5), pp. 356–359.

Pomerantz, M. and Akbari, H. (1998) 'Cooler paving materials for heat island mitigation', in *Proceedings of the 1998 ACEEE summer study on energy efficiency in buildings*, p. 135.

Pouranian, M. R. and Shishehbor, M. (2019) 'Sustainability assessment of green asphalt mixtures: A review', *Environments*. MDPI, 6(6), p. 73.

Qiao, Y. *et al.* (2020) 'Flexible pavements and climate change: A comprehensive review and implications', *Sustainability*. Multidisciplinary Digital Publishing Institute, 12(3), p. 1057.

Qin, Y. (2015) 'A review on the development of cool pavements to mitigate urban heat island effect', *Renewable and sustainable energy reviews*. Elsevier, 52, pp. 445–459.

Qin, Y. (2016) 'Pavement surface maximum temperature increases linearly with solar absorption and reciprocal thermal inertial', *International Journal of Heat and Mass Transfer*. Elsevier, 97, pp. 391–399.

Qin, Y. and Hiller, J. E. (2011) 'Modeling temperature distribution in rigid pavement slabs: impact of air temperature', *Construction and building materials*. Elsevier, 25(9), pp. 3753–3761.

Qin, Y. and Hiller, J. E. (2013) 'Ways of formulating wind speed in heat convection significantly influencing pavement temperature prediction', *Heat and Mass Transfer*. Springer, 49(5), pp. 745–752.

Qin, Y. and Hiller, J. E. (2014) 'Understanding pavement-surface energy balance and its implications on cool pavement development', *Energy and Buildings*. Elsevier, 85, pp. 389–399.

Rajbongshi, P. (2011) 'Comparative study on temperature stresses in asphalt material using nonlinear viscoelastic approach', *Journal of transportation engineering*. American Society of Civil Engineers, 137(10), pp. 717–722.

Ramond, G. and Lesueur, D. (2004) 'Adhesion liant granulat', *Materiaux routiers bitumineux,* 1, pp. 177–203.

Roffa, A. A. O. and Farhat, F. A. (2013) ‘The Influence of Climate on Libyan Roads Deterioration’, in *Sustainable Construction Materials 2012*, pp. 430–440.

Roque, R. *et al.* (2010) *Top-down cracking of hot mix asphalt layers: Models for initiation and propagation*.

Saleh, N. F. *et al.* (2020) ‘Effects of aging on asphalt mixture and pavement performance’, *Construction and Building Materials*. Elsevier, 258, p. 120309.

Salem-Hassan, A. (2015) ‘Research of the relevant temperatures for the design of pavement constructions on the desert roads in Libya’, *Универзитет у Новом Саду*. Универзитет у Новом Саду, Факултет техничких наука.

Salem, H. M. *et al.* (2004) ‘Using long-term pavement performance data to predict seasonal variation in asphalt concrete modulus’, *Transportation Research Record*. SAGE Publications Sage CA: Los Angeles, CA, 1896(1), pp. 119–128.

Schwartz, C. W. *et al.* (2013) ‘Global Sensitivity Analysis of Mechanistic–Empirical Performance Predictions for Flexible Pavements’, *Transportation research record*. SAGE Publications Sage CA: Los Angeles, CA, 2368(1), pp. 12–23.

SCRB/R9 (2003) ‘No Title General Specification for Roads and Bridges”, Section R/9, Hot mix Asphalt Concrete Pavement, Revised Edition. State Corporation of Roads and Bridges, Ministry of Housing and Construction, Republic of Iraq.’, in.

Sebaaly, P. E., Hitti, E. and Weitzel, D. (2003) ‘Effectiveness of lime in hot mix asphalt pavements’, *Transportation Research Record*. SAGE Publications Sage CA: Los Angeles, CA, 1832(1), pp. 34–41.

Shahin, M. Y. and McCullough, B. F. (1972) *Prediction of Low Temperature and Thermal-Fatigue Cracking in Flexible Pavements*.

Shahrour, M. A. and Saloukeh, B. G. (1992) ‘Effect of quality and quantity of locally produced filler (passing sieve No. 200) on asphaltic mixtures in Dubai’, *Effects of Aggregates and Mineral Fillers on Asphalt Mixture Performance, ASTM STP*, 1147, pp. 187–208.

Shen, S., Chiu, H.-M. and Huang, H. (2010) ‘Characterization of fatigue and healing in asphalt binders’, *Journal of Materials in Civil Engineering*. American Society of Civil

Engineers, 22(9), pp. 846–852.

Sievers, U. and Zdunkowski, W. (1985) 'A numerical simulation scheme for the albedo of city street canyons', *Boundary-layer meteorology*. Springer, 33(3), pp. 245–257.

Singh, D. and Kataware, A. V (2016) 'Comparison of different rheological parameters for rutting susceptibility of SBS+ WMA modified binders', *Innovative Infrastructure Solutions*. Springer, 1, pp. 1–10.

Solaimanian, M. and Bolzan, P. (1993) *Analysis of the integrated model of climatic effects on pavements*. Strategic Highway Research Program, National Research Council.

Solaimanian, M. and Kennedy, T. W. (1993) 'Predicting maximum pavement surface temperature using maximum air temperature and hourly solar radiation', *Transportation Research Record*. NATIONAL ACADEMY OF SCIENCES, p. 1.

Solutions, R. (2016) 'Roger Johnson Consulting Ltd. Langley, BC. www.rjcsolutions.com/calculators/grav-den.html.'

Song, J. and Pellinen, T. (2007) 'Dilation behavior of hot mix asphalt under triaxial loading: A mechanism of permanent deformation generation', *Road materials and pavement design*. Taylor & Francis, 8(1), pp. 103–125.

Southgate, H. F. *et al.* (1976) 'Kentucky research: A flexible pavement design and management system'.

Souza, F. V, Allen, D. H. and Kim, Y.-R. (2008) 'Multiscale model for predicting damage evolution in composites due to impact loading', *Composites science and technology*. Elsevier, 68(13), pp. 2624–2634.

Stoffels, S. M. and Kwanda, F. D. (1996) 'Determination of the coefficient of thermal contraction of asphalt concrete using the resistance strain gage technique', in *Asphalt Paving Technology: Association of Asphalt Paving Technologists-Proceedings of the Technical Sessions*. Association of Asphalt Paving Technologist, pp. 73–98.

Stroup-Gardiner, M. and Newcomb, D. (1990) 'Comparison of dolomitic and normally hydrated lime as antistripping additives', *Transportation Research Record*, 1269, pp. 56–68.

Su, Y. M., Hossiney, N. and Tia, M. (2013) 'Indirect tensile strength of concrete containing reclaimed asphalt pavement using the superpave indirect tensile test', in *Advanced Materials Research*. Trans Tech Publ, pp. 368–375.

Sugawara, T. A. and A, M. (1984) 'Thermal Fracture of Bituminous Mixtures. Proceedings of the Paving in Cold Areas, Mini-Workshop, pp.291-320.'

Suh, Y.-C., Cho, N.-H. and Mun, S. (2011) 'Development of mechanistic–empirical design method for an asphalt pavement rutting model using APT', *Construction and Building Materials*. Elsevier, 25(4), pp. 1685–1690.

Sun, D. *et al.* (2015) 'Calculation and evaluation of activation energy as a self-healing indication of asphalt mastic', *Construction and Building Materials*. Elsevier, 95, pp. 431–436.

Sun, L. (2016) 'Distribution of the temperature field in a pavement structure', *Structural Behavior of Asphalt Pavements; Butterworth-Heinemann: Cambridge, MA, USA*, pp. 61–177.

Sun, L., Hudson, W. R. and Zhang, Z. (2003) 'Empirical-mechanistic method based stochastic modeling of fatigue damage to predict flexible pavement cracking for transportation infrastructure management', *Journal of transportation engineering*. American Society of Civil Engineers, 129(2), pp. 109–117.

Sun, Q. *et al.* (2017) 'Effect of variable confining pressure on cyclic behaviour of granular soil under triaxial tests', *Canadian Geotechnical Journal*. NRC Research Press, 54(6), pp. 768–777.

Sun, Y. *et al.* (2020) 'Effect of temperature field on damage initiation in asphalt pavement: A microstructure-based multiscale finite element method', *Mechanics of Materials*. Elsevier, 144, p. 103367.

Sun, Y. *et al.* (2022) '3D Multiscale Modeling of Asphalt Pavement Responses under Coupled Temperature–Stress Fields', *Journal of Engineering Mechanics*. American Society of Civil Engineers, 148(3), p. 4022010.

Tabatabaie, S. A., Ziari, H. and Khalili, M. (2008) 'Modeling temperature and resilient modulus of asphalt pavements for tropic zones of Iran', *Asian Journal of Scientific Research*, 1(6), pp. 579–588.

Taherkhani, H. and Tajdini, M. (2019) ‘Comparing the effects of nano-silica and hydrated lime on the properties of asphalt concrete’, *Construction and Building Materials*. Elsevier, 218, pp. 308–315.

Tan, S.-A., Low, B.-H. and Fwa, T.-F. (1992) ‘Determination of thermal conductivity and diffusivity by transient heating of a thin slab’, *Building and environment*. Elsevier, 27(1), pp. 71–76.

Tangella, S. C. S. R. *et al.* (1990) *Summary report on fatigue response of asphalt mixtures*.

Tayebali, A. A., Rowe, G. M. and Sousa, J. B. (1992) ‘Fatigue response of asphalt-aggregate mixtures (with discussion)’, *Journal of the Association of Asphalt Paving Technologists*, 61.

Terrel, R. L. and Al-Swailmi, S. (1994) *Water sensitivity of asphalt-aggregate mixes: test selection*.

Terrel, R. L. and Shute, J. W. (1989) *Summery report on water sensitivity SHRP-A*. IR-89-003.

Thom, N. (2008) *Principles of pavement engineering*. Thomas Telford London.

Thom, N. H. and Brown, S. F. (1987) *Effect of moisture on the structural performance of a crushed-limestone road base*.

Timm, D. H., Turochy, R. E. and Davis, K. P. (2010) *Guidance for ME pavement design implementation*.

ToolBox, E. (2016) *Thermal Conductivity of Some Common Materials and Gases. www.engineeringtoolbox.com/thermal-conductivity-d_429.html.*

Tye, R. P. and Brazel, J. P. (1969) *Thermophysical Properties of Hot-Pressed Beryllium.* Dynatech Corp., Cambridge, Mass.

Vehrencamp, J. E. (1953) ‘Experimental investigation of heat transfer at an air-Earth interface’, *Eos, Transactions American Geophysical Union*. Wiley Online Library, 34(1), pp. 22–30.

Verhasselt, A. and Puiatti, D. (2004) ‘Effect of hydrated lime on ageing behaviour of bituminous mastics’, in *Proceedings of The 3rd Eurasphalt and Eurobitume Congress Held*

Vienna, May 2004.

Vinson, T. S., Janoo, V. C. and Haas, R. C. G. (1989) *Low temperature and thermal fatigue cracking*. Strategic Highway Research Program, National Research Council.

Wahhab, H. I. A.-A., Asi, I. M. and Ramadhan, R. H. (2001) 'Modeling resilient modulus and temperature correction for Saudi roads', *Journal of Materials in Civil Engineering*. American Society of Civil Engineers, 13(4), pp. 298–305.

Walker, D. (1984) 'How vehicle loads affect pavement performance', Wisconsin Transportation Bulletin.', p. 1.

Walubita, L.-T. *et al.* (2013) 'Exploring the flow number (FN) index as a means to characterise the HMA permanent deformation response under FN testing', *Journal of the South African Institution of Civil Engineering= Joernaal van die Suid-Afrikaanse Instituut van Siviele Ingenieurswese*. South African Institution of Civil Engineering (SAICE), 55(3), pp. 103–112.

Wang, D. (2010) *Analytical solutions for temperature profile prediction in multi-layered pavement systems*. University of Illinois at Urbana-Champaign.

Wang, D. (2012) 'Analytical approach to predict temperature profile in a multilayered pavement system based on measured surface temperature data', *Journal of Transportation Engineering*. American Society of Civil Engineers, 138(5), pp. 674–679.

Wang, D. (2013) 'Prediction of asphalt pavement temperature profile during FWD testing: simplified analytical solution with model validation based on LTPP data', *Journal of transportation engineering*. American Society of Civil Engineers, 139(1), pp. 109–113.

Wang, D. and Roesler, J. R. (2014) 'One-dimensional temperature profile prediction in multi-layered rigid pavement systems using a separation of variables method', *International Journal of Pavement Engineering*. Taylor & Francis, 15(5), pp. 373–382.

Wang, D., Roesler, J. R. and Guo, D.-Z. (2009) 'Analytical approach to predicting temperature fields in multilayered pavement systems', *Journal of engineering mechanics*. American Society of Civil Engineers, 135(4), pp. 334–344.

Wang, F. *et al.* (2021) 'Comparative assessments for environmental impacts from three advanced asphalt pavement construction cases', *Journal of Cleaner Production*. Elsevier, 297, p. 126659.

Wang, H., Wang, J. and Chen, J. (2014) 'Micromechanical analysis of asphalt mixture fracture with adhesive and cohesive failure', *Engineering Fracture Mechanics*. Elsevier, 132, pp. 104–119.

Wang, L. *et al.* (2005) 'Anisotropic properties of asphalt concrete: characterization and implications for pavement design and analysis', *Journal of materials in civil engineering*. American Society of Civil Engineers, 17(5), pp. 535–543.

Wang, L. B. *et al.* (2003) 'Micromechanics study on top-down cracking', *Transportation Research Record*. SAGE Publications Sage CA: Los Angeles, CA, 1853(1), pp. 121–133.

Wang, Y., Al Ashaibi, A., Albayati, A. and Haynes, J. (2022) 'Experimental study of temperature effect on the mechanical tensile fatigue of hydrated lime modified asphalt concrete and case application for the analysis of climatic effect on constructed pavement', *Case Studies in Construction Materials*. Elsevier, p. e01622.

Wang, Y., Al Ashaibi, A., Albayati, A. and Haynes, B. J. (2022) 'Thermal fatigue analysis of pavement design using hydrated lime modified asphalt concrete', *The International Journal of Pavement Engineering and Asphalt Technology*. Liverpool John Moores University, 23.

Wang, Y. D., Keshavarzi, B. and Kim, Y. R. (2018) 'Fatigue performance analysis of pavements with RAP using viscoelastic continuum damage theory', *KSCE Journal of Civil Engineering*. Springer, 22(6), pp. 2118–2125.

Williamson, R. H. (1972) 'Effects of environment on pavement temperatures', in *Intl Conf Structural Design Proc*.

Willway, T. *et al.* (2008) 'The effects of climate change on highway pavements and how to minimise them: Technical report', *The Effects of Climate Change on Highway Pavements and how to Minimise them: Technical Report*, 1(1), pp. 1–111.

Witczak, M. W. (1972) 'Design of full-depth asphalt airfield pavements', in *Presented at the Third International Conference on the Structural Design of Asphalt Pavements, Grosvenor House, Park Lane, London, England, Sept. 11-15, 1972.*

Witczak, M. W. (2002) *Simple performance test for superpave mix design*. Transportation Research Board.

Witczak, M. W. (2007) *Specification criteria for simple performance tests for rutting*. Transportation Research Board.

Witczak, M. W. and Bari, J. (2004) 'Development of a master curve (E*) database for lime modified asphaltic mixtures', *Arizona State University Research Report, Tempe, AZ*.

Wolfe, R. K., Heath, G. L. and Colony, D. C. (1980) *University of Toledo Time-Temperature Model Laboratory and Field Validation*.

Won, M. (2005) 'Improvements of testing procedures for concrete coefficient of thermal expansion', *Transportation Research Record*. SAGE Publications Sage CA: Los Angeles, CA, 1919(1), pp. 23–28.

Wong, L. T. and Chow, W. K. (2001) 'Solar radiation model', *Applied energy*. Elsevier, 69(3), pp. 191–224.

Wortelboer, J. P. *et al.* (1996) 'Rheological properties of bitumen/filler mixtures', in *EURASPHALT & EUROBITUME CONGRESS, STRASBOURG, 7-10 MAY 1996. VOLUME 2. PAPER E&E. 4.079*.

Wu, H. *et al.* (2018) 'Characterizing thermal behaviors of various pavement materials and their thermal impacts on ambient environment', *Journal of cleaner production*. Elsevier, 172, pp. 1358–1367.

Xia, C. *et al.* (2019) 'Unified strength model of asphalt mixture under various loading modes', *Materials*. MDPI, 12(6), p. 889.

Xie, J. and Yang, Y. (2019) 'Numerical Simulation Virtual Test of Torsion Shear for Asphalt Mixture', *Advances in Materials Science and Engineering*. Hindawi, 2019.

Xie, J., Zhan, Y. and Wang, Y. (2019) 'Analysis of a methodology for torsional test under normal stress and shear performance for asphalt mixtures', *Advances in Civil Engineering*. Hindawi, 2019.

Xu, Q. and Solaimanian, M. (2008) 'Measurement and evaluation of asphalt concrete thermal expansion and contraction', *Journal of Testing and Evaluation*. ASTM International, 36(2), pp. 140–149.

Xu, Q. and Solaimanian, M. (2010) ‘Modeling temperature distribution and thermal property of asphalt concrete for laboratory testing applications’, *Construction and building materials*. Elsevier, 24(4), pp. 487–497.

Yang, B. *et al.* (2014) ‘Study on mechanical property of large particle size modified asphalt mixture with multipore’, *Materials Research Innovations*. Taylor & Francis, 18(sup2), pp. S2-811.

Yang, X. *et al.* (2017) ‘Sensitivity of flexible pavement design to Michigan’s climatic inputs using pavement ME design’, *International Journal of Pavement Engineering*. Taylor & Francis, 18(7), pp. 622–632.

Yavuzturk, C., Ksaibati, K. and Chiasson, A. D. (2005) ‘Assessment of temperature fluctuations in asphalt pavements due to thermal environmental conditions using a two-dimensional, transient finite-difference approach’, *Journal of Materials in Civil Engineering*. American Society of Civil Engineers, 17(4), pp. 465–475.

Yaws, C. L. (1997) ‘Physical properties’, in *Handbook of Chemical Compound Data for Process Safety*. Elsevier, pp. 1–26.

Yin, F. *et al.* (2017) ‘Long-term ageing of asphalt mixtures’, *Road Materials and Pavement Design*. Taylor & Francis, 18(sup1), pp. 2–27.

Zapata, C. E. *et al.* (2007) ‘Incorporation of environmental effects in pavement design’, *Road Materials and Pavement Design*. Taylor & Francis, 8(4), pp. 667–693.

Zapata, C. E. and Houston, W. N. (2008) *Calibration and validation of the enhanced integrated climatic model for pavement design*. Transportation Research Board.

Zeng, M. and Shields, D. H. (1999) ‘Nonlinear thermal expansion and contraction of asphalt concrete’, *Canadian Journal of Civil Engineering*. NRC Research Press Ottawa, Canada, 26(1), pp. 26–34.

Zhang, H. *et al.* (2022) ‘Experimental and statistical analysis of bitumen’s field ageing in asphalt pavements’, *Transportation Research Record*. SAGE Publications Sage CA: Los Angeles, CA, 2676(7), pp. 495–511.

Zhang, J. *et al.* (2016) 'Evaluation of dilatancy behavior of asphalt mixtures using partial triaxial compression tests', *Journal of Materials in Civil Engineering*. American Society of Civil Engineers, 28(1), p. 4015081.

Zhang, K., Xie, W. and Zhao, Y. (2021) 'Permanent deformation characteristic of asphalt mixture under coupling effect of moisture, overload and loading frequency', *Construction and Building Materials*. Elsevier, 272, p. 121985.

Zhang, N. *et al.* (2019) 'Numerical Model for Calculating the Unstable State Temperature in Asphalt Pavement Structure', *Coatings*. Multidisciplinary Digital Publishing Institute, 9(4), p. 271.

Zhang, Y. *et al.* (2019) 'A novel application of strain energy for fracturing process analysis of hard rock under true triaxial compression', *Rock Mechanics and Rock Engineering*. Springer, 52(11), pp. 4257–4272.

Zhao, J. *et al.* (2021) 'Study on time-dependent fracturing behaviour for three different hard rock under high true triaxial stress', *Rock Mechanics and Rock Engineering*. Springer, 54(3), pp. 1239–1255.

Zheng, J. and Huang, T. (2015) 'Study on triaxial test method and failure criterion of asphalt mixture', *Journal of Traffic and Transportation Engineering (English Edition)*. Elsevier, 2(2), pp. 93–106.

Zheng, Y., Cai, Y. and Zhang, Y. (2011) 'Study on temperature field of asphalt concrete pavement', in *Emerging Technologies for Material, Design, Rehabilitation, and Inspection of Roadway Pavements*, pp. 266–273.

Zhou, L. and Sun, Y. (2020) 'Determination of Hydrated Lime Content Based on Asphalt Mastic High Temperature Performances', in *E3S Web of Conferences*. EDP Sciences, p. 2029.

Zhou, W. *et al.* (2021) 'Effects of Hydrated Lime on High-Temperature Rheological Properties of High-Viscosity Modified Asphalt', *Advances in Materials Science and Engineering*. Hindawi, 2021.

Zhu, T. *et al.* (2016) 'Evaluating the rutting resistance of asphalt mixtures using a simplified triaxial repeated load test', *Construction and Building Materials*. Elsevier, 116, pp. 72–78.

Zou, J. *et al.* (2005) 'Measurement and evaluation of asphalt concrete thermal expansion and contraction', *Journal of Materials in Civil Engineering*. American Society of Civil Engineers, 36(1), pp. 140–149.

Zou, J. *et al.* (2013) 'Effect of hydrated lime on fracture performance of asphalt mixture', *Construction and Building Materials*. Elsevier, 44, pp. 302–308.

APPENDIX A

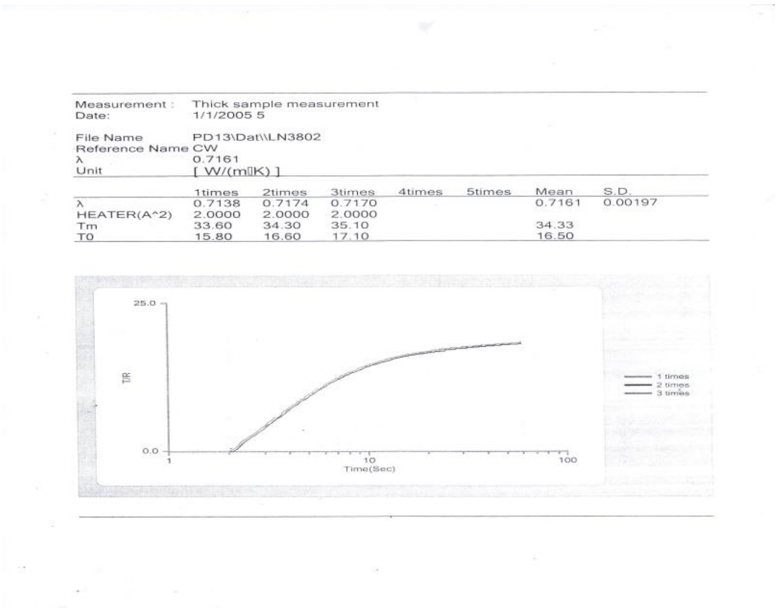

Figure A-1 Thermal Conductivity Chart for 0 HL CW

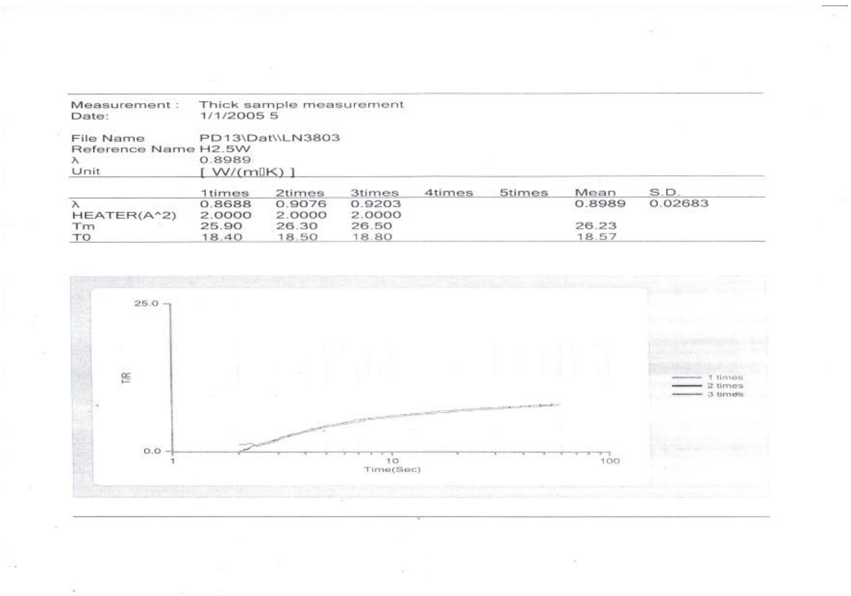

Measurement : Thick sample measurement
Date: 1/1/2005 5

File Name PD13\Dat\\LN3803
Reference Name H2.5W
λ 0.8989
Unit [W/(m·K)]

	1times	2times	3times	4times	5times	Mean	S.D.
λ	0.8688	0.9076	0.9203			0.8989	0.02683
HEATER(A^2)	2.0000	2.0000	2.0000				
Tm	25.90	26.30	26.50			26.23	
T0	18.40	18.50	18.80			18.57	

Figure A-2 Thermal Conductivity Chart for 2.5 % HLW

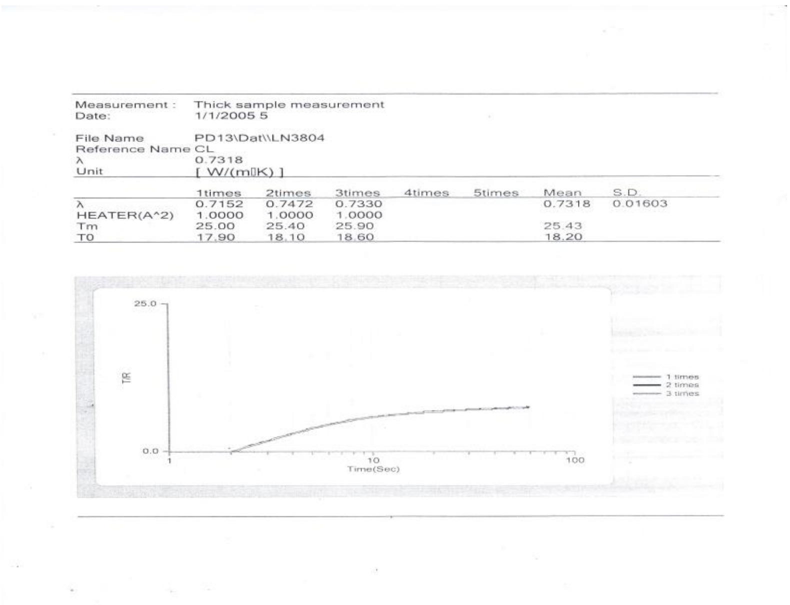

Measurement : Thick sample measurement
Date: 1/1/2005 5

File Name PD13\Dat\\LN3804
Reference Name CL
λ 0.7318
Unit [W/(m K)]

	1times	2times	3times	4times	5times	Mean	S.D.
λ	0.7152	0.7472	0.7330			0.7318	0.01603
HEATER(A^2)	1.0000	1.0000	1.0000				
Tm	25.00	25.40	25.90			25.43	
T0	17.90	18.10	18.60			18.20	

Sample CL
Times 1
λ 0.7318 W/(m· K)

	1times	2times	3times	4times	5times	Mean	S.D.
λ	0.7152	0.7472	0.7330			0.7318	0.01603
Current (A^2)	1.0000	1.0000	1.0000				
Tm	25.00	25.40	25.90			25.43	
T0	17.90	18.10	18.60			18.20	

Figure A-3 Thermal Conductivity Chart for 0 HL CL

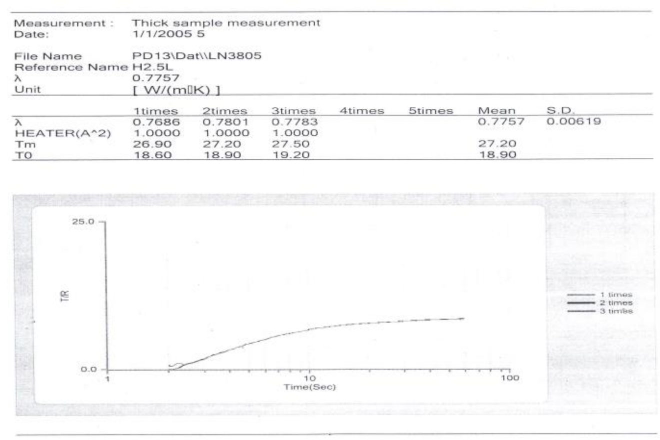

Measurement : Thick sample measurement
Date: 1/1/2005 5

File Name PD13\Dat\\LN3805
Reference Name H2.5L
λ 0.7757
Unit [W/(m K)]

	1times	2times	3times	4times	5times	Mean	S.D.
λ	0.7686	0.7801	0.7783			0.7757	0.00619
HEATER(A^2)	1.0000	1.0000	1.0000				
Tm	26.90	27.20	27.50			27.20	
T0	18.60	18.90	19.20			18.90	

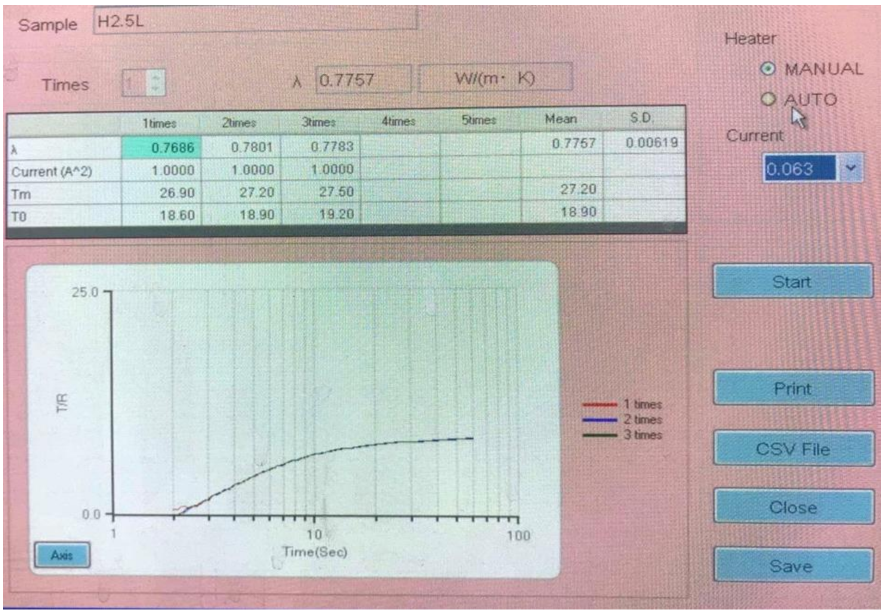

Figure A-4 Thermal Conductivity Chart for 2.5% HL L

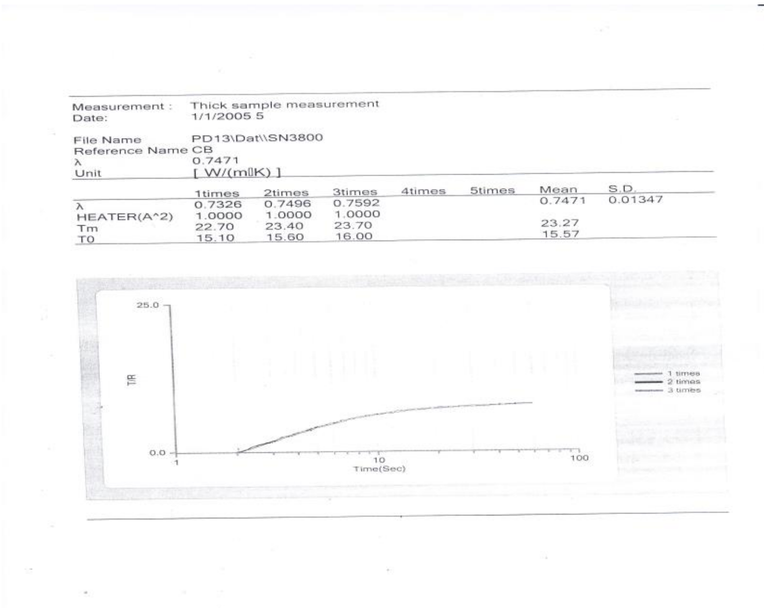

Measurement : Thick sample measurement
Date: 1/1/2005 5

File Name PD13\Dat\\SN3800
Reference Name CB
λ 0.7471
Unit [W/(m K)]

	1times	2times	3times	4times	5times	Mean	S.D.
λ	0.7326	0.7496	0.7592			0.7471	0.01347
HEATER(A^2)	1.0000	1.0000	1.0000				
Tm	22.70	23.40	23.70			23.27	
T0	15.10	15.60	16.00			15.57	

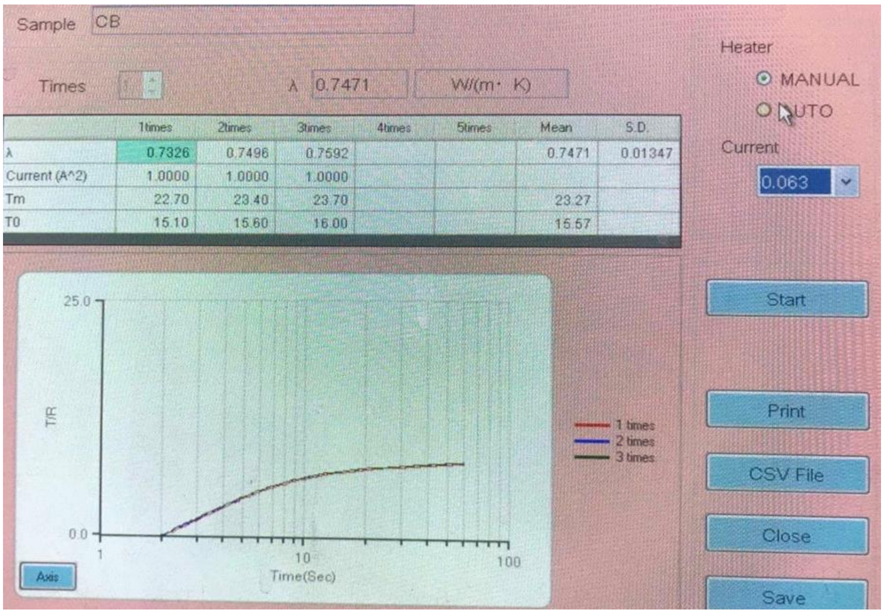

Figure A-5 Thermal Conductivity Chart for 0 HL B

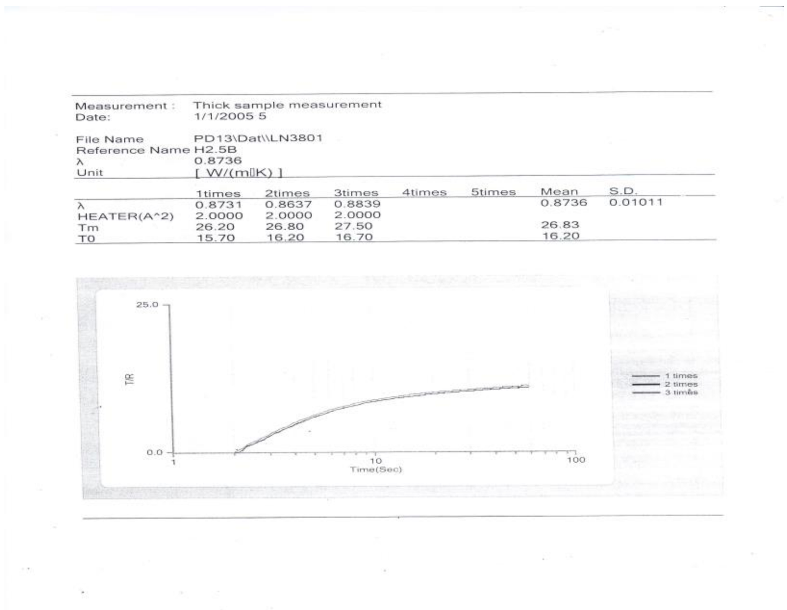

Measurement : Thick sample measurement
Date: 1/1/2005 5

File Name PD13\Dat\\LN3801
Reference Name H2.5B
λ 0.8736
Unit [W/(m K)]

	1times	2times	3times	4times	5times	Mean	S.D.
λ	0.8731	0.8637	0.8839			0.8736	0.01011
HEATER(A^2)	2.0000	2.0000	2.0000				
Tm	26.20	26.80	27.50			26.83	
T0	15.70	16.20	16.70			16.20	

Figure A-6 Thermal Conductivity Chart for 2.5% HL B

Table A-1 Thermal Properties Calculations

	Bulk density (g/cm^3)	Thermal Conductivity (W/m.K)	Specfiific heat (J/kg.K)	Thermal Diffusivity (mm^2/sec)	T0	Tm	ΔT	t1	t2	ln(t2/t1)	π	Q	mass (g)	mass (kg)
CW	2340	0.7161	1062.60	0.288	17	34	17.8	2	60	3.4	3.141592654	47.17403716	2489.9	2.4899
H2.5W	2320	0.8989	1333.48	0.291	19	26	7.66	2	60	3.4	3.141592654	25.44006274	2490.6	2.4906
CL	2320	0.7318	1092.79	0.289	18	25	7.23	2	60	3.4	3.141592654	19.54828807	2474.2	2.4742
H2.5L	2300	0.7757	1155.49	0.292	19	27	8.3	2	60	3.4	3.141592654	23.78756082	2480.3	2.4803
CB	2310	0.7471	1121.12	0.288	16	23	7.7	2	60	3.4	3.141592654	21.25433344	2462.1	2.4621
H2.5B	2297	0.8763	1303.09	0.293	16	27	10.6	2	60	3.4	3.141592654	34.41629409	2484.6	2.4846

$$Q = \frac{K\,4\pi(T_2 - T_1)}{\ln(t_2 \,/\, t_1)}$$

With thermal conductivity given by K in W/m K, while Q generated heat per unit length of sample W/m, and duration is given by t1, t2 in seconds, while T1, T2 gives temperature for t1, t2, and k

$$\boldsymbol{a} = \frac{\boldsymbol{K}}{\rho \boldsymbol{C_P}}$$

In which k is thermal conductivity in W/m K and density is given by ρ in kg/m3, while specific heat capacity, C_P is shown in J/kg K.

Table A-3 Marshal Test Result for Mix Layers 0 HL

HL	AC %	Density (g/cm3)	Gmm (g/cm3)	Stability (kN)	Flow (mm)	Air Voids (%)	VMA (%)	VFA (%)	Layer
0	4.3	2.31928	2.44332	9.8	2.5	5.0767	14.4863	64.9552	**Wearing**
0	4.6	2.32671	2.43515	11	3	4.45315	14.4813	69.2489	
0	4.9	2.34109	2.4391	11.6	3.25	4.01853	14.2235	71.7473	
0	5.2	2.33742	2.43008	10.5	3.75	3.81288	14.6279	73.9342	
0	5.5	2.32691	2.4028	9.45	4	3.15831	15.2806	79.3313	
0	4	2.29989	2.433	8.54082	2.5	5.47121	14.2129	61.5052	**Levelling**
0	4.3	2.31681	2.43231	10.1449	2.75	4.74839	13.5815	65.0378	
0	4.6	2.32839	2.42614	10.5714	3.25	4.02894	13.1495	69.3606	
0	4.9	2.32209	2.41305	9.78571	3.75	3.76964	13.3847	71.8361	
0	5.2	2.3103	2.38804	8.36735	4.25	3.25511	13.8243	76.4537	
0	3.7	2.2861	2.43707	7.25	2.24	6.19473	14.5302	57.3664	**Base**
0	4	2.30292	2.4276	8.5	2.46	5.13569	14.1694	63.755	
0	4.3	2.31444	2.41825	8.9	2.92	4.29302	14.0099	69.3573	
0	4.6	2.30817	2.40903	8.3	3.37	4.18675	14.5115	71.1488	
0	4.9	2.29645	2.39993	7	3.8	4.31179	15.213	71.6572	

Table A-4 Marshal Test Result for Mix Layers 1 HL

HL	AC %	Density (g/cm3)	Gmm (g/cm3)	Stability (kN)	Flow (mm)	Air Voids (%)	VMA (%)	VFA (%)	Layer
1	4.3	2.31277	2.436539	10.21	2.5	5.079705	14.63223	65.28412	**Wearing**
1	4.6	2.324137	2.434819	10.8	2.75	4.5458	14.48158	68.60978	
1	4.9	2.339515	2.437343	12.13	3	4.013715	14.18644	71.70738	
1	5.2	2.33595	2.430298	11.32	3.5	3.882158	14.5875	73.38709	
1	5.5	2.32457	2.403742	10.44	3.75	3.293698	15.27257	78.4339	
1	4	2.304162	2.444697	8.93877551	2.25	5.748548788	13.98842	58.90493	**Levelling**
1	4.3	2.315835	2.445115	9.687755102	2.75	5.287253812	13.55267	60.98737	
1	4.6	2.326365	2.437453	10.32244898	3	4.557550282	13.15961	65.36714	
1	4.9	2.325616	2.425889	10.30408163	3.25	4.133448113	13.18757	68.65649	
1	5.2	2.316424	2.403162	9.23877551	4	3.609338581	13.5307	73.32481	
1	4	2.304162	2.444697	8.93877551	2.25	5.748548788	13.98842	58.90493	**Base**
1	4.3	2.315835	2.445115	9.687755102	2.75	5.287253812	13.55267	60.98737	
1	4.6	2.326365	2.437453	10.32244898	3	4.557550282	13.15961	65.36714	
1	4.9	2.325616	2.425889	10.30408163	3.25	4.133448113	13.18757	68.65649	
1	5.2	2.316424	2.403162	9.23877551	4	3.609338581	13.5307	73.32	

Table A-5 Marshal Test Result for Mix Layers 1.5 HL

HL	AC %	Density (g/cm3)	Gmm (g/cm3)	Stability (kN)	Flow (mm)	Air Voids (%)	VMA (%)	VFA (%)	Layer
1.5	4.3	2.310986	2.439976	9.8	2.25	5.286527	14.65103	63.91704	**Wearing**
1.5	4.6	2.321004	2.434387	10.6	2.5	4.657559	14.54976	67.98877	
1.5	4.9	2.332536	2.431891	12.5	2.75	4.085504	14.39525	71.61908	
1.5	5.2	2.333408	2.42088	11.3	3.25	3.613232	14.63339	75.30831	
1.5	5.5	2.321704	2.402448	10.4	3.5	3.360905	15.33037	78.07681	
1.5	4	2.297904	2.446707	9.510204082	2	6.081785362	14.18964	57.13924	**Levelling**
1.5	4.3	2.307337	2.443113	10.22857143	2.5	5.557501846	13.83738	59.83705	
1.5	4.6	2.317936	2.433511	10.79183673	2.75	4.74929949	13.44157	64.66707	
1.5	4.9	2.321594	2.425199	10.20408163	3	4.272037442	13.30497	67.89142	
1.5	5.2	2.307622	2.398722	9.612244898	3.75	3.797884797	13.82673	72.53231	
1.5	3.7	2.284128	2.433408	8	1.8	6.134606281	14.46361	57.58593	**Base**
1.5	4	2.293504	2.423974	8.65	2.2	5.382483475	14.38006	62.56981	
1.5	4.3	2.30404	2.414667	9.16	2.4	4.581459887	14.25553	67.86187	
1.5	4.6	2.307676	2.405483	8.4	2.65	4.066002545	14.38943	71.74313	
1.5	4.9	2.293788	2.396421	8.14	3.37	4.282761668	15.17224	71.77239	

Table A-6 Marshal Test Result for Mix Layers 2 HL

HL	AC %	Density (g/cm3)	Gmm (g/cm3)	Stability (kN)	Flow (mm)	Air Voids (%)	VMA (%)	VFA (%)	Layer
2	4.3	2.306179	2.443825	9.44	2	5.6324	14.78167	61.89605	**Wearing**
2	4.6	2.313414	2.435259	11.23	2.5	5.003369	14.7823	66.15297	
2	4.9	2.326401	2.438339	13.8	2.75	4.590748	14.57339	68.49911	
2	5.2	2.330798	2.431671	14.4	3	4.1483	14.68193	71.74553	
2	5.5	2.316994	2.408957	11.87	3.5	3.817544	15.45561	75.29995	
2	4	2.295528	2.445706	9.142857143	2	6.140495495	14.246	56.8967	**Levelling**
2	4.3	2.306988	2.448118	10.34693878	2.25	5.764835225	13.81789	58.27991	
2	4.6	2.316396	2.437464	11.50408163	2.5	4.966974913	13.46643	63.11587	
2	4.9	2.319	2.424651	11.19591837	3	4.357382342	13.36915	67.4072	
2	5.2	2.311763	2.403508	9.912244898	3.5	3.817136766	13.63951	72.01412	
2	3.7	2.281766	2.43219	7.76	1.75	6.184714188	14.50535	57.36254	**Base**
2	4	2.293158	2.422769	8.75	2	5.349705234	14.34618	62.70989	
2	4.3	2.302509	2.413474	9.74	2.25	4.597729248	14.26566	67.77065	
2	4.6	2.305098	2.404303	9.5	2.7	4.126143835	14.43832	71.42227	
2	4.9	2.297904	2.395253	8.4	3.15	4.064247075	14.97357	72.8572	

Table A-7 Marshal Test Result for Mix Layers 2.5 HL

HL	AC %	Density (g/cm3)	Gmm (g/cm3)	Stability (kN)	Flow (mm)	Air Voids (%)	VMA (%)	VFA (%)	Layer
2.5	4.3	2.29961	2.448482	9.25	2	6.080175	14.97763	59.40495	Wearing
2.5	4.6	2.30868	2.443248	11.24	2.25	5.50775	14.90986	63.05969	
2.5	4.9	2.31722	2.433453	12.93	2.5	4.776464	14.86368	67.86486	
2.5	5.2	2.318507	2.422751	13.7	2.75	4.302712	15.08511	71.47709	
2.5	5.5	2.311843	2.408141	10.23	3	3.998852	15.59712	74.36161	
2.5	4	2.291477	2.452713	9.571429	1.75	6.573785	14.36501	54.23752	Levelling
2.5	4.3	2.303903	2.444634	9.77551	2	5.756716	13.90062	58.58662	
2.5	4.6	2.311019	2.432759	10.83673	2.25	5.004189	13.63469	63.29811	
2.5	4.9	2.311443	2.422649	12.55102	2.75	4.590281	13.61888	66.29471	
2.5	5.2	2.298328	2.39576	9.23152	3.25	4.066825	14.10897	71.17561	
2.5	3.7	2.27774	2.430973	8.15	1.56	6.303361	14.60956	56.85453	Base
2.5	4	2.290091	2.421565	8.3	1.8	5.429299	14.41398	62.33311	
2.5	4.3	2.29961	2.448482	9.25	2	6.080175	14.97763	59.40495	
2.5	4.6	2.30868	2.443248	11.24	2.25	5.50775	14.90986	63.05969	
2.5	4.9	2.31722	2.433453	12.93	2.5	4.776464	14.86368	67.86486	

Table A-8 Marshal Test Result for Mix Layers 3 HL

HL	AC %	Density (g/cm3)	Gmm (g/cm3)	Stability (kN)	Flow (mm)	Air Voids (%)	VMA (%)	VFA (%)	Layer
3	4.3	2.288804	2.444398	9.6	1.75	6.36533	15.33057	58.4795	Wearing
3	4.6	2.297582	2.438534	10.85	2	5.780194	15.27229	62.1524	
3	4.9	2.306516	2.432704	11.6	2.25	5.18715	15.2103	65.89713	
3	5.2	2.312002	2.422193	12.02	2.5	4.549225	15.27675	70.22124	
3	5.5	2.300483	2.398792	10	2.75	4.098271	15.96563	74.33067	
3	4	2.281174	2.453714	8.408163265	1.5	7.031780543	14.71787	52.22284	Levelling
3	4.3	2.291805	2.452422	9.469387755	1.75	6.549320864	14.32044	54.26593	
3	4.6	2.305349	2.435762	10.69387755	2	5.354117457	13.81411	61.24166	
3	4.9	2.300763	2.41364	11.06122449	2.5	4.676629936	13.98554	66.56097	
3	5.2	2.298607	2.407772	8.653061224	3	4.53382763	14.06613	67.76777	
3	3.7	2.267498	2.429757	7.2	1.35	6.677992902	14.9471	55.32248	Base
3	4	2.278066	2.420362	8	1.57	5.879120561	14.81689	60.3215	
3	4.3	2.28697	2.411092	9.1	1.75	5.147957855	14.75119	65.1014	
3	4.6	2.291528	2.401946	9.4	2.23	4.597022581	14.84905	69.04165	
3	4.9	2.284827	2.392921	7.35	2.75	4.517240644	15.36504	70.6	

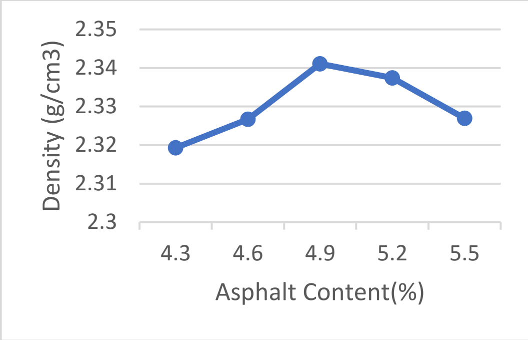

Density

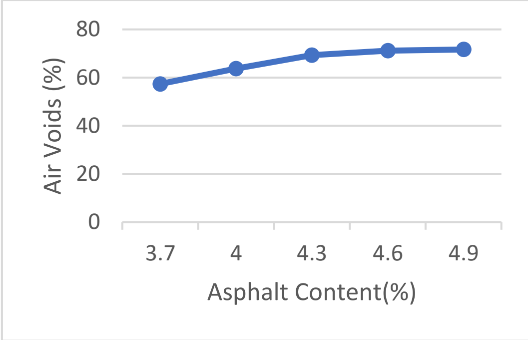

Air Voids (AV)

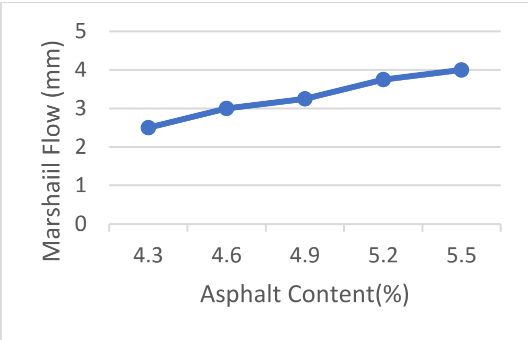

Marshall Flow

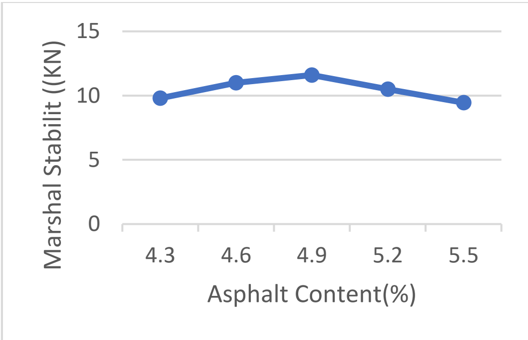

Marshall Stability

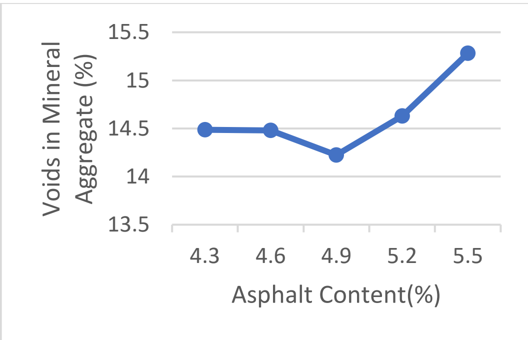

Voids in Mineral Aggregate (VMA)

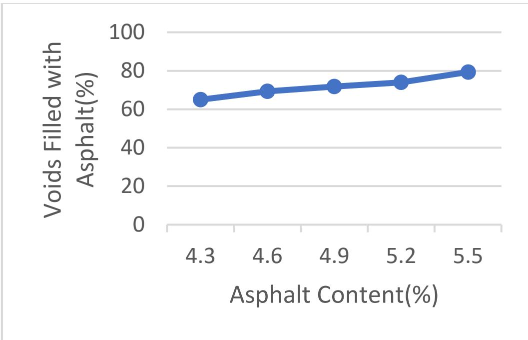

Voids Filled with Asphalt (VFA)

Figure A-7 Marshall Mix Design Properties for 0 HL Wearing (CW) Mixture

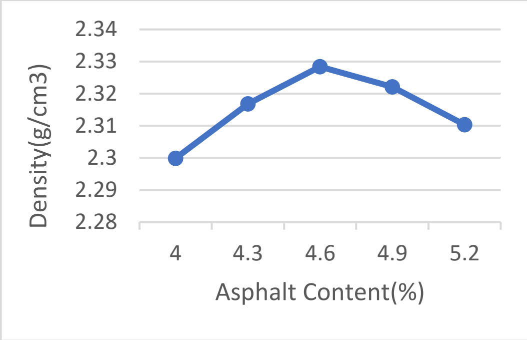

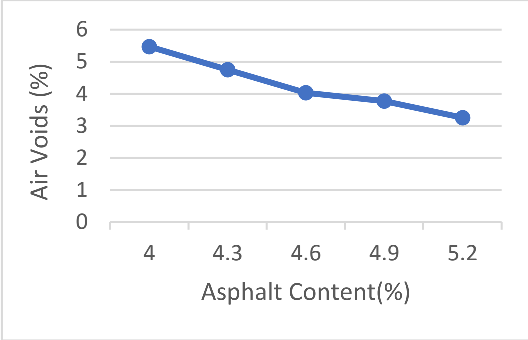

Density

Air Voids (AV)

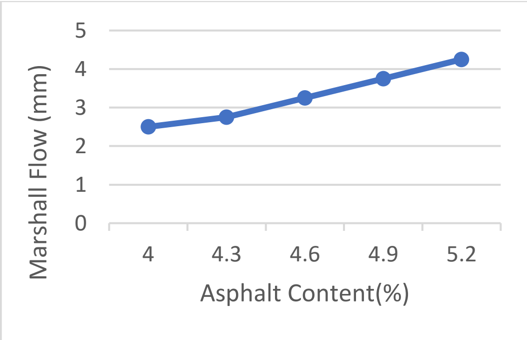

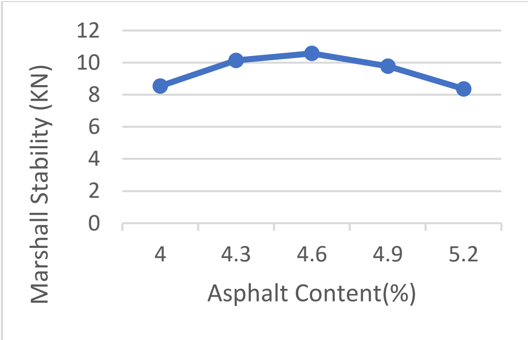

Marshall Flow

Marshall Stability

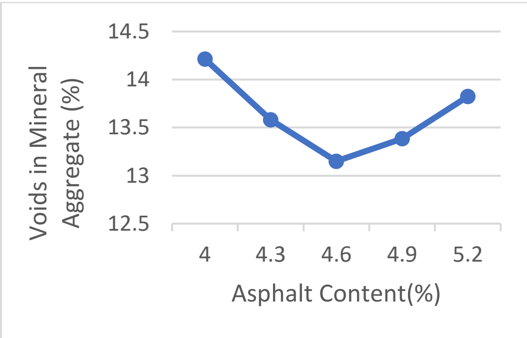

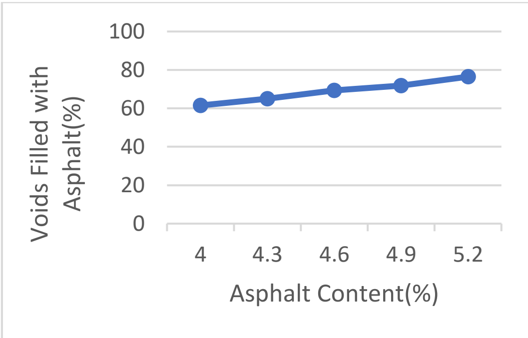

Voids in Mineral Aggregate (VMA)

Voids Filled with Asphalt (VFA)

Figure A-8 Marshall Mix Design Properties for 0 HL Leveling (CL) Mixture

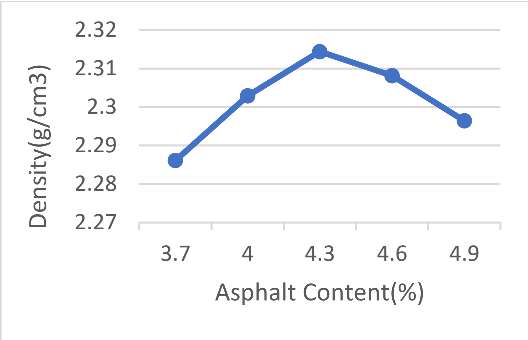

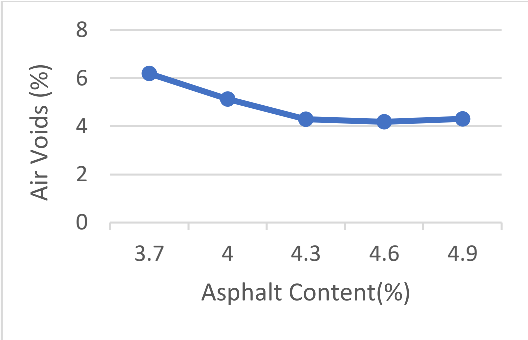

Density

Air Voids (AV)

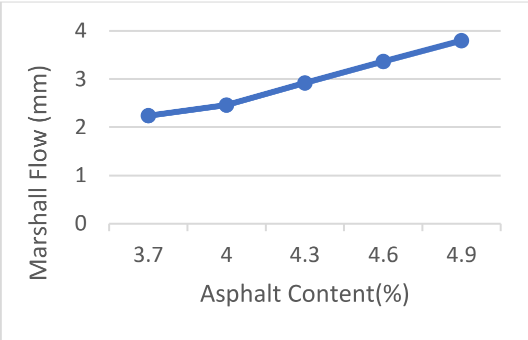

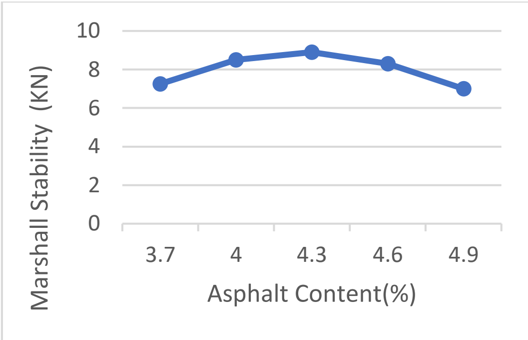

Marshall Flow

Marshal Stability

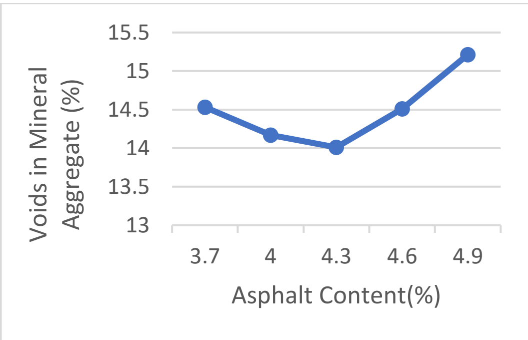

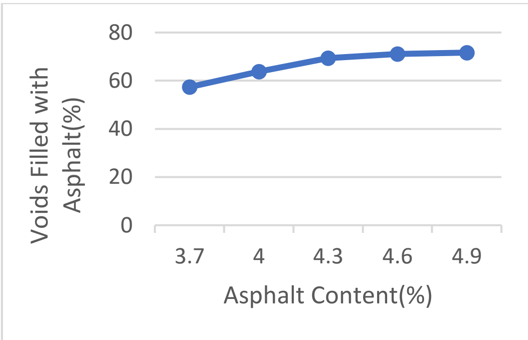

Voids in Mineral Aggregate (VMA) Voids Filled with Asphalt (VFA)

Figure A-9 Marshall Mix Design Properties for 0 HL Base (CB) Mixture

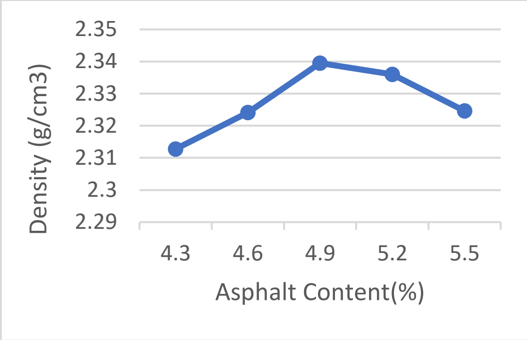

Density

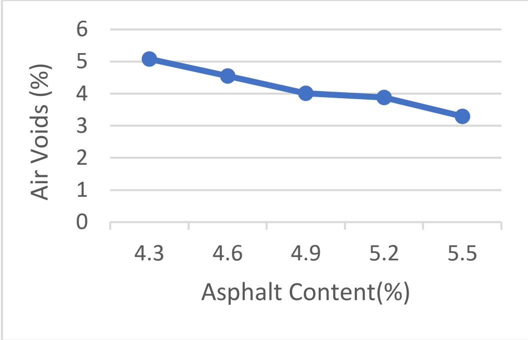

Air Voids

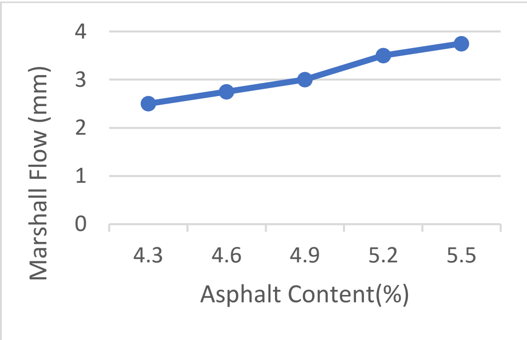

Marshall Flow

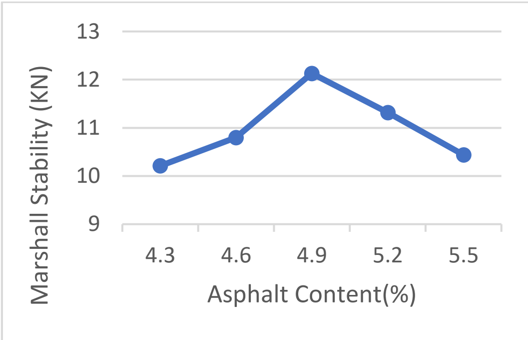

Marshall Stability

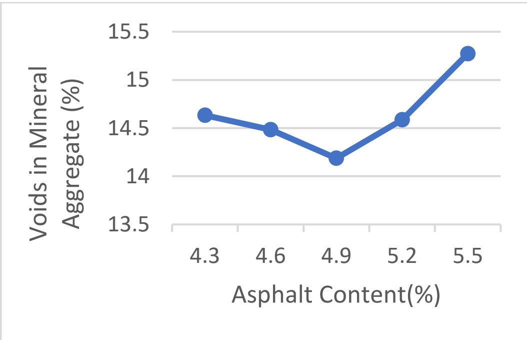

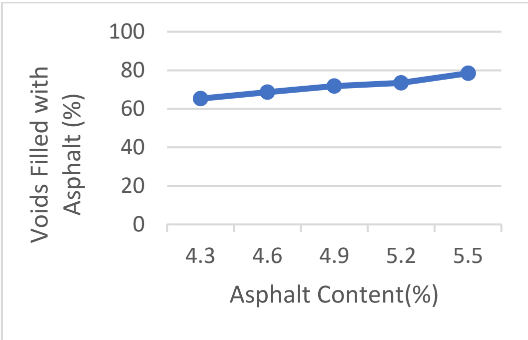

Voids in Mineral Aggregate (VMA) Voids Filled with Asphalt (VFA)

Figure A-10 Marshall Mix Design Properties for 1% HL Wearing Mixture

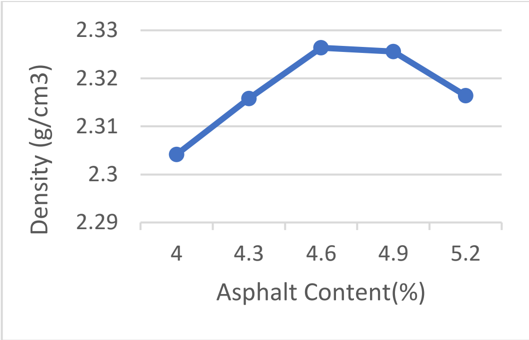

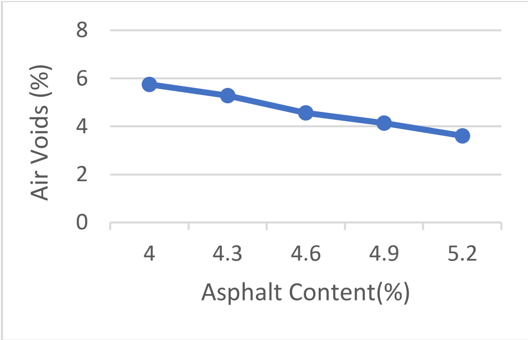

Density

Air Voids (AV)

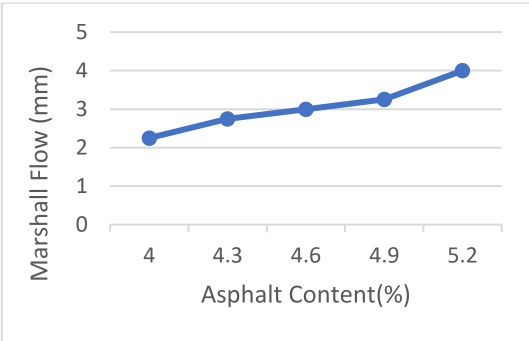

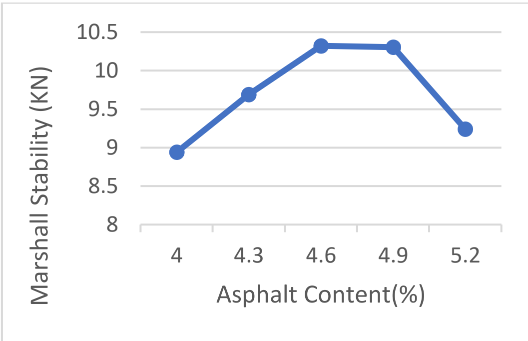

Marshall Flow

Marshall Stability

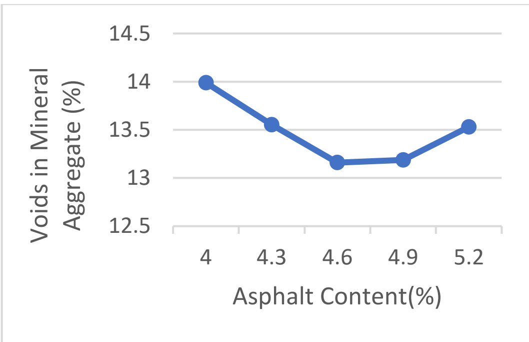

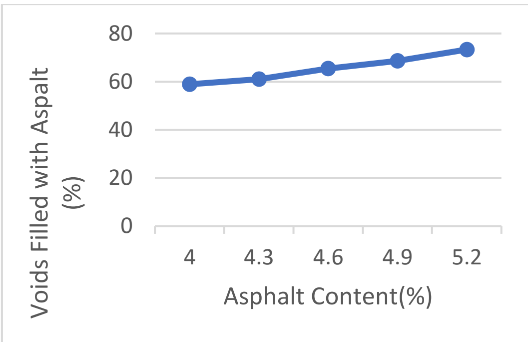

Voids in Mineral Aggregate (VMA) Voids Filled with Asphalt (VFA)

Figure A-11 Marshall Mix Design Properties for 1% HL Leveling Mixture

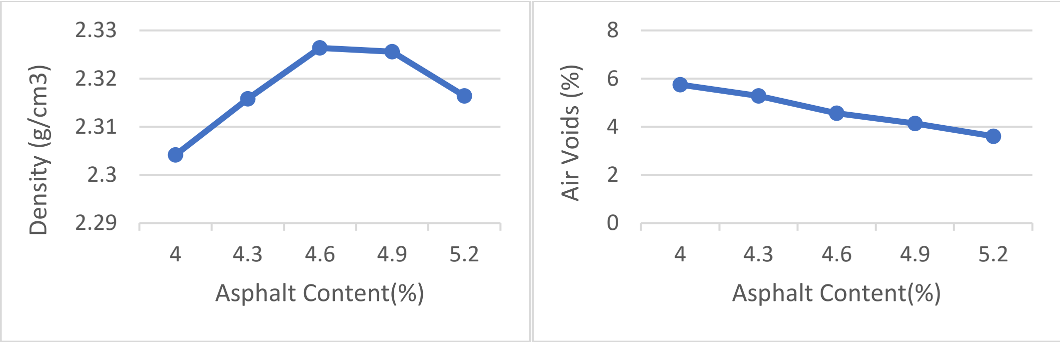

Density Air Voids (AV)

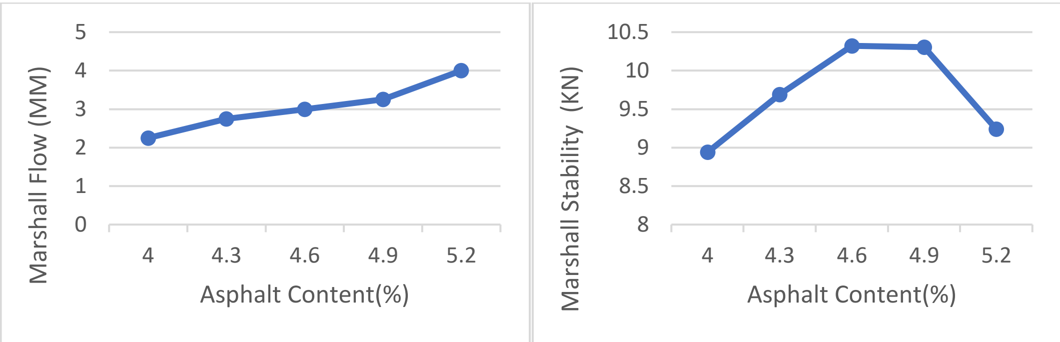

Marshall Flow Marshall Stability

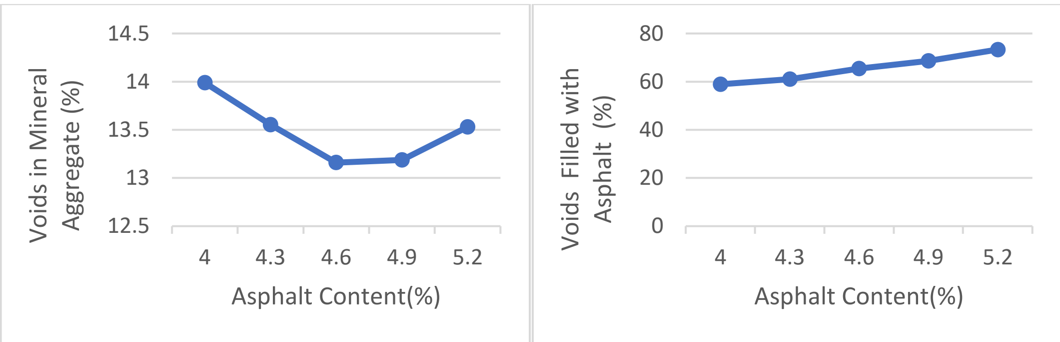

Voids in Mineral Aggregate (VMA) Voids Filled with Asphalt (VFA)

Figure A-12 Marshall Mix Design Properties for 1% HL Base Mixture

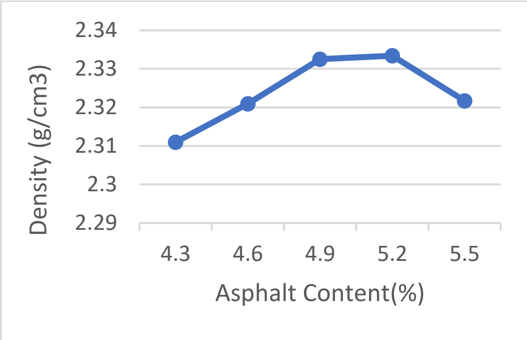

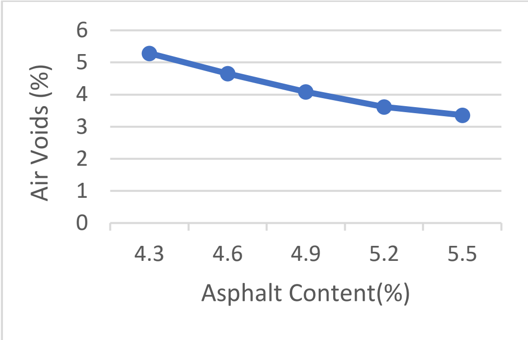

Density Air Voids (AV)

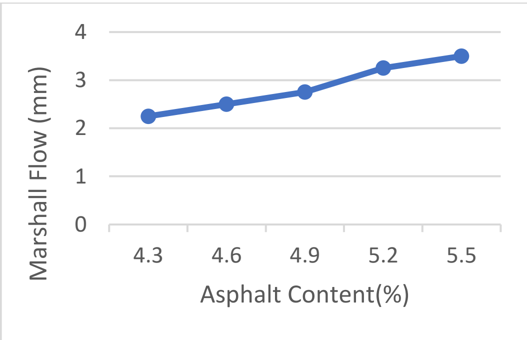

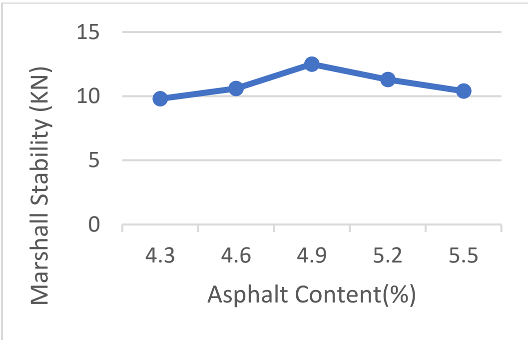

Marshall Flow Marshall Stability

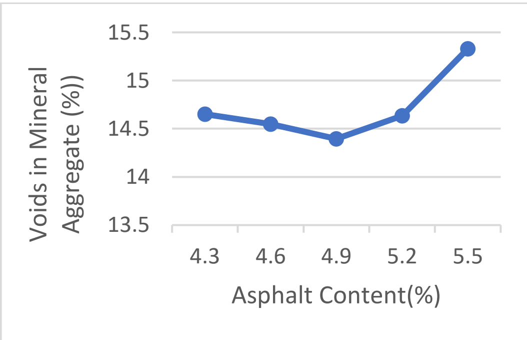

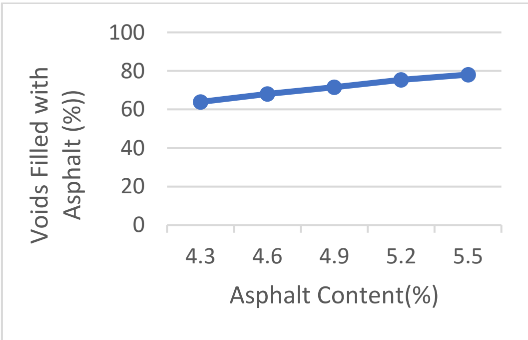

Voids in Mineral Aggregate (VMA) Voids Filled with Asphalt (VFA)

Figure A-13 Marshall Mix Design Properties for 1.5% Wearing Mixture

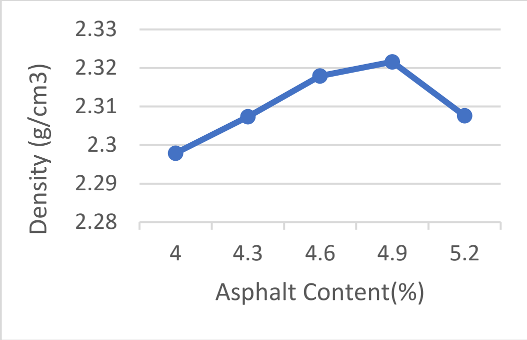

Density

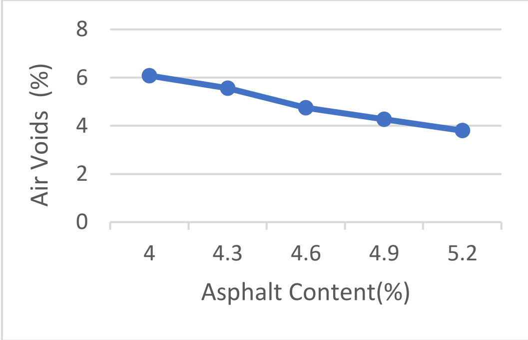

Air Voids (AV)

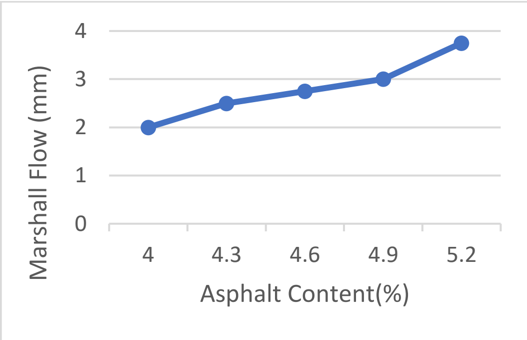

Marshall Flow

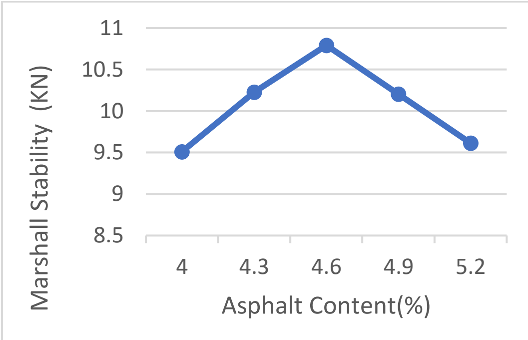

Marshall Stability

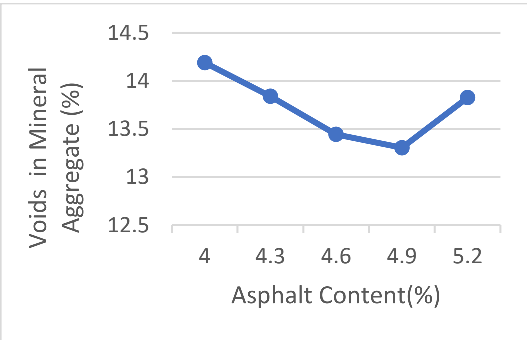

Voids in Mineral Aggregate (VMA)

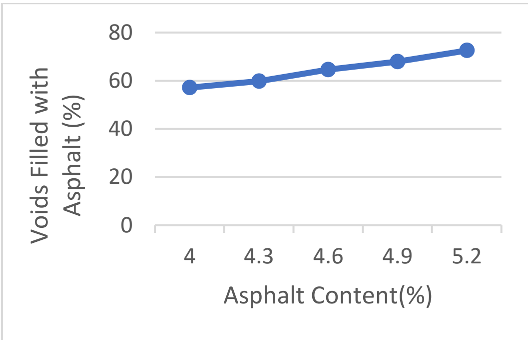

Voids Filled with Asphalt (VFA)

Figure A- 14 Marshall Mix Design Properties for 1.5% HL levelling Mixture

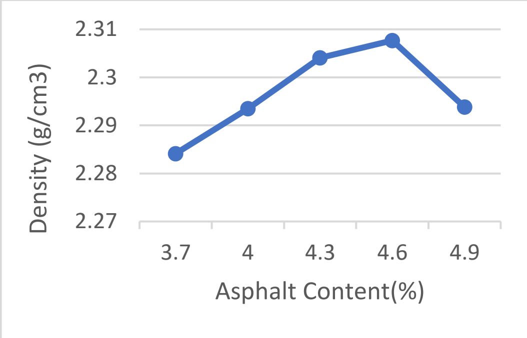

Density

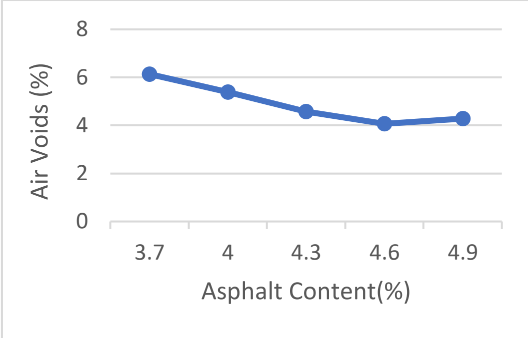

Air Voids (AV)

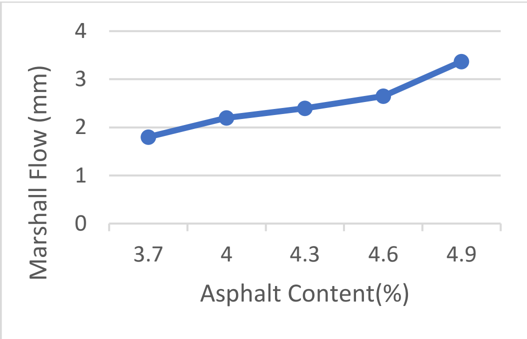

Marshall Flow

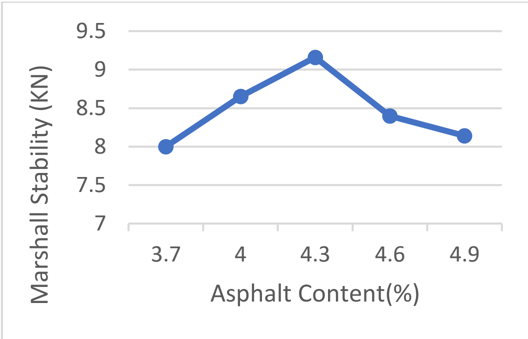

Marshall Stability

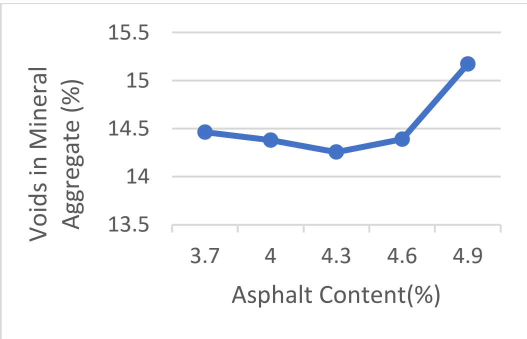

Voids in Mineral Aggregate (VMA)

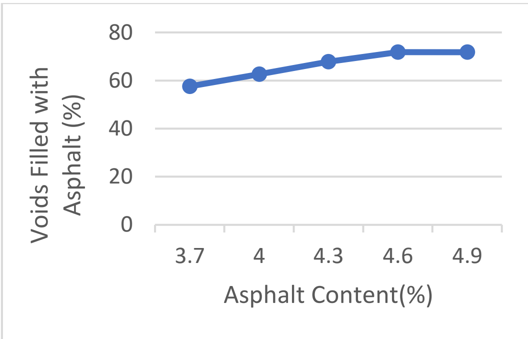

Voids Filled with Asphalt (VFA)

Figure A-15 Marshall Mix Design Properties for 1.5% HL Base Mixture

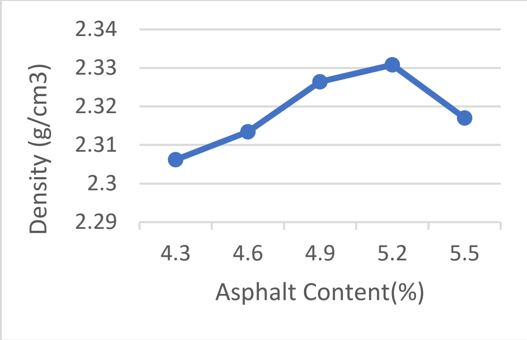

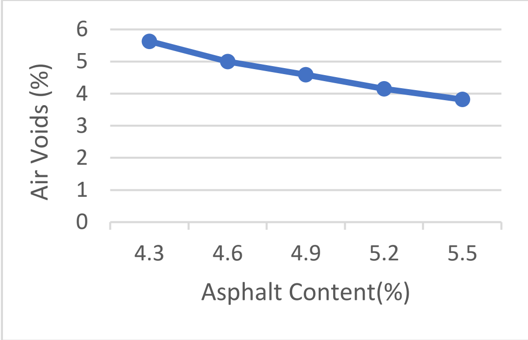

Density Air Voids (AV)

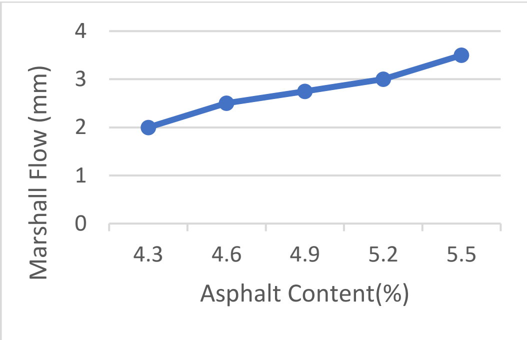

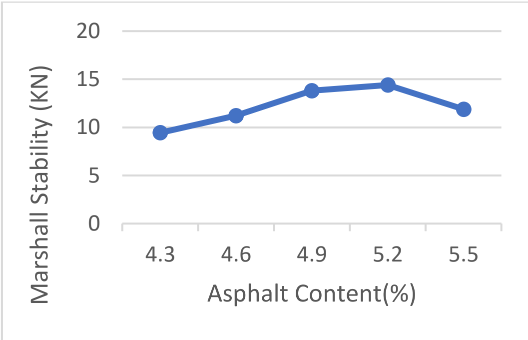

Marshall Flow Marshall Stability

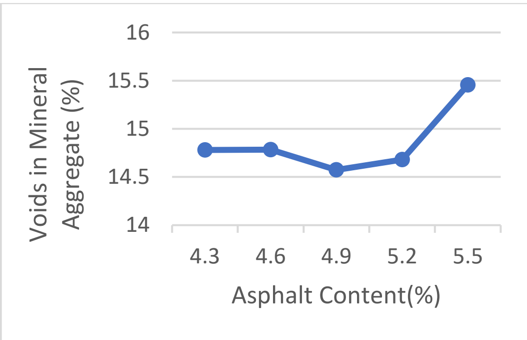

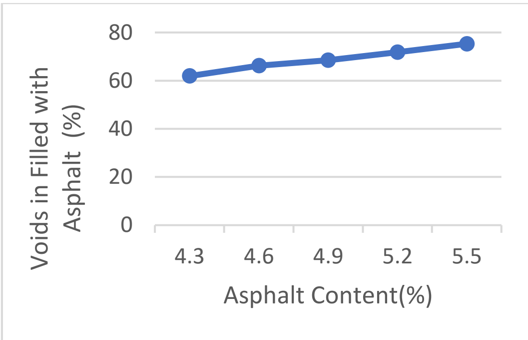

Voids in Mineral Aggregate (VMA) Voids Filled with Asphalt (VFA)

Figure A-16 Marshall Mix Design Properties for 2% HL Wearing Mixture

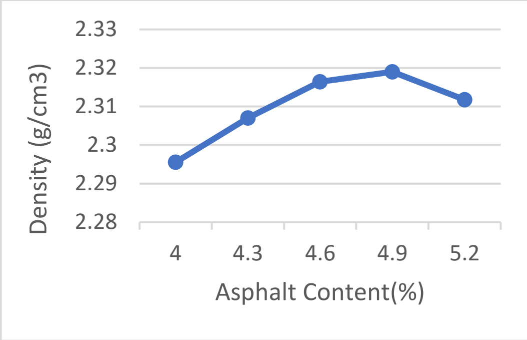

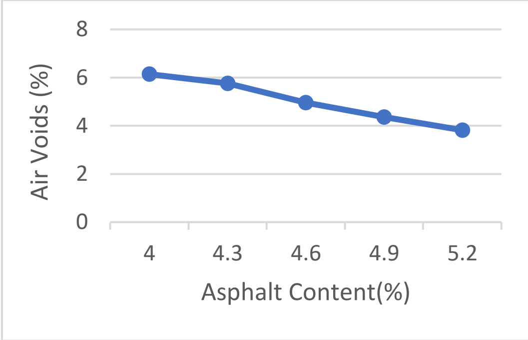

Density Air Voids (AV)

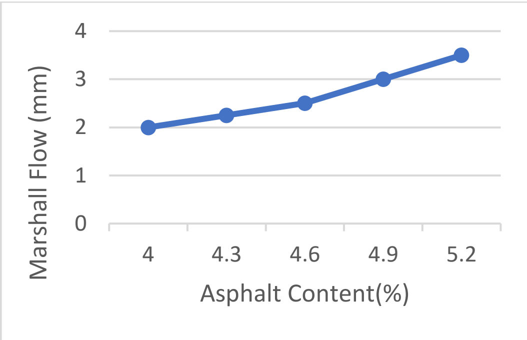

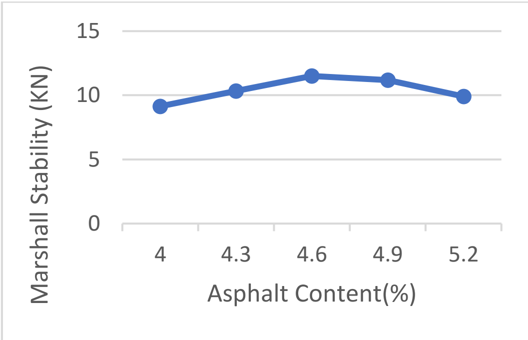

Marshall Flow Marshall Stability

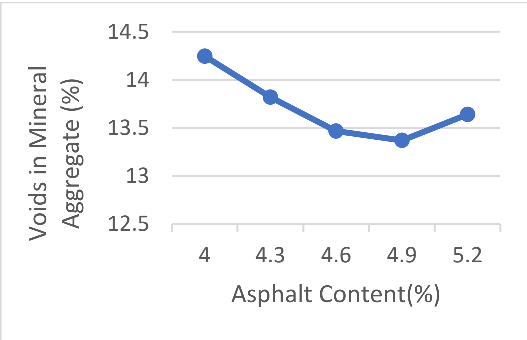

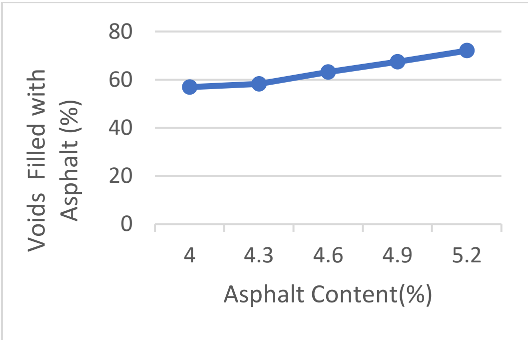

Voids in Mineral Aggregate (VMA) Voids Filled with Asphalt (VFA)

Figure A-17 Marshall Mix Design Properties for 2% HL Leveling Mixture

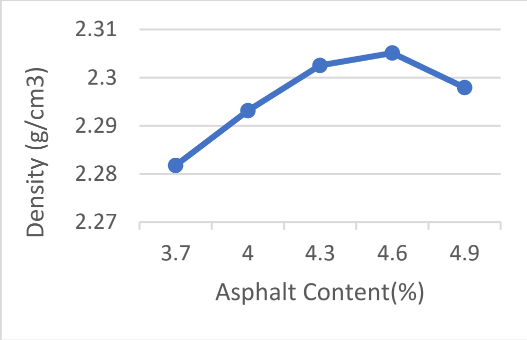

Density

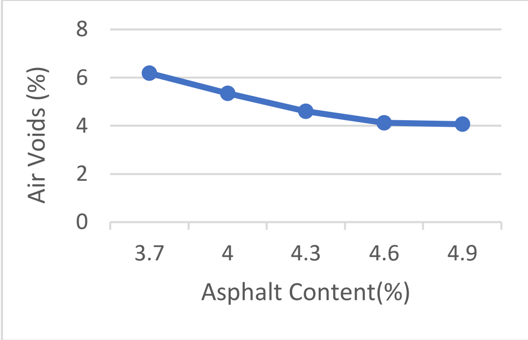

Air Voids (%)

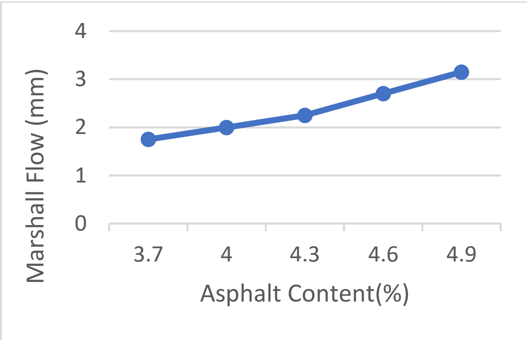

Marshall Flow

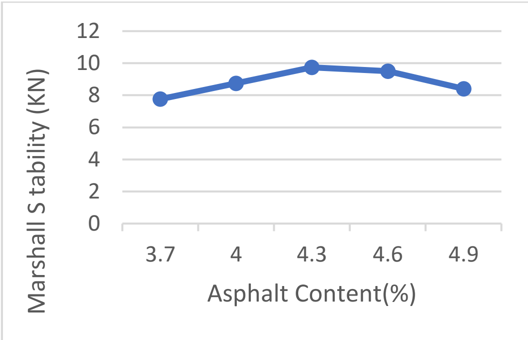

Marshall Stability

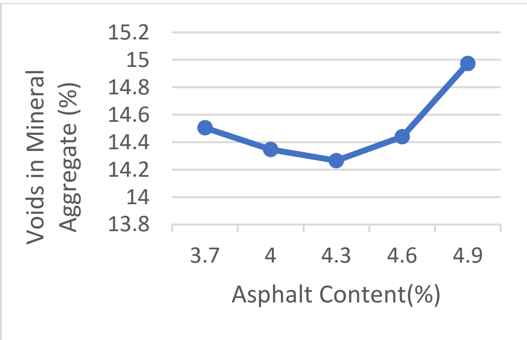

Voids in Mineral Aggregate (VMA)

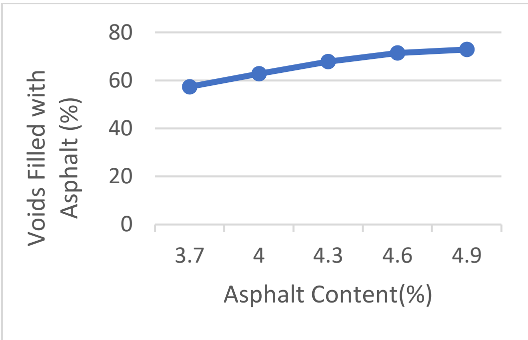

Voids Filled with Asphalt (VFA)

Figure A-18 Marshall Mix Design Properties for 2% HL Base Mixture

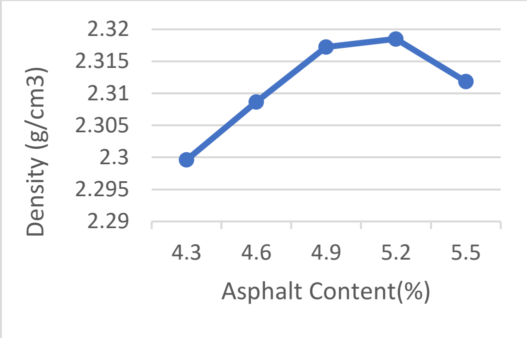

Density

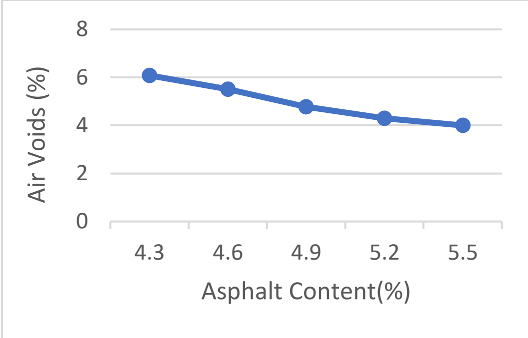

Air Voids (AV)

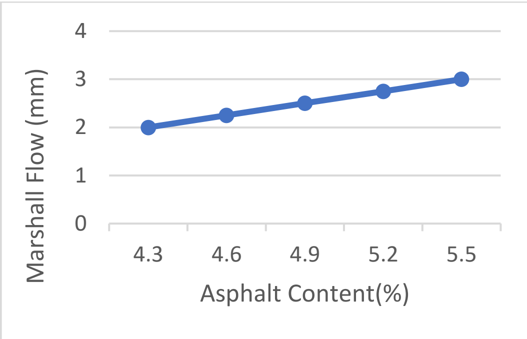

Marshall Flow

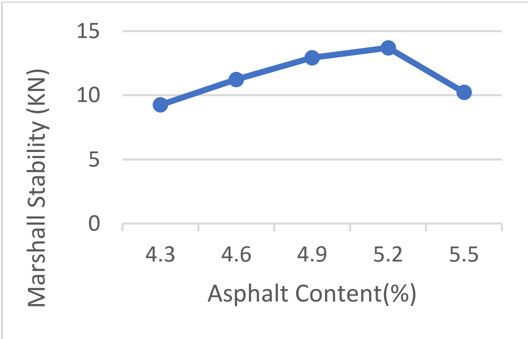

Marshall Stability

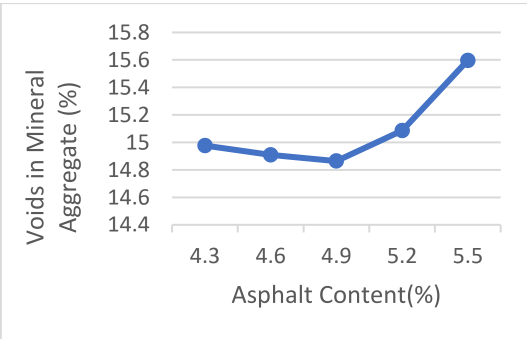

Voids in Mineral Aggregate (VMA)

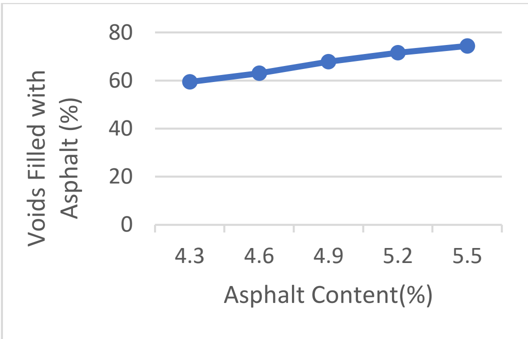

Voids Filled with Asphalt

Figure A-19 Marshall Mix Design Properties for 2.5% HL Wearing Mixture

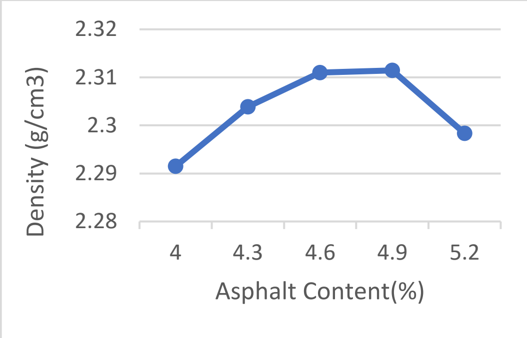

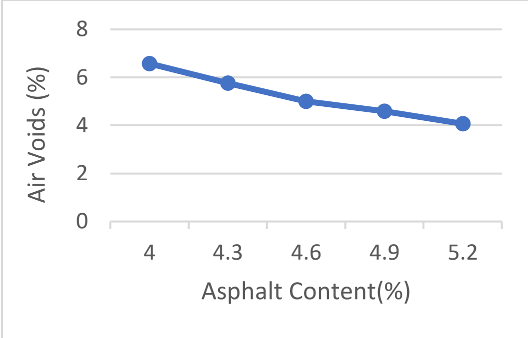

Density Air voids (AV)

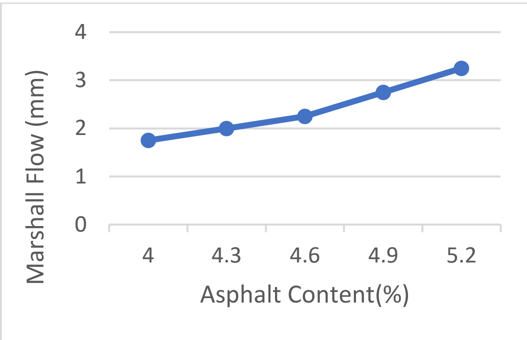

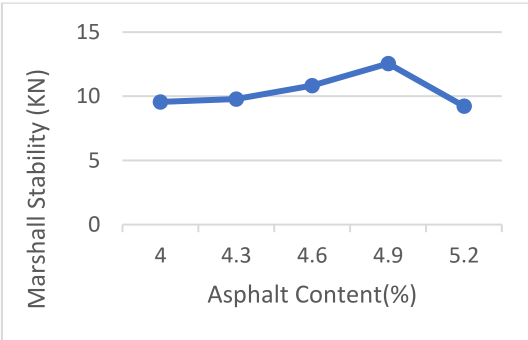

Marshall Flow Marshall Stability

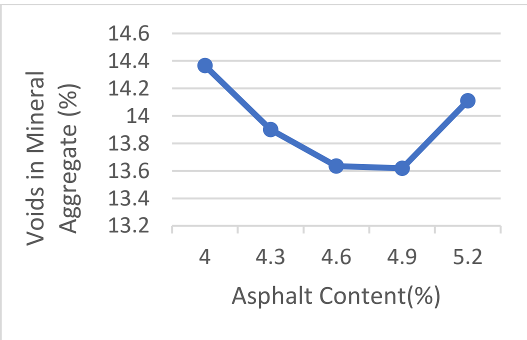

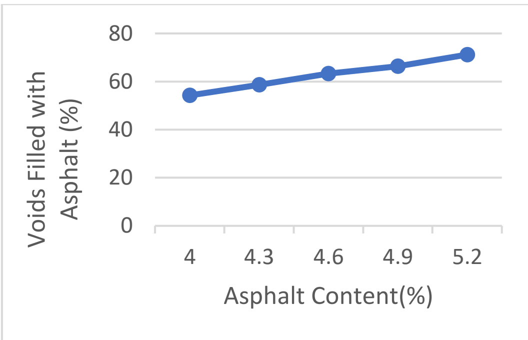

Voids in Mineral Aggregate (VMA) Voids Filled with Aggregate (VFA)

Figure A-20 Marshall Mix Design Properties for 2.5% HL Levelling Mixture

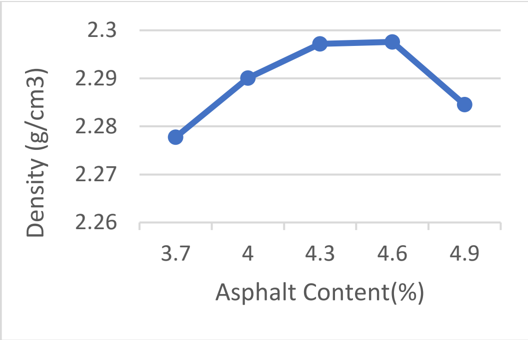

Density

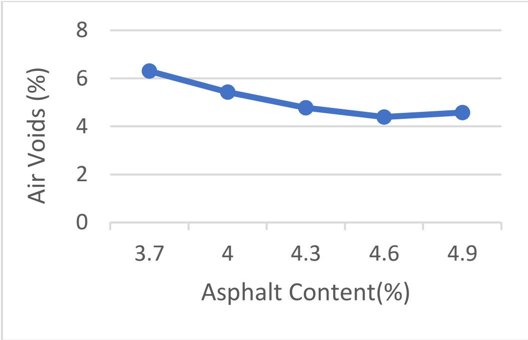

Air Voids (AV)

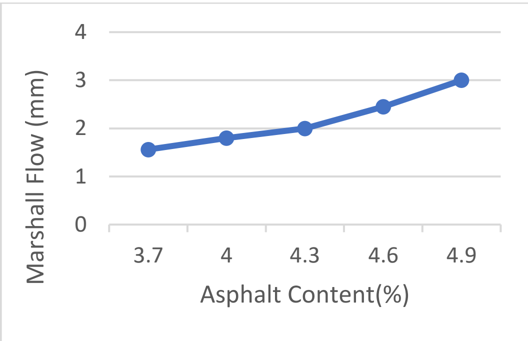

Marshall Flow

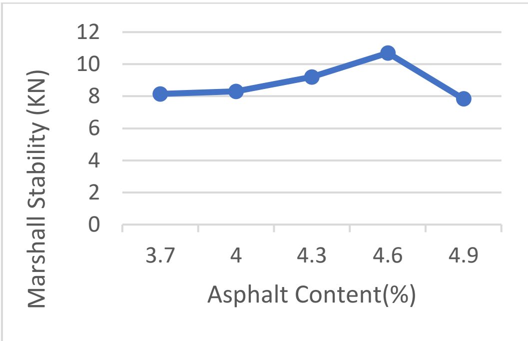

Marshall Stability

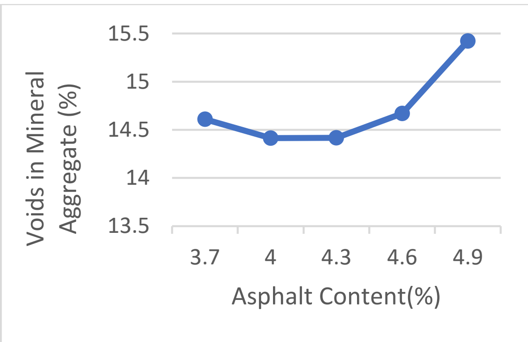

Voids in Mineral Aggregate (VMA)

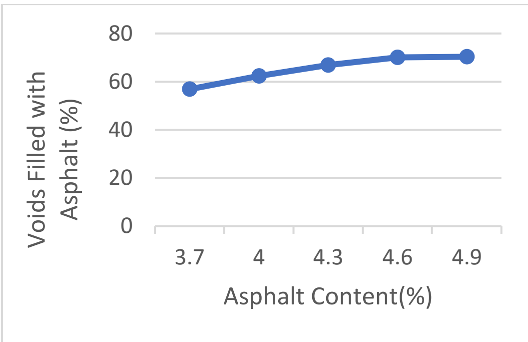

Voids Filled with Asphalt (VFA)

Figure A- 21 Marshall Mix Design Properties for 2.5% HL Base Mixture

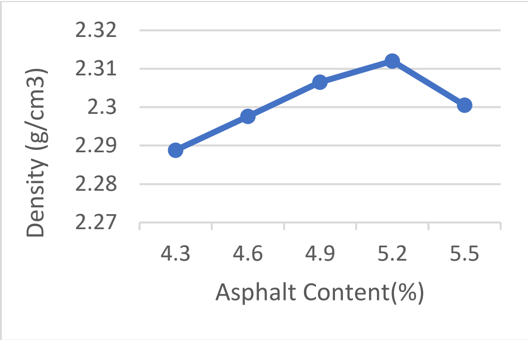

Density

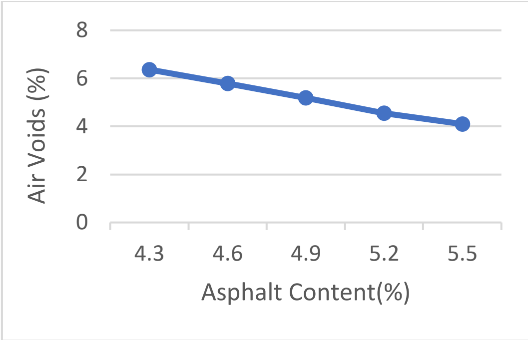

Air Voids (AV)

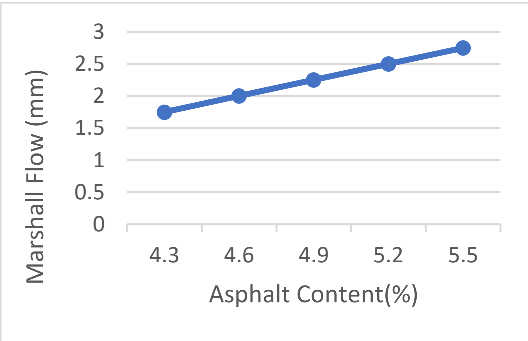

Marshall Flow

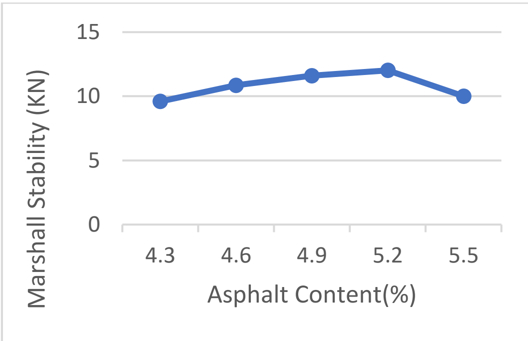

Marshall Stability

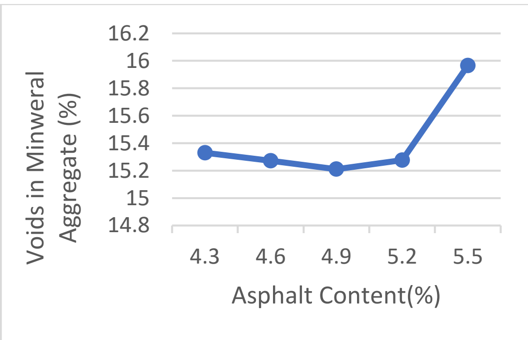

Voids in Mineral Aggregate (VMA)

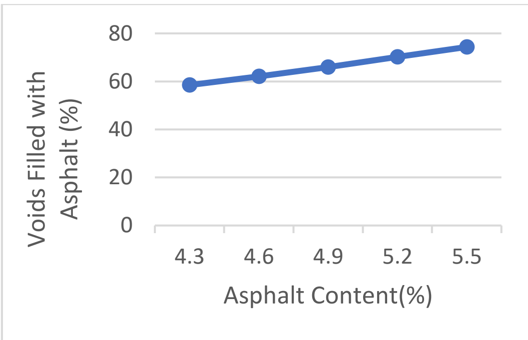

Voids Filled with Asphalt (VFA)

Figure A-22 Marshall Mix Design Properties for 3% HL Wearing Mixture

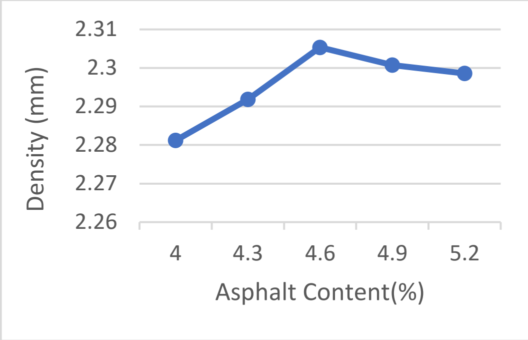

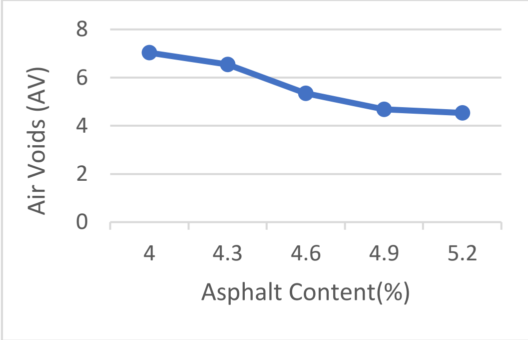

Density Air Void (AV)

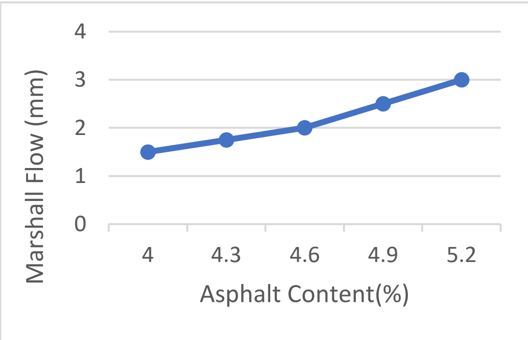

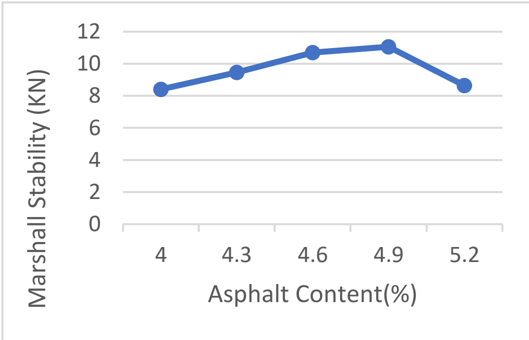

Marshall Flow Marshall Stability

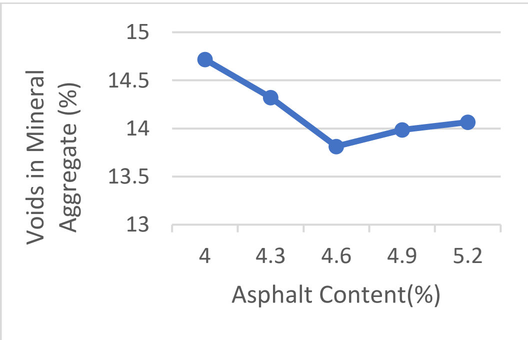

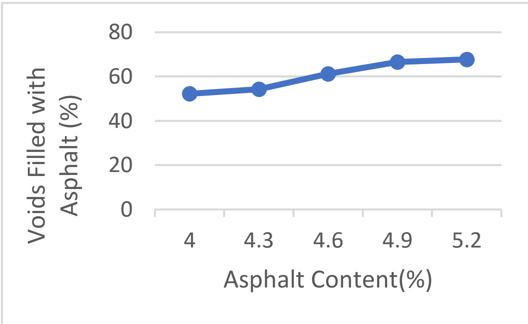

Voids in Mineral Aggregate (VMA) Voids Filled with Asphalt (VFA)

Figure A-23 Marshall Mix Design Properties for 3% HL Leveling Mixture

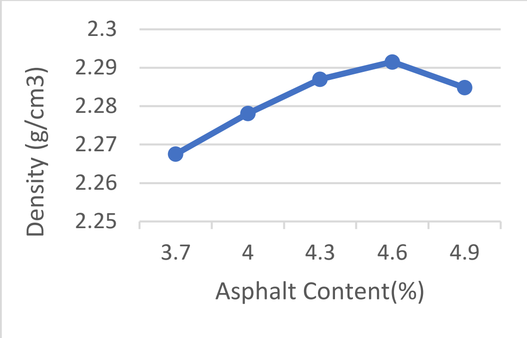

Density

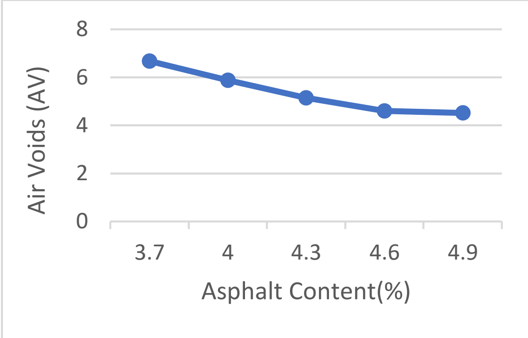

Air Void (AV)

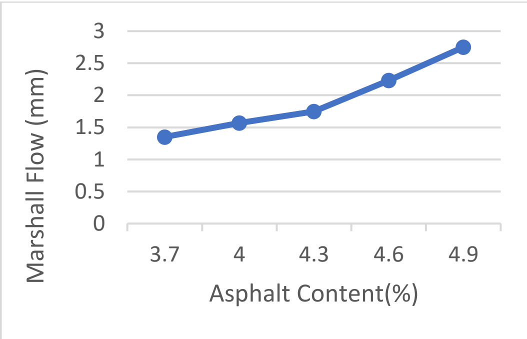

Marshall Flow

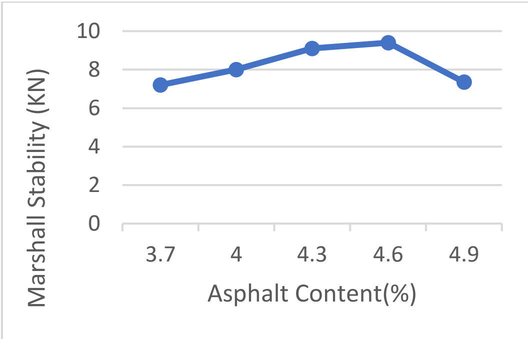

Marshall Stability

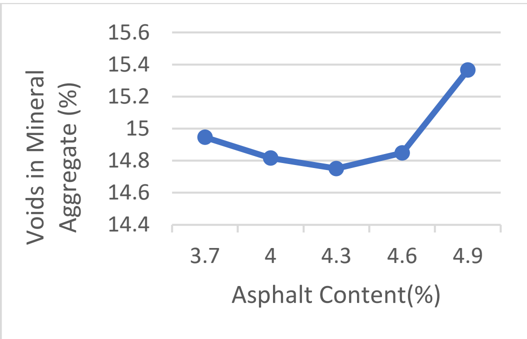

Voids in Mineral Aggregate (VMA)

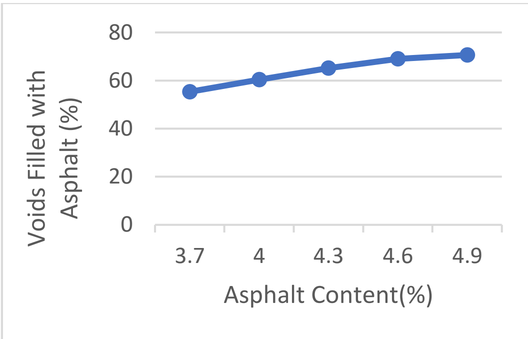

Voids Filled with ASPHALT(VFA)

Figure A-24 Marshall Mix Design Properties for 3% HL Base Mixture

Triaxial Test Results

Tables from Table A-9 -Table presented the triaxial test result for all layers in both mixes 2.5 %HL and 0%HL at temperatures degree 20°C, 40°C and 60°C and deviator pressure. 68.9 (kPa), 137.9 (kPa) and 206.9 (kPa).

The acquired deformation data analyses include the following.

- Determination of the permanent deformation at the following load repetitions: 1,2,10,100,500,1000,2000,3000,4000,5000,6000,7000,8000,9000 and 10000

$$\boldsymbol{\varepsilon_p = \frac{pd \times 10^6}{h}}$$

Where:

ε_p= Axial Permanent Micro strain, pd = Axial Permanent Deformation and h = Specimen Height

- **The resilient strain (ε_r) and resilient modulus (M_r) are calculated as follows:**

The resilient displacement is determined at the load repetition of 50 to 100.

$$\boldsymbol{\varepsilon_r = \frac{rd \times 10^6}{h}}$$

Where: ε_r = Axial Resilient Microstrain, rd = axial resilient deformation and h = Specimen Height

$$M_r = \frac{\sigma}{\varepsilon_r}$$

Where: M_r= Resilient modulus (psi), σ = repeated Axial Stress (psi) and ε_r = axial resilient strain.

Table A-9 Triaxial Cyclic Compression Test for 68.9 (kPa) at 20°C Wearing 0% HL

	AASHTOT307 Triaxial Cyclic Compression test (conducted at 20°C)														
Mix Type	0%HL-W														
Diameter (mm)	101.6mm														
Specimen Height (mm)	152.4 mm														
Bulk Density (g/cm^3)	2.340														
Height of Block Pulse (kPa)	68.9														
Confining Stress (kPa)	0														
Deviator Stress (KPa)	68.9														
Number of Load Repetition	1	2	10	100	500	1000	2000	3000	4000	5000	6000	7000	8000	9000	10000
Axial Permanent Microstrain	29	30	33	37	41	42	44	45	46	46	47	47	47	48	49
Axial Resilient Microstrain	25	25	24	25	25	25	25	25	25	25	26	26	25	25	25

Table A-10 Triaxial Cyclic Compression Test for 68.9 (kPa) at 20°C) Leveling 0% HL

	AASHTOT307 Triaxial Cyclic Compression test (conducted at 20°C)														
Mix Type	0%HL-L														
Diameter (mm)	101.6mm														
Specimen Height (mm)	152.4 mm														
Bulk Density (g/cm^3)	2.320														
Height of Block Pulse (kPa)	68.9														
Confining Stress (kPa)	0														
Deviator Stress (KPa)	68.9														
Number of Load Repetition	1	2	10	100	500	1000	2000	3000	4000	5000	6000	7000	8000	9000	10000
Axial Permanent Microstrain	34	36	40	47	52	55	57	59	60	16	62	62	63	63	64
Axial Resilient Microstrain	30	30	30	30	30	30	30	30	30	30	30	30	30	31	31

Table A-11 Triaxial Cyclic Compression Test for 68.9 (kPa) at 20°C Base 0%HL

	AASHTOT307 Triaxial Cyclic Compression test (conducted at 20°C)														
Mix Type	0%HL-B														
Diameter (mm)	101.6mm														
Specimen Height (mm)	152.4 mm														
Bulk Density (g/cm^3)	2.310														
Height of Block Pulse (kPa)	68.9														
Confining Stress (kPa)	0														
Deviator Stress (KPa)	68.9														
Number of Load Repetition	1	2	10	100	500	1000	2000	3000	4000	5000	6000	7000	8000	9000	10000
Axial Permanent Microstrain	37	39	44	53	61	64	68	69	71	72	73	74	75	76	77
Axial Resilient Microstrain	38	38	38	38	39	39	39	39	40	40	40	40	40	40	40

Table A-12 Triaxial Cyclic Compression Test for 68.9 (kPa) at 40°C Wearing 0% HL

	AASHTOT307 Triaxial Cyclic Compression test (conducted at 40°C)														
Mix Type	0%HL-W														
Diameter (mm)	101.6mm														
Specimen Height (mm)	152.4 mm														
Bulk Density (g/cm^3)	2.340														
Height of Block Pulse (kPa)	68.9														
Confining Stress (kPa)	0														
Deviator Stress (KPa)	68.9														
Number of Load Repetition	1	2	10	100	500	1000	2000	3000	4000	5000	6000	7000	8000	9000	10000
Axial Permanent Microstrain	69	82	135	164	336	405	449	510	532	562	586	600	630	630	694
Axial Resilient Microstrain	30	30	30	30	30	31	31	31	31	31	31	31	31	31	31

Table A-13 Triaxial Cyclic Compression Test for 68.9 (kPa) at 40°C leveling 0% HL

	AASHTOT307 Triaxial Cyclic Compression test (conducted at 40°C)														
Mix Type	0%HL-L														
Diameter (mm)	101.6mm														
Specimen Height (mm)	152.4 mm														
Bulk Density (g/cm3)	2.320														
Height of Block Pulse (kPa)	68.9														
Confining Stress (kPa)	0														
Deviator Stress (KPa)	68.9														
Number of Load Repetition	1	2	10	100	500	1000	2000	3000	4000	5000	6000	7000	8000	9000	10000
Axial Permanent Microstrain	78	89	116	395	404	445	630	651	674	710	772	791	834	863	880
Axial Resilient Microstrain	38	38	38	39	39	39	39	39	40	40	40	40	40	40	40

Table A-14 Triaxial Cyclic Compression Test for 68.9 (kPa) at 40°C Base 0% HL

	AASHTOT307 Triaxial Cyclic Compression test (conducted at 40°C)														
Mix Type	0%HL-B														
Diameter (mm)	101.6mm														
Specimen Height (mm)	152.4 mm														
Bulk Density (g/cm3)	2.310														
Height of Block Pulse (kPa)	68.9														
Confining Stress (kPa)	0														
Deviator Stress (KPa)	68.9														
Number of Load Repetition	1	2	10	100	500	1000	2000	3000	4000	5000	6000	7000	8000	9000	10000
Axial Permanent Microstrain	92	120	154	364	400	666	702	810	835	999	1028	1100	1127	1164	1226
Axial Resilient Microstrain	64	64	64	65	65	65	66	66	66	66	66	66	66	66	66

Table A-15 Triaxial Cyclic Compression Test for 68.9 (kPa) at 60°CWearing 0% HL

	AASHTOT307 Triaxial Cyclic Compression test (conducted at 60°C)														
Mix Type	0%HL-W														
Diameter (mm)	101.6mm														
Specimen Height (mm)	152.4 mm														
Bulk Density (g/cm3)	2.340														
Height of Block Pulse (kPa)	68.9														
Confining Stress (kPa)	0														
Deviator Stress (KPa)	68.9														
Number of Load Repetition	1	2	10	100	500	1000	2000	3000	4000	5000	6000	7000	7033		
Axial Permanent Microstrain	183	236	420	961	1245	1843	2254	2745	3866	4285	4495	4800	4879		
Axial Resilient Microstrain	61	62	62	63	63	63	63	63	63	63	63	63	63		

Table A-16Triaxial Cyclic Compression Test for 68.9 (kPa) at 60°C Leveling 0% HL

	AASHTOT307 Triaxial Cyclic Compression test (conducted at 60°C)														
Mix Type	0%HL-L														
Diameter (mm)	101.6mm														
Specimen Height (mm)	152.4 mm														
Bulk Density (g/cm3)	2.320														
Height of Block Pulse (kPa)	68.9														
Confining Stress (kPa)	0														
Deviator Stress (KPa)	68.9														
Number of Load Repetition	1	2	10	100	500	1000	2000	3000	4000	5000	5398				
Axial Permanent Microstrain	211	278	532	1082	1745	2493	3542	4863	5938	6485	6689				
Axial Resilient Microstrain	69	69	69	70	70	70	70	70	70	70	70				

Table A-17 Triaxial Cyclic Compression Test for 68.9 (kPa) at 60°C Base 0%HL

	AASHTOT307 Triaxial Cyclic Compression test (conducted at 60°C)														
Mix Type	0%HL-B														
Diameter (mm)	101.6mm														
Specimen Height (mm)	152.4 mm														
Bulk Density (g/cm3)	2.310														
Height of Block Pulse (kPa)	68.9														
Confining Stress (kPa)	0														
Deviator Stress (KPa)	68.9														
Number of Load Repetition	1	2	10	100	500	1000	2000	3000	4000	5000	5212				
Axial Permanent Microstrain	256	343	672	1386	2386	3689	4532	6736	7996	8996	9155				
Axial Resilient Microstrain	110	111	111	111	111	111	111	111	111	111	111				

Table A-18 Triaxial Cyclic Compression Test for 137.895 (kPa) at 20°C Wearing 0% HL

	AASHTOT307 Triaxial Cyclic Compression test (conducted at 20°C)														
Mix Type	0%HL-W														
Diameter (mm)	101.6mm														
Specimen Height (mm)	152.4 mm														
Bulk Density (g/cm3)	2.340														
Height of Block Pulse (kPa)	206.843														
Confining Stress (kPa)	68.9														
Deviator Stress (KPa)	137.895														
Number of Load Repetition	1	2	10	100	500	1000	2000	3000	4000	5000	6000	7000	8000	9000	10000
Axial Permanent Microstrain	73	78	91	112	131	140	149	151	160	163	165	168	170	172	174
Axial Resilient Microstrain	50	50	50	50	50	50	50	50	51	51	51	51	51	51	51

Table A-19 Triaxial Cyclic Compression Test for 137.895 (kPa) at 20°C Leveling 0% HL

	AASHTOT307 Triaxial Cyclic Compression test (conducted at 20°C)														
Mix Type	0%HL-L														
Diameter (mm)	101.6mm														
Specimen Height (mm)	152.4 mm														
Bulk Density (g/cm3)	2.320														
Height of Block Pulse (kPa)	206.843														
Confining Stress (kPa)	68.9														
Deviator Stress (KPa)	137.895														
Number of Load Repetition	1	2	10	100	500	1000	2000	3000	4000	5000	6000	7000	8000	9000	10000
Axial Permanent Microstrain	69	75	92	123	152	165	181	190	197	203	208	212	215	218	221
Axial Resilient Microstrain	57	57	57	57	57	57	58	58	58	58	58	58	58	58	58

Table A-20 Triaxial Cyclic Compression Test for 137.895 (kPa) at 20°C Base 0% HL

	AASHTOT307 Triaxial Cyclic Compression test (conducted at 20°C)														
Mix Type	0%HL-B														
Diameter (mm)	101.6mm														
Specimen Height (mm)	152.4 mm														
Bulk Density (g/cm3)	2.320														
Height of Block Pulse (kPa)	206.843														
Confining Stress (kPa)	68.9														
Deviator Stress (KPa)	137.895														
Number of Load Repetition	1	2	10	100	500	1000	2000	3000	4000	5000	6000	7000	8000	9000	10000
Axial Permanent Microstrain	85	96	124	179	233	260	291	311	326	338	349	357	366	371	381
Axial Resilient Microstrain	80	80	80	80	80	80	81	81	81	81	81	82	82	82	82

Table A-21 Triaxial Cyclic Compression Test for 137.895 (kPa) at 40°C Wearing 0% HL

	AASHTOT307 Triaxial Cyclic Compression test (conducted at 40°C)														
Mix Type	0%HL-W														
Diameter (mm)	101.6mm														
Specimen Height (mm)	152.4 mm														
Bulk Density (g/cm3)	2.340														
Height of Block Pulse (kPa)	206.843														
Confining Stress (kPa)	68.9														
Deviator Stress (KPa)	137.895														
Number of Load Repetition	1	2	10	100	500	1000	2000	3000	4000	5000	6000	7000	7800		
Axial Permanent Microstrain	127	151	230	478	574	819	911	938	999	1029	1170	1202	1265		
Axial Resilient Microstrain	69	69	69	70	70	70	70	70	70	70	70	70	70		

Table A-22 Triaxial Cyclic Compression Test for 137.895 (kPa) at 40°C Leveling 0% HL

	AASHTOT307 Triaxial Cyclic Compression test (conducted at 40°C)														
Mix Type	0%HL-L														
Diameter (mm)	101.6mm														
Specimen Height (mm)	152.4 mm														
Bulk Density (g/cm3)	2.320														
Height of Block Pulse (kPa)	206.843														
Confining Stress (kPa)	68.9														
Deviator Stress (KPa)	137.895														
Number of Load Repetition	1	2	10	100	500	1000	2000	3000	4000	5000	6000	7000	7348		
Axial Permanent Microstrain	140	171	268	544	658	799	1254	1401	1485	1568	1567	1620	1764		
Axial Resilient Microstrain	76	76	77	77	77	77	77	77	77	77	77	77	77		

Table A-23 Triaxial Cyclic Compression Test for 137.895 (kPa) at 40°C Base 0% HL

	AASHTOT307 Triaxial Cyclic Compression test (conducted at 40°C)														
Mix Type	0%HL-B														
Diameter (mm)	101.6mm														
Specimen Height (mm)	152.4 mm														
Bulk Density (g/cm3)	2.310														
Height of Block Pulse (kPa)	206.843														
Confining Stress (kPa)	68.9														
Deviator Stress (KPa)	137.895														
Number of Load Repetition	1	2	10	100	500	1000	2000	3000	4000	5000	6000	6760			
Axial Permanent Microstrain	116	142	235	562	600	900	1213	1275	1327	1633	1669	1754			
Axial Resilient Microstrain	120	120	120	121	121	121	121	121	121	121	121	121			

Table A-24 Triaxial Cyclic Compression Test for 137.895 (kPa) at 60°C Wearing 0% HL

	AASHTOT307 Triaxial Cyclic Compression test (conducted at 60°C)														
Mix Type	0%HL-W														
Diameter (mm)	101.6mm														
Specimen Height (mm)	152.4 mm														
Bulk Density (g/cm3)	2.340														
Height of Block Pulse (kPa)	206.843														
Confining Stress (kPa)	68.9														
Deviator Stress (KPa)	137.895														
Number of Load Repetition	1	2	10	100	500	1000	2000	3000	4000	5000	5747				
Axial Permanent Microstrain	328	426	885	1569	2854	3456	4125	6100	6984	7698	8594				
Axial Resilient Microstrain	125	126	126	126	126	126	126	126	126	126	126				

Table A-25 Triaxial Cyclic Compression Test for 137.895 (kPa) at 60°C Leveling 0% HL

	AASHTOT307 Triaxial Cyclic Compression test (conducted at 60°C)														
Mix Type	0%HL-L														
Diameter (mm)	101.6mm														
Specimen Height (mm)	152.4 mm														
Bulk Density (g/cm3)	2.320														
Height of Block Pulse (kPa)	206.843														
Confining Stress (kPa)	68.9														
Deviator Stress (KPa)	137.895														
Number of Load Repetition	1	2	10	100	500	1000	2000	3000	4000	4228					
Axial Permanent Microstrain	358	484	965	1985	5987	7525	8543	10072	11668	13079					
Axial Resilient Microstrain	130	130	131	131	132	132	132	132	132	132					

Table A-26 Triaxial Cyclic Compression Test for 137.895 (kPa) at 60°C Base 0% HL

	AASHTOT307 Triaxial Cyclic Compression test (conducted at 60°C)														
Mix Type	0%HL-B														
Diameter (mm)	101.6mm														
Specimen Height (mm)	152.4 mm														
Bulk Density (g/cm3)	2.310														
Height of Block Pulse (kPa)	206.843														
Confining Stress (kPa)	68.9														
Deviator Stress (KPa)	137.895														
Number of Load Repetition	1	2	10	100	500	1000	2000	3000	3568						
Axial Permanent Microstrain	405	552	1110	3153	5236	6396	8743	13402	15565						
Axial Resilient Microstrain	228	229	229	229	229	229	229	229	229						

Table A-27 Triaxial Cyclic Compression Test for 206.89 (kPa) at 20°C Wearing 0% HL

	AASHTOT307 Triaxial Cyclic Compression test (conducted at 20°C)														
Mix Type	0%HL-W														
Diameter (mm)	101.6mm														
Specimen Height (mm)	152.4 mm														
Bulk Density (g/cm3)	2.340														
Height of Block Pulse (kPa)	275.79														
Confining Stress (kPa)	68.9														
Deviator Stress (KPa)	206.89														
Number of Load Repetition	1	2	10	100	500	1000	2000	3000	4000	5000	6000	7000	8000	9000	10000
Axial Permanent Microstrain	113	122	148	195	237	257	279	293	303	311	318	323	329	334	338
Axial Resilient Microstrain	76	76	76	76	76	76	77	77	77	77	77	77	77	77	77

Table A-28 Triaxial Cyclic Compression Test for 206.89 (kPa) at 20°C Leveling 0% HL

	AASHTOT307 Triaxial Cyclic Compression test (conducted at 20°C)														
Mix Type	0%HL-L														
Diameter (mm)	101.6mm														
Specimen Height (mm)	152.4 mm														
Bulk Density (g/cm3)	2.320														
Height of Block Pulse (kPa)	275.79														
Confining Stress (kPa)	68.9														
Deviator Stress (KPa)	206.89														
Number of Load Repetition	1	2	10	100	500	1000	2000	3000	4000	5000	6000	7000	8000	9000	10000
Axial Permanent Microstrain	131	146	186	264	236	376	418	443	464	480	494	507	516	525	533
Axial Resilient Microstrain	85	85	85	85	85	85	86	86	86	86	86	87	87	87	87

Table A-29 Triaxial Cyclic Compression Test for 206.89 (kPa) at 20°C Base 0% HL

	AASHTOT307 Triaxial Cyclic Compression test (conducted at 20°C)														
Mix Type	0%HL-B														
Diameter (mm)	101.6mm														
Specimen Height (mm)	152.4 mm														
Bulk Density (g/cm3)	2.310														
Height of Block Pulse (kPa)	275.79														
Confining Stress (kPa)	68.9														
Deviator Stress (KPa)	206.89														
Number of Load Repetition	1	2	10	100	500	1000	2000	3000	4000	5000	6000	7000	8000	9000	10000
Axial Permanent Microstrain	161	184	252	394	540	618	707	764	810	845	876	902	927	948	968
Axial Resilient Microstrain	120	120	120	121	121	121	121	121	121	122	122	123	123	123	123

Table A-30 Triaxial Cyclic Compression Test for 206.89 (kPa) at 40°C Wearing 0% HL

	AASHTOT307 Triaxial Cyclic Compression test (conducted at 40°C)														
Mix Type	0%HL-W														
Diameter (mm)	101.6mm														
Specimen Height (mm)	152.4 mm														
Bulk Density (g/cm3)	2.340														
Height of Block Pulse (kPa)	275.79														
Confining Stress (kPa)	68.9														
Deviator Stress (KPa)	206.89														
Number of Load Repetition	1	2	10	100	500	1000	2000	3000	4000	5000	6000				
Axial Permanent Microstrain	191	225	367	511	1254	1398	1457	1655	1785	1815	1872				
Axial Resilient Microstrain	111	111	111	112	112	112	113	113	113	113	113				

Table A-40 Triaxial Cyclic Compression Test for 206.89 (kPa) at 40°C Leveling 0% HL

	AASHTOT307 Triaxial Cyclic Compression test (conducted at 40°C)														
Mix Type	0%HL-L														
Diameter (mm)	101.6mm														
Specimen Height (mm)	152.4 mm														
Bulk Density (g/cm3)	2.320														
Height of Block Pulse (kPa)	275.79														
Confining Stress (kPa)	68.9														
Deviator Stress (KPa)	206.89														
Number of Load Repetition	1	2	10	100	500	1000	2000	3000	4000	5000	5465				
Axial Permanent Microstrain	201	258	385	742	1042	1896	2077	2100	2210	2419	2841				
Axial Resilient Microstrain	120	120	121	121	121	121	121	121	121	121	121				

Table A-41 Triaxial Cyclic Compression Test for 206.89 (kPa) at 40°C Base 0% HL

	AASHTOT307 Triaxial Cyclic Compression test (conducted at 40°C)														
Mix Type	0%HL-B														
Diameter (mm)	101.6mm														
Specimen Height (mm)	152.4 mm														
Bulk Density (g/cm3)	2.310														
Height of Block Pulse (kPa)	275.79														
Confining Stress (kPa)	68.9														
Deviator Stress (KPa)	206.89														
Number of Load Repetition	1	2	10	100	500	1000	2000	3000	4000	4241					
Axial Permanent Microstrain	225	284	479	807	1348	2191	2305	2446	2987	3340					
Axial Resilient Microstrain	234	234	235	235	235	235	235	235	235	235					

Table A-42 Triaxial Cyclic Compression Test for 206.89 (kPa) at 60°C Wearing 0% HL

	AASHTOT307 Triaxial Cyclic Compression test (conducted at 60°C)														
Mix Type	0%HL-W														
Diameter (mm)	101.6mm														
Specimen Height (mm)	152.4 mm														
Bulk Density (g/cm3)	2.340														
Height of Block Pulse (kPa)	275.79														
Confining Stress (kPa)	68.9														
Deviator Stress (KPa)	206.89														
Number of Load Repetition	1	2	10	100	500	1000	2000	3000	3888						
Axial Permanent Microstrain	382	498	977	2985	5292	5742	7524	9315	12628						
Axial Resilient Microstrain	176	176	176	176	176	176	176	176	176						

Table A-43 Triaxial Cyclic Compression Test for 206.89 (kPa) at 60°C Leveling 0% HL

	AASHTOT307 Triaxial Cyclic Compression test (conducted at 60°C)													
Mix Type	0%HL-L													
Diameter (mm)	101.6mm													
Specimen Height (mm)	152.4 mm													
Bulk Density (g/cm3)	2.320													
Height of Block Pulse (kPa)	275.79													
Confining Stress (kPa)	68.9													
Deviator Stress (KPa)	206.89													
Number of Load Repetition	1	2	10	100	500	1000	2000	3000	3190					
Axial Permanent Microstrain	436	589	1165	6061	10864	14408	17364	19735	21777					
Axial Resilient Microstrain	200	200	201	201	201	201	201	201	201					

Table A-44 Triaxial Cyclic Compression Test for 206.89 (kPa) at 60°C Base 0% HL

	AASHTOT307 Triaxial Cyclic Compression test (conducted at 60°C)															
Mix Type	0%HL-B															
Diameter (mm)	101.6mm															
Specimen Height (mm)	152.4 mm															
Bulk Density (g/cm3)	2.310															
Height of Block Pulse (kPa)	275.79															
Confining Stress (kPa)	68.9															
Deviator Stress (KPa)	206.89															
Number of Load Repetition	1	2	10	100	500	1000	1963									
Axial Permanent Microstrain	507	733	1716	5732	11074	22261	27489									
Axial Resilient Microstrain	342	342	342	342	342	342	342									

Table A- 45 Triaxial Cyclic Compression Test for 68.9 (kPa) at 20°CWearing 2.5% HL

	AASHTOT307 Triaxial Cyclic Compression test (conducted at 20°C)														
Mix Type	2.5%HL-W														
Diameter (mm)	101.6mm														
Specimen Height (mm)	152.4 mm														
Bulk Density (g/cm3)	2.320														
Height of Block Pulse (kPa)	68.9														
Confining Stress (kPa)	0														
Deviator Stress (KPa)	68.9														
Number of Load Repetition	1	2	10	100	500	1000	2000	3000	4000	5000	6000	7000	8000	9000	10000
Axial Permanent Microstrain	29	30	33	37	41	42	44	45	46	46	47	47	47	48	48
Axial Resilient Microstrain	20	20	20	20	20	20	20	20	21	21	21	21	21	21	21

Table A -46 Triaxial Cyclic Compression Test for 68.9 (kPa) at 20°C Leveling 2.5% HL

	AASHTOT307 Triaxial Cyclic Compression test (conducted at 20°C)														
Mix Type	2.5%HL-L														
Diameter (mm)	101.6mm														
Specimen Height (mm)	152.4 mm														
Bulk Density (g/cm3)	2.300														
Height of Block Pulse (kPa)	68.9														
Confining Stress (kPa)	0														
Deviator Stress (KPa)	68.9														
Number of Load Repetition	1	2	10	100	500	1000	2000	3000	4000	5000	6000	7000	8000	9000	10000
Axial Permanent Microstrain	32	34	37	44	49	51	53	55	56	56	57	58	59	59	59
Axial Resilient Microstrain	26	26	26	27	27	27	27	27	27	27	27	27	27	27	27

Table A-47 Triaxial Cyclic Compression Test for 68.9 (kPa) at 20°C Base 2.5% HL

	AASHTOT307 Triaxial Cyclic Compression test (conducted at 20°C)														
Mix Type	2.5%HL-B														
Diameter (mm)	101.6mm														
Specimen Height (mm)	152.4 mm														
Bulk Density (g/cm3)	2.297														
Height of Block Pulse (kPa)	68.9														
Confining Stress (kPa)	0														
Deviator Stress (KPa)	68.9														
Number of Load Repetition	1	2	10	100	500	1000	2000	3000	4000	5000	6000	7000	8000	9000	10000
Axial Permanent Microstrain	27	28	32	38	42	44	46	48	49	50	50	51	52	52	54
Axial Resilient Microstrain	35	35	35	35	35	35	36	36	36	36	36	36	36	36	36

TableA-48 Triaxial Cyclic Compression Test for 68.9 (kPa) at 40°C Wearing 2.5% HL

	AASHTOT307 Triaxial Cyclic Compression test (conducted at 40°C)														
Mix Type	2.5%HL-W														
Diameter (mm)	101.6mm														
Specimen Height (mm)	152.4 mm														
Bulk Density (g/cm3)	2.320														
Height of Block Pulse (kPa)	68.9														
Confining Stress (kPa)	0														
Deviator Stress (KPa)	68.9														
Number of Load Repetition	1	2	10	100	500	1000	2000	3000	4000	5000	6000	7000	8000	9000	10000
Axial Permanent Microstrain	62	75	85	214	295	343	352	385	465	485	480	490	500	549	565
Axial Resilient Microstrain	26	26	26	26	26	27	27	27	27	27	27	27	27	27	27

Table A-49 Triaxial Cyclic Compression Test for 68.9 (kPa) at 40°C Leveling 2.5% HL

	AASHTOT307 Triaxial Cyclic Compression test (conducted at 40°C)														
Mix Type	2.5%HL-L														
Diameter (mm)	101.6mm														
Specimen Height (mm)	152.4 mm														
Bulk Density (g/cm3)	2.300														
Height of Block Pulse (kPa)	68.9														
Confining Stress (kPa)	0														
Deviator Stress (KPa)	68.9														
Number of Load Repetition	1	2	10	100	500	1000	2000	3000	4000	5000	6000	7000	8000	9000	10000
Axial Permanent Microstrain	77	113	129	200	352	385	562	598	660	687	694	701	722	795	807
Axial Resilient Microstrain	33	33	33	33	34	34	34	34	35	35	35	35	35	35	35

Table A-50 Triaxial Cyclic Compression Test for 68.9 (kPa) at 40°C Base 2.5% HL

	AASHTOT307 Triaxial Cyclic Compression test (conducted at 40°C)														
Mix Type	2.5%HL-B														
Diameter (mm)	101.6mm														
Specimen Height (mm)	152.4 mm														
Bulk Density (g/cm3)	2.297														
Height of Block Pulse (kPa)	68.9														
Confining Stress (kPa)	0														
Deviator Stress (KPa)	68.9														
Number of Load Repetition	1	2	10	100	500	1000	2000	3000	4000	5000	6000	7000	8000	9000	10000
Axial Permanent Microstrain	80	114	122	273	350	550	603	672	725	740	787	842	872	927	945
Axial Resilient Microstrain	55	55	56	56	56	56	56	57	57	57	57	58	58	58	58

Table A-51 Triaxial Cyclic Compression Test for 68.9 (kPa) at 60°C Wearing 2.5% HL

	AASHTOT307 Triaxial Cyclic Compression test (conducted at 60°C)														
Mix Type	2.5%HL-W														
Diameter (mm)	101.6mm														
Specimen Height (mm)	152.4 mm														
Bulk Density (g/cm3)	2.297														
Height of Block Pulse (kPa)	68.9														
Confining Stress (kPa)	0														
Deviator Stress (KPa)	68.9														
Number of Load Repetition	1	2	10	100	500	1000	2000	3000	4000	5000	6000	7000	8000	9000	9266
Axial Permanent Microstrain	174	224	410	940	1145	1732	2351	2857	3425	3944	4217	4462	4529	4893	4945
Axial Resilient Microstrain	52	52	52	52	53	53	53	53	53	53	53	53	53	53	53

Table A-52 Triaxial Cyclic Compression Test for 68.9 (kPa) at 60°C Leveling 2.5% HL

	AASHTOT307 Triaxial Cyclic Compression test (conducted at 60°C)														
Mix Type	2.5%HL-L														
Diameter (mm)	101.6mm														
Specimen Height (mm)	152.4 mm														
Bulk Density (g/cm3)	2.300														
Height of Block Pulse (kPa)	68.9														
Confining Stress (kPa)	0														
Deviator Stress (KPa)	68.9														
Number of Load Repetition	1	2	10	100	500	1000	2000	3000	4000	5000	6000	7000	7729		
Axial Permanent Microstrain	193	250	456	956	1348	2589	2743	3128	4153	4598	4789	5163	5498		
Axial Resilient Microstrain	63	63	63	64	64	64	65	65	65	65	65	65	65		

Table A-53 Triaxial Cyclic Compression Test for 68.9 (kPa) at 60°C Base 2.5% HL

	AASHTOT307 Triaxial Cyclic Compression test (conducted at 60°C)														
Mix Type	2.5%HL-B														
Diameter (mm)	101.6mm														
Specimen Height (mm)	152.4 mm														
Bulk Density (g/cm3)	2.297														
Height of Block Pulse (kPa)	68.9														
Confining Stress (kPa)	0														
Deviator Stress (KPa)	68.9														
Number of Load Repetition	1	2	10	100	500	1000	2000	3000	4000	5000	6000	7000	7273		
Axial Permanent Microstrain	225	329	581	1239	1987	2654	3548	5603	6464	7073	7616	7935	8232		
Axial Resilient Microstrain	96	97	97	97	97	97	97	97	97	97	97	97	97		

Table A-54 Triaxial Cyclic Compression Test for 137.895 (kPa) at 20°C Wearing 2.5% HL

	AASHTOT307 Triaxial Cyclic Compression test (conducted at 20°C)														
Mix Type	2.5%HL-W														
Diameter (mm)	101.6mm														
Specimen Height (mm)	152.4 mm														
Bulk Density (g/cm3)	2.320														
Height of Block Pulse (kPa)	206.843														
Confining Stress (kPa)	68.9														
Deviator Stress (KPa)	137.895														
Number of Load Repetition	1	2	10	100	500	1000	2000	3000	4000	5000	6000	7000	8000	9000	10000
Axial Permanent Microstrain	67	77	81	99	114	121	128	133	136	139	141	143	145	146	149
Axial Resilient Microstrain	38	38	38	38	38	38	38	39	39	39	39	39	39	39	39

Table A-55 Triaxial Cyclic Compression Test for 137.895 (kPa) at 20°C Leveling 2.5% HL

	AASHTOT307 Triaxial Cyclic Compression test (conducted at 20°C)														
Mix Type	2.5%HL-L														
Diameter (mm)	101.6mm														
Specimen Height (mm)	152.4 mm														
Bulk Density (g/cm3)	2.300														
Height of Block Pulse (kPa)	206.843														
Confining Stress (kPa)	68.9														
Deviator Stress (KPa)	137.895														
Number of Load Repetition	1	2	10	100	500	1000	2000	3000	4000	5000	6000	7000	8000	9000	10000
Axial Permanent Microstrain	55	60	71	92	112	120	130	136	140	144	147	150	154	155	157
Axial Resilient Microstrain	45	45	45	45	45	45	45	45	46	46	46	46	46	46	46

TableA-56 Triaxial Cyclic Compression Test for 137.895 (kPa) at 20°C Base 2.5% HL

	AASHTOT307 Triaxial Cyclic Compression test (conducted at 20°C)														
Mix Type	2.5%HL-B														
Diameter (mm)	101.6mm														
Specimen Height (mm)	152.4 mm														
Bulk Density (g/cm3)	2.297														
Height of Block Pulse (kPa)	206.843														
Confining Stress (kPa)	68.9														
Deviator Stress (KPa)	137.895														
Number of Load Repetition	1	2	10	100	500	1000	2000	3000	4000	5000	6000	7000	8000	9000	10000
Axial Permanent Microstrain	80	89	114	164	213	237	263	281	294	304	313	321	327	334	339
Axial Resilient Microstrain	71	71	71	71	71	71	72	72	72	72	72	73	73	73	73

Table A-57 Triaxial Cyclic Compression Test for 137.895 (kPa) at 40°C Wearing 2.5% HL

	AASHTOT307 Triaxial Cyclic Compression test (conducted at 40°C)														
Mix Type	2.5%HL-W														
Diameter (mm)	101.6mm														
Specimen Height (mm)	152.4 mm														
Bulk Density (g/cm3)	2.320														
Height of Block Pulse (kPa)	206.843														
Confining Stress (kPa)	68.9														
Deviator Stress (KPa)	137.895														
Number of Load Repetition	1	2	10	100	500	1000	2000	3000	4000	5000	6000	7000	8000	9000	10000
Axial Permanent Microstrain	116	128	202	386	430	615	640	675	732	802	830	920	940	971	1059
Axial Resilient Microstrain	53	53	53	54	54	54	54	54	54	54	54	54	54	54	54

Table A-58 Triaxial Cyclic Compression Test for 137.895 (kPa) at 40°C Leveling 2.5% HL

	AASHTOT307 Triaxial Cyclic Compression test (conducted at 40°C)														
Mix Type	2.5%HL-L														
Diameter (mm)	101.6mm														
Specimen Height (mm)	152.4 mm														
Bulk Density (g/cm3)	2.300														
Height of Block Pulse (kPa)	206.843														
Confining Stress (kPa)	68.9														
Deviator Stress (KPa)	137.895														
Number of Load Repetition	1	2	10	100	500	1000	2000	3000	4000	5000	6000	7000	8000	9000	10000
Axial Permanent Microstrain	130	158	244	640	709	854	989	1252	1299	1325	1390	1449	1500	1521	1687
Axial Resilient Microstrain	60	60	60	60	60	61	61	61	61	61	61	61	61	61	61

Table A-59 Triaxial Cyclic Compression Test for 137.895 (kPa) at 40°C Base 2.5% HL

	AASHTOT307 Triaxial Cyclic Compression test (conducted at 40°C)														
Mix Type	2.5%HL-B														
Diameter (mm)	101.6mm														
Specimen Height (mm)	152.4 mm														
Bulk Density (g/cm3)	2.297														
Height of Block Pulse (kPa)	206.843														
Confining Stress (kPa)	68.9														
Deviator Stress (KPa)	137.895														
Number of Load Repetition	1	2	10	100	500	1000	2000	3000	4000	5000	6000	7000	8000	9000	9022
Axial Permanent Microstrain	120	144	213	652	767	840	1020	1210	1355	1599	1611	1683	1757	1800	1810
Axial Resilient Microstrain	100	100	101	101	101	101	101	101	101	101	101	101	101	101	101

Table A-60 Triaxial Cyclic Compression Test for 137.895 (kPa) at 60°C Wearing 2.5% HL

	AASHTOT307 Triaxial Cyclic Compression test (conducted at 60°C)														
Mix Type	2.5%HL-W														
Diameter (mm)	101.6mm														
Specimen Height (mm)	152.4 mm														
Bulk Density (g/cm3)	2.320														
Height of Block Pulse (kPa)	206.843														
Confining Stress (kPa)	68.9														
Deviator Stress (KPa)	137.895														
Number of Load Repetition	1	2	10	100	500	1000	2000	3000	4000	5000	6000	7000	8000	8558	
Axial Permanent Microstrain	255	324	570	987	2448	2856	3024	3458	3846	4008	4329	4631	5649	6052	
Axial Resilient Microstrain	1000	100	100	101	101	101	101	101	101	101	101	101	101	101	

Table A-61 Triaxial Cyclic Compression Test for 137.895 (kPa) at 60°C Leveling 2.5% HL

	AASHTOT307 Triaxial Cyclic Compression test (conducted at 60°C)														
Mix Type	2.5%HL-L														
Diameter (mm)	101.6mm														
Specimen Height (mm)	152.4 mm														
Bulk Density (g/cm3)	2.300														
Height of Block Pulse (kPa)	206.843														
Confining Stress (kPa)	68.9														
Deviator Stress (KPa)	137.895														
Number of Load Repetition	1	2	10	100	500	1000	2000	3000	4000	5000	6000	6267			
Axial Permanent Microstrain	288	379	721	1456	3924	5133	5735	6235	6743	7438	8023	8984			
Axial Resilient Microstrain	118	118	118	118	119	119	119	119	119	119	119	119			

Table A-62 Triaxial Cyclic Compression Test for 137.895 (kPa) at 60°C Base 2.5% HL

	AASHTOT307 Triaxial Cyclic Compression test (conducted at 60°C)														
Mix Type	2.5%HL-B														
Diameter (mm)	101.6mm														
Specimen Height (mm)	152.4 mm														
Bulk Density (g/cm3)	2.297														
Height of Block Pulse (kPa)	206.843														
Confining Stress (kPa)	68.9														
Deviator Stress (KPa)	137.895														
Number of Load Repetition	1	2	10	100	500	1000	2000	3000	4000	4408					
Axial Permanent Microstrain	365	488	954	2823	4956	5629	7258	10908	11743	12344					
Axial Resilient Microstrain	187	187	187	187	187	187	187	187	187	187					

Table A-63 Triaxial Cyclic Compression Test for 206.843 (kPa) at 20°C Wearing 2.5% HL

	AASHTOT307 Triaxial Cyclic Compression test (conducted at 20°C)														
Mix Type	2.5%HL-W														
Diameter (mm)	101.6mm														
Specimen Height (mm)	152.4 mm														
Bulk Density (g/cm3)	2.320														
Height of Block Pulse (kPa)	275.79														
Confining Stress (kPa)	68.9														
Deviator Stress (KPa)	206.843														
Number of Load Repetition	1	2	10	100	500	1000	2000	3000	4000	5000	6000	7000	8000	9000	10000
Axial Permanent Microstrain	100	108	128	165	195	211	227	237	245	251	256	261	264	268	271
Axial Resilient Microstrain	60	60	60	60	61	61	61	61	61	61	61	61	61	61	61

Table A-64 Triaxial Cyclic Compression Test for 206.843 (kPa) at 20°C Leveling 2.5% HL

	AASHTOT307 Triaxial Cyclic Compression test (conducted at 20°C)														
Mix Type	2.5%HL-L														
Diameter (mm)	101.6mm														
Specimen Height (mm)	152.4 mm														
Bulk Density (g/cm3)	2.300														
Height of Block Pulse (kPa)	275.79														
Confining Stress (kPa)	68.9														
Deviator Stress (KPa)	206.843														
Number of Load Repetition	1	2	10	100	500	1000	2000	3000	4000	5000	6000	7000	8000	9000	10000
Axial Permanent Microstrain	120	132	163	221	275	301	330	349	363	374	383	387	397	404	409
Axial Resilient Microstrain	70	70	70	71	71	71	71	71	72	72	72	72	73	73	73

Table A-65 Triaxial Cyclic Compression Test for 206.843 (kPa) at 20°C Base 2.5% HL

	AASHTOT307 Triaxial Cyclic Compression test (conducted at 20°C)														
Mix Type	2.5%HL-B														
Diameter (mm)	101.6mm														
Specimen Height (mm)	152.4 mm														
Bulk Density (g/cm3)	2.297														
Height of Block Pulse (kPa)	275.79														
Confining Stress (kPa)	68.9														
Deviator Stress (KPa)	206.843														
Number of Load Repetition	1	2	10	100	500	1000	2000	3000	4000	5000	6000	7000	8000	9000	10000
Axial Permanent Microstrain	141	159	212	319	425	481	543	582	615	639	661	679	696	710	724
Axial Resilient Microstrain	111	111	111	111	111	112	112	112	112	112	112	112	112	112	112

Table A-66 Triaxial Cyclic Compression Test for 206.843 (kPa) at 40°C Wearing 2.5% HL

	AASHTOT307 Triaxial Cyclic Compression test (conducted at 40°C)														
Mix Type	2.5%HL-W														
Diameter (mm)	101.6mm														
Specimen Height (mm)	152.4 mm														
Bulk Density (g/cm3)	2.297														
Height of Block Pulse (kPa)	275.79														
Confining Stress (kPa)	68.9														
Deviator Stress (KPa)	206.843														
Number of Load Repetition	1	2	10	100	500	1000	2000	3000	4000	5000	6000	7000	8000	9000	10000
Axial Permanent Microstrain	160	191	279	422	613	860	998	1022	1165	1200	1274	1288	1344	1438	1488
Axial Resilient Microstrain	79	79	80	80	80	80	80	80	80	80	80	80	80	80	80

Table A-67 Triaxial Cyclic Compression Test for 206.843 (kPa) at 40°C Leveling 2.5% HL

	AASHTOT307 Triaxial Cyclic Compression test (conducted at 40°C)														
Mix Type	2.5%HL-L														
Diameter (mm)	101.6mm														
Specimen Height (mm)	152.4 mm														
Bulk Density (g/cm3)	2.300														
Height of Block Pulse (kPa)	275.79														
Confining Stress (kPa)	68.9														
Deviator Stress (KPa)	206.843														
Number of Load Repetition	1	2	10	100	500	1000	2000	3000	4000	5000	6000	7000	8000	8853	
Axial Permanent Microstrain	206	248	398	638	857	1488	1826	2139	2215	2374	2411	2555	2601	2782	
Axial Resilient Microstrain	92	93	93	93	93	93	93	93	93	93	93	93	93	93	

Table A-68 Triaxial Cyclic Compression Test for 206.843 (kPa) at 40°C Base 2.5% HL

	AASHTOT307 Triaxial Cyclic Compression test (conducted at 40°C)														
Mix Type	2.5%HL-B														
Diameter (mm)	101.6mm														
Specimen Height (mm)	152.4 mm														
Bulk Density (g/cm3)	2.297														
Height of Block Pulse (kPa)	275.79														
Confining Stress (kPa)	68.9														
Deviator Stress (KPa)	206.843														
Number of Load Repetition	1	2	10	100	500	1000	2000	3000	4000	5000	6000	7000	7568		
Axial Permanent Microstrain	239	294	498	809	1294	1433	1849	2189	2771	3008	3145	3259	3325		
Axial Resilient Microstrain	153	153	153	153	153	153	153	153	153	153	153	153	153		

Table A-69 Triaxial Cyclic Compression Test for 206.843 (kPa) at 60°C Wearing 2.5% HL

	AASHTOT307 Triaxial Cyclic Compression test (conducted at 40°C)														
Mix Type	2.5%HL-W														
Diameter (mm)	101.6mm														
Specimen Height (mm)	152.4 mm														
Bulk Density (g/cm3)	2.320														
Height of Block Pulse (kPa)	275.79														
Confining Stress (kPa)	68.9														
Deviator Stress (KPa)	206.843														
Number of Load Repetition	1	2	10	100	500	1000	2000	3000	4000	5000	5366				
Axial Permanent Microstrain	333	430	830	2585	3143	4096	6143	7347	8021	9964	10141				
Axial Resilient Microstrain	155	156	156	156	156	156	156	156	156	156	256				

Table A-70 Triaxial Cyclic Compression Test for 206.843 (kPa) at 60°C Leveling 2.5% HL

	AASHTOT307 Triaxial Cyclic Compression test (conducted at 60°C)														
Mix Type	2.5%HL-L														
Diameter (mm)	101.6mm														
Specimen Height (mm)	152.4 mm														
Bulk Density (g/cm3)	2.300														
Height of Block Pulse (kPa)	275.79														
Confining Stress (kPa)	68.9														
Deviator Stress (KPa)	206.843														
Number of Load Repetition	1	2	10	100	500	1000	2000	3000	4000	4544					
Axial Permanent Microstrain	372	502	980	4684	5354	7215	9714	10567	12484	13817					
Axial Resilient Microstrain	188	188	188	188	188	188	188	188	188	188					

Table A-71 Triaxial Cyclic Compression Test for 206.843 (kPa) at 60°C Base 2.5% HL

	AASHTOT307 Triaxial Cyclic Compression test (conducted at 60°C)													
Mix Type	2.5%HL-B													
Diameter (mm)	101.6mm													
Specimen Height (mm)	152.4 mm													
Bulk Density (g/cm3)	2.297													
Height of Block Pulse (kPa)	275.79													
Confining Stress (kPa)	68.9													
Deviator Stress (KPa)	206.843													
Number of Load Repetition	1	2	10	100	500	1000	2000	3000	3654					
Axial Permanent Microstrain	489	691	1531	4849	9288	17931	19918	23323	29043					
Axial Resilient Microstrain	305	305	305	306	306	306	306	306	306					